



HAL
open science

Reformage autotherme de biogaz modèle sur des catalyseurs au nickel

Mathilde Luneau

► **To cite this version:**

Mathilde Luneau. Reformage autotherme de biogaz modèle sur des catalyseurs au nickel. Catalyse. Université de Lyon, 2016. Français. NNT : 2016LYSE1129 . tel-01570864

HAL Id: tel-01570864

<https://theses.hal.science/tel-01570864>

Submitted on 1 Aug 2017

HAL is a multi-disciplinary open access archive for the deposit and dissemination of scientific research documents, whether they are published or not. The documents may come from teaching and research institutions in France or abroad, or from public or private research centers.

L'archive ouverte pluridisciplinaire **HAL**, est destinée au dépôt et à la diffusion de documents scientifiques de niveau recherche, publiés ou non, émanant des établissements d'enseignement et de recherche français ou étrangers, des laboratoires publics ou privés.



N°d'ordre NNT :

THESE de DOCTORAT DE L'UNIVERSITE DE LYON

opérée au sein de
l'Université Claude Bernard Lyon 1

Ecole Doctorale N° 206
Ecole Doctorale de Chimie de Lyon

Soutenue publiquement le 22/07/2016, par :

Mathilde Luneau

Reformage autotherme de biogaz modèle sur des catalyseurs au nickel

Devant le jury composé de :

Anne Giroir-Fendler	Professeur	Université Lyon 1	
Florence Epron	Directrice de Recherche	CNRS, Poitiers	rapporteur
Anne-Cécile Roger	Professeur	Université Strasbourg	rapporteur
Patrick Da Costa	Professeur	UPMC	
Daniel Gary	Ingénieur de Recherche	Air Liquide	
Nolven Guillaume	Chargée de Recherche	IRCELYon	Directrice de thèse
Frédéric Meunier	Chargé de Recherche	IRCELYon	Co-directeur de thèse
Yves Schuurman	Directeur de Recherche	IRCELYon	

UNIVERSITE CLAUDE BERNARD - LYON 1

Président de l'Université

Président du Conseil Académique

Vice-président du Conseil d'Administration

Vice-président du Conseil Formation et Vie Universitaire

Vice-président de la Commission Recherche

Directeur Général des Services

M. le Professeur Frédéric FLEURY

M. le Professeur Hamda BEN HADID

M. le Professeur Didier REVEL

M. le Professeur Philippe CHEVALIER

M. Fabrice VALLÉE

M. Alain HELLEU

COMPOSANTES SANTE

Faculté de Médecine Lyon Est – Claude Bernard

Faculté de Médecine et de Maïeutique Lyon Sud – Charles Mérieux

Faculté d'Odontologie

Institut des Sciences Pharmaceutiques et Biologiques

Institut des Sciences et Techniques de la Réadaptation

Département de formation et Centre de Recherche en Biologie Humaine

Directeur : M. le Professeur J. ETIENNE

Directeur : Mme la Professeure C. BURILLON

Directeur : M. le Professeur D. BOURGEOIS

Directeur : Mme la Professeure C. VINCIGUERRA

Directeur : M. le Professeur Y. MATILLON

Directeur : Mme la Professeure A-M. SCHOTT

COMPOSANTES ET DEPARTEMENTS DE SCIENCES ET TECHNOLOGIE

Faculté des Sciences et Technologies

Département Biologie

Département Chimie Biochimie

Département GEP

Département Informatique

Département Mathématiques

Département Mécanique

Département Physique

UFR Sciences et Techniques des Activités Physiques et Sportives

Observatoire des Sciences de l'Univers de Lyon

Polytech Lyon

Ecole Supérieure de Chimie Physique Electronique

Institut Universitaire de Technologie de Lyon 1

Ecole Supérieure du Professorat et de l'Education

Institut de Science Financière et d'Assurances

Directeur : M. F. DE MARCHI

Directeur : M. le Professeur F. THEVENARD

Directeur : Mme C. FELIX

Directeur : M. Hassan HAMMOURI

Directeur : M. le Professeur S. AKKOUCHE

Directeur : M. le Professeur G. TOMANOV

Directeur : M. le Professeur H. BEN HADID

Directeur : M. le Professeur J-C PLENET

Directeur : M. Y. VANPOULLE

Directeur : M. B. GUIDERDONI

Directeur : M. le Professeur E. PERRIN

Directeur : M. G. PIGNAULT

Directeur : M. le Professeur C. VITON

Directeur : M. le Professeur A. MOUGNIOTTE

Directeur : M. N. LEBOISNE

Remerciements

Cette thèse a été réalisée à l'Institut de Recherches sur la Catalyse et l'Environnement de Lyon, Unité Mixte de Recherches 5256 CNRS – Université de Lyon 1. Elle a été financée par le programme de recherche Fuel Cells and Hydrogen Joint Undertaking de l'Union Européenne dans le cadre du projet européen BioRobur.

Je remercie en premier lieu Mr Michel Lacroix, ancien directeur, et Mme Catherine Pinel actuelle directrice de l'IRCELYon pour leur accueil dans l'Institut.

Je tiens à remercier mes encadrants Nolven, Frédéric et Yves qui m'ont fait confiance et m'ont donné l'opportunité de travailler sur ce projet européen à leurs côtés. Merci pour votre accompagnement et les échanges scientifiques lors de ces 3 années. Votre encadrement m'a permis de réaliser cette thèse dans les meilleures conditions et dans la bonne humeur. J'en retiens également de très bons moments passés lors des différentes réunions de projet en Allemagne, Grèce, Italie et Suisse.

Je voudrais également remercier Claude Mirodatos qui a participé à l'élaboration du projet avec les partenaires européens et Eric Puzenat pour son apport scientifique.

Merci à Elia qui a contribué à ces travaux et avec qui j'ai pu travailler sur le projet pendant une année.

Merci au personnel administratif de l'Institut qui a toujours été très disponible. Un grand merci également à tous les membres des services scientifiques avec qui j'ai eu l'occasion de travailler. Merci notamment à Pascale, Noëlle, Laurence, Françoise et Yoann. Je remercie également les membres de l'atelier qui ont été d'une grande aide même dans les projets les plus étonnants.

Merci aux membres (actuels et anciens) de l'équipe Ingénierie. La bonne humeur et la bonne entente dans cette équipe facilitent les échanges scientifiques et l'entraide. Ces bons moments passés lors des pauses cafés et déjeuners ont également été bénéfiques à mon travail et m'ont permis de dépasser certains obstacles rencontrés lors de cette thèse.

Je remercie particulièrement David Farrusseng pour son accueil dans l'équipe et pour avoir organisé les meilleurs barbecues de l'Institut.

Je souhaite remercier Marie Rochoux qui m'a donné des conseils précieux en début de thèse.

Merci à Florian et Manu qui, grâce à leurs expertises, m'ont permis de réaliser les tests et les expériences dans les meilleures conditions. Plus particulièrement, je remercie Manu qui a toujours été prêt à m'aider pour résoudre des problèmes techniques, avec le sourire.

Je tiens à remercier Jérôme pour tous les cafés con leche et pour son soutien pendant les 3 ans.

Merci à tous les collègues du bureau 212. Merci notamment à David Laprun, mon collègue de bureau préféré.

Je tiens à remercier Cindy qui a permis ma bonne intégration dans l'équipe et dans l'institut et dont l'amitié m'a été précieuse pendant ces 3 années.

Enfin, je tiens à remercier ma famille, mes parents, ma sœur et Annabelle pour leur soutien sans faille.

Table of Contents

Résumé des travaux de thèse	2
Chapter 1: Literature review and thermodynamic study	10
1.1 General context	11
1.2 Autothermal reforming of biogas	13
1.2.1 Description of the reforming process	13
1.2.2 Thermodynamic study of the autothermal reforming of methane	15
1.3 Catalysts	19
1.3.1 Metals	19
1.3.2 Supports	20
1.3.3 Hydrotalcite-type precursors	23
1.4 Mechanism of ATR over nickel based catalysts	24
1.4.1 Mechanism of the partial oxidation of methane	24
1.4.2 Mechanism of the steam reforming of methane	26
1.4.3 Mechanism of the Water Gas Shift	27
1.5 Catalyst deactivation	28
1.5.1 Poisoning	28
1.5.2 Sintering	29
1.5.3 Carbon formation	30
1.5.4 Nickel oxidation and NiAl ₂ O ₄ spinel formation	32
1.6 The BioRobur project	33
1.7 Conclusion and description of Ph.D. work	35
Chapter 2: Experimental methods	42
2.1 Catalysts preparation	43
2.1.1 Supports	43
2.1.2 Impregnations with Ni, Ni-Rh and Rh	45
2.2 Characterizations	45
2.2.1 X-Ray Diffraction (XRD)	45
2.2.2 Transmission Electron Microscopy (TEM)	46
2.2.3 Inductively Coupled Plasma (ICP)	46
2.2.4 Brunauer, Emmet and Tellet (BET) –Specific Surface Areas	46
2.2.5 XPS	46
2.2.6 UV-vis DRS	46
2.3 Catalytic tests	48
2.3.1 Catalytic tests on powders	48

2.3.2	Catalytic tests on coated SiSiC foams.....	52
2.4	Evaluation of performances.....	53
2.4.1	Mass Spectrometer Online Analysis.....	53
2.4.2	Description of conditions and activity analysis.....	54
2.5	Evaluation of diffusion limitations	55
2.5.1	External mass transport limitation.....	55
2.5.2	Internal mass transport limitation.....	56
2.5.3	External heat transfer limitation	57
2.5.4	Internal heat transfer limitation	58
2.6.	Conclusions	58
Chapter 3: Catalyst screening for the autothermal reforming of model biogas		61
3.1	Prepared catalysts and characterizations.....	62
3.2	Set-up validation on commercial catalyst	65
3.3	ATR of model biogas over prepared catalysts.....	69
3.4	Influence of Ni loading on LaAlO ₃ and Mg _{0.7} Al ₂ O _{3.7}	73
3.5	Conclusions	76
Chapter 4: Investigation of the deactivation process of Ni catalysts supported on Mg _x Al ₂ O _{3+x}		79
4.1	Deactivation investigation.....	80
4.1.1	Preliminary observations	80
4.1.2	Carbon formation	81
4.1.3	Sintering.....	82
4.1.4	Quantification of oxidized nickel by hydrogen pulses	83
4.1.5	ATR of model biogas on NiO vs NiAl ₂ O ₄	92
4.1.6	X-ray photoelectron spectroscopy on Ni/Mg _{0.7} Al ₂ O _{3.7} , NiO and NiAl ₂ O ₄	94
4.1.7	Temperature profile during ATR of model biogas on 5 wt.% Ni/Mg _{0.4} Al ₂ O _{3.4}	95
4.1.8	UV-vis DRS analysis of catalyst at different time-on-stream durations	98
4.2	Influence of Mg:Al ratio.....	105
4.3	Promotion of Ni/Mg _x Al ₂ O _{3+x} catalyst by rhodium.....	108
4.3.1	Addition of Rh on a nickel catalyst.....	108
4.3.2	Dual-bed catalyst coupling 0.05 wt.% Rh/Mg _{1.1} Al ₂ O _{4.1} with 5 wt.% Ni/Mg _{0.4} Al ₂ O _{3.4}	109
4.4	Discussion	113
4.5	Conclusions	116
Chapter 5: Kinetic modelling of autothermal biogas reforming over NiRh catalyst supported on SiSiC foams.....		118
5.1	SiSiC foams as catalyst supports for autothermal reforming of biogas.....	119
5.1.1	SiSiC foams	119

5.1.2	Characterizations of the coated SiSiC foams	121
5.2	Autothermal reforming of model biogas over nickel catalyst supported on SiSiC foams	123
5.2.1	Activity and stability of the coated SiSiC foams.....	123
5.2.2	Temperature profile	124
5.3	Kinetic model	126
5.3.1	Influence of temperature, CO ₂ /CH ₄ and Steam/CH ₄ ratio on methane conversions and H ₂ /CO ratio	127
5.3.2	One-dimensional model assumptions.....	128
5.3.3	Reactions.....	129
5.3.4	Mass, energy and momentum balance equations	132
5.3.5	Results.....	135
5.3.6	Discussion	139
5.4	Deactivation profile over Ni/Mg _x Al ₂ O _{3+x} catalyst powders.....	141
5.5	Conclusions	142
	General conclusions and perspectives.....	145
	Annex	151

Abbreviations

ATR: Autothermal Reforming Reaction

BE: Binding Energy

BET: Brunauer, Emmet and Teller

CCD: Charge Couple Device

CERTH: Centre for Research and Technology Hellas

CRR: Combustion and Reforming Reaction

DPO: Direct Partial Oxidation

DR: Dry Reforming

DRS: Diffuse Reflectance Spectroscopy

EDTA: Ethylenediaminetetraacetic acid

EDX: Energy Dispersive X-ray

GHSV: Gas Hourly Space Velocity

ICP: Inductively Coupled Plasma

KM: Kubelka Munk

MCFC: Molten Carbonate Fuel Cell

MET: Modernos E-Technologijos

MS: Mass Spectrometer

PEM: Proton Exchange Membrane

PGM: Platinum Group Metals

POLITO: Politecnico di Torino

POx: Partial Oxidation

r.d.s.: rate determining step

SOFC: Solid Oxide Fuel Cell

SR: Steam Reforming

SSA: Specific Surface Area

SUPSI: Scuola Universitaria Professionale della Svizzera Italiana

TEM: Transmission Electron Microscopy

TGA: Thermogravimetric analysis

TOS: Time On Stream

TPR: Temperature Programmed Reduction

TUBAF: Technical University Bergakademie Freiberg

UV-vis DRS: UV and Visible Diffuse Reflectance Spectroscopy

WGS: Water Gas Shift

XPS: X-ray Photoelectron Spectroscopy

XRD: X-Ray Diffraction

Résumé des travaux de thèse

L'hydrogène pourrait être une des sources d'énergies prédominantes dans les années à venir. De nos jours, la production d'hydrogène provient majoritairement de ressources fossiles et notamment du reformage de gaz naturel. En vue de l'augmentation de la demande d'hydrogène et de l'impact néfaste de l'utilisation de ressources fossiles sur l'environnement, la production d'hydrogène à partir de ressources renouvelables présente un grand intérêt. On parle alors d'un modèle économique appelé « économie hydrogène » qui viendrait remplacer l'actuelle économie basée sur le pétrole.

Afin de profiter de cette économie, de nombreux obstacles technologiques et économiques doivent être surmontés, autant pour le stockage que pour la production d'hydrogène. Dans nos travaux, le reformage autotherme du biogaz, une source renouvelable de méthane, a été étudié. Cette étude s'inscrit dans le projet Européen « BioRobur » qui vise à développer un reformeur autotherme de biogaz pour la production d'électricité par une pile à combustible alimentée en hydrogène.

1) Contexte et objectifs de la thèse

Le reformage autotherme consiste à faire réagir le biogaz avec de l'oxygène (contenu dans l'air) et de la vapeur d'eau. L'oxygène, présent en quantité sous stœchiométrique, permet de réaliser la combustion d'une partie du méthane. Cette réaction exotherme va générer la chaleur nécessaire aux réactions endothermiques de reformage à sec ou à la vapeur. Un mélange d'hydrogène et de monoxyde de carbone, plus couramment appelé gaz de synthèse, est obtenu.

Le reformage catalytique du méthane est communément réalisé sur des catalyseurs au nickel [1]. Bien qu'étant moins actif pour le reformage de méthane que certains métaux nobles tels que le rhodium ou le ruthénium, le nickel est incontestablement moins cher et est donc plus utilisé à l'échelle industrielle [2]. Cependant, le nickel est plus enclin à la désactivation par phénomènes d'empoisonnement, de formation de carbone, de frittage ou encore d'oxydation.

Notre étude portera sur le reformage autotherme de biogaz modèle composé à 60% de méthane et 40% de dioxyde de carbone en présence de vapeur d'eau et d'oxygène respectant les ratios $H_2O/CH_4 = 3$ et $O_2/CH_4 = 0.5$, à $700^\circ C$ et sous pression atmosphérique.

Dans un premier temps, un criblage haut débit de différents catalyseurs au nickel sera réalisé afin de sélectionner un catalyseur actif et stable pour la réaction autotherme (ATR).

Dans un second temps, le phénomène de désactivation de catalyseurs au nickel supportés sur un spinelle de magnésium sera élucidé et décrit. Grâce à la compréhension du phénomène, des solutions seront apportées afin de prévenir cette désactivation.

Enfin, dans une troisième et dernière partie, la cinétique de la réaction de reformage autotherme de biogaz sera étudiée sur des catalyseurs structurés. Un modèle cinétique sera proposé.

2) Criblage des catalyseurs au nickel pour le reformage autotherme du biogaz

Un système de criblage haut débit a été mis en place afin de réaliser des tests de vieillissement de longue durée. Ce système, constitué de six réacteurs identiques fonctionnant en parallèle, permet de tester six catalyseurs dans les mêmes conditions de température et de pression et sous le même flux de réactifs. Il permet donc une économie de temps et une comparaison précise des différents catalyseurs entre eux.

Avant de tester les catalyseurs d'intérêt, le système de réacteurs parallèles a été validé avec un catalyseur de reformage commercial fourni par Alfa Aesar [HiFUEL, R110, Alfa Aesar, ref. 45465]. 6 réacteurs ont donc été chargés de façon identique avec la même masse de catalyseur. Devant la similarité des profils de conversions et les performances dans les six réacteurs, la répétabilité et la fiabilité du système ont été validées.

9 catalyseurs tous composés de 5 % de nickel ont été préparés. Certains possèdent également une faible quantité de Rh (0.05 %) (Tableau 1).

Tableau 1 : Liste des catalyseurs préparés

Catalyseurs préparés	Code
5 wt.% Ni/Mg _{0.7} Al ₂ O _{3.7}	NM
5-0.05 wt.% NiRh/Mg _{0.7} Al ₂ O _{3.7}	NRM
5 wt.% Ni/ZnAl ₂ O ₄	NZ
5 wt.% Ni/LaAlO ₃	NL
5-0.05 wt.% NiRh/LaAlO ₃	NRL
LaNiO ₃	LN
5 wt.% Ni/CeO ₂ -Al ₂ O ₃	NCA
5 wt.% Ni/ZrO ₂ -Al ₂ O ₃	NZA
Hydrotalcite-type precursor	HT

3 catalyseurs disponibles dans le laboratoire ont été testés avec les 9 catalyseurs préparés : 20 % Ni/Al₂O₃ (NA), 20 % Ni/SiO (NS) et NiO/CaAl₁₂O₁₉ (NC). Après réduction à 700°C pendant 3h avec un mélange constitué de 20% d'H₂ dans l'Ar, la réaction a été réalisée à 700°C dans des conditions standards avec un mélange de réactif composé de 42% de vapeur d'eau, 14% CH₄, 9% CO₂, 7% O₂ dilué dans de l'Ar. Ceci correspond aux rapports molaires suivant : H₂O/CH₄ = 3 et O₂/CH₄ = 0.5. La Figure 1 montre les conversions de méthane pour chaque catalyseur en fonction du temps.

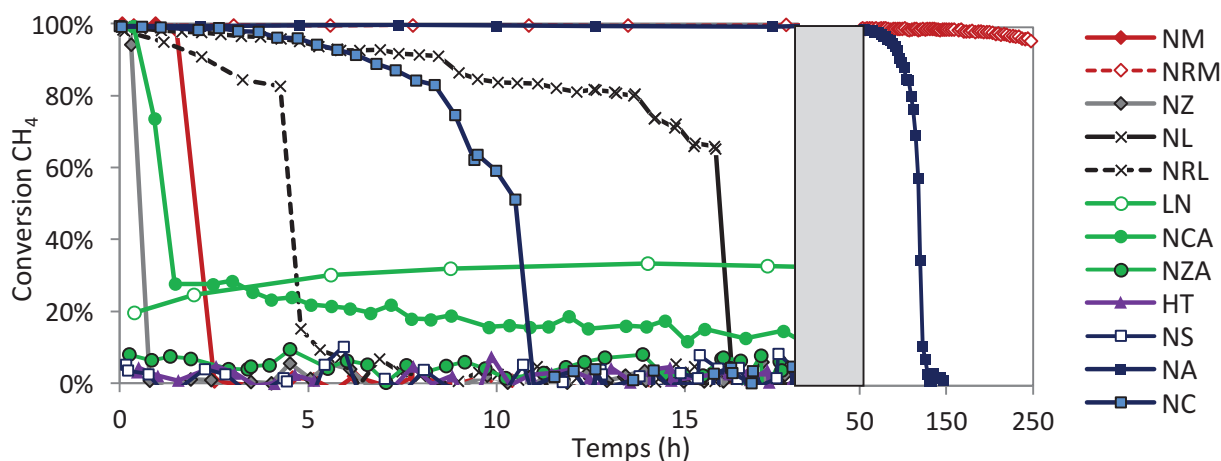


Figure 1: Conversion du méthane pendant le reformage autotherme du biogaz modèle à 700°C. Conditions de réaction: $H_2O/CH_4 = 3$ et $O_2/CH_4 = 0.5$ et $CH_4:CO_2 = 60\%:40\%$

La majorité des catalyseurs se désactivent avant 20 h. Parmi les catalyseurs ne contenant que 5 % en masse de Ni, 5 % Ni/LaAlO₃ s'est révélé être le plus résistant, se désactivant après 16 heures. Le catalyseur le plus résistant est 5-0.05 % NiRh/Mg_{0.7}Al₂O_{3.7}, montrant une conversion totale du méthane après 200 heures de réaction.

3) Etude de la désactivation du catalyseur Ni/MgAl₂O₄

Lors du criblage, 5-0.05 % NiRh/ Mg_{0.7}Al₂O_{3.7} s'est montré être le plus actif et le plus stable des catalyseurs tandis que son équivalent Ni/Mg_{0.7}Al₂O_{3.7}, ne possédant pas de Rh, s'est désactivé après seulement 2 heures de réaction. Les premières caractérisations post-réaction du catalyseur désactivé permettent d'exclure la formation de carbone, le frittage ou encore l'empoisonnement du catalyseur comme causes principales de désactivation. Restent alors l'hypothèse que la désactivation du catalyseur est due à l'oxydation du nickel et/ou à la formation du spinelle de nickel NiAl₂O₄.

Il est important de noter ici que lors de la réaction, la couleur du catalyseur passe du noir (nickel réduit) avant réaction au bleu/vert clair après désactivation. Le nickel sous sa forme NiO est vert tandis que le spinelle de Ni est bleu. Un catalyseur de type Ni/Mg_{0.4}Al₂O_{3.4} est testé à nouveau dans les mêmes conditions que précédemment mais dans un réacteur tubulaire dans lequel six thermocouples sont placés à différentes hauteurs de lit catalytique. Le test permet d'observer que la zone exotherme, située à l'entrée du lit en début de réaction, se déplace jusqu'à la sortie tout au long du test, jusqu'à désactivation totale du catalyseur.

Une nouvelle série de tests est réalisée avec ce même catalyseur. Quatre réacteurs sont préparés avec ce même catalyseur. Dans chaque réacteur, le lit catalytique a été séparé en quatre tranches de 10 mg de catalyseur. Les tests catalytiques sont stoppés à 4 temps de réaction différents afin d'observer l'évolution de la couleur du lit en fonction du temps. Grâce à des analyses UV-vis-DRS

permettant de discriminer les espèces de nickel oxydées NiO et NiAl₂O₄, il est observé que le spinelle de nickel se forme progressivement depuis le haut du lit en début de réaction jusqu'à la fin du lit (Figure 2). Après désactivation totale, le nickel n'est présent que sous forme de spinelle, inactif.

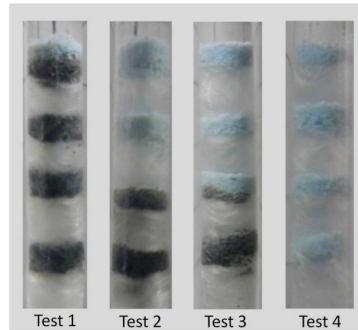


Figure 2 : Photographies du catalyseur Ni/Mg_{0.4}Al₂O_{3.4} à différents temps de réaction montrant la progression du spinelle de nickel (bleu ciel) sur le nickel réduit (noir)

Alors le processus de désactivation peut être décrit de la manière suivante : Avant réaction et après réduction à 700°C, la plus grande partie du nickel est présente sous forme de nickel réduit. La réaction de reformage autotherme est lancée. La réaction exothermique de combustion se fait à l'entrée du lit, convertissant la totalité de l'oxygène et une partie du méthane. Dans cet environnement oxydant, le nickel à l'entrée du lit se ré-oxyde en NiO à l'entrée du lit. Le reste du méthane est reformé plus en aval, là où le nickel est encore sous sa forme réduite car l'oxygène est déjà entièrement converti. Or, dans la partie exotherme, les hautes températures induisent un désordre dans la structure cristalline du support qui permet alors aux ions Ni²⁺ de diffuser dans les lacunes et de créer une phase NiAl₂O₄. NiAl₂O₄ étant inactif pour la combustion, celle-ci doit alors se dérouler en aval. Le nickel jusqu'ici réduit se ré-oxyde et le processus se répète jusqu'à la fin du lit et entraîne une désactivation totale du catalyseur. La Figure 3 illustre ce processus de désactivation.

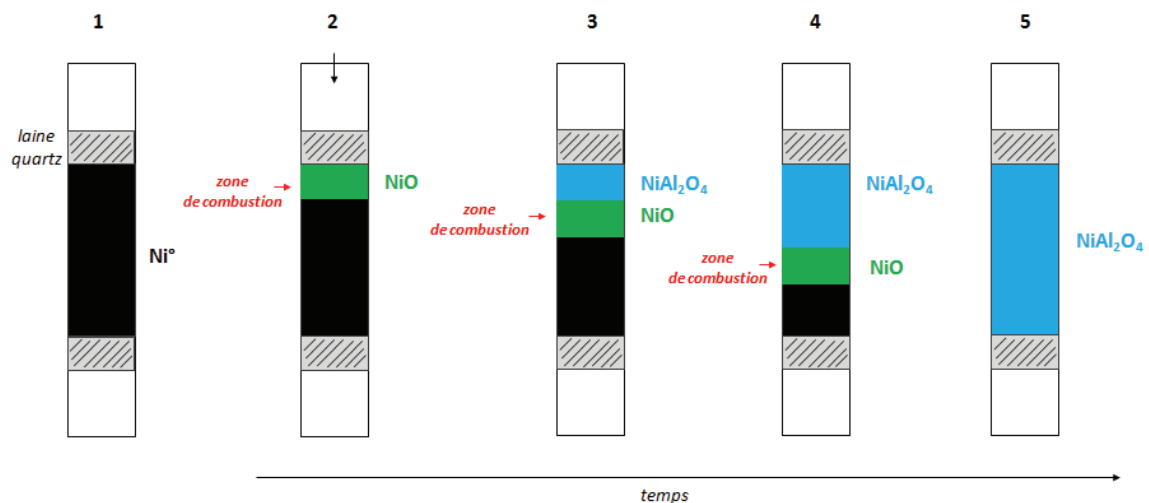


Figure 3 : schéma représentant le processus de désactivation d'un catalyseur Ni/Mg_xAl₂O_{3+x} lors du reformage autotherme de biogaz modèle à 700°C

La stabilité du catalyseur bimétallique NiRh lors du criblage peut être expliquée par la stabilisation de la zone de combustion grâce à la présence d'une faible quantité de Rh qui est très actif pour les réactions de combustion et de reformage.

Réaliser la réaction sur un lit catalytique composé de 2 catalyseurs s'est également avéré être bénéfique : Le premier catalyseur, un catalyseur très peu chargé en Rh mais très stable, permet de convertir la totalité de l'oxygène en réalisant la réaction de combustion. Le deuxième, un catalyseur au Ni, ne réalise que le reformage et le water gas shift en absence d'oxygène et de température très élevée. Ce système permet d'obtenir un catalyseur actif et très stable.

4) Modèle cinétique

A l'échelle du pilote de démonstration, la réaction a été réalisée sur des supports de type « mousse » composés de SiSiC sur lesquelles le catalyseur NiRh/MgAl₂O₄ a été déposé par des partenaires du projet (Figure 4). L'intérêt principal de ce type de support est qu'il présente une grande conductivité thermique ainsi qu'une géométrie complexe permettant une bonne distribution du flux. Ces catalyseurs structurés présentent une grande résistance à des températures élevées et n'entraînent pas de perte de charges importantes.



Figure 4: Photographie du catalyseur structuré composé d'un support en SiSiC sur lequel a été déposé le catalyseur NiRh/MgAl₂O₄.

Afin d'optimiser le procédé, la cinétique de la réaction a été étudiée. Contrairement au reformage à la vapeur, peu de modèles cinétiques ont été proposés dans la littérature pour le reformage autotherme du méthane.

Le catalyseur structuré a tout d'abord été testé dans les conditions de reformage autotherme du biogaz modèle. Pendant les 28 heures de réaction, la conversion du méthane était totale et le ratio molaire H₂/CO était de 4. Le catalyseur est actif et stable.

Deux modèles inspirés de la littérature ont été choisis et comparés pour décrire la réaction. Ces deux modèles consistent en l'association d'un modèle cinétique décrivant la réaction de combustion du méthane à un modèle cinétique décrivant la réaction de reformage à la vapeur du méthane. Le

modèle cinétique de combustion est le même dans les 2 modèles. Il a été proposé par Trimm & Lam [3]. Les deux modèles diffèrent alors par les paramètres cinétiques décrivant le reformage à la vapeur. Le premier modèle s'appuie sur l'étude du reformage à la vapeur proposée par Hou & Hughes [4]. Le deuxième s'appuie sur le modèle proposé par Xu & Froment [5].

Les performances des modèles ont été évaluées en s'appuyant sur les données suivantes : la conversion de méthane, le ratio H_2/CO en sortie et la température de sortie.

Après optimisation, les deux modèles décrivent bien les expériences. Cependant, le profil de température dans le lit catalytique est mieux décrit par le second modèle (Xu & Froment + Trimm & Lam). Ce dernier modèle a donc été retenu. La Figure 5 présente une comparaison entre les valeurs expérimentales et celles estimées avec le modèle.

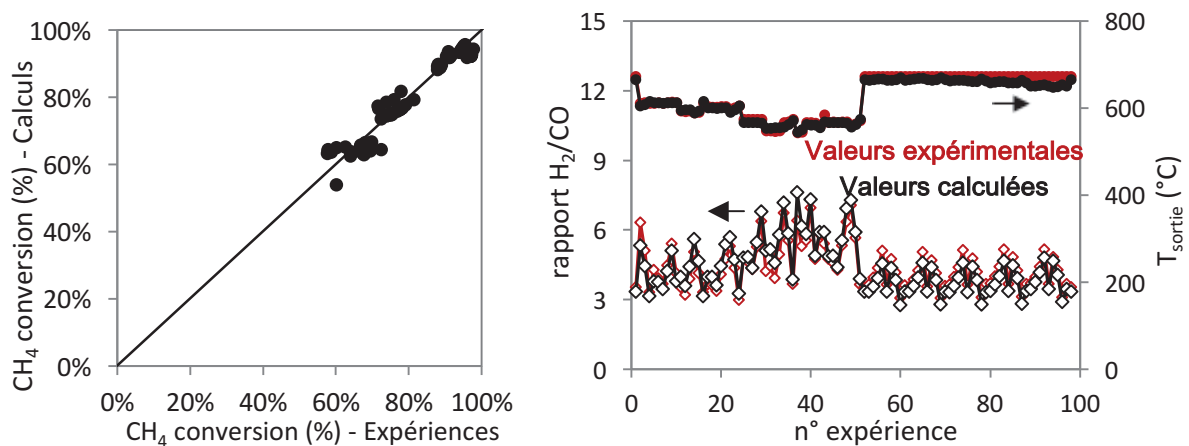


Figure 5 : a) Comparaison des conversions de méthane observées expérimentalement et celles estimées avec le modèle b) Comparaison des valeurs expérimentales avec les valeurs estimées des ratios H_2/CO et des températures de sortie

Quelques écarts peuvent être observés entre l'expérience et le modèle. Ceux-ci peuvent être expliqués par la présence d'un point chaud dans nos catalyseurs structurés lors de la réaction. Cette réaction mettant en jeu à la fois des réactions exothermique et endothermique, le profil de température s'avère être un paramètre très important mais qu'il est difficile d'estimer dans cette configuration.

Le modèle a également permis de décrire le profil de désactivation singulier observé lors des tests sur poudre.

Conclusion Générale

Le reformage autotherme du biogaz modèle a été étudié sur des catalyseurs au nickel à 700°C en présence d'oxygène et de vapeur d'eau respectant la composition de mélange suivante: $H_2O/CH_4 = 3$ et $O_2/CH_4 = 0.5$ et $CH_4:CO_2 = 60\%:40\%$. L'objectif de ces travaux de thèse consistait en la sélection d'un catalyseur actif et stable et le développement d'un modèle cinétique dans ces conditions pour la production d'un gaz de synthèse riche en H_2 pour des applications en production d'électricité via des piles à combustibles.

Dans un premier temps, un système de six réacteurs en parallèle a permis le criblage de 12 catalyseurs au nickel sur différents supports. Le catalyseur 5-0.05 wt.% NiRh/ $Mg_{0.7}Al_2O_{3.7}$ s'est révélé être actif et très stable, convertissant la totalité du méthane après 200 heures de réaction.

Son équivalent sans métal noble Ni/ $Mg_{0.7}Al_2O_{3.7}$ s'est désactivé après seulement 2 heures de réaction. La deuxième partie de cette étude a permis d'élucider le processus de désactivation: la présence de température élevée dans la zone de combustion induit un désordre dans les structures cristallines du support $MgAl_2O_4$. Dans cette zone, le nickel est présent sous sa forme oxydée NiO. Les ions Ni^{2+} vont ainsi pouvoir diffuser dans les lacunes du support, créant une phase inactive $NiAl_2O_4$.

Grace à la compréhension de ce phénomène très peu décrit jusqu'ici dans la littérature dans le cas du reformage autotherme, la stabilité du catalyseur bimétallique NiRh peut s'expliquer par la stabilisation de la zone de combustion en présence de Rh. Un autre système a été mis en place afin de prévenir la désactivation de type de catalyseur. Un lit catalytique a été préparé avec un catalyseur au Rh en amont et un catalyseur au Ni en aval. Le catalyseur s'est montré actif et très stable.

Enfin, des catalyseurs structurés composés de NiRh/ $MgAl_2O_4$ déposé sur des « mousses » en SiSiC ont été testés pour la réaction de reformage autotherme du biogaz modèle à 700°C avec $H_2O/CH_4 = 3$ et $O_2/CH_4 = 0.5$ et $CH_4:CO_2 = 60\%:40\%$. Ces catalyseurs se sont montrés actifs et très stables. Un modèle cinétique inspiré de la littérature a été comparé aux données expérimentales. Malgré les difficultés rencontrées lors de la description du profil de température, l'accord entre les performances du catalyseur observées expérimentalement et celles estimées par le modèle est satisfaisant. Le modèle a également permis de décrire le profil de désactivation singulier observé lors des tests sur poudre, validant ainsi le processus de désactivation proposé dans le chapitre consacré à l'étude de la désactivation.

Références bibliographiques

- [1] J. R. Rostrup-Nielsen, Catalytic Steam Reforming, *Catalysis*, 1–117, 1984.
- [2] G. Jones *et al.*, *Journal of Catalysis*, 259, 147–160, 2008.
- [3] D. L. Trimm, C. W. Lam, *Chemical Engineering Science*, 36, 1405–1413, 1980.
- [4] K. Hou, R. Hughes, *Chemical Engineering Journal*, 82, 311–328, 2001.
- [5] J. Xu, G. F. Froment, *American Institute of Chemical Engineers*, 35, 88–96, 1989.

Chapter 1

Literature review and thermodynamic study

1.1. General context

Fossil fuels have powered our society since the industrial revolution in the 18th century. The extensive and global use of these non-renewable energy sources causes societal issues such as air pollution and the release of greenhouse gases that are responsible for global warming. One of the major challenges of nowadays society is to transition from fossil fuels to renewable fuels while facing an increasing global demand for energy.

Hydrogen is foreseen to be a promising alternative to fossil fuels. It presents unique properties, being the lightest gas while possessing the highest energy content per unit mass of all fuels. It also diffuses very quickly. In fuel cells, hydrogen reacts with oxygen to produce electricity along with water as the only co-product. This technology has led to the emergence of a new energy system called the hydrogen economy which is based on hydrogen and electricity [1]. However, in order to achieve the benefits of the hydrogen economy, major technological challenges have to be overcome. Notably, storage is critical. Indeed, H₂ has a high energy density by weight but a low energy density by volume. Advanced storage methods that have potential for high energy density and safe storage need to be developed.

Another limitation is its cost of production. Nowadays, hydrogen is a major primary feedstock in the chemical industry. It is currently used for the syntheses of various chemicals such as methanol, ethanol, dimethyl-ether but also of ammonia and fertilisers. It is also highly demanded in refineries for different processes such as hydrotreatment and hydrodesulfurization of petroleum fractions [2].

Hydrogen originates from different sources and processes. Main sources are natural gas, oil (crude oil, rapeseed oil, palm oil, soybean oil), coal and water (Figure 1.1). Steam reforming of natural gas is the most common process used for H₂ production [3].

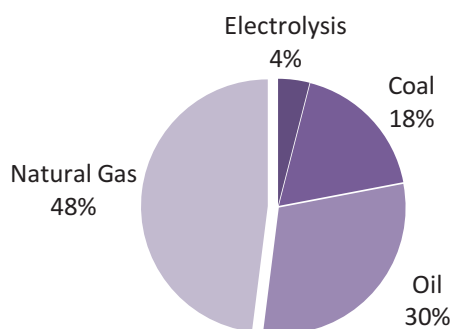


Figure 1.1: Global sources of hydrogen production [4]

Therefore, nearly 96% of H₂ is generated from fossil fuels nowadays. In the near-future hydrogen should ultimately be produced from non-fossil resources. Electrolysis of water is one solution provided that the power used comes from renewable sources such as wind or solar. It is however the most expensive process for H₂ production.

Another approach is to use a renewable methane feedstock instead of natural gas and perform reforming to produce hydrogen.

Biogas can be produced from anaerobic digestion processes of several biological feedstocks such as sewage sludge, manure and other type of organic matters. Many substrates can be used for biogas production as long as they contain carbohydrates, proteins, fats, cellulose and hemicelluloses. Biogas is thus a renewable resource composed primarily of methane and carbon dioxide. It also contains trace compounds such as hydrogen sulfide and ammonia (Table 1.1). Composition, yield and parameters vary with the process and feedstock from which the biogas originates. For instance, landfill gases are more prone to present contaminants such as halogenated compounds or siloxanes [5].

Biogas presents a significant potential considering the available amount of organic materials that can be valorized [6]. In the European Union, 1.500 million tons of biomass could be digested each year and some estimate that above 25% of all future bioenergy could come from biogas produced from wet organic materials [7] [8]. In their report on biogas valorization, the French Environment and Energy Management Agency (ADEME) presented a scenario in which the number of biogas installations in France would increase from *ca.* 300 in 2012 to 6,000 by 2030 [9].

Table 1.1: Parameters and composition of biogas [5]

Parameters	
Lower heating value	23 MJ/nm ³
Density	1.2 kg/nm ³
Methane number	>135
Composition	
Methane	53-70 vol-%
Carbon dioxide	30-47 vol-%
Nitrogen	0.2 vol-%
Hydrogen sulphide	0-10 000 ppm
Ammonia	<100 ppm
Total chlorine (as Cl ⁻)	0-5 mg/nm ³

Biogas can be used in various ways (Figure 1.2). First, it can be used as an energy source for production of heat or steam. It can also be used for electricity production or combined heat and power (CHP). Other utilization purposes include vehicle fuel and production of chemicals [5]. Biogas is thus mostly burned but the important content of carbon dioxide lower efficiencies by decreasing the heating value and flame stability of the mixture.

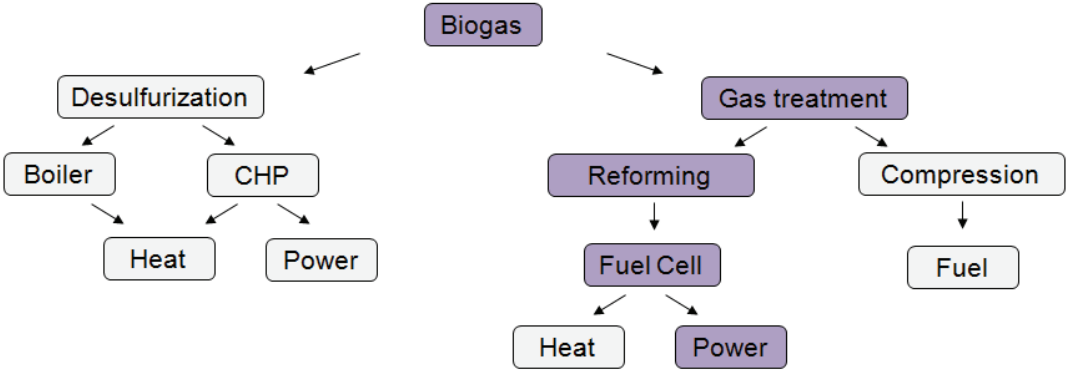


Figure 1.2: Utilization purposes of biogas (adapted from Persson *et al.*) [5]

Hydrogen can be produced by autothermal reforming of biogas. Using biogas as a renewable source for H₂ and electricity production presents several advantages. First, biogas is a local resource. In this way, it can be used as a domestic energy resource and thus imports of other fuels would be limited. Moreover, no delivery infrastructure such as expensive pipeline systems would be needed. Biogas also presents economic benefits as it can be obtained at little cost and can generate local employment [10].

1.2. Autothermal reforming of biogas

1.2.1 Description of the reforming process

The reforming process converts methane into a mixture of “syngas” and carbon dioxide. “Syngas” commonly refers to a mixture of hydrogen and carbon monoxide.

Catalytic interaction between hydrocarbons and metals is believed to have been first observed as early as in 1817 [11]. During the following century, very few studies were reported, until the early 1900s with the first industrial patents. In 1924, the first detailed study of the catalytic reaction between steam and methane was described by Neumann and Jacob.

Industrial interests and the number of patents increased from then, especially because of application to natural gas conversion for the production of ammonia and methanol. The first steam reformer was commissioned in 1930 to produce hydrogen at Baton Rouge, Louisiana by Standard Oil of New Jersey. In Europe, the first steam reformer was commissioned 6 years later by ICI in Billingham [11].

Since then, the industrial process for steam reforming (SR) has evolved and is now well established. It remains the main source of production of hydrogen. Figure 1.3 presents a simplified scheme of a typical steam reforming process of natural gas.

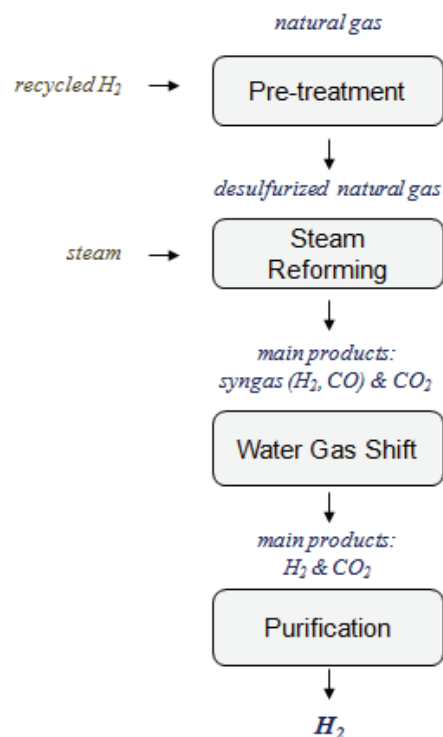


Figure 1.3: Simplified process scheme for the steam reforming of natural gas for the production of high purity hydrogen

A typical layout of a hydrogen plant based on steam reforming of natural gas thus includes the following steps [12], [13]:

- Pre-treatment: Sulfur compounds must be removed in order to avoid catalyst poisoning. The hydrocarbon feed is mixed with recycled hydrogen and organic sulfur compounds are converted into H₂S over a hydrogenation catalyst. A second step consists in the removal of H₂S by adsorption.
- Steam reforming: The desulfurized feed is mixed with steam in tubular reactors filled with a reforming catalyst. The reaction is performed at high temperatures (800-900°C) with a controlled steam/hydrocarbon ratio. It results in a mixture of hydrogen, carbon monoxide and carbon dioxide.

- Water Gas Shift: The outlet gas is cooled by steam production before entering a shift converter. CO and steam are converted into CO₂ and H₂ which leads to higher hydrogen yield.
- Purification: The shifted gas is cooled to room temperature. Separation of hydrogen is performed by Pressure Swing Absorption (PSA) unit. High purity hydrogen can be obtained.

A different type of reforming called autothermal reforming (ATR) was developed by Haldor Topsøe and Société Belge de l'Azote in the late 1950s. The process is similar to steam reforming except that oxygen or air is added to the mixture of steam and natural gas. ATR thus combines oxidation and reforming reactions in one vessel where the methane reforming is made possible by the heat released by the oxidation reaction. The major assets of performing autothermal reforming instead of steam reforming are related to the lower operational temperature. Lower temperature implies wider choice of materials and thus lower cost. Although ATR is more expensive in terms of operational costs, it is less demanding than SR in terms of energy requirements and investment costs [14].

The other advantages over other reforming reactions are related to the performances and selectivities. Higher and easily regulated H₂/CO ratio can be obtained by controlling and varying the inlet composition [15]. The unit size is also smaller than most reforming process.

Although very similar to natural gas reforming, biogas reforming brings new challenges that are related to its composition. Indeed, biogas contains no other hydrocarbons than methane after purification and its composition in terms of CH₄, CO₂ and pollutants varies with the source of biomass.

1.2.2 Thermodynamic study of the autothermal reforming of methane

The reaction of autothermal reforming is actually a combination of different reactions. The involved reactions will be described here along with thermodynamic calculations. The thermodynamic study was carried out with the chemical reaction and equilibrium software HSC.

a) Reactions

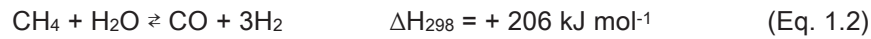
In order to convert biogas into syngas, methane can be reformed by steam and carbon dioxide. Since biogas contains methane and carbon dioxide, the dry reforming of methane is an obvious pathway (Eq. 1.1)

Dry Reforming (DR):



This reaction is strongly endothermic and must be conducted at high temperatures (800–900 °C), whereas the CH₄/CO₂ ratio in biogas is generally closer to 1.5 than to 1 and is thus not suitable for complete CH₄ conversion. Methane can also be converted into syngas by steam reforming (Eq. 1.2):

Steam Reforming (SR):



Steam reforming is also an endothermic reaction but yields more hydrogen than DR.

At high temperatures (> 800 °C), DR and SR reactions coupled with the Water Gas Shift reaction (Eq. 1.3) lead to more CO production at the reactor outlet (Fig. 1.4). Indeed, it pushes the shift reaction to the left.

Water Gas Shift (WGS):

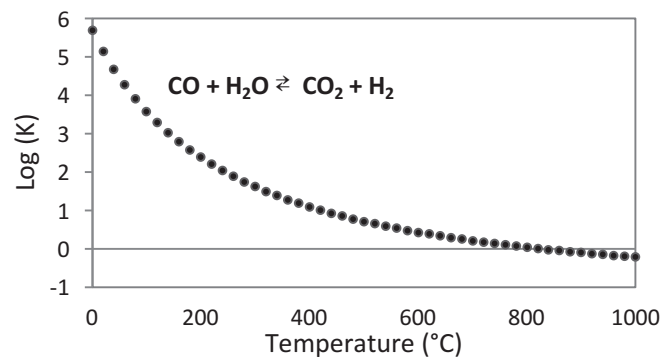
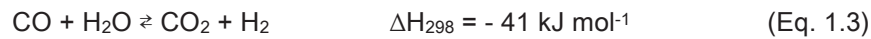


Figure 1.4: Equilibrium constant for the water gas shift reaction as a function of temperature

Therefore, operating at high temperatures implies high energy demand and limited overall production of hydrogen. In order to avoid such disadvantages, autothermal reforming is seen as a good option. ATR consists of adding oxygen (or air) which results in a combination of reforming reactions and catalytic partial oxidation (Eq. 1.4).

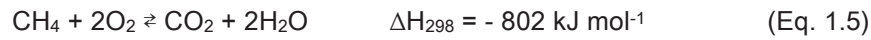
Catalytic Partial Oxidation (POx):



Partial oxidation is a slightly exothermic reaction which mechanism is still discussed and sometimes described as the result of two consecutive reactions: first the highly exothermic combustion of

methane (Eq. 1.5) at the beginning of the catalyst bed, followed by steam and dry reforming of the remaining methane and the WGS reaction. The mechanism will be discussed later on.

Methane combustion



Heat is thus directly provided by oxidation of methane, which is an exothermic reaction. Figure 1.5 presents the equilibrium constants of the reforming and oxidation reactions calculated at temperatures ranging from 0 to 1,000°C.

Formation of CO and H₂ by steam and dry reforming is favored (LogK > 0) when T > 630°C (Figure 1.5).

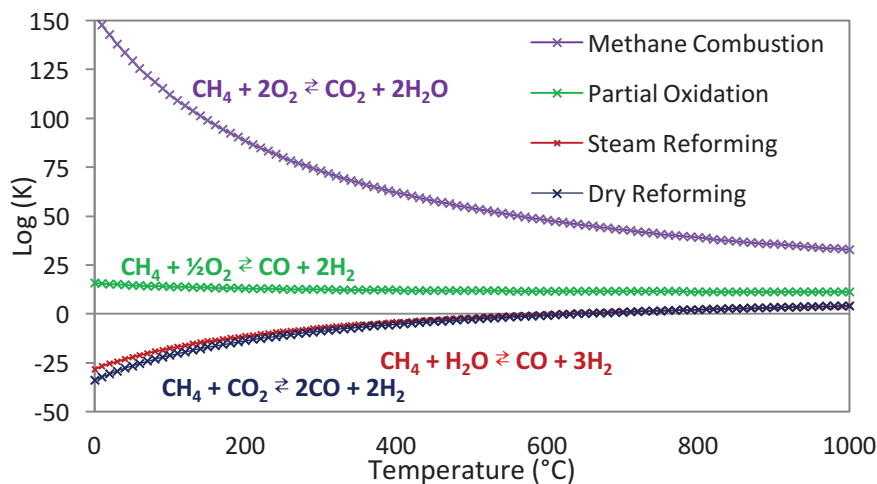


Figure 1.5: Equilibrium constants for the reforming and oxidation reactions as a function of temperature

b) O₂/CH₄ ratio

In order to reach the thermal balance between exothermic and endothermic reactions, the O₂/CH₄ molar ratio must be adjusted.

If we consider a standard biogas composition of 60% CH₄ and 40% CO₂ reacting with steam with a steam/CH₄ molar ratio of 3, the O₂/CH₄ molar ratio must be adjusted to 0.42. Figure 1.6 displays the total reaction enthalpy as a function of the O₂/CH₄ molar ratio under these conditions.

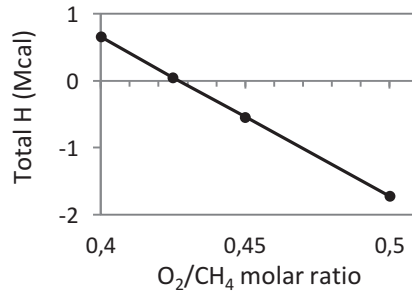


Figure 1.6: Total reaction enthalpy as a function of O₂/CH₄ ratio calculated with the HSC software; T=700°C; Steam/CH₄ ratio = 3 ; CH₄:CO₂=60%:40%

During the catalytic test, the ratio should however be a little higher than 0.425 to compensate for the heat loss through reactor walls.

c) Steam/CH₄ ratio

The Steam/CH₄ ratio will influence the hydrogen production. Figure 1.7 presents the equilibrium compositions between 0 and 800°C when the ATR reaction is performed with O₂/CH₄ = 0.5, CH₄:CO₂ = 60:40 (vol.%) and when the steam/CH₄ varies from 2 to 3.

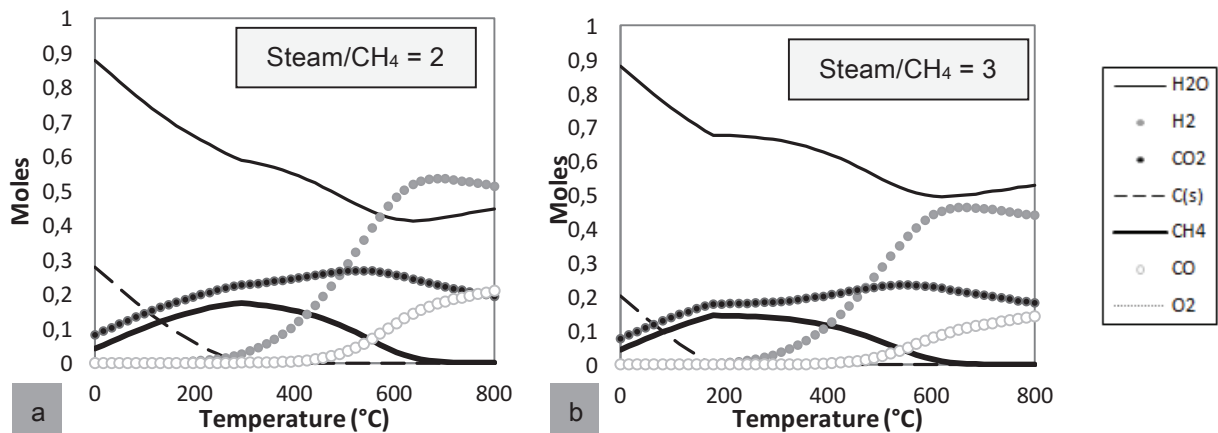


Figure 1.7: Equilibrium compositions between 0 and 800°C; O₂/CH₄ = 0.5; CH₄:CO₂=60%:40% ; calculated with the HSC software at atmospheric pressure- a) Steam/CH₄ ratio = 2 and b) Steam/CH₄ ratio = 3

At 700°C, the H₂/CO increases with increasing steam/CH₄ ratio. When using a ratio of 3 instead of 2, the equilibrium calculations show that the H₂/CO ratio increases from 3 to 3.9. Moreover, the carbon formation would be thermodynamically favored until 200°C when steam/CH₄ = 3 instead of 300°C when steam/CH₄ = 2.

1.3. Catalysts

Methane reforming has been widely studied and is generally performed on a catalyst. Throughout the years, it has been carried out over different supported catalysts that were chosen to both enhance the catalyst activity and improve its resistance to deactivation. Very few studies have been performed with biogas.

1.3.1 Metals

Methane reforming has been mainly studied over Rh, Ni, Ru, Pt, Pd and Ir. Different studies have investigated the order of reactivity over different pure transition metals [16]–[18]. There appears to be a general consensus:



Although it should be noted that Wei and Inglesia have observed otherwise [19]



Catalytic reforming of methane is traditionally performed over Ni-based catalysts since those present acceptable activity and low costs. Noble metals such as Rh, Ru, Pd, Ir and Pt are less prone to deactivation but are usually too expensive to be used in conventional industrial reformers [16], [20].

Bi-metallic catalysts have also been studied for the reforming of methane. The addition of a second metal leads to geometric and electronic modifications. Geometric modifications will usually result in a better metal dispersion and thus higher active surface. Electronic modifications will have an effect on adsorption/desorption of reactants and products which can affect activity and selectivity. Therefore, positive interactions between the two metals generally allow to increase activity, improve resistance to deactivation and extend catalysts lifetime [21]. In the case of methane autothermal reforming, Ni is generally coupled with a very small amount of noble metals [22]. The addition of Rh, Pd or Pt showed different beneficial effects such as increasing activity, improving Ni reducibility and suppression of hot-spot [23]–[26].

Our study will focus on Ni and NiRh-based catalysts.

1.3.2 Supports

The choice of the support is fundamental for the reforming reactions. The support should be stable under the reaction conditions and should provide a high surface area for the active metal. It will also determine important features such as the dispersion of the metal particles, the resistance to sintering or the resistance to carbon formation. It can thus affect the reactivity of the catalyst and may even participate in the reaction.

Acidic supports are expected to facilitate the decomposition of methane. However, they will also promote cracking and polymerization, producing carbon that can lead to catalyst deactivation. Supports possessing a strong Lewis basicity are thus preferred. Basicity is expected to favor carbon gasification. Therefore, the addition of basic metal oxides such as Na, K, Mg, and Ca to a catalyst supported on alumina has proven to prevent carbon deposition [27].

One of the most employed supports for methane reforming reactions is Al_2O_3 . However, a wide range of supports has been used and studied. Table 1.2 presents examples of catalyst compositions used for SR, DR, POx and ATR of methane in the literature. It illustrates the diversity of the supports studied.

Table 1.2: Examples of catalysts used for the reforming reactions of methane taken from the literature

Reforming reaction	Catalysts	Ref.
Steam Reforming	12-7 wt.% NiCo/ Al_2O_3	[28]
	5 wt.% Ru/ Al_2O_3	[29]
	5 wt.% NiO/ NiAl_2O_4	[30]
	15 wt.% Ni/ $\text{Ce}_x\text{Zr}_{1-x}\text{O}_2$	[31]
	10 wt.% Ni/ LaAlO_3 , 10 wt.% Ni/ SrTiO_3	[32]
Dry Reforming	10 wt.% Ni/ CeO_2 , 10 wt.% Ni/ La_2O_3 , 10 wt.% Ni/ ZrO_2	[33]
	5 wt.% LaNiO_3	[34]
	1 wt.% Ru/ SiO_2 , 1 wt.% Ru/ $\gamma\text{-Al}_2\text{O}_3$	[35]
	0.05-5 wt.% RhNi/ $\text{CeO}_2\text{-Al}_2\text{O}_3$	[36]
	5 wt.% Ni/ MgAl_2O_4	[37]
Partial Oxidation	13 wt.% Ni/ MgO , 13 wt.% Ni/ CaO , 13 wt.% Ni/ CeO_2	[38]
	2.5 wt.% Ni/ Al_2O_3	[39]
	1.5 wt.% Pt/ $\text{Ce}_{0.5}\text{Zr}_{0.5}\text{O}_2\text{-Al}_2\text{O}_3$	[40]
	10 wt.% Ni/ MgAl_2O_4	[41]
Autothermal Reforming	10 wt.% Ni/ $\gamma\text{-Al}_2\text{O}_3$, 10 wt.% Ni/ $\text{CeO}_2\text{-}\gamma\text{-Al}_2\text{O}_3$	[42]
	8 wt.% Ni/ $\alpha\text{-Al}_2\text{O}_3$, 8 wt.% Ni/ $\text{Y}_2\text{O}_3\text{-}\alpha\text{-Al}_2\text{O}_3$	[43]
	5 wt.% Ni/ MgAl_2O_4	[44]
	0.3 wt.% Rh/ $\alpha\text{-Al}_2\text{O}_3$, 0.6 wt.% Pt/ $\alpha\text{-Al}_2\text{O}_3$, 0.3 wt.% Pd/ $\alpha\text{-Al}_2\text{O}_3$	[45]
	10 wt.% Ni/ $\text{CeO}_2\text{-Al}_2\text{O}_3$, 10 wt.% Ni/ $\text{Ce}_{0.5}\text{Zr}_{0.5}\text{O}_2\text{/Al}_2\text{O}_3$	[46]

In our study, three types of supports were selected:

- spinels: MgAl_2O_4 , ZnAl_2O_4
- perovskite: LaAlO_3
- mixed oxides: $\text{CeO}_2\text{-Al}_2\text{O}_3$, $\text{ZrO}_2\text{-Al}_2\text{O}_3$

They were selected based on the fact that they displayed different compositions, structures, porosities, basicity and oxygen-transport properties that could all be beneficial in ATR conditions.

LaNiO_3 was selected as a catalyst precursor. Although it is not a support, it is a perovskite and therefore its properties will be discussed along with LaAlO_3 .

a) Spinel

The general formula for spinel is AB_2X_4 . "A" and "B" are metal cations while "X" is an anion. "A" metal ion can be Mg, Cr, Mn, Fe, Co, Ni, Cu, Zn, Cd and Sn. "B" metal ion can be Ti, V, Cr, Mn, Fe, Co, Ni, Rh, Al, Ga and In. "X" metal ion can be O, S, Se, Te. However, magnesium aluminate spinel MgAl_2O_4 is usually referred to as "real" spinel.

Figure 1.8 presents the crystal structure of MgAl_2O_4 and illustrates the cations distributions. The figures were obtained using the visualization program VESTA.

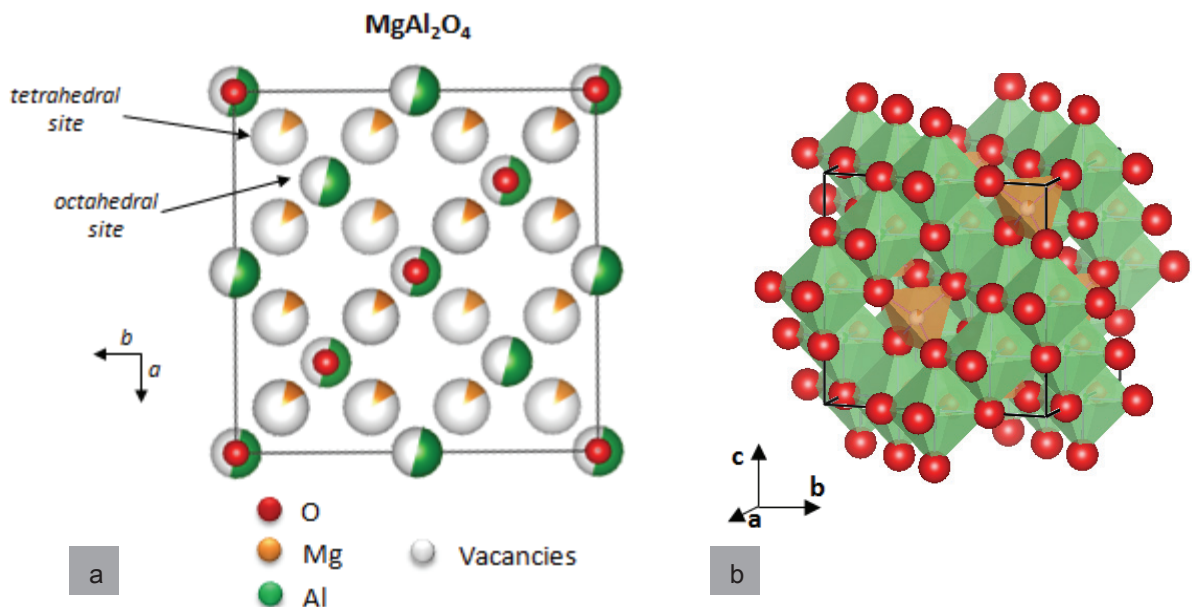


Figure 1.8: Crystal structure of MgAl_2O_4 a) representation of the occupancy and distribution of the cations, b) representation of the octahedral (green) and tetrahedral (orange) sites

The majority of spinel compounds belong to the space group $Fd3m$. The unit cell consists of 32 anions and 24 cations. There are 96 interstices between the anions in the unit cell. However, only 24 are occupied by cations. Of the 64 tetrahedral interstices that exist between the anions, 8 are occupied by A^{2+} cations. The remaining 16 B^{3+} cations occupy half of the 32 octahedral interstices [47].

Magnesium aluminate spinel presents interesting properties such as high melting temperature ($>2000^{\circ}\text{C}$), good chemical stability and mechanical strength at high temperature, good thermal shock resistance, strong basicity and catalytic properties [48]. Mosayebi *et al* and Guo *et al* carried out autothermal and dry reforming of methane respectively on nickel catalysts supported on MgAl_2O_4 spinel [37], [44]. Both concluded that such catalyst presents high activity and stability. This improvement has partly been attributed to the fact that Ni particles were highly dispersed on the spinel support [49].

ZnAl_2O_4 spinel has been less studied than MgAl_2O_4 for methane reforming. Nieva *et al* studied steam methane reforming on both $\text{Ni/MgAl}_2\text{O}_4$ and $\text{Ni/ZnAl}_2\text{O}_4$. Catalytic activities over spinel based catalysts were higher than over $\text{Ni}/\alpha\text{-Al}_2\text{O}_3$ and Ni/SiO_2 catalysts. After reduction, smaller particles were obtained in the case of the spinels. While carbon nanofibers were found on $\text{Ni}/\alpha\text{-Al}_2\text{O}_3$ and Ni/SiO_2 catalysts, they were present in a smaller extent on $\text{Ni/MgAl}_2\text{O}_4$. On $\text{Ni/ZnAl}_2\text{O}_4$ catalyst, only amorphous carbon was found [50].

In addition to promoting catalyst activity and preventing sintering of nickel particles, spinel supports present another major interest related to their crystal structure. The diffusion of Ni^{2+} ions to structure vacancies of Al_2O_3 leads to the formation of inactive NiAl_2O_4 [11]. In spinel supports, part of the tetrahedral vacancies is already occupied by A^{2+} ions (Mg^{2+} or Zn^{2+}).

Performing the autothermal reforming reaction over nickel supported on MgAl_2O_4 and ZnAl_2O_4 is thus expected to improve the catalyst resistance to deactivation by limiting the diffusion of Ni^{2+} in these vacancies.

b) Perovskites

The general formula of perovskite oxides is ABX_3 with “A” being the larger cation, “B” the smaller cation and “X” an anion. Although the original perovskite structure is cubic with space group $\text{Pm}\bar{3}\text{m}$ [51], LaAlO_3 presents a distortion and has a rhombohedral $\text{R}\bar{3}\text{c}$ structure at room temperature [52].

Perovskite oxides are widely used in catalysis as they present high activity, thermal stability and good performances [53]. Many perovskites exhibit basic properties [51]. Certain perovskites also present

mobile lattice oxygen which is interesting in the case of hydrocarbon reforming since they can promote the oxidation of inactive carbon. Urasaki *et al.* have reported that inactive carbon species were not observed after steam reforming of methane on Ni/LaAlO₃ catalyst while conventional Ni/Al₂O₃ was deactivated due to carbon deposition in the same conditions [32]. In this way, using perovskites as supports is expected to limit coking problems.

Introduction of nickel into the perovskite structure as LaNiO₃ is also interesting for methane reforming reactions. Reduction of the LaNiO₃ at 700°C results in Ni⁰/La₂O₃ with well dispersed Ni particles leading to high activities and high resistance to carbon formation [34][54].

Performing the ATR reaction over nickel supported on LaAlO₃ and over LaNiO₃ is thus expected to limit deactivation by carbon formation. It should be noted that one of the drawbacks of perovskites is that they present low surface area.

c) Mixed oxides

CeO₂ is also reported to be a suitable support for both reforming and WGS reactions since it presents high oxygen storage capacity, high thermal stability and redox properties [55]. ZrO₂ presents high thermal stability [56]. Their contribution is not just about supporting the catalyst but they might also participate in the reaction. Indeed, CeO₂ and ZrO₂ can limit carbon deposition by oxidizing the CH_x fragments adsorbed on metallic nickel. Ceria generally presents low surface area and the catalytic activity of Ni/CeO₂ is limited. However, when used as a promoter to Ni/γ-Al₂O₃, CeO₂ has proven to have a positive effect on catalytic activity, stability and carbon suppression [57].

Thanks to the ability of ZrO₂ and CeO₂ to store, release and transfer oxygen, Ni catalysts supported on CeO₂-Al₂O₃ and ZrO₂-Al₂O₃ are expected to prevent coking problems during ATR of model biogas.

1.3.3 Hydrotalcite-type precursors

An alternative to classical catalyst preparation is to prepare precursors that undergo phase transition during calcination. More especially, the use of hydrotalcites as precursors in preparation of nickel-aluminium mixed oxides has been proposed. The general formula of hydrotalcites is Mg₆Al₂(CO₃)(OH)₁₆, mH₂O, in which a part of Mg²⁺ can be replaced by Ni²⁺. They are formed with layered mixed hydroxides where the substitution of M²⁺cations by M³⁺ cations results in overall positively charged layers. Anions and water molecules are located in the interlamellar space in order to balance the charge [58].

After calcination, hydrotalcites undergo phase transition resulting in large specific areas, high metallic dispersion and high particle stability [59]. Incorporation of Ni²⁺ and Mg²⁺ cations in the layered double hydroxides results in Ni/Mg/Al hydrotalcite-type precursors.

Takehira *et al* studied autothermal reforming of CH₄ on Ni/MgAl catalysts prepared from Ni-Mg-Al hydrotalcite precursors [60]. Fonseca & Assaf performed methane SR on comparable catalyst [61]. Both reported high activity and stability. Takeri *et al.* attributed the performances to the stability of Ni species even under presence of oxygen while conventional Ni catalysts quickly deactivated due to the surface oxidation of Ni particles. Fonseca & Assaf attributed the performances to the homogeneous and high distribution of Ni which limited the formation of carbon.

1.4. Mechanism of ATR over nickel based catalysts

Only a few studies describe the mechanisms and kinetics of the ATR of methane [15], [62]. There is a general agreement that the most significant reactions occurring are: methane oxidation, steam reforming and water gas shift reactions. This section will deal with the main mechanisms proposed in the literature for these three reactions.

1.4.1. Mechanism of the partial oxidation of methane

Oxidation of methane occurs first. During catalytic partial oxidation of methane, NiO and Ni species are present on the surface. The reaction leads to syngas production and requires reduced nickel sites. If only NiO is present, only the combustion of methane occurs resulting in water and CO₂ as the only products [63].

The methane partial oxidation has been widely studied in the literature. However, there is still an ongoing debate about the mechanism. Two main routes are reported:

- A direct route, commonly referred to as “Direct Partial Oxidation mechanism” (DPO), in which H₂ and CO are produced on the catalyst surface and then desorbed.
- An indirect route, referred to as “Combustion and Reforming Reactions mechanism” (CRR), in which combustion occurs first with full O₂ conversion, producing H₂O and CO₂ that can participate in the reforming of the remaining CH₄ to H₂ and CO.

Figure 1.9 shows a representation of the two routes

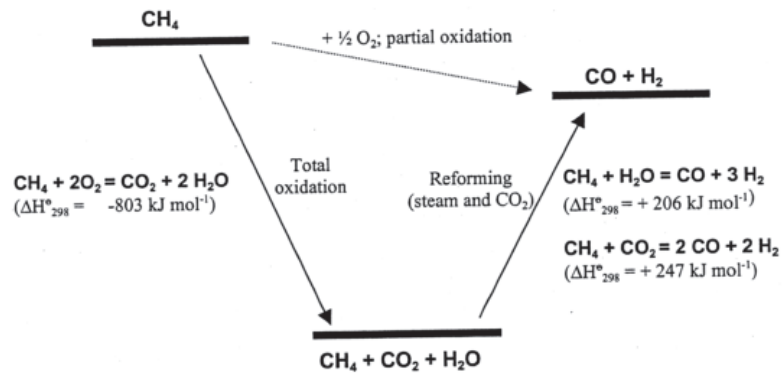
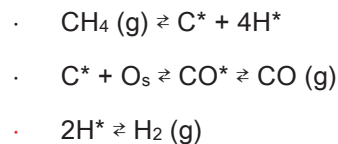


Figure 1.9: Scheme of the two proposed routes for the partial oxidation of methane [64]

It appears that both mechanisms can occur over noble metal and transition metal catalysts. Depending on different parameters such as the residence time, the active metal, the support and the temperature, the mechanism can be DPO or CRR [64].

- DPO mechanism

The mechanism for the direct route is still discussed. Hickman and Schmidt studied partial oxidation of methane over Rh and Pt catalysts. They proposed a mechanism at very short residence time. The most important steps are described below [65]:



It consists in the dehydrogenation of CH₄ to H₂ and surface carbon species. Surface carbon species then react with surface oxygen species to produce CO.

- CRR mechanism:

This route was already suggested by Prettre in the 1940s [66]. The CRR mechanism is a combination of the combustion mechanism and the reforming mechanism.

Trimm & Lam proposed a mechanism for CH₄ combustion over Pt/Al₂O₃. It consists in the reaction between adsorbed CH₄ with surface oxygen adsorbed monoatomically and diatomically on two different sites [67].

Another well accepted model was proposed by Dewaele *et al.* who studied CH₄ combustion over Ni/Al₂O₃: chemisorbed oxygen abstracts hydrogen from gas-phase methane and from adsorbed CH_x

species. Lattice oxygen is responsible for the carbon-oxygen bond formation in CO₂ [63]. Figure 1.10 presents a scheme of this reaction mechanism.

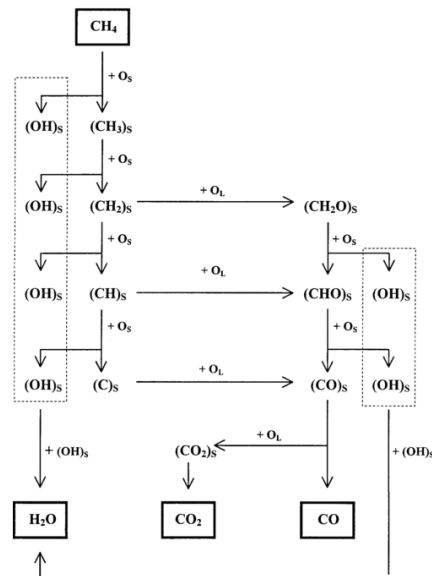


Figure 1.10: Scheme of the combustion reaction mechanism proposed by Dewaele and Froment [63]

They suggested that combining this mechanism with their previously published steam reforming mechanism (described in the next part 1.4.2) would result in the POx reaction mechanism.

One of the major challenges when investigating methane partial oxidation mechanism is the presence of important temperature gradients in the catalytic bed due to the fact that this reaction is fast and exothermic. According to Enger *et al.* it is generally accepted that no uniform mechanism can be found for methane POx specially because of the temperature gradients that can alter the state of the catalyst and conditions and thus the reaction pathways [68].

1.4.2. Mechanism of the steam reforming of methane

Xu & Froment studied the steam reforming of methane over Ni/MgAl₂O₄ catalyst and proposed the following mechanism [69]:

H₂O reacts with surface nickel atoms, yielding adsorbed oxygen and gaseous hydrogen. The H₂ formed is directly released into the gas phase and/or the gaseous H₂ is in equilibrium with adsorbed H₂ and H.

Methane is adsorbed on surface nickel atoms. The adsorbed methane either reacts with the adsorbed oxygen or dissociates to form CH_x . The adsorbed oxygen and the carbon-containing radicals react to form chemisorbed CH_2O , CHO , CO , or CO_2 . CO and CO_2 are formed out of CHO and CH_2O species.

In this mechanism, the reactions of carbon-intermediates with adsorbed oxygen are rate determining steps (r.d.s.). However, Wei and Iglesia proposed otherwise. They suggested a sole kinetic relevance of C-H bond activation step over Ni and noble metals for reactions of CH_4 with H_2O , CO_2 as well as for CH_4 decomposition and water gas shift reactions. Figure 1.11 presents both mechanisms.

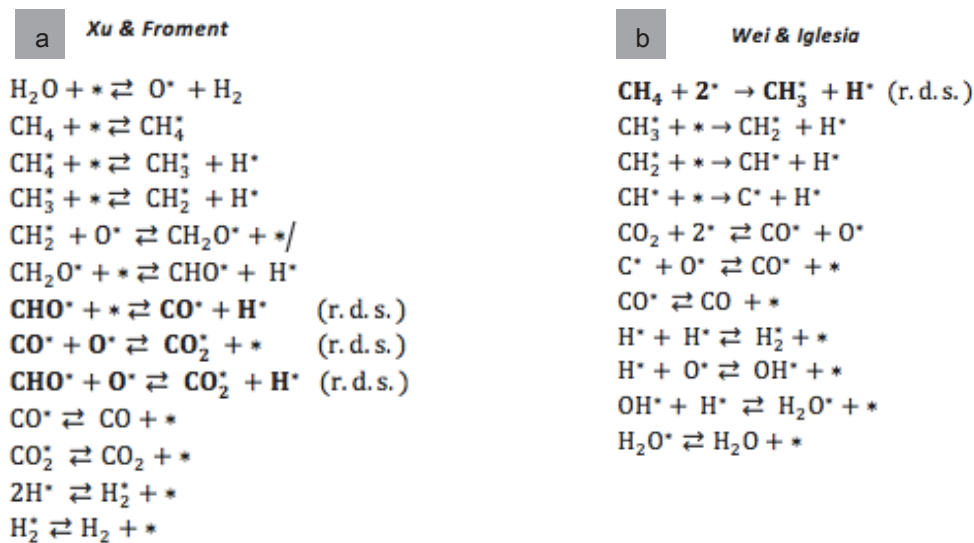


Figure 1.11: Reaction schemes for steam reforming proposed by a) Xu & Froment [69] b) Wei & Iglesia [19]

1.4.3. Mechanism of the Water Gas Shift

The reaction mechanism of the WGS reaction has been widely studied. Two main types of mechanisms can be distinguished:

One type is referred to as the “redox mechanism”. It relies on an Eley-Rideal mechanism in which alternate reduction and oxidation of the surface occurs. The surface is reduced when gas phase CO reacts with surface oxygen to produce CO_2 . It is oxidized when an oxygen atom is removed from gas phase H_2O and results in the production of H_2 [70].

The second type of mechanism proposed in the literature is a Langmuir-Hinshelwood mechanism in which CO adsorbs on the surface while H_2O adsorbs and dissociates to adsorbed H s and O . Adsorbed CO and O will then react to form CO_2 . Adsorbed H s will form gas phase H_2 [70].

During methane SR over nickel-based catalyst, some studies reported WGS to be at equilibrium and some not. These differences can arise from different catalyst formulation. Sprung *et al.* also pointed that the difference could come from the fact that the studies were performed in different conditions: methane conversions were different. At high conversion of methane (> 50%), equilibrium could be expected [71].

1.5. Catalyst deactivation

While deactivation during SR, DR or POx over Ni-based catalyst has been well investigated over the years, few deactivation studies have been reported on ATR of methane and even less on ATR of biogas. Solutions have to be found regarding aspects of catalyst deactivation. Catalyst deactivation can occur through different processes. The most common causes are: poisoning, particles sintering, carbon formation and nickel oxidation.

1.5.1 Poisoning

Poisoning refers to the strong chemisorptions of undesired species on catalytic sites, thereby reducing the number of sites available for the catalytic reaction. As mentioned before, raw biogas contains other compounds than methane and carbon dioxide. In current applications, a purification step is performed in order to remove contaminants and H₂S traces in particular. Both physico-chemical and biological methods are used [72]. Indeed, H₂S is reactive with most metals and acts as a poison as it can inhibit chemisorptions of other molecules. Thus its occurrence deactivates the catalysts [73]. This irreversible phenomenon is widely referred to as sulfur poisoning.

Biogas can also contain traces of ammonia (100-800 ppm). Nitrogen compounds can poison the acid sites of catalysts as they are basic compounds [74]. However, ammonia does not seem to be an issue for catalytic reforming of biogas [75].

Chloride occurrence in a feed increases the surface acidity of the catalyst. This leads to a change in H₂/CO ratio due to poisoning of the water gas shift reaction. However, chloride adsorption is reversible and at high temperature (>700°C) the effects are far less noticeable [76].

Our study will focus on ATR of model biogas composed of clean CH₄ and CO₂ only with a composition CH₄:CO₂ = 60:40 (vol.%). Poisoning will thus not be considered as a cause of deactivation.

1.5.2 Sintering

Sintering refers to the agglomeration and the growth of the crystallites of the active phase (Figure 1.12). It also refers to support collapse leading to the loss of surface area. Both phenomena result in the loss of active surface and thus a decrease in activity [77].

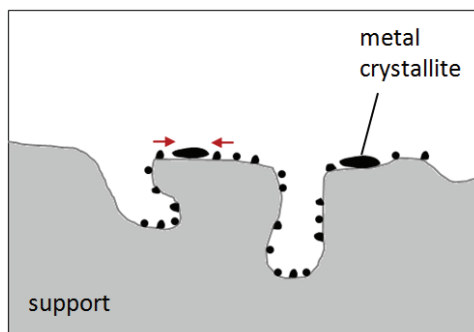


Figure 1.12: Scheme of the sintering process by crystallites growth leading to loss of active surface

Sintering is a thermal degradation that is favored by high temperatures and high pressures of steam [78]. These processes are irreversible or difficult to reverse.

In conventional fixed bed reactors, reforming reactions involving O_2 as a reactant lead to the formation of hot spot. During catalytic partial oxidation of methane, the combustion reaction is much faster than the reforming reactions. Therefore, exothermic combustion occurs at the bed inlet in a first zone. Once all oxygen is consumed, the endothermic reforming takes place in a second zone. The two zones generally do not overlap and thus the temperature in the first zone is very high leading to an important temperature gradient. In the exothermic zone, high temperatures can be reached and can thus lead to phase transformation, loss of surface area and particles agglomeration.

In the presence of CO_2 and steam, the hotspot formation will be limited. The two zones might overlap. The more they overlap, the higher the methane conversion [45].

The presence of steam can be both beneficial and detrimental. Steam is likely to create a reasonable temperature gradient or at least a lower gradient than if no steam was introduced. However, high pressures of steam increase the sintering rate of supported metals. Cai *et al.* attributed the loss of activity during ATR of methane over Ni catalysts to phase transformation or active metal sintering [79]. Therefore, because ATR reaction combines high temperatures and high pressures of steam, sintering should be considered if deactivation occurs.

1.5.3 Carbon formation

Carbon formation is commonly described as the principal cause of deactivation during hydrocarbon reforming reaction. Nickel is particularly prone to carbon deposition which can lead to deactivation.

During methane reforming, carbon formation can occur through three main different reactions: Boudouard reaction (Eq. 1.6), methane pyrolysis (Eq. 1.7) but also reverse gasification (Eq. 1.8).

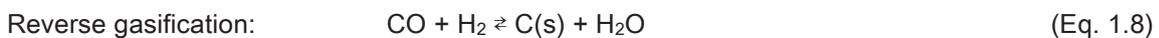
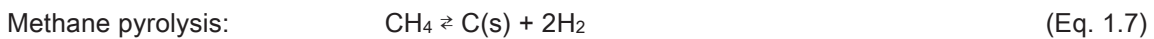
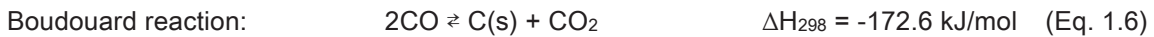


Figure 1.13 presents the equilibrium constants for these three reactions calculated with the software HSC.

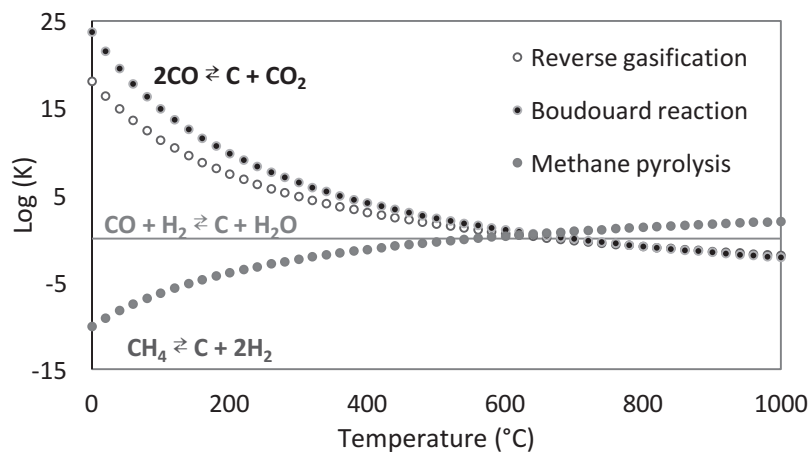


Figure 1.13: Equilibrium constants for the three considered carbon formation reactions as a function of temperature

At low temperatures, the formation of carbon by Boudouard reaction and reverse gasification is favored. In order to avoid carbon formation from CO dissociation, the temperature should reach $T > 660^\circ\text{C}$. However, starting from this temperature, carbon formation can happen through methane pyrolysis.

Different types of carbon can thus be formed over nickel-based catalysts. Carbon deposition can lead to deactivation by encapsulation of the particle. It can thus stay at the metal surface, decreasing active nickel surface by encapsulating the particle [77].

Another carbon formation route can be observed. Carbon can diffuse under the surface into the bulk and then further diffuse at the support interface, creating graphene layers [80]. This will lead to the formation of nanofibers also called “carbon whiskers” and result in the separation of the nickel from the surface. Whisker-like carbon formation does not lead to immediate deactivation of the Ni-surface but leads to a blockage of the porosity and catalyst breakdown[11]. Figure 1.14 displays a scheme of the different types of carbon that can be encountered and a TEM image of a catalyst presenting whisker carbon.

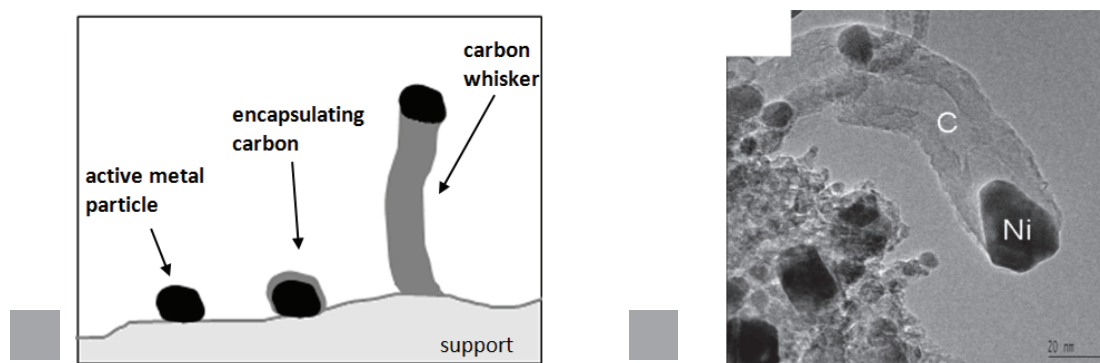


Figure 1.14: a) Scheme representing an active metal particle, a particle encapsulated by carbon and a metal particle on top of a carbon whisker, b) HRTEM image of carbon whiskers taken from [81]

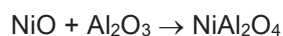
We have seen that carbon formation depends on the temperature. Deactivation by carbon is influenced by other parameters such as the nature of the reactants, the steam/CH₄ ratio, the presence of acid sites on the catalyst surface, metal loading and particle size for instance. Bengaard *et al.* studied thoroughly the formation of graphite during methane SR over Ni catalysts. They arrived at the generally accepted conclusion that the nucleation of graphite is extremely structure sensitive. Step sites are much more reactive than close-packed facets. When the metal particles are very small, the step edges become too small for graphite nucleation to proceed. Therefore, the smaller the particle, the lower the ability to grow graphite [80].

Steam/CH₄ ratio is also a critical parameter when investigating carbon formation. H₂O can eliminate surface carbon by gasification. The risk of carbon formation is thus reduced by increasing the steam to CH₄ ratio [11].

During ATR, carbon formation is also usually avoided by adjusting steam/CH₄ and O₂/CH₄ ratios or working within an ideal range of temperature. Even though carbon formation is less likely to occur because of the presence of oxygen and steam, it has also been speculated to be the cause of deactivation during autothermal reforming of methane [43], [46].

1.5.4 Nickel oxidation and NiAl₂O₄ spinel formation

During SR, DR and POx reaction, Ni oxide has been reported to react with alumina at high temperature to form inactive nickel aluminate NiAl₂O₄ [11], [39], [82].



Nickel aluminate is commonly referred to as nickel spinel. The temperature at which its formation starts is not well-defined.

The structure of γ -alumina is generally described as a cubic defect spinel type. The oxygen atoms are arranged in a cubic close packing while aluminum atoms occupy the octahedral and tetrahedral sites [83]. As described earlier, the normal spinel structure is AB₂O₄ with 8 A atoms at tetrahedral positions and 16 B atoms at octahedral positions. γ -Al₂O₃ is thus called “defect” spinel because the Al atomic positions are not fully occupied in order to respect the stoichiometry. Its formula is B_{8/3}O₄ [84]. Therefore, vacancies can exist over both tetrahedral and octahedral cationic sites. Although it is generally accepted that there is a preference for vacancies on octahedral sites, there is an ongoing debate about the precise distributions of the Al atoms and the vacancies [85]. Some studies even suggested that some cations occupy non-spinel site [86]. Ni²⁺ ions can diffuse into the vacant coordination cationic sites present in γ -Al₂O₃ resulting in the formation of the nickel spinel.

NiAl₂O₄ is considered to be an “inverse” spinel. The distribution of cations in spinel can be represented by the formula (A_{1-x}B_x)_T [A_x B_{2-x}]_O O₄ where x is the degree of inversion and T and O correspond to tetrahedral and octahedral sites respectively. A normal spinel, magnesium spinel for instance, will correspond to (Mg)_T[Al₂]_OO₄. An inverse spinel such as NiFe₂O₄ for instance, will correspond to (Fe)_T[Fe Ni]_OO₄ [87], [88]. NiAl₂O₄ structure is however only partially inverse. Although its degree of inversion depends slightly on temperature, x is generally 0.8 at temperatures ranging from 1000 to 1500 °C [87]. Ni²⁺ ions are thus preferably located in octahedral sites rather than tetrahedral sites.

Figure 1.15 presents the crystal structure of NiAl₂O₄ with x = 0.8 in order to illustrate the cations distributions.

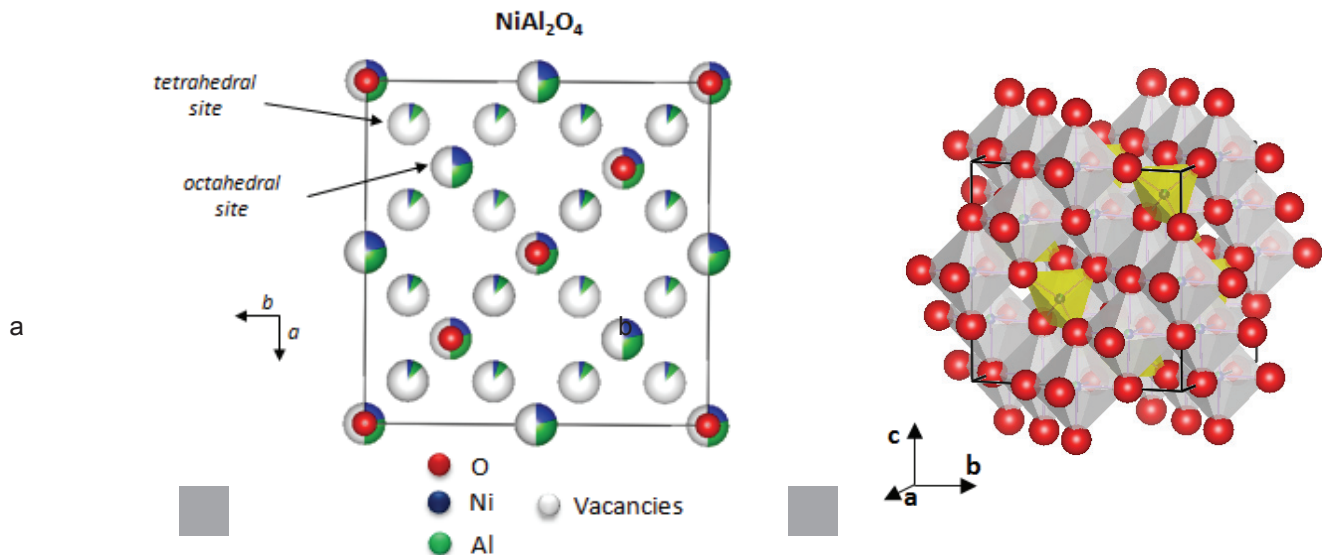


Figure 1.15: Crystal structure of NiAl₂O₄ corresponding to a degree inversion $x = 0.8$, resulting in $(\text{Ni}_{0.2}\text{Al}_{0.8})_{\text{T}}[\text{Ni}_{0.8}\text{B}_{1.2}]_{\text{O}}\text{O}_4$. a) representation of the occupancy and distribution of the cations, b) representation of the octahedral (gray) and tetrahedral (yellow) sites

Although Ni has been reported to react with alumina and magnesium spinel to form inactive NiAl₂O₄ during SR, DR and POx reactions [39], [82], it has not yet been proven to be the case during ATR of methane. Araki *et al.* performed ATR of biogas on a Ni/Mg/Al catalyst and related deactivation to the oxidation of Ni to Ni₂O₃ [89]. Nickel oxidation was speculated to be the cause of deactivation in different ATR studies but formation of NiAl₂O₄ has not been clearly evidenced [60][90][44].

1.6. The BioRobur project

This Ph.D. work was done in the scope of the European project called “BioRobur”, acronym for “Biogas robust processing with combined catalytic reformer and trap”. It is a collaborative project which is part of the Fuel Cells and Hydrogen Joint Undertaking (FCH-JU) initiative and involves both academic and industrial partners:

- Politecnico di Torino – POLITO
- Institut de recherche sur la catalyse et l’environnement de Lyon - IRCELyon
- Technical University Bergakademie Freiberg – TUBAF
- Hysytech SRL
- Scuola Universitaria Professionale della Svizzera Italiana – SUPSI
- Erbicol SA
- Modernios E-Technologijos – MET
- Centre for Research and Technology Hellas – CERTH

The BioRobur project seeks to develop a robust and efficient biogas reformer aimed at covering a wide span of potential applications, from fuel cells feed (both high temperature Solide Oxide Fuel Cell SOFC or Molten Carbonate Fuell Cell MCFC fuel cells and low temperature PEM ones, requiring a significantly lower inlet CO concentration) up to the production of pure, PEM-grade hydrogen. Rather than reforming an upgraded bio-methane, direct biogas reforming will be carried out. This is expected to reduce the costs and increase the well-to-wheel efficiency of producing renewable hydrogen. Figure 1.16 displays a scheme presenting the project in terms of core innovations and the involvement of the partners.

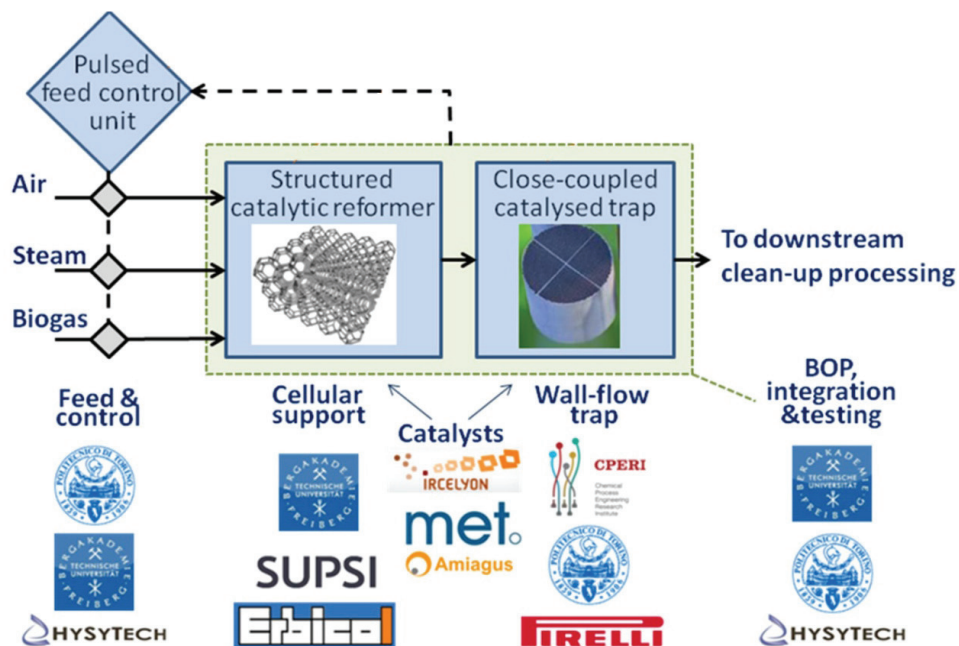


Figure 1.16: Scheme of the BioRobur reformer core innovations and partners' roles

Figure 1.17 presents a flow diagram of the BioRobur process without heat integration. It can be separated into three main parts:

1. Educt Processing: It consists in the compression, pre-heating and mixing of air, steam and biogas.
2. ATR Unit: In this second part, the biogas reformer is closely coupled to a wall flow filter used to retain the possible soot produced in the reformer.
3. Gas purification: The last part involves a High-Temperature followed by Low-Temperature Water Gas Shift units (HT-WGS and LT-WGS) as well as PSA unit.

The first two sections will be implemented within the BioRobur project on a pre-commercial reformer unit run at TUBAF in Germany. The last sections will not be implemented at the BioRobur unit. It will however be considered for process optimization and efficiency calculations.

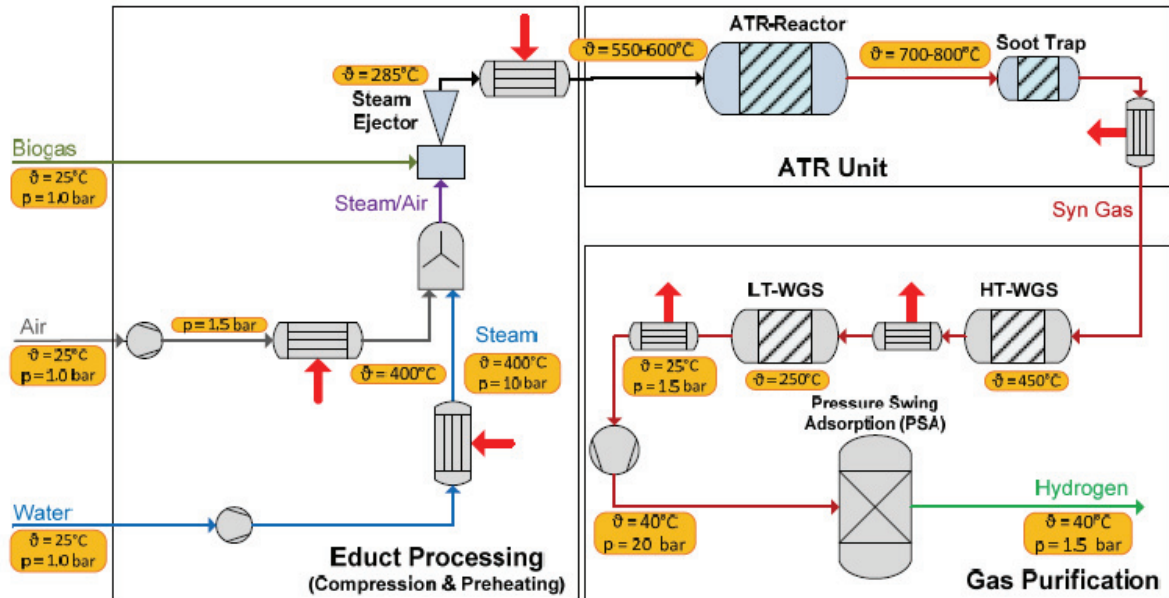


Figure 1.17: Block flow diagram of BioRobur process without heat integration

The objectives of this Ph.D. work concerned the selection of the catalyst for the reforming process. The ATR unit will rely on an active and stable nickel reforming catalyst. The noble metal involvement should be minimized for cost reduction purposes. The chosen catalyst will be deposited on high-thermal conductivity cellular support SiSiC by partners.

Initial parameters for the ATR of model biogas were defined:

- A biogas composition of 60% CH₄ and 40% CO₂
- A steam to CH₄ ratio of 3
- A O₂ to CH₄ ratio of 0.5
- An outlet reformer temperature of nearly 690°C
- An absolute reactor pressure of 1.5 bar

The nominal production rate of pure hydrogen of the BioRobur fuel processor will be 50 Nm³/h with an overall efficiency of the conversion of biogas to hydrogen of 65%.

1.7. Conclusion and description of Ph.D. work

Our study will focus on the autothermal reforming of model biogas over nickel-based catalyst for hydrogen production for fuel cell applications.

Biogas is a renewable source of methane. Autothermal reforming of biogas consists in the reaction between biogas, O_2 and steam, resulting in a hydrogen-rich syngas.

The thermodynamic study shows that full methane conversion can be expected at 700°C , with $\text{steam}/\text{CH}_4 = 3$, $O_2/\text{CH}_4 = 0.5$ and a biogas composed of 60% CH_4 and 40% CO_2 . Methane reforming is generally performed over nickel catalysts since those combine good activity and reasonable price. Promotion of nickel catalysts with a noble metal and more notably Rh has also proven to be beneficial in the literature.

The ATR mechanism can be described as a combination of partial oxidation and reforming reactions mechanisms or a combination of combustion and reforming reactions mechanisms. The most common causes of deactivation during hydrocarbon reforming are poisoning, particles sintering, carbon formation and nickel oxidation. Different types of supports were thus chosen for their ability to improve the performances of the catalysts and to prevent deactivation. While spinels are expected to prevent or limit the formation of inactive nickel spinel, perovskites and mixed oxides are expected to prevent or limit carbon formation. Hydrotalcite-type precursors are expected to improve the catalysts activity and performances by presenting well dispersed metallic particles after reduction.

Experimental methods will be presented in Chapter 2. The catalysts preparation and characterization will be described. The implementation of the set-ups and the methodology used to evaluate and monitor the catalysts performances will be detailed.

Chapter 3 will focus on the screening of various nickel based catalysts for the ATR of model biogas at 700°C . The tests will be performed on powders using a six parallel-flow reactor set-up allowing saving time on time-consuming long-term stability tests. The screening will enable to select a robust catalyst for the reaction.

ATR of model biogas over Ni supported on magnesium spinel will be studied in Chapter 4. More specifically, the catalyst deactivation will be investigated. Once the process of deactivation will be understood, our aim will be to prevent it, ensuring high activity and stability with lowest noble metal involvement.

Chapter 5 will focus on SiSiC foams coated with NiRh catalyst. The performances of these structured catalysts will be evaluated for the ATR of model biogas and a kinetic model will be developed.

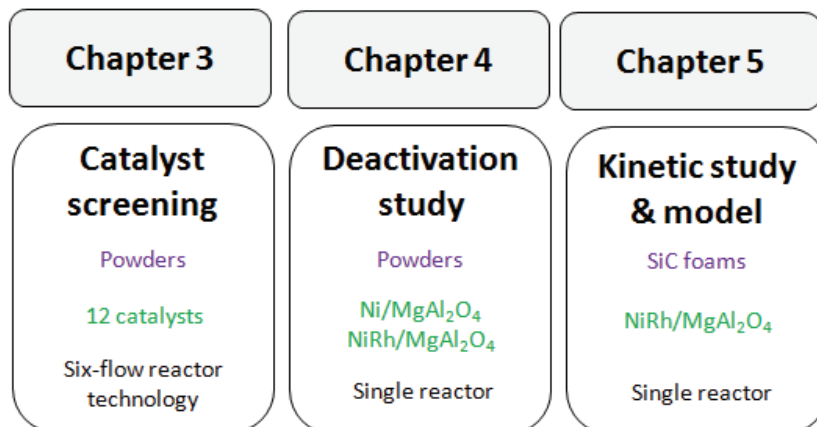


Figure 1.18: Outline of the study

REFERENCES:

1. Crabtree, G. W., Dresselhaus, M. S. & Buchanan, M. V., *Physics Today*, 39–45, 2004.
2. Armor, J. N., *Applied Catalysis A: General*, 176, 159–176, 2005.
3. Kothari, R., Buddhi, D. & Sawhney, R. L., *Renewable and Sustainable Energy Reviews*, 12, 553–563, 2008.
4. International Partnership for Hydrogen and Fuel Cells in the Economy. IPHE Renewable Hydrogen Report, 2011.
5. Persson, M., Jönsson, O. & Wellinger, A., Biogas Upgrading to Vehicle Fuel Standards and Grid Injection, 2006.
6. Rasi, S., Läntelä, J. & Rintala, J., *Energy Conversion and Management*, 52, 3369–3375, 2011.
7. Weiland, P., *Applied microbiology and biotechnology*, 85, 849–60, 2010.
8. Holm-Nielsen, J. B., Al Seadi, T. & Oleskowicz-Popiel, P., *Bioresource technology*, 100, 5478–84, 2009.
9. ADEME. « Benchmark des stratégies européennes des filières de production et de valorisation de biogaz et perspectives pour la filière française de méthanisation », 2015.
10. Muradov, N., Smith, F. & T-Raissi, A., *International Journal of Hydrogen Energy*, 33, 2023–2035, 2008.
11. Rostrup-Nielsen, J. R., *Catalysis*, 5, 1–117, 1984.
12. Hydrogen. Air Liquide E&C Communications
13. Rostrup-Nielsen, J. R. & Rostrup-Nielsen, T. Large-scale hydrogen production. Topsoe Technologies, 2002.
14. Pena, M. A., Gomez, J. P. & Fierro, J. L. G., *Applied Catalysis A: General*, 144, 7–57, 1996.
15. Halabi, M., Decroon, M., Vanderschaaf, J., Cobden, P. & Schouten, J., *Chemical Engineering Journal*, 137, 568–578, 2008.
16. Jones, G. et al., *Journal of Catalysis*, 259, 147–160, 2008.
17. Qin, D. & Lapszewicz, J., *Catalysis Today*, 21, 551–560, 1994.
18. Rostrup-Nielsen, J. R. & Bak Hansen, J.-H., *Journal of Catalysis*, 144, 38–49, 1993.
19. Wei, J. & Iglesia, E., *Journal of Catalysis*, 224, 370–383, 2004.
20. Ferreira-Aparicio, P., Guerrero-Ruiz, A. & Rodríguez-Ramos, I., *Applied Catalysis A: General*, 170, 177–187, 1998.
21. Dal Santo, V., Gallo, A., Naldoni, A., Guidotti, M. & Psaro, R., *Catalysis Today*, 197, 190–205, 2012.
22. Li, D., Nakagawa, Y. & Tomishige, K., *Applied Catalysis A: General*, 408, 1–24, 2011.
23. Nagaoka, K., Jentys, a & Lercher, J., *Journal of Catalysis*, 229, 185–196, 2005.
24. Dias, J. a. C. & Assaf, J. M., *Applied Catalysis A: General*, 334, 243–250, 2008.
25. Tomishige, K., Kanazawa, S., Sato, M., Ikushima, K. & Kunimori, K., *Catalysis Letters*, 84, 69–74 (2002).

26. Tomishige, K., Kanazawa, S., Ito, S. & Kunimori, K., *Applied Catalysis A: General*, 244, 71–82, 2003.
27. Horiuchi, T. et al., *Applied Catalysis A: General*, 144, 111–120, 1996.
28. You, X. et al., *ChemCatChem*, 6, 3377–3386, 2014.
29. Avraam, D. G., Halkides, T. I., Liguras, D. K., Bereketidou, O. A. & Goula, M. A. *International Journal of Hydrogen Energy* 35, 9818–9827, 2010.
30. Salhi, N., Boulahouache, A., Petit, C., Kiennemann, A. & Rabia, C., *International Journal of Hydrogen Energy*, 36, 11433–11439, 2011.
31. Roh, H. S., Eum, I. H. & Jeong, D. W., *Renewable Energy*, 42, 212–216, 2012.
32. Urasaki, K., Sekine, Y., Kawabe, S., Kikuchi, E. & Matsukata, M., *Applied Catalysis A: General*, 286, 23–29, 2005.
33. Barroso-Quiroga, M. M. & Castro-Luna, A. E., *International Journal of Hydrogen Energy*, 35, 6052–6056, 2010.
34. Gallego, G. S., Mondragón, F., Barrault, J., Tatibouët, J.-M. & Batiot-Dupeyrat, C., *Applied Catalysis A: General*, 311, 164–171, 2006.
35. Ferreira-Aparicio, P., Rodriguez-Ramos, I., Anderson, J. A. & Guerrero-Ruiz, A., *Applied Catalysis A: General*, 202, 183–196, 2000.
36. Ocsachoque, M., Pompeo, F. & Gonzalez, G., *Catalysis Today*, 172, 226–231, 2011.
37. Guo, J., Lou, H., Zhao, H., Chai, D. & Zheng, X., *Applied Catalysis A: General* 273, 75–82, 2004.
38. Tang, S., Lin, J. & Tan, K. L., *Catalysis Letters*, 51, 169–175, 1998.
39. Dissanayake, D., Rosynek, M. P., Kharas, K. C. C. & Lunsford, J. H., *Journal of Catalysis*, 132, 117–127, 1991.
40. Silva, P. P. et al., *Catalysis Today*, 107-108, 734–740, 2005.
41. Özdemir, H., Öksüzömer, M. A. F. & Gürkaynak, M. A., *Fuel*, 116, 63–70, 2014.
42. Kim, T. Y., Kim, S. M., Lee, W. S. & Woo, S. I., *International Journal of Hydrogen Energy*, 38, 6027–6032, 2013.
43. Santos, D. C. R. M., Madeira, L. & Passos, F. B., *Catalysis Today* 149, 401–406, 2010.
44. Mosayebi, Z., Rezaei, M., Ravandi, A. B. & Hadian, N., *International Journal of Hydrogen Energy*, 37, 1236–1242, 2012.
45. Li, B., Maruyama, K., Nurunnabi, M., Kunimori, K. & Tomishige, K., *Applied Catalysis A: General*, 275, 157–172, 2004.
46. Escritori, J. C., Dantas, S. C., Soares, R. R. & Hori, C. E., *Catalysis Communications*, 10, 1090–1094, 2009.
47. Sickafus, K. E., Wills, J. M. & Grimes, N. W., *Journal of the American Ceramic Society*, 82, 3279–3292, 1999.
48. Salmones, J., Galicia, J. A., Wang, J. A. & Valenzuela, M. A., *Journal of Materials Science Letters*, 19, 1033–1037, 2000.

49. Damyanova, S., Pawelec, B., Arishtirova, K. & Fierro, J. L. G., *International Journal of Hydrogen Energy*, 37, 15966–15975, 2012.
50. Nieva, M. A., Villaverde, M. M., Monzón, A., Garetto, T. F. & Marchi, A. J., *Chemical Engineering Journal*, 235, 158–166, 2014.
51. Pena, M. A. & Fierro, J. L. G., *Chemical Reviews*, 101, 1981–2017, 2001.
52. Mitra, C., Lin, C., Robertson, J. & Demkov, A. A., *Physical Review B*, 86, 2012.
53. Li, R., Yu, C. & Shen, S., *Journal of Natural Gas Chemistry*, 11, 137–144, 2002.
54. Valderrama, G. et al., *Catalysis Today*, 107-108, 785–791, 2005.
55. Lin, K.-H., Chang, H.-F. & Chang, A. C.-C., *International Journal of Hydrogen Energy*, 37, 15696–15703, 2012.
56. Asencios, Y. J. O., Bellido, J. D. a. & Assaf, E. M., *Applied Catalysis A: General* 397, 138–144, 2011.
57. Wang, S. & Lu, G. Q. M., *Applied Catalysis B: Environmental*, 19, 267–277, 1998.
58. Basile, F., Benito, P., Fornasari, G. & Vaccari, A., *Applied Clay Science*, 48, 250–259, 2010.
59. Clause, O., Rebours, B., Merlen, E., Trifiro, F. & Vaccari, A., *Journal of Catalysis*, 133, 231–246, 1992.
60. Takehira, K., Shishido, T., Wang, P., Kosaka, T. & Takaki, K., *Journal of Catalysis*, 221, 43–54, 2004.
61. Fonseca, A. & Assaf, E. M., *Journal of Power Sources*, 142, 154–159, 2005.
62. Hoang, D. L. & Chan, S. H., *Applied Catalysis A: General*, 268, 207–216, 2004.
63. Dewaele, O. & Froment, G. F., *Journal of Catalysis*, 184, 499–513, 1999.
64. York, A. P. E., Xiao, T. & Green, M. L. H., *Topics in Catalysis*, 22, 345–358, 2003.
65. Hickman, D. A. & Schmidt, L. D., *Journal of Catalysis* 138, 267–282, 1992.
66. Prettre, M., Eichner, C. & Perrin, M., *Transactions of the Faraday Society*, 42, 335–340, 1946.
67. Trimm, D. L. & Lam, C. W., *Chemical Engineering Science*, 36, 1405–1413, 1980.
68. Christian Enger, B., Lødeng, R. & Holmen, A., *Applied Catalysis A: General* 346, 1–27, 2008.
69. Xu, J. & Froment, G. F., *American Institute of Chemical Engineers*, 35, 88–96, 1989.
70. Ratnasamy, C. & Wagner, J. P., *Catalysis Reviews*, 51, 325–440, 2009.
71. Sprung, C., Arstad, B. & Olsbye, U., *ChemCatChem*, 6, 1969–1982, 2014.
72. Alves, H. J. et al., *International Journal of Hydrogen Energy*, 38, 5215–5225, 2013.
73. Appari, S., Janardhanan, V. M., Bauri, R., Jayanti, S. & Deutschmann, O., *Applied Catalysis A: General*, 471, 118–125, 2014.
74. Izquierdo, U. et al., *International Journal of Hydrogen Energy*, 37, 13829–13842, 2012.
75. Effendi, a, Hellgardt, K., Zhang, Z. & Yoshida, T., *Fuel*, 84, 869–874, 2005.
76. Kohn, M. P., Castaldi, M. J. & Farrauto, R. J., *Applied Catalysis B: Environmental*, 144, 353–361, 2014.
77. Bartholomew, C. H., *Applied Catalysis A: General*, 212, 17–60, 2001.
78. Sehested, J., *Catalysis Today*, 111, 103–110, 2006.

79. Cai, X., Cai, Y. & Lin, W., *Journal of Natural Gas Chemistry*, 17, 201–207, 2008.
80. Bengaard, H. S. et al., *Journal of Catalysis*, 209, 365–384, 2002.
81. Helveg, S., Sehested, J. & Rostrup-Nielsen, J. R., *Catalysis Today*, 178, 42–46, 2011.
82. Gadalla, A. M. & Bower, B., *Chemical Engineering Science*, 43, 3049–3062, 1988.
83. Samain, L. et al., *Journal of Solid State Chemistry*, 217, 1–8, 2014.
84. Wang, Y. G. et al., *Journal of the American Ceramic Society*, 81, 1655–1660, 1998.
85. Wolverton, C. & Hass, K. C., *Physical Review B*, 63, 024102, 2000.
86. Zhou, R. & Snyder, R. L., *Acta Crystallographica*, 47, 617–630, 1991.
87. Han, Y. S., Li, J. B., Ning, X. S. & Chi, B., *Journal of the American Ceramic Society*, 88, 3455–3457, 2005.
88. Shinoda, K., Sugiyama, K., Omote, K. & Waseda, Y., *International Journal of the Society of Materials Engineering for Resources*, 4, 20–29, 1996.
89. Araki, S., Hino, N., Mori, T. & Hikazudani, S., *International Journal of Hydrogen Energy*, 34, 4727–4734, 2009.
90. Ayabe, S. et al., *Applied Catalysis A: General*, 241, 261–269, 2003.

Chapter 2

Experimental methods

In this chapter, the methods for preparation of supports and catalysts will be reported. Characterization techniques will be also be presented. The set-ups that were implemented to study the ATR of model biogas both on powders and coated foams will be described. Moreover, the methodology used for the performances analysis and the evaluation of diffusion limitations will be detailed.

2.1. Catalysts preparation

2.1.1. Supports

a. Preparation of LaAlO_3 and LaNiO_3 perovskites

LaAlO_3 was prepared by a modified sol-gel method (Pechini). Ethylenediaminetetraacetic acid (EDTA, Sigma-Aldrich) was added to an aqueous solution containing the metal nitrates (concentration of 0.5 mol L^{-1} , Sigma-Aldrich) with a La:Al molar ratio of 1:1. EDTA is used as a chelating agent. A few milliliters of ammonia solution were added to obtain a clear solution. Finally, a solution of citric acid (2.5 mol L^{-1} , $n(\text{citric acid}) = n(\text{Al}) + n(\text{La})$) was added to the solution containing the chelated metals. The temperature of the solution was slowly heated to 100°C . Stirring was continued until evaporation of water led to a transparent gel. The gel was then dried and calcined following four different steps ($120^\circ\text{C} - 3\text{h}$; $300^\circ\text{C} - 3\text{h}$; $400^\circ\text{C} - 3\text{h}$; $800^\circ\text{C} - 5\text{h}$).

The same procedure was applied to prepare LaNiO_3 with nitrates of lanthanum and nickel with a La:Ni molar ratio of 1:1.

b. Preparation of MgAl_2O_4 and ZnAl_2O_4 spinel supports

Magnesium spinel (MgAl_2O_4) was prepared by co-precipitation. Three aqueous solution containing Mg and Al nitrates (Sigma-Aldrich and Fluka) with three different Al:Mg molar ratio were prepared. Each of them was added drop by drop into an aqueous solution of ammonium carbonate (Sigma-Aldrich) under vigorous stirring. The ammonium carbonate solution was prepared in order to contain large excess of carbonates, ensuring precipitation of all the metallic cations. The precipitates were aged for 3 h at room temperature. After centrifugation and washing with de-ionized water, the powders were dried overnight at 120°C . The dry deposit was then calcined at 800°C for 5h in air in order to obtain $\text{Mg}_{0.4}\text{Al}_2\text{O}_4$, $\text{Mg}_{0.7}\text{Al}_2\text{O}_4$ and $\text{Mg}_{1.1}\text{Al}_2\text{O}_4$.

The same procedure was applied to synthesize ZnAl_2O_4 spinel, using nitrates of Al and Zn (Sigma-Aldrich) with a Al:Zn molar ratio of 2:1.

c. Preparation of $\text{CeO}_2\text{-Al}_2\text{O}_3$ and $\text{ZrO}_2\text{-Al}_2\text{O}_3$ mixed oxides

$\text{CeO}_2\text{-Al}_2\text{O}_3$ was prepared by co-precipitation. An aqueous solution containing Ce and Al nitrates (Fluka) with a Ce:Al molar ratio of 1:2 (concentrations of 0.17 and 0.34 mol L⁻¹) was gradually added to an aqueous solution of ammonium carbonate under fast stirring. The carbonate solution was prepared in order to contain large excess of carbonates, ensuring precipitation of all metallic cations. The precipitate was aged for 3 h. After centrifugation and several washing cycles with de-ionized water, the precipitated powder was dried overnight at 120°C, then calcined at 800°C for 5 h.

The same method was used to prepare $\text{ZrO}_2\text{-Al}_2\text{O}_3$ with nitrates of zirconium and aluminium (Aldrich and Fluka) with a Zr:Al molar ratio of 1:2.

d. Preparation of Ni:Mg:Al hydrotalcite-type precursors

Hydrotalcite-type precursors were prepared by co-precipitation. An aqueous solution containing nitrates of Ni, Mg and Al respecting a molar ratio of $(\text{Ni} + \text{Mg})/\text{Al} = 3$ (Fluka and Sigma-Aldrich) was added dropwise to a saturated solution containing NaHCO_3 and NaOH . The precipitate was aged for 1 h. After centrifugation and washing with de-ionized water, the deposit was dried over night at 120°C. The dry deposit was then calcined at 800°C for 5 h in air.

e. Preparation of NiAl_2O_4

NiAl_2O_4 spinel was prepared by co-precipitation. An aqueous solution of ammonium hydroxide NH_4OH (concentration of 0.6 M) was added drop by drop into an aqueous solution containing Ni and Al nitrates (Fluka) with a Al:Ni molar ratio of 2:1 (concentrations of 0.34 and 0.17 mol L⁻¹ respectively). During addition, the solution was continuously stirred and the evolution of pH was followed closely. The addition of NH_4OH was stopped at pH 8.5. After centrifugation and several washing cycles at room temperature, the powder was dried overnight at 100°C. The dry deposit was then calcined at 800°C for 5h in air.

2.1.2 Impregnations with Ni, Ni-Rh and Rh

a) Ni impregnation

Ni was deposited on the different supports (spinel, perovskites, mixed oxides) by deposition-precipitation using nickel nitrate $\text{Ni}(\text{NO}_3)_2 \cdot 6\text{H}_2\text{O}$ (Fluka) and urea (Sigma-Aldrich). Stirring was continued for 4 h while the temperature was increased to 100°C in order to remove excess urea. After centrifugation and several washing with de-ionized water, the samples were dried at 120°C overnight and calcined at 550°C for 4 h in air.

b) NiRh impregnation

NiRh/ MgAl_2O_4 and NiRh/ LaAlO_3 were prepared by wet impregnation of MgAl_2O_4 or LaAlO_3 with a solution containing nickel nitrate $\text{Ni}(\text{NO}_3)_2 \cdot 6\text{H}_2\text{O}$ (Fluka), rhodium nitrate $\text{Rh}(\text{NO}_3)_3 \cdot 2\text{H}_2\text{O}$ (Alfa Aesar). Stirring was continued for 6 h. After evaporation of water, the slurry was dried at 120°C overnight and calcined at 550°C for 4 h in air.

c) Rh impregnation

0.05 wt.% Rh/ $\text{Mg}_{1.1}\text{Al}_2\text{O}_4$ was prepared by wet impregnation of MgAl_2O_4 with a solution containing rhodium nitrates $\text{Rh}(\text{NO}_3)_3 \cdot 2\text{H}_2\text{O}$ (Alfa Aesar). The solution was stirred for 4 h. After evaporation of water, the slurry was dried at 120°C overnight and calcined at 550°C for 4 h in air in order to obtain 0.05 wt.% Rh/ $\text{Mg}_{1.1}\text{Al}_2\text{O}_4$.

2.2. Characterizations

Different techniques were used to gather information on the catalysts structure, morphology and composition before and/or after reaction.

2.2.1 X-Ray Diffraction (XRD)

Supports and catalysts structures were investigated by XRD. Powder X-ray diffraction patterns were recorded using a Bruker D5005 diffractometer with a CuK radiation at $\lambda = 1.5418 \text{ \AA}$.

2.2.2 Transmission Electron Microscopy (TEM)

The morphology of the catalysts was studied by TEM. It was performed using a Jeol 2010 LaB₆ instrument operating at 200 kV.

2.2.3 Inductively Coupled Plasma (ICP)

Catalysts composition in terms of Ni loading as well as Ni:Al and Mg:Al molar ratios were obtained by ICP analysis using a Jobin Yvon Activa Spectrometer D ICP-OES. The measurements were made after dissolution of sample powder in sulphuric and nitric acids and injection of the solution into a plasma torch that atomizes the elements.

2.2.4 Brunauer, Emmet and Tellet (BET) –Specific Surface Areas

Specific surface areas (SSA) were measured by nitrogen adsorption on catalysts at -196°C on a BELSORP-Mini (Bel-Japan).

2.2.5 XPS

X-ray photoelectron spectroscopy was used to evaluate the surface chemical composition of the catalysts. The measurements were carried out with a AXIS Ultra DLD (KRATOS Analytical) spectrometer. The regions of interest were C 1s, O 1s, Al 2p, Ni 2p, Na 1s, Mg 2p and Si 2p. C 1s or Al 2p bands were used as standard for the XPS analysis. The depth of analysis is around 50 Å.

The carbon content and nickel oxidation states at the surface of the catalyst will be investigated with this technique.

2.2.6 UV-vis DRS

UV-visible diffuse reflectance spectroscopy was performed on catalysts in order to investigate the nature of the nickel species before and after reaction. A Deuterium-Halogen lamp emitting between 210 and 1000 nm was used as the light source. The light was conducted to an optical fiber probe

(FCR-7UV-400-2ME). Reflectance was measured by a Charge Couple Device (CCD) detector equipped with a monochromator in a Czerny-Turner configuration.

The Kubelka Munk (KM) approximation was used. This model is based on several assumptions:

- The incident light is perfectly diffuse and homogeneous,
- The only interactions of light are scattering and absorption,
- No external or internal surface reflection occur,
- The medium (here particles) is isotropic, homogeneous and is able to disperse light

The KM remission function was calculated:

$$F(R) = \frac{(1 - R)^2}{2R} = \frac{K}{S}$$

where R is the reflectance (relative to a standard), K is the absorption coefficient and S the scattering coefficient

The samples were mixed with BaSO₄, which was also used as “white” reference standard. The dilution of samples into BaSO₄ is enough to consider that the light scattering constant is similar for all measurement. Figure 2.1-a) shows its spectrum in the 210-1100nm region. Figure 2.1-b) shows the relative reflectance of a NiO sample relative to BaSO₄ and its KM transform.

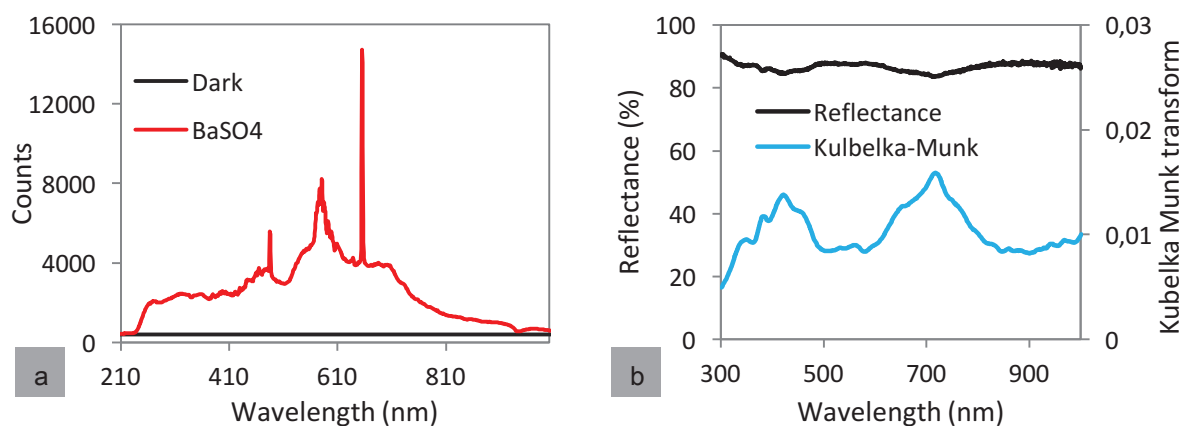


Figure 2.1: DRS spectra of a) the dark reference and the white reference BaSO₄ and b) Relative reflectance (%) of NiO and its Kubelka Munk transform

The sample thickness is enough to prevent any transmission effect.

Contrary to XPS which is a good technique for surface analysis, UV-vis DRS allows to investigate the bulk samples. Moreover, depending on the coordination of Ni in the catalyst, its color will be different. For instance, NiO and NiAl₂O₄ display green and blue colors respectively. Therefore, using this technique seemed well suited to discriminate nickel species before and after ATR reaction.

2.3. Catalytic tests

Two different types of catalytic tests were performed. The first catalytic tests were performed on powders in order to select and study a catalyst for the ATR reaction. Other catalytic tests were performed over SiSiC foams coated with the best catalyst with the objective of investigating the kinetics of the reaction.

2.3.1. Catalytic tests on powders

a. Reactors

Tubular fixed-bed quartz reactors were used. Quartz is high-temperature resistant and will be able to handle reaction temperature of 700 °C and higher. The reactors presented an internal diameter of 4 mm. Length was then adapted to the oven size. Figure 2.2 presents a scheme and a picture of type of reactors used.

Reactors were tapered and their design presented a reduction from i.d. of 4 to 2 mm in order to prevent the catalytic bed to be carried with the flow. Moreover, they were generally filled with quartz powder on top of the catalyst bed in order to reduce dead volume.

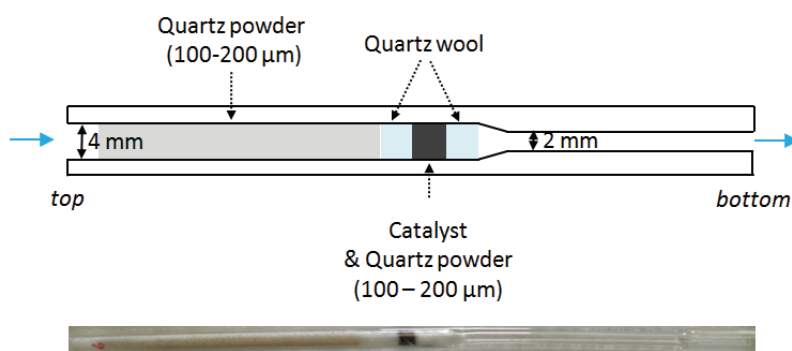


Figure 2.2: Scheme and picture of fixed bed reactors

Catalysts were sometimes diluted with quartz powder, both previously sieved between 100-200 microns.

Dilution should not be of influence on conversion as long as the following equation is respected [1]:

$$\frac{2.5 b d_p}{(1 - b)L_b} < 0.05 \quad Eq (2.1)$$

where b stands for inert fraction, d_p for particle diameter (m) and L_b for bed length (m).

b. Six-parallel flow reactor set up

A proprietary automated six-parallel reactor technology was implemented (Figure 2.3) to perform high-throughput long-term testing of the catalysts.

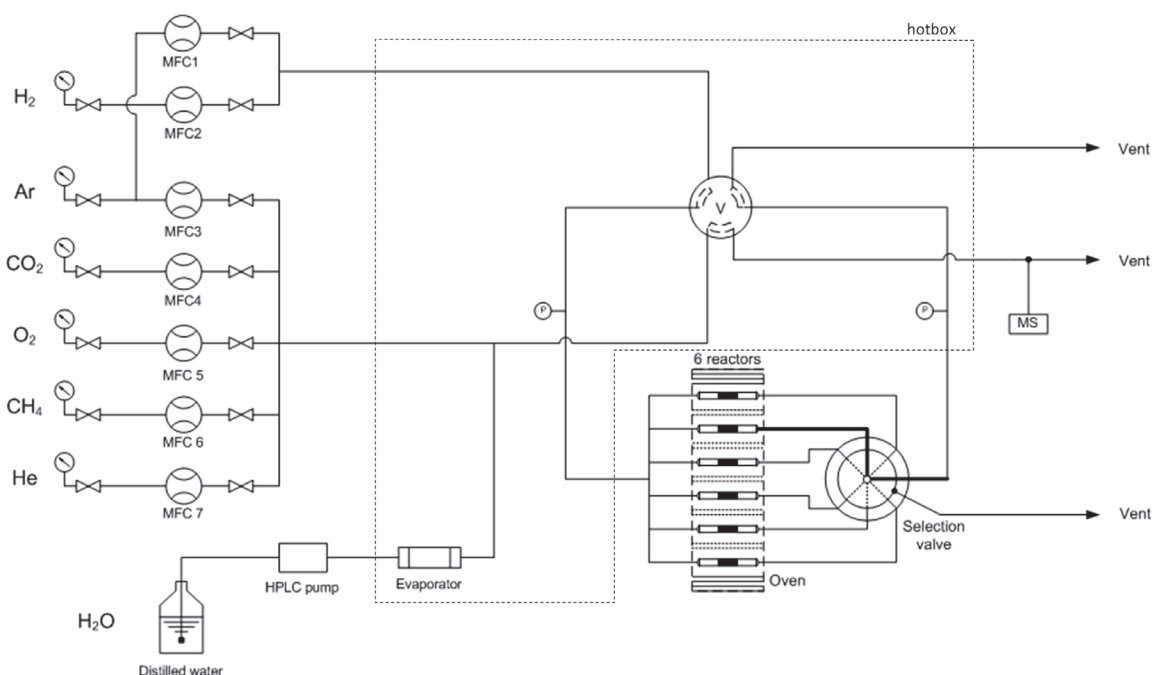


Figure 2.3: Scheme of the implemented set-up for ATR of model biogas with a six-parallel reactor technology

The liquid water flow rate was controlled by a HPLC pump (Shimadzu LC 20-AD) and vaporized in a custom-made evaporator at 200 °C. After vaporization, steam was mixed with the gaseous reactants whose flow rates were controlled by mass-flow controllers. All gas lines and valves were heated at 160 °C to prevent steam condensation. Six tubular quartz reactors (length 180 mm, 4 mm ID) were placed in a tubular furnace with six positions (Figure 2.4-a)

After mixing the reactants, the main gas stream was split into six flows, each being directed into a reactor. Special attention was given to distribute the flows equally, since the six different catalyst beds each create different pressure drops and can cause uneven flow distribution. To solve this issue, six identical stainless steel capillaries with small internal diameters (1/16" OD, 0.01" ID, 200 mm length)

were placed upstream to the reactors (Figure 2.4-b). The pressure drop created by the capillaries was much more important than that created by the catalyst bed. Measurement of the individual flows through the reactor showed deviations of $\pm 4 \text{ mL min}^{-1}$ for a flow of 80 mL min^{-1} per reactor.

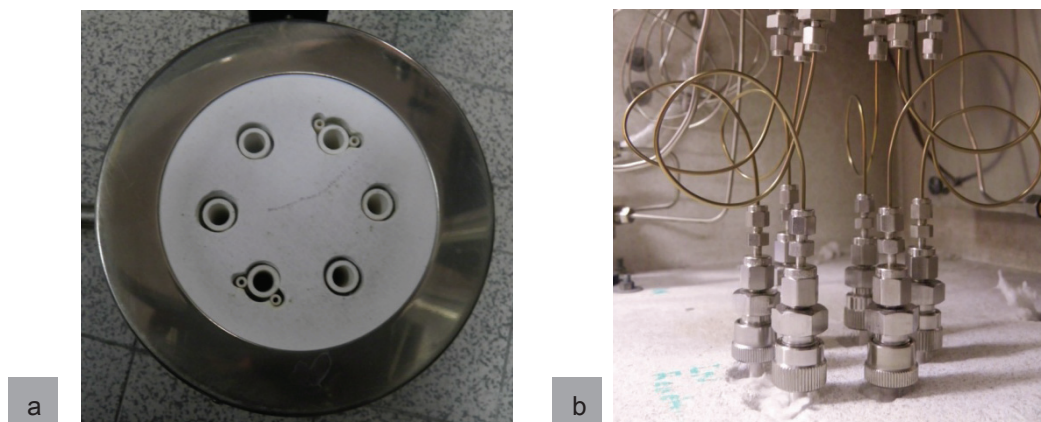


Figure 2.4: Pictures of a) the furnace with six reactor positions b) the capillaries added upstream to the reactors inside the hotbox

A 6-port automatic selection valve placed at the reactor outlet allowed selection of the effluent of one specific reactor to be sent to a mass spectrometer for gaseous product analysis. The selection valve was automatically switched every five minutes in order to measure sequentially the performance of each reactor using an online mass spectrometer. Pressure transducers placed upstream and downstream the reactors also measured the pressure drop in each reactor being analysed, to check for a possible increase in the pressure due to extensive coke deposition.

The temperature profile in each reactor was measured under inert gas flow and at $700 \text{ }^\circ\text{C}$ (Figure 2.5). Differences of $\pm 8 \text{ }^\circ\text{C}$ between the 6 reactors were found. Taking an activation energy of 110 kJ mol^{-1} for the steam reforming of methane [2], this will lead to a $\pm 10\%$ variation in the reaction rate at $700 \text{ }^\circ\text{C}$. The temperature was considered homogeneous between 4.3 and 5.3 cm. This means that the catalytic bed should be placed in this homogeneous zone and its height should not be over 1cm.

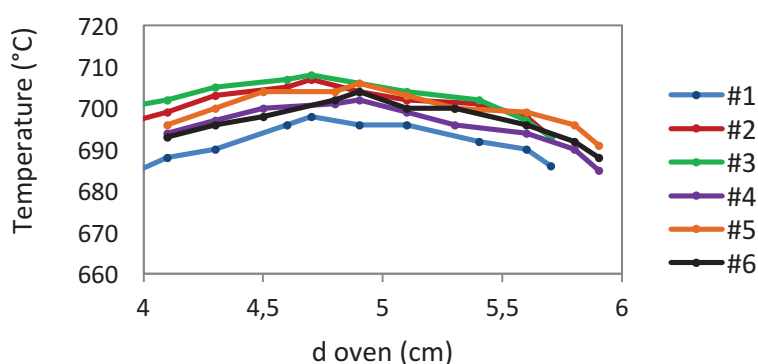


Figure 2.5: Temperature profile in empty reactors placed in the oven. Set point = $700 \text{ }^\circ\text{C}$.

c. Single reactor set up

Later in the study, the six parallel-flow reactor technology was replaced with a single reactor. Except for the replacement of the six-position furnace to a single and larger furnace, the set-up did not undergo major modifications (Figure 2.6). It should be noted that it was designed so that tests could be performed with flow rates of 40 to 250 mL min⁻¹.

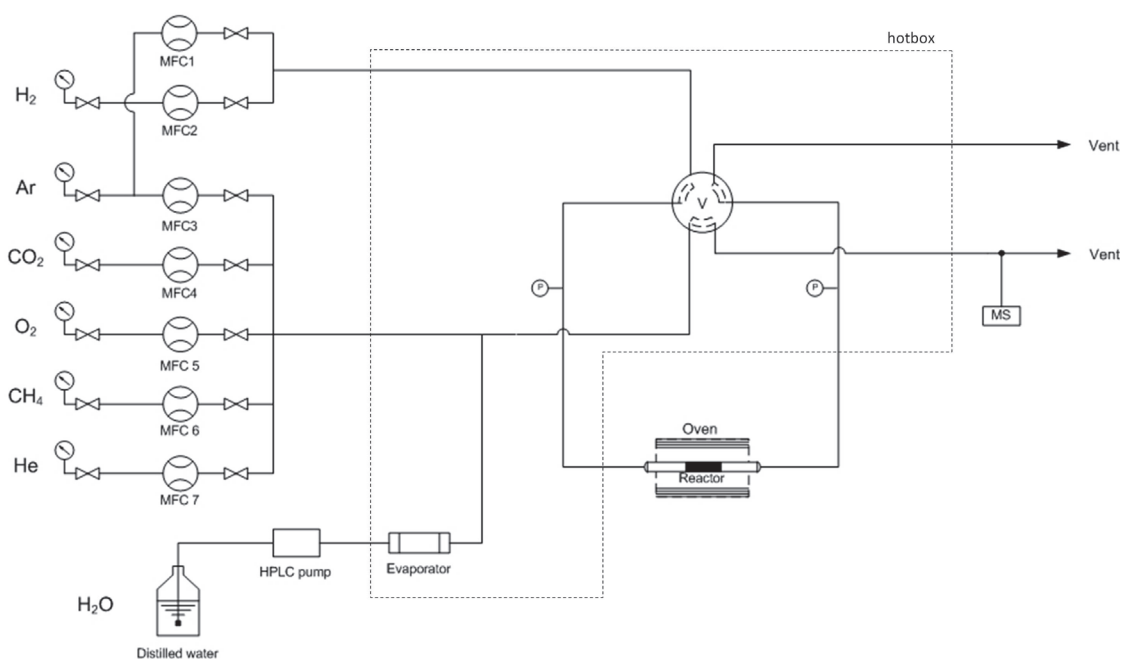


Figure 2.6: Scheme of implemented set-up for ATR of model biogas with a single reactor.

The temperature profile in the reactor was measured under inert gas flow and at set point of 700 °C (Figure 2.7). This time, the temperature was homogeneous in a larger zone from about 18 to 24 cm.

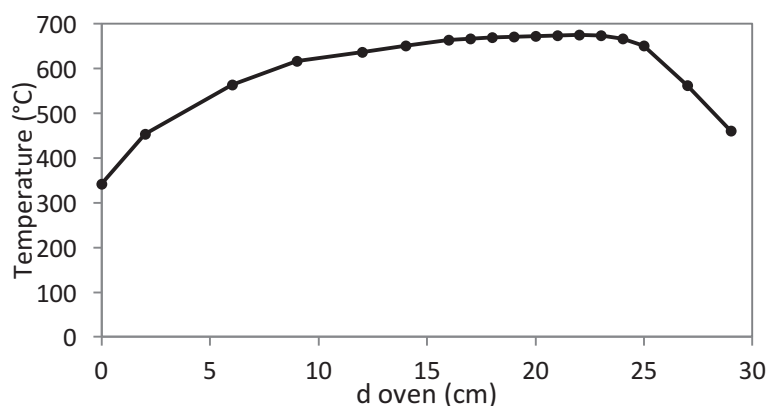


Figure 2.7: Temperature profile in empty single reactor placed in the oven. Set point = 700 °C.

At a set-point of 700 °C, the highest temperature measured inside the empty reactor was 675 °C. Therefore, the oven set-temperature was increased to 725 °C in order to reach 700 °C.

2.3.2. Catalytic tests on coated SiSiC foams

a. SiSiC foams

The silicon-infiltrated silicon carbide (SiSiC) foams were designed and manufactured by SUPSI and Erbicol SA who are both involved in the BioRobur project (see Chapter 1). The foams were aged at 1,400 °C. After mechanical tests and flow structure analyses, they were given to UAB Modernios E-Technologijos, another BioRobur partner, in charge of catalyst coating. Dip-slurry coating process was used in order to impregnate the supports with a NiRh/MgAl₂O₄ washcoat. It involves the following steps:

- Deposition of spinel slurry using dip-coating technology
- Drying at 60°C for 1 hour followed by calcination at 800°C for 4 hours
- Impregnation with Ni nitrate solution
- Drying at 60°C for 1 hour followed by calcination at 550°C for 4 hours
- Impregnation with Rh nitrate solution
- Drying at 60°C for 1 hour followed by calcination at 550°C for 4 hours

For the catalytic tests, the coated foam was placed in a quartz cylindrical reactor between two layers of quartz wool, as shown in Figure 2.8.

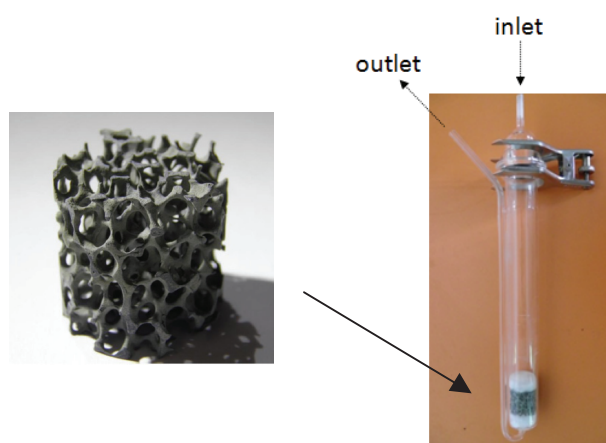


Figure 2.8: SiC foam coated with 15 wt.% Ni-0.05 wt.% Rh/MgAl₂O₄ catalyst and quartz reactor before reaction

The foams had a diameter of 2.5 cm and two different lengths of 2.5 and 1.4 cm.

b. Set-up

In order to test the coated foams in similar conditions as the powders, a new set-up was built as a replica of the one previously described (Figure 2.6). The only changing feature was the range of the mass flow controllers. In order to work at comparable GHSV as on the powders, much higher flows had to be reached. The set-up was thus designed to reach total flows of up to 3,000 mL min⁻¹.

Using an inlet mixture containing CH₄ and O₂ and such large flows implied that important safety measures had to be taken. The hotbox was swept by inert argon in order to prevent explosion in case of reactor breakdown or leaks. The mass flow controllers were also automatically shut off if too high temperatures or high pressures were reached in the reactor.

2.4. Evaluation of performances

2.4.1 Mass Spectrometer Online Analysis

Online analysis of the reactors exit streams was performed with a mass spectrometer (MS). Table 2.1 presents the monitored m/z fragments. It should be noted that fragment m/z = 15 was chosen for CH₄ rather than the molecular ion because it is nearly as intense (90%) as mass 16 in the methane fragmentation spectrum, whereas O₂ significantly contributes to mass 16, and also CO, CO₂ and H₂O to a lesser extent. Fragment m/z = 28 was chosen for CO but corrected for the contribution of CO₂ (≈ 10%).

Table 2.1: Table of monitored m/z fragments on mass spectrometer and their corresponding compounds

m/z fragment	Compound
2	H ₂
4	He
15	CH ₄
18	H ₂ O
28	CO (CO ₂ ≈ 10%)
32	O ₂
40	Ar
44	CO ₂

Quantitative analysis was performed by calibrating the MS response using different partial pressures of all relevant compounds diluted in argon. The Ar signal was used as an internal standard and the other ion current intensities were converted to molar flows knowing the molar flow rate of Ar and the sensitivity coefficient ($S_{m/z}$) of each m/z fragment relative to Ar, which is constant (Eq. 2.2).

$$S_{m/z} = \frac{I_{m/z}}{I_{Ar}} \times \frac{F_{Ar}}{F_{m/z}} \quad \text{Eq. 2.2}$$

Accurate water quantification with a MS is difficult, but the liquid water flow rate was precisely controlled by a calibrated HPLC pump, therefore the molar flow rate of steam at the reactor inlet was known accurately.

2.4.2 Description of conditions and activity analysis

Most reaction conditions were described in terms of Gas Hourly Space Velocity (GHSV) and sometimes Contact time (W/F):

- GHSV

$$GHSV = \frac{Q_{inlet}}{V_{cat}} \quad (\text{h}^{-1})$$

Where Q is the volumetric flow ($\text{m}^3 \text{h}^{-1}$) and V_{cat} is the volume of the catalyst bed

- Contact time

$$\frac{W}{F} = \frac{\text{catalyst mass}}{\text{molar flow rate}}$$

The performances were analysed and discussed in terms of conversions, productions and molar compositions according to the following calculations:

- O_2 and CH_4 conversions:

$$X_{\text{CH}_4, \text{O}_2} = \frac{F_{inlet} - F_{outlet}}{F_{inlet}} \times 100\%$$

Where F is the molar flow rate

- H_2/CO ratio

$$R = \frac{F_{outlet, \text{H}_2}}{F_{outlet, \text{CO}}}$$

- Gas composition on a dry basis

For each i compound, the molar fraction was calculated on a dry basis *i.e.* without the steam.

$$Y_i = \frac{F_{outlet, i}}{F_{outlet, total}} \times 100\%$$

2.5. Evaluation of diffusion limitations

Heterogeneous catalytic reactions are usually described with seven classical steps:

1. Diffusion of the reactants from the bulk phase to the external surface of the catalyst (external diffusion)
2. Diffusion of the reactants from the external surface to the active catalytic surface inside the pore (internal diffusion)
3. Adsorption of the reactants on the catalytic surface
4. Catalytic reaction
5. Desorption of the products from the catalytic surface
6. Diffusion of the products from the pore to the external surface
7. Diffusion of the products from the external surface to the bulk phase

When the catalytic reaction is fast, reaction rate can be limited by diffusions steps. Therefore, mass transfer limitations play an important role on the rate of conversions and formations of products.

Heat transfer limitations within the catalyst particles but also throughout the film surrounding the catalyst particles can alter the reaction rates as well.

This section discusses the evaluation of the mass and heat transfer limitations and gives criteria that should be respected in order to perform a study in conditions where the reaction rates are only determined by the intrinsic kinetics of the reaction.

2.5.1. External mass transport limitation

In order to make sure that the reaction rate is determined by catalytic reactions rather than by the diffusion of the reactants from the bulk to the external surface of the catalyst (step 1), Eq. 2.3 must be satisfied.

$$f_{ex} \equiv \frac{C_{Aex} - C_{Asu}}{C_{Aex}} = \frac{R_p \times L}{k_D \times C_{Aex}} < 0.05 \quad Eq. 2.3$$

where f_{ex} is the external mass transfer resistance fraction,

C_{Aex} is the concentration of reactant A in the bulk (mol m⁻³)

C_{Asu} is the concentration of A at the external surface of the catalyst (mol m⁻³).

R_p is the apparent rate of reaction per volume of catalyst (mol m⁻³cat s⁻¹)

L is the specific particle length (m).

k_D refers to external mass transfer coefficient (m s⁻¹) with x_f taking convection into account:

$$k_D = \frac{k_D^0}{x_f}$$

k_D^0 can be calculated from the Sherwood number:

$$Sh = \frac{k_D^0 \times d_p}{D_m} = 2 + 1.8 Re^{1/2} Sc^{1/3}$$

and the Reynolds number Re and the Schmidt number Sc can be calculated as follows:

$$Re = \frac{\rho u_v d_p}{\mu} \quad , \quad Sc = \frac{\mu}{\rho D_m}$$

where ρ is the average gas volumetric mass density (kg m⁻³),

u_v is the axial velocity (m s⁻¹),

D_m is the average molecular diffusivity (m² s⁻¹)

and μ is the gas viscosity (kg m⁻¹ s⁻¹) which can be estimated from Reid 1987 [3]

$$\mu = \frac{2.669 \cdot 10^{-6} T^{1/2} M^{1/2}}{d^2}$$

where T is temperature (K), M molecular weight (g mol⁻¹) and d hard-sphere diameter (Å).

2.5.2. Internal mass transport limitation

In order to make sure that the reaction rate is not determined by the diffusion of the reactants from the external surface to the catalytic surface, the Thiele modulus (ϕ) for a first-order reaction can be calculated with Eq. 2.4 and should be lower than 1 [4]:

$$\phi = \sqrt{\frac{k L^2}{D_e}} < 1 \quad \text{Eq. 2.4}$$

where k is the rate constant (s^{-1}),

L is the specific particle length (m)

D_e is the effective molecular diffusivity ($\text{m}^2 \text{s}^{-1}$):

$$D_e = \frac{\varepsilon}{\tau} D \quad \text{and} \quad \frac{1}{D} = \frac{1}{D_m} + \frac{1}{D_k}$$

where ε refers to catalyst porosity and τ catalyst tortuosity

Knudsen diffusion coefficient can be calculated from the following equation:

$$D_k = \frac{4 r}{3} \sqrt{\frac{2 R T}{\pi M}}$$

where r is the pore diameter (\AA),

T is the temperature (K)

M is the molecular weight (g mol^{-1})

Catalysts porosity and tortuosity are not known for the catalysts tested. However, values can be extracted from the literature. For instance, for 3 different typical Ni catalysts supported on Al_2O_3 [5], MgAl_2O_4 [6] and YSZ [7], the catalyst porosity and tortuosity were: $0.35 < \varepsilon < 0.5$ and $3.5 < \tau < 3.8$.

2.5.3. External heat transfer limitation

The effects of heat transfer are analogous to those of mass transfer. Heat transfer limitations throughout the film surrounding the catalyst particle can be evaluated. The criterion for external maximum temperature difference ΔT_{film} over the film surrounding the spherical catalyst particles is expressed as follows [8]:

$$\Delta T_{\text{film}} = \frac{R_p |\Delta H| d_p}{6 \alpha_p} < \frac{0.05 R T_G^2}{E_a} \quad \text{Eq. 2.5}$$

where R_p is the reaction rate per unit of catalyst volume [$\text{mol m}^{-3} \text{cat s}^{-1}$]

ΔH is the reaction enthalpy [J mol^{-1}]

d_p is the particles diameter [m]

R is the ideal gas constant [$\text{J mol}^{-1} \text{K}^{-1}$]

T_G is the bulk gas temperature [K]

E_a is the activation energy of the reaction [J mol⁻¹]

and α_p is the heat transfer coefficient from the gas to the catalyst particle [W m⁻² K⁻¹]:

$$\alpha_p = \frac{Nu \times \lambda_G}{d_p}$$

where λ_G is the thermal conductivity of the gas mixture [W m⁻¹ K⁻¹]

and the Nusselt number: $Nu = 2 + 1.1 Re^{0.6} Pr^{1/3}$ in the range $0.1 < Re < 100$

The Prandtl number is defined as $Pr = \frac{c_p \mu_G}{\lambda_G}$

where C_p is the gas heat capacity [J kg⁻¹ K⁻¹]

2.5.4. Internal heat transfer limitation

Heat transfer limitations throughout the catalyst particle can also affect the reaction rate. The maximum temperature difference ΔT_{int} between the edge and the middle of the particle is expressed as follows [8]:

$$\Delta T_{int} = \frac{R_p \Delta H d_p^2}{\lambda_p} < \frac{0.05 R T^2}{E_a} \quad Eq. 2.6$$

where λ_p is the thermal conductivity of the catalyst particle [W m⁻¹ K⁻¹]

2.6. Conclusions

The supports were for the most part prepared by co-precipitation method except for the perovskites which were prepared by a modified sol-gel method (Pechini). They were all calcined at 800°C in air. Ni or Rh deposition was performed by wet-impregnation and deposition-precipitation. Catalysts were calcined at 550°C in air. Techniques such as XRD, ICP, TEM, UV-vis DRS and BET were used to characterize the supports and catalysts.

Reactions were carried out using quartz reactors. In some cases, catalysts were mixed with quartz powder and particular attention must be given to the dilution factor so that it would not affect the catalysts performances.

A first set-up was implemented consisting in a six-parallel flow reactor technology. Equilibration of the flows was ensured by the addition of capillaries upstream to the reactors. The set-up was subsequently changed to a simpler design enabling to test catalysts in single reactors. A second set-up was implemented and was specifically designed to test structured catalysts.

The performances were monitored by online analysis with a mass spectrometer after calibration of the reactants and products using Ar as an internal standard.

REFERENCES

1. Pérez-ramirez, J., Berger, R. J., Mul, G., Kapteijn, F. & Moulijn, J. A., *Catalysis Today*, 60, 93–109, 2000
2. Rostrup-Nielsen, J. R., *Catalysis*, 5, 1–117, 1984.
3. Reid, R. C., Prausnitz, J. M. & Poling, B. E., *The properties of gases and liquid*, 1987.
4. Froment, G. F. & Bischoff, K., *Chemical Reactor Analysis and Design*, J. Wiley & Sons, New York, 1990.
5. Metaxas, K. C. & Papayannakos, N. G., *Chemical Engineering Journal*, 140, 352–357, 2008.
6. Xu, J. & Froment, G. F., *American Institute of Chemical Engineers*, 35, 88–96, 1989.
7. Janardhanan, V. M. & Deutschmann, O., *Journal of Power Sources*, 162, 1192–1202, 2006.
8. Mears, D. E., *Journal of Catalysis*, 20, 127–131, 1971.

Chapter 3

Catalyst screening for the autothermal reforming of model biogas

Autothermal reforming of model biogas was studied over different catalysts compositions in order to identify the best candidate.

High-throughput screening is a powerful tool that enables comparison of catalysts activity, stability and selectivity. It is a pragmatic approach that relies on fast and systematic screening of libraries of samples [1]. Within the past couple of decades, it has been applied in the field of catalysis.

A six flow reactor technology has been used widely by the team of Moulijn for different reactions such as NO_x oxidation and soot oxidation [2], [3]. To our knowledge, this type of technology has never been used for reforming reaction. In addition, many catalysts have been tested for methane or biogas reforming with different combinations of active metals on various supports [4]. However, these tests were performed under different conditions of temperature and pressure with different feed ratios, flow rates and reactor designs, making a fair comparison difficult. In the present chapter, long-term catalyst stability was assessed using a proprietary six parallel-flow reactor set-up, specially implemented to test simultaneously six catalysts for ATR of model biogas under essentially identical flow rate, temperature and feed composition.

First and foremost, the supports and catalysts were characterized. Before testing the catalysts of interest, the set-up reliability was evaluated on a commercial catalyst in order to verify that it would be an adequate tool for our catalyst screening.

After validation, the long term stability of 12 catalyst compositions was assessed for ATR of model biogas at 700°C.

3.1. Prepared catalysts and characterizations

Five supports were prepared: magnesium spinel MgAl₂O₄, zinc spinel ZnAl₂O₄, perovskite LaAlO₃, mixed oxides CeO₂-Al₂O₃ and ZrO₂-Al₂O₃. As described in Chapter 1, the spinels were chosen for their ability to limit or prevent the formation of inactive NiAl₂O₄. The perovskite and mixed oxides were chosen for their ability to limit or prevent carbon formation.

All of them were impregnated with 5 wt.% Ni loading following a method described in Chapter 2. MgAl₂O₄ and LaAlO₃ were also impregnated with 5 wt.% Ni and 0.05 wt.% Rh. LaNiO₃ and a hydrotalcite-type precursor Ni/Mg/Al were also prepared. They were chosen for the fact that very well dispersed Ni particles can be expected after reduction. This added up to 9 prepared catalysts.

ICP analyses were performed on all catalysts. BET Surface Areas were also measured. The nickel loading and surface areas of all catalysts are reported in Table 3.1.

Table 3.1: Nickel and rhodium loadings and specific surface area of prepared catalysts

prepared catalysts		Ni loading (wt. %)	Rh loading (wt. %)	BET Surface Area (m ² .g ⁻¹)
5 wt.% Ni/Mg _{0.7} Al ₂ O _{3.7}	NM	5.1	-	158
5-0.05wt.%NiRh/Mg _{0.7} Al ₂ O _{3.7}	NRM	5.1	0.051	118
5 wt.% Ni/ZnAl ₂ O ₄	NZ	4.5	-	99
5 wt.% Ni/LaAlO ₃	NL	4.5	-	15
5-0.05 wt.% NiRh/LaAlO ₃	NRL	3.9	0.052	7.8
LaNiO ₃	LN	26	-	2.7
5 wt.% Ni/CeO ₂ -Al ₂ O ₃	NCA	5	-	57
5 wt.% Ni/ZrO ₂ -Al ₂ O ₃	NZA	5	-	119
Hydrotalcite-type precursor	HT	4.3	-	116

The magnesium spinel support actually presented a sub-stoichiometric amount of Mg resulting in a composition Mg_{0.7}Al₂O_{3.7}. Either this difference is a result of the highly hygroscopic properties of the magnesium nitrates used for the preparation or this is due to incomplete precipitation of magnesium hydroxide during preparation.

A similar amount of Ni, around the nominal value of 5 wt.% was generally deposited on the catalysts, with the exception of sample NRL, which exhibited a lower loading (3.9 wt%), and sample LN (LaNiO₃ perovskite) for which the bulk nickel concentration was 26 wt%. The catalysts exhibited important variations in specific surface areas. It was generally high for spinel and hydrotalcite-type catalysts, with NM presenting the highest value (158 m² g⁻¹). The perovskites had lower surface areas, ranging from 2.7 to 15 m² g⁻¹. The specific surface areas of mixed oxides catalysts were 57 and 119 m² g⁻¹ for NCA and NZA, respectively.

X-ray diffraction patterns of the supports after calcination at 800°C along with LN and HT are presented in Figure 3.1.

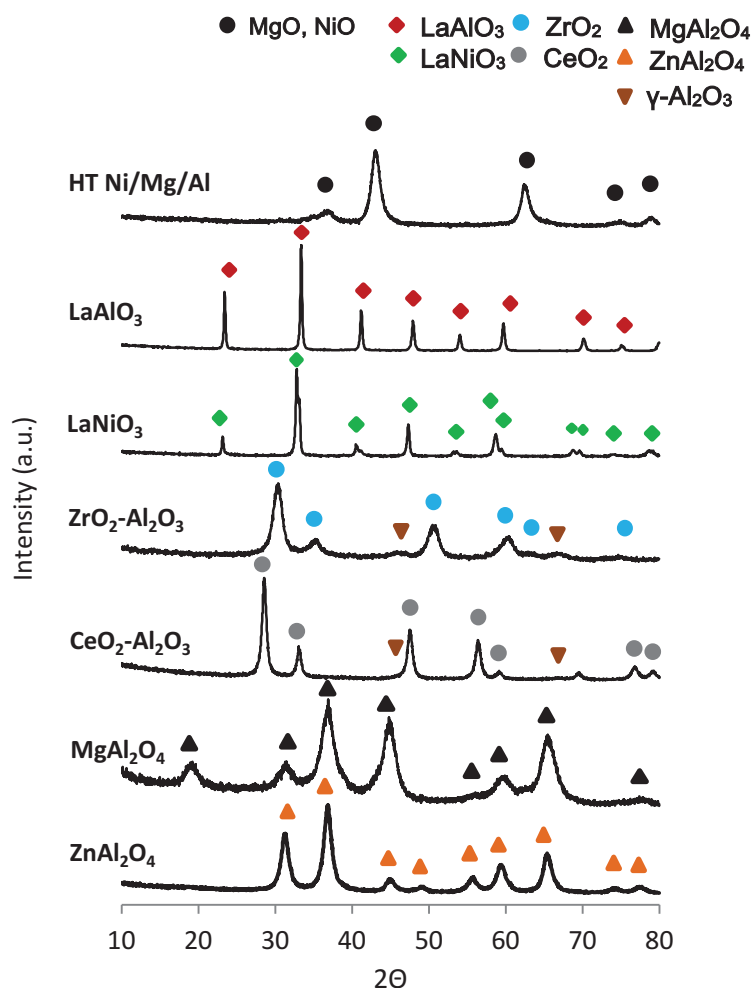


Figure 3.1: X-ray diffractograms of prepared supports after calcination at 800°C for 5h in air

The perovskites showed thin and intense diffraction lines, which is consistent with their low specific surface areas.

On the contrary, spinels and mixed oxides showed broad lines which is also in agreement with their high specific surface areas. $ZnAl_2O_4$ diffractogram displayed characteristic lines of the spinel structure only. No ZnO lines were evidenced. Similarly, $MgAl_2O_4$ showed the characteristic lines of the spinel structure and no MgO lines were observed.

$CeO_2-Al_2O_3$ diffractogram displayed very intense CeO_2 lines and less intense $\gamma-Al_2O_3$. $ZrO_2-Al_2O_3$ patterns were very similar, evidencing the presence of ZrO_2 and $\gamma-Al_2O_3$. Some ZrO_2 lines could also have a contribution from a mixed $Zr_{0.5}Al_{0.5}O_2$ oxide.

$LaNiO_3$ and $LaAlO_3$ diffractograms both evidenced the presence of the expected perovskite structure only.

Finally the Ni/Mg/Al catalyst prepared from a hydrotalcite precursor showed lines that could be attributed to a hydrotalcite structure $(\text{Ni,Mg})_6\text{Al}_2(\text{CO}_3)(\text{OH})_{16}, 4\text{H}_2\text{O}$ before calcinations (not shown). After calcination at 800°C , the hydrotalcite structure was not observed anymore as expected from the decomposition of the hydrotalcite into oxide phases. Characteristic lines of both NiO and MgO were evidenced instead. No spinel lines were observed.

X-ray diffractograms of the catalysts after nickel impregnation and calcination were performed as well but showed no significant modification compared to the supports. No Ni or NiO lines were evidenced except on LN and NL. Figure 3.2 displays the diffractograms of ZnAl_2O_4 and NZ to illustrate this. The metal loading could be too low to observe specific lines from nickel species. The particles might also be too small or are interacting strongly with the support.

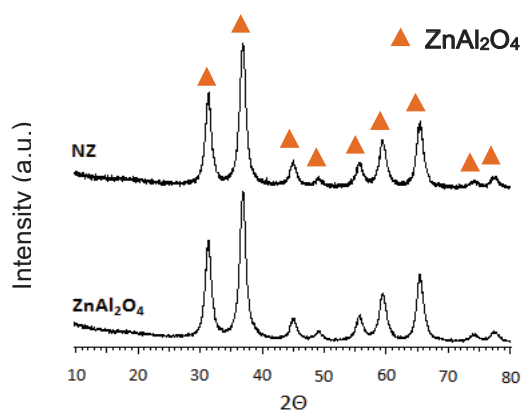


Figure 3.2: X-ray diffractograms of support ZnAl_2O_4 after calcination at 800°C for 5h in air and catalyst 5 wt.% Ni/ ZnAl_2O_4 (NZ) after impregnation and calcination at 550°C for 4h in air

Though the catalysts contained the same loading of nickel, the supports presented distinct features. They varied by composition, structures, specific surface area and crystallinity.

3.2. Set-up validation on commercial catalyst

Before carrying out the screening of prepared catalysts, the reliability of the six parallel-flow reactor set-up was verified. Six identical reactors were loaded with the same mass of commercial nickel based catalyst (HiFUEL, R110, Alfa Aesar, ref. 45465) in order to assess the repeatability of the results. All reactors were expected to present the same performances in terms of stability, methane conversion and H_2/CO selectivity.

This preliminary test was first performed over 10 mg of catalyst. *In-situ* reduction was carried out with a H_2/Ar mixture (4:1 ; vol:vol) for 3 hours at 700°C . The reaction mixture consisted of 42% steam, 14%

CH₄, 9% CO₂, 7% O₂ in an argon balance. This composition represents a model biogas composed of 60% CH₄ and 40% CO₂, reacting with a mixture of O₂ and steam under the conditions O₂/CH₄ = 0.5 and Steam/CH₄ = 3.

If oxygen were supplied as air, the balance gas would be nitrogen. Argon was substituted for nitrogen because N₂ would forbid analyzing CO by mass spectrometry (same molecular ion). Moreover, Ar was also used as internal standard for quantification of products.

The reaction was started with a total reactant flow rate was 380 mL min⁻¹ resulting in 63.3 mL min⁻¹ in each reactor. At the reactors exit, the selection valve was switched automatically every 5 minutes. By doing so, the performances of the first reactor were monitored using an online mass spectrometer between t = 0 to 5 minutes. Then, as the valve was switched, the performances of the second reactor were monitored between t = 5 to 10 minutes and so on and so forth. Figure 3.3 illustrates the sequential analysis of the reactors during ATR reaction.

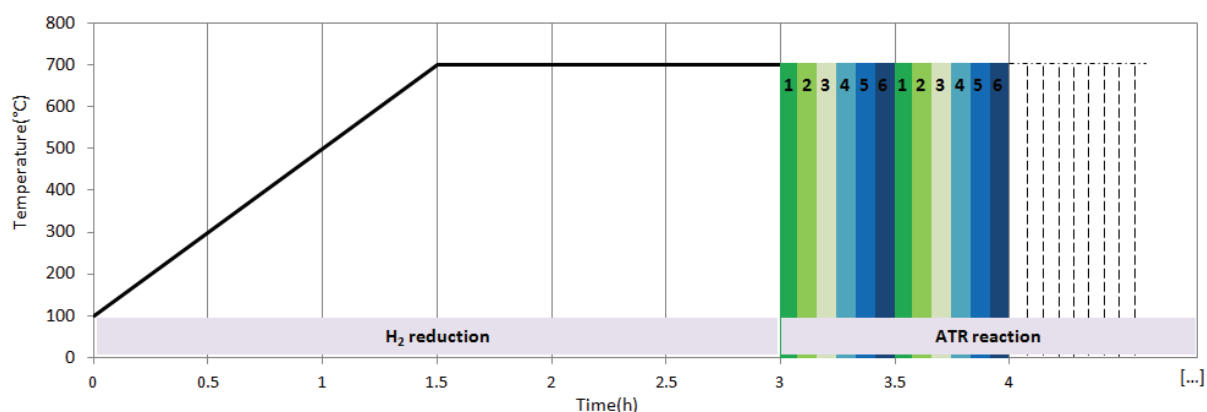


Figure 3.3: Test sequence consisting in a reduction step for 3 hours with a H₂/Ar mixture followed by the ATR of model biogas.

H₂, CH₄, CO, O₂ and CO₂ were monitored using online mass spectrometer calibrated for quantitative analysis (see Chapter 2). Figure 3.4 presents the methane conversions in each reactor as a function of time on stream.

In reactor R1, the methane conversion was close to 92 % at the beginning of the reaction then decreased steadily until complete deactivation after 11 hours. The other catalysts showed similar profiles but their stability was different. The catalyst in reactor 5 was the first to deactivate after only 7 hours of reaction. Complete deactivation occurred after 9, 10, 11, 13 hours over catalysts in reactors 6, 2, 1 and 3 respectively. The catalyst in reactor 4 was the last to deactivate at t = 16 h, 9 hours after reactor 5.

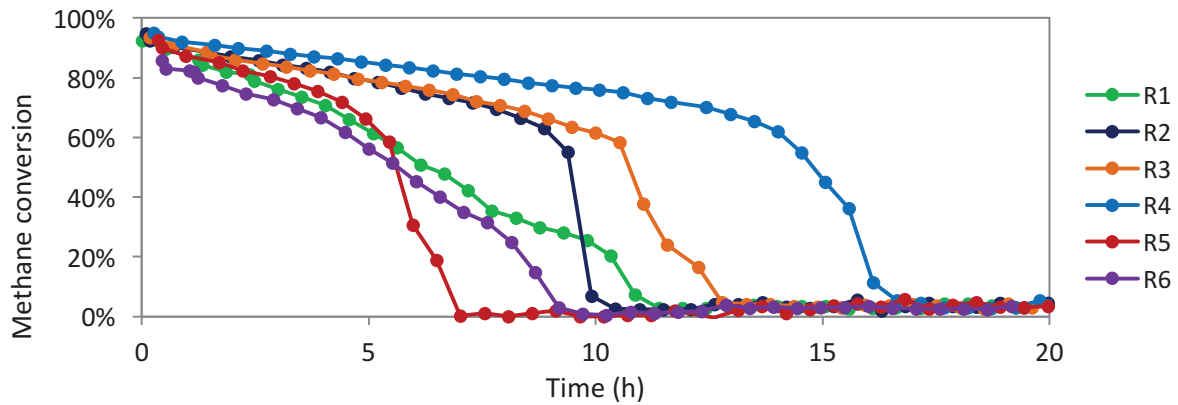


Figure 3.4: Methane conversion during ATR of model biogas over 6 x 10 mg of commercial nickel catalyst. Reaction conditions: $T = 700^{\circ}\text{C}$, $\text{Steam}/\text{CH}_4 = 3$, $\text{O}_2/\text{CH}_4 = 0.5$, $\text{CH}_4:\text{CO}_2 = 60:40$

It was assumed that the uncertainty on the mass was too important when using only 10 mg of catalyst. Another test was thus performed over 20 mg of catalyst instead of 10 mg. *In-situ* reduction was carried out with a H_2/Ar mixture (4:1 ; vol:vol) for 3 hours at 700°C . The reaction conditions and flow rates were kept unchanged resulting in a GHSV twice less important. Prior to testing, the flow rate in each reactor was measured under inert Ar flow. The deviation in flow distribution between all reactors was 2%.

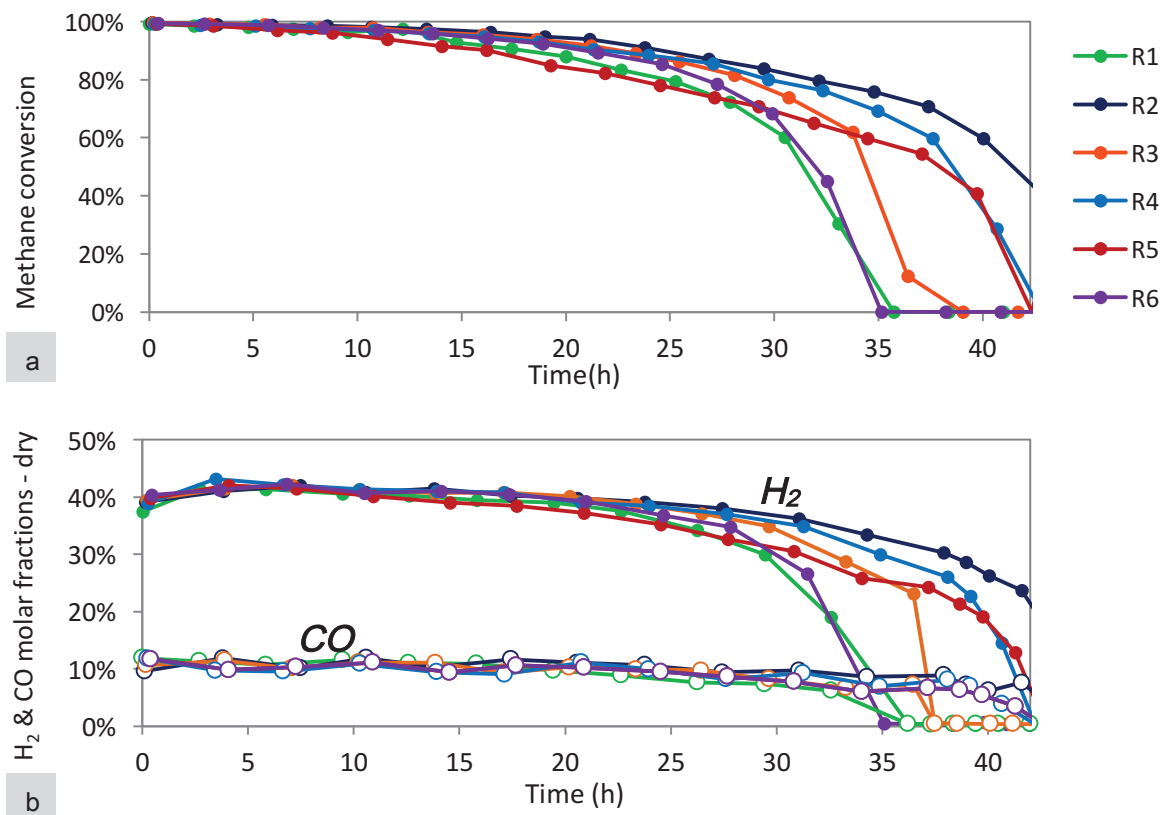


Figure 3.5: a) Methane conversion and b) H_2 & CO molar fractions during ATR of model biogas over 6 x 20 mg of commercial nickel catalyst. Reaction conditions: $T = 700^{\circ}\text{C}$, $\text{Steam}/\text{CH}_4 = 3$, $\text{O}_2/\text{CH}_4 = 0.5$, $\text{CH}_4:\text{CO}_2 = 60:40$

Methane conversions were complete in all reactors during the first hours but declined steadily (Figure 3.5-a). Catalysts in reactor 1 and 6 were the first to deactivate after about 35 hours, followed by the catalyst in reactor 3 which deactivated after 37.5 hours. Catalysts in reactor 4 and 5 deactivated after 42 hours while 40% of the methane was still converted in reactor 2.

The performances in terms of H₂/CO selectivity were similar in all reactors. Molar fractions of H₂ and CO were calculated on a dry basis, i.e. not taking the steam into account. At full methane conversion, they reached about 40% and 10% respectively in all reactors (Figure 3.5-b). Their production dropped as the methane conversion dropped as well.

Figure 3.6 displays the molar fractions of all compounds on a dry basis at the outlet of reactor #1. Complete conversion of methane and oxygen is observed during the first hours. After 15 hours, the CH₄ molar fraction increases while the O₂ molar fraction remains zero. As the catalyst becomes less active for the reforming reaction, the oxygen is still fully converted from the combustion reaction. When the CH₄ molar fraction reaches about 10% (corresponding to 60% conversion), the oxygen conversion is no longer complete. Methane and oxygen conversions suddenly drop to zero and hydrogen and carbon monoxide productions drop similarly. The catalyst is fully deactivated. The outlet composition corresponds to the inlet composition on dry basis (24% CH₄, 12% O₂, 16% CO₂) and the carbon balance was 100 ± 2 %. Similar behaviour was observed on all the reactors.

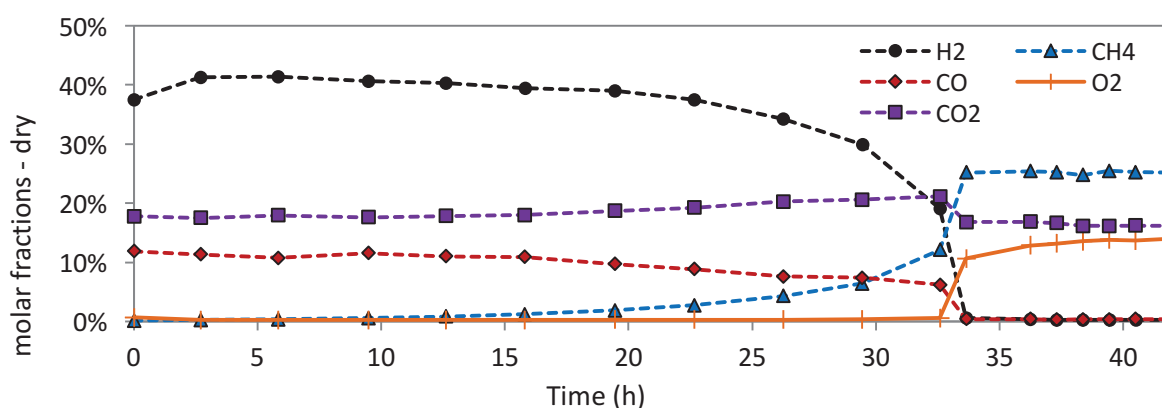


Figure 3.6: Dry outlet gas concentrations during autothermal reforming of model biogas over 20 mg of commercial nickel catalyst. Reaction conditions: T = 700°C, Steam/CH₄ = 3, O₂/CH₄ = 0.5, CH₄:CO₂ = 60:40

After 43 hours and before complete deactivation of catalysts in reactors 2 and 5, oxygen was removed from the reactants feed gas. As soon as O₂ was removed, both catalysts started to convert methane again (Figure 3.7).

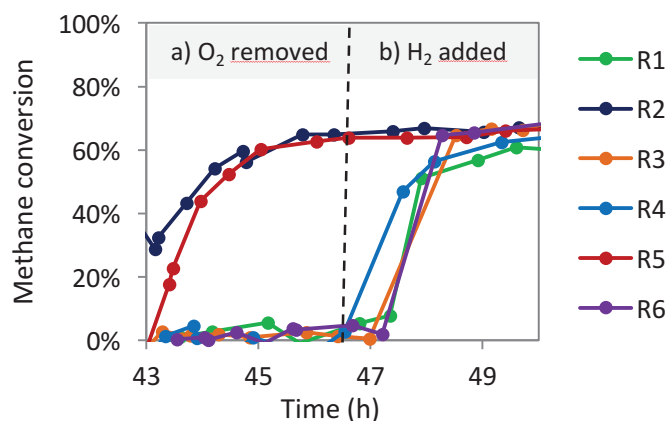


Figure 3.7: Methane conversion during ATR of model biogas at $T = 700\text{ }^{\circ}\text{C}$ a) with $\text{Steam}/\text{CH}_4 = 3$, $\text{CH}_4/\text{CO}_2 = 60/40$ and in the absence of oxygen and b) at $T = 700\text{ }^{\circ}\text{C}$ with $\text{Steam}/\text{CH}_4 = 3$, $\text{CH}_4/\text{CO}_2 = 60/40$ and addition of hydrogen

However, catalysts in reactors 1, 3, 4 and 6 did not convert methane again until hydrogen was added to the feed after 46 hours. At this point, methane conversions ranging from *ca.* 65 to 70% were observed in all the six reactors. Given these results, oxidation of Ni appears to play an important part in the deactivation process. The role of O_2 and nickel oxidation will be investigated more thoroughly in Chapter 4.

In conclusion, complete deactivation on commercial catalyst occurred after around 40 ± 5 hours. This variation could be attributed to the slight differences in catalyst mass, inlet flow rates and temperatures. The six deactivation profiles and performances, however, were sufficiently similar to allow unambiguous discrimination between fast-deactivating and stable catalysts.

3.3. ATR of model biogas over prepared catalysts

After evaluation and validation of the six parallel-flow reactor set-up, various nickel catalysts were tested for the ATR of model biogas. The influence of the support on the catalyst stability was investigated by testing different compositions.

The prepared catalysts were tested along with 3 catalysts with higher nickel loadings for comparison purposes: 14 wt. % $\text{NiO}/\text{CaAl}_2\text{O}_9$ (NC), 20 wt.% Ni/SiO_2 (NS) and 20 wt.% $\text{Ni}/\text{Al}_2\text{O}_3$ (NA).

It should be noted that the catalysts densities depended on their compositions. Therefore, some catalytic beds were diluted in quartz powder in order to maintain both the mass of catalyst and the GHSV constant. An identical bed length of 8 mm was obtained for all catalyst beds. The only changing

parameter was thus the dilution factor. Considering the bed length and particle diameter, the dilution factor should remain between 0 and 52 vol.% according to Eq. (2.1) in Chapter 2.

The catalyst beds were composed of 20 mg of catalyst. All catalysts except NM and NRM were diluted with quartz powder respecting inert fractions varying between 35-50%. *In-situ* reduction was performed at 700°C for 3 hours with a H₂/Ar mixture (4:1, vol:vol). The reaction was then carried out at 700°C, with Steam/CH₄ = 3, O₂/CH₄ = 0.5 and CH₄:CO₂ = 60:40. The total flow rate of the reactant gases was 380 mL min⁻¹ resulting in 63.3 mL min⁻¹ for each reactor. Prior to testing, the deviation in flow distribution in each reactor was measured. For all tests, the deviation always represented less than 4% of the flow and was 2.5% in most cases.

Figure 3.8 shows the results of the screening in terms of methane conversion.

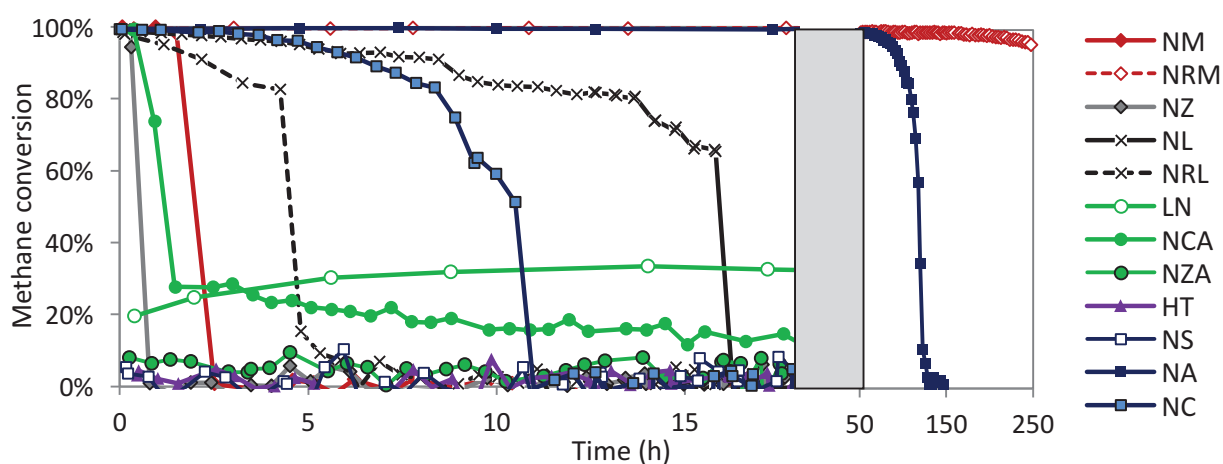


Figure 3.8: Methane conversion during ATR of model biogas at T = 700°C. Reaction conditions: Steam/CH₄ = 3, O₂/CH₄ = 0.5 and CH₄:CO₂ = 60:40

No conversion was observed over NS, NZA and HT catalysts. On the one hand, this could mean that they are inactive for the ATR of model biogas. The reduction temperature might have been too low to reduce and extract Ni from the mixed-oxide structure in the case of HT, since the Ni reduction in Ni–Mg–Al hydrotalcite catalysts has been shown to take place between 750 and 900 °C [5]. On the other hand, NS, NZA and HT were tested in reactors 3, 4 and 6 respectively. During the first 10 minutes, the performances of reactor 1 then reactor 2 were monitored. NS might have been active at the very beginning of the reaction but deactivated before we could monitor its performances. In the same way, it is thus also possible that NZA was active during the first 15 minutes and HT during the first 25 minutes.

NM, NZ and NCA exhibited full initial methane conversion but deactivated within 2 hours. NRL, NC and NL catalysts deactivated more gradually and were fully deactivated after 5, 11 and 16 h respectively. NA deactivated after about 130 h. NRM was still active after 250 h of reaction.

LN catalyst revealed peculiar performance, with a moderate but constant methane conversion ($\approx 30\%$), which gradually dropped to zero after 20 h (not shown), probably due to the negative combination of high Ni loading and very low surface area. Slagtern and Olsbye [6] reported that LaNiO_3 deactivation during partial oxidation of methane was probably related to coke formation. It is also possible that Ni oxidation occurred in the oxygen-rich combustion zone and led to the reformation of the LaNiO_3 perovskite [7].

Increasing the Ni loading was expected to delay the catalyst deactivation, since more Ni is available in the reactor, provided that it is dispersed enough and that the support exhibits the appropriate acid–base properties. This was generally verified since all 5 wt% Ni catalysts except NL deactivated before NC (14% Ni) catalysts, which in turn deactivated before NA (20% Ni). Therefore LaAlO_3 appears as an interesting support, despite its low SSA. A noticeable exception was NS (20% Ni), which deactivated so rapidly that no methane conversion was observed, evidencing that SiO_2 is not a good support in this reaction.

Rh doping had a very strong influence on the stability of NM since NRM still fully converted methane after 200 h of reaction. In contrast, NRL deactivated before NL, which might be attributed to the very low surface area of the catalyst. As described in the literature review (Chapter 1), Rh addition have been shown to exhibit enhanced stability for methane tri-reforming [8] and dry-reforming reactions [9], similarly to Ni-Pd [10]–[12] Ni-Pt [13] and Ni-Co formulations [14], [15].

With the exception of LN, the deactivation profiles of all the tested catalysts were rather similar to that of the commercial catalyst: the methane conversion decreased slowly for a certain time, then rapidly fell to zero. The order of deactivation time $\text{NS-HT-NZA} < \text{NZ} < \text{NCA} < \text{NM} < \text{NRL} < \text{NC} < \text{NL} < \text{NA} < \text{NRM}$ was observed.

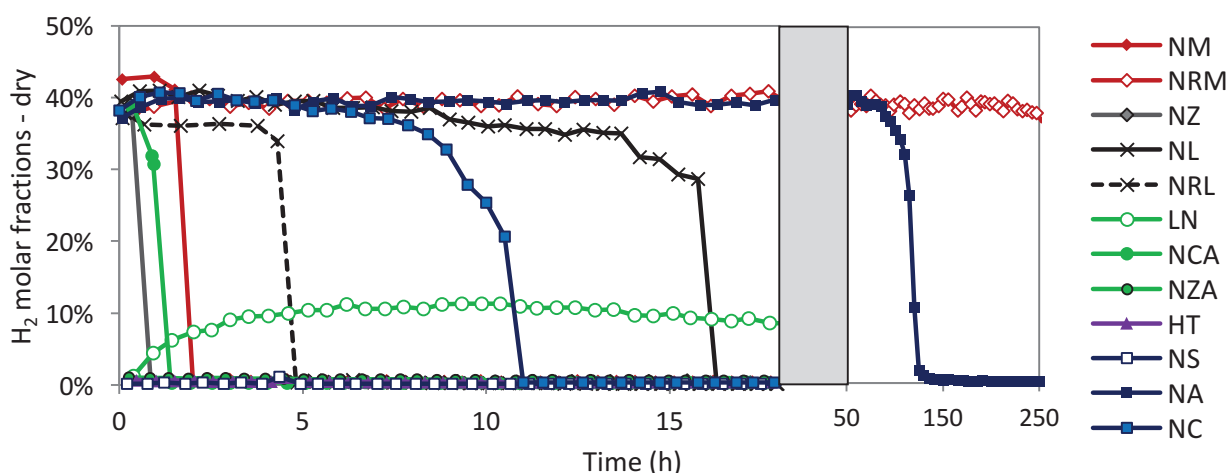


Figure 3.9: Dry outlet H₂ concentrations during ATR of model biogas at T= 700°C. Reaction conditions: Steam/CH₄ = 3, O₂/CH₄ = 0.5, CH₄:CO₂ = 60:40

The hydrogen production profiles matched well the conversion profiles of methane (Figure 3.9). As soon as the methane conversion drops, the hydrogen production also becomes null. The order of deactivation was respected.

At full methane conversion, the molar fractions of H₂ and CO (on a dry basis) revolved around 40% and 10% respectively for all active catalysts except LN. In agreement with the low methane conversion, the reaction over LN produced much less hydrogen and carbon monoxide than the other catalysts.

After 10 hours, the production of H₂ and CO reached a maximum corresponding to molar fractions of 11.3 and 3% respectively. CO₂ production was observed over all active catalysts, resulting in a molar fraction of about 18% at full methane conversion. These results are consistent with those previously described during the system validation over Ni commercial catalyst.

During the validation of the set-up, we had observed that the commercial catalysts deactivated after 40 ± 5 hours. In order to assess the accuracy of the deactivation times, some prepared catalysts were tested again. It should be noted that they were tested in different reactors than previously in order to make sure that no systematic deactivation profile was observed in one specific reactor. After *in-situ* reduction, the reaction was carried out at 700°C, with Steam/CH₄ = 3, O₂/CH₄ = 0.5 and CH₄:CO₂ = 60:40 over 20 mg of NC, NZ, NM, NL and NRL catalysts.

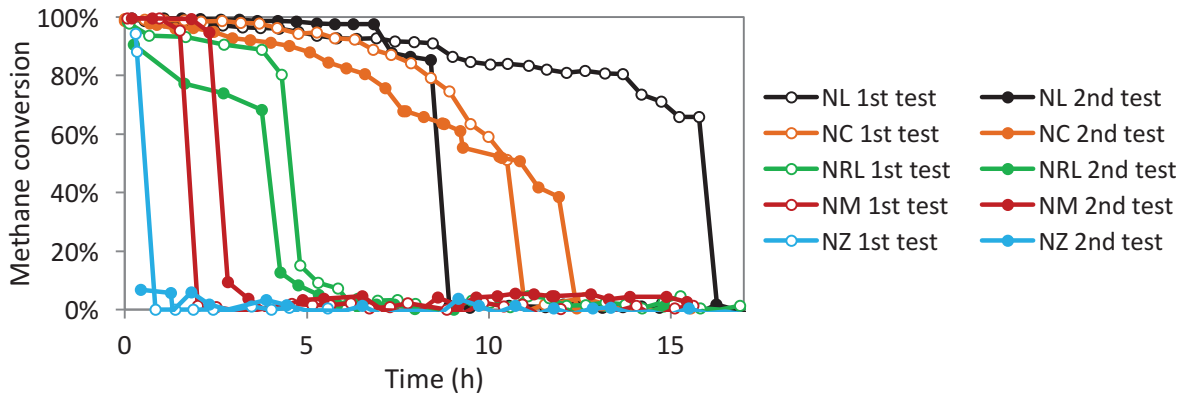


Figure 3.10: Methane conversion during ATR of model biogas at $T = 700^{\circ}\text{C}$. Reaction conditions: $\text{Steam}/\text{CH}_4 = 3$, $\text{O}_2/\text{CH}_4 = 0.5$ and $\text{CH}_4:\text{CO}_2 = 60:40$

The results from the two tests were very similar. The deactivation happened at the same time ± 1 h for NZ, NM, NRL and NC (Figure 3.10). NL in the 2nd test deactivated 6 hours before the 1st test which is consistent with the precision of the set-up.

3.4. Influence of Ni loading on LaAlO_3 and $\text{Mg}_{0.7}\text{Al}_2\text{O}_{3.7}$

NL and NM were the two PGM(Platinum Group Metal)-free catalysts with 5 wt.% Ni loading that did not deactivate within the first hour. Four additional catalysts were prepared in order to study the influence of Ni loading on LaAlO_3 and $\text{Mg}_{0.7}\text{Al}_2\text{O}_{3.7}$: 10 wt.% Ni/ LaAlO_3 , 15 wt.% Ni/ LaAlO_3 , 10 wt.% Ni/ $\text{Mg}_{0.7}\text{Al}_2\text{O}_{3.7}$ and 15 wt.% Ni/ $\text{Mg}_{0.7}\text{Al}_2\text{O}_{3.7}$. The Ni loading was measured by ICP analyses (Table 3.2). They were all very close to their nominal values except for 10 wt.% Ni/ $\text{Mg}_{0.7}\text{Al}_2\text{O}_{3.7}$.

Table 3.2: Ni loading of prepared catalyst supported on MgAl_2O_4 and LaAlO_3

prepared catalysts	Code name	Ni loading (%)
10 wt.% Ni/ $\text{Mg}_{0.7}\text{Al}_2\text{O}_{3.7}$	10NM	8.8
15 wt.% Ni/ $\text{Mg}_{0.7}\text{Al}_2\text{O}_{3.7}$	15NM	14.6
10 wt.% Ni/ LaAlO_3	10NL	9.7
15 wt.% Ni/ LaAlO_3	15NL	14

As mentioned before, no Ni or NiO diffraction lines were evidenced on 5NM after calcinations at 550°C for 4h in air. X-ray diffractograms of prepared 10NM and 15NM are shown in Figure 3.11. 10NM presented only the lines corresponding to spinel structures (MgAl_2O_4 or NiAl_2O_4). Still no NiO lines were observed. 15NM, on the other hand, displayed two different structures: the spinel structure and nickel oxide.

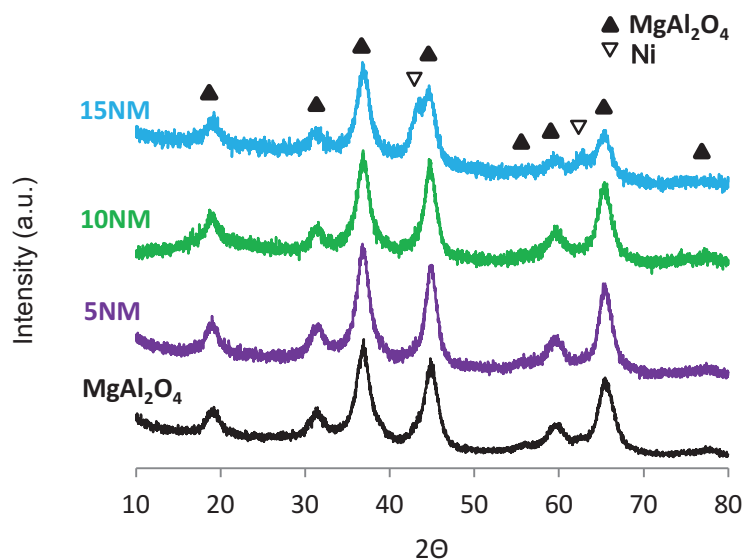


Figure 3.11: X-ray diffractograms of fresh nickel based catalysts supported on MgAl_2O_4 (5NM, 10NM, 15NM) after calcination at 550°C for 4h in air

The reaction was carried out under the same conditions as before. Reactors were filled with 20 mg of catalyst. Quartz powder (100-200 microns) was added when needed in order to obtain a similar bed length. After *in-situ* reaction with a H_2 -Ar mixture at 700°C for 3 hours, the reaction was started with $\text{Steam}/\text{CH}_4 = 3$, $\text{O}_2/\text{CH}_4 = 0.5$ and $\text{CH}_4:\text{CO}_2 = 60:40$. Figure 3.12 displays methane conversion over time. 5NM and 5NL were added on the figures for comparison purposes.

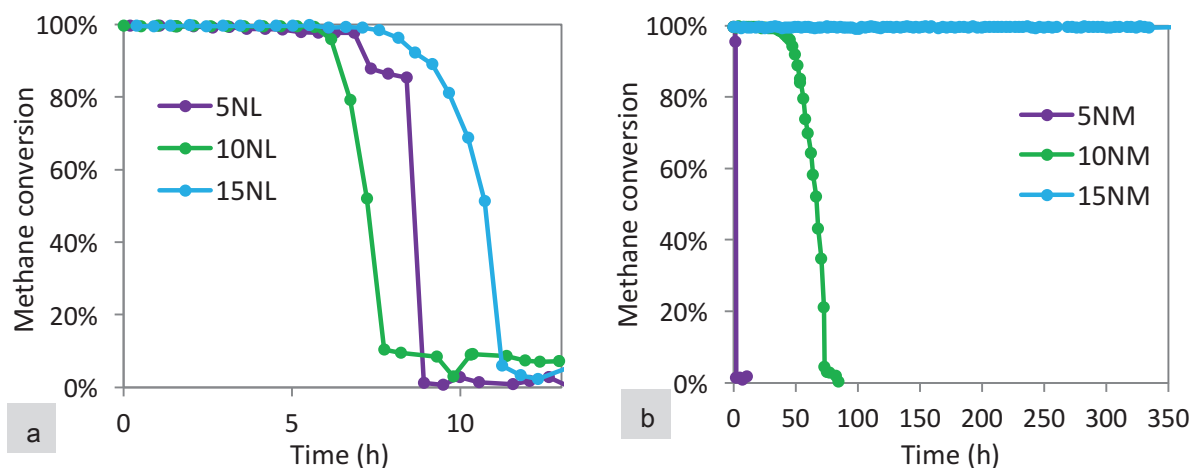


Figure 3.12: Methane conversion during ATR of model biogas at $T = 700^\circ\text{C}$ over Ni supported on a) LaAlO_3 and b) MgAl_2O_4 . Reaction conditions: $\text{Steam}/\text{CH}_4 = 3$, $\text{O}_2/\text{CH}_4 = 0.5$ and $\text{CH}_4:\text{CO}_2 = 60:40$

Whatever the nickel loading, the catalysts supported on LaAlO_3 perovskite all deactivated after $10 \pm 1\text{h}$ (Figure 3.12-a). Increasing the nickel loading on LaAlO_3 did not increase the deactivation time. This might be caused by the low specific surface area of the perovskite which does not ensure a correct dispersion of Ni.

Contrary to LaAlO_3 , the nickel loading had a great influence on catalysts supported on magnesium spinel $\text{Mg}_{0.7}\text{Al}_2\text{O}_{3.7}$ (Figure 3.12). 5NM deactivated after 2 h (as described in the previous part) while 10NM deactivated after 77 h. 15NM still presented full methane conversions after 350 h.

X-ray diffractogram of 5NL after deactivation was performed (Figure 3.13-a). 5NM had been diluted with quartz powder when the reactor was prepared in order to be tested in the same GHSV conditions as the other 5 catalysts. Therefore, characteristic SiO_2 lines are evidenced. Apart from the quartz patterns, no major modification can be observed before and after reaction over 5NL. No Ni or NiO lines are evidenced. However, TEM images (Figure 3.13-b) did show the presence of NiO particles after reaction. Encapsulating carbon was also present. Deactivation on NL catalyst is thus likely to be related to Ni oxidation and carbon formation.

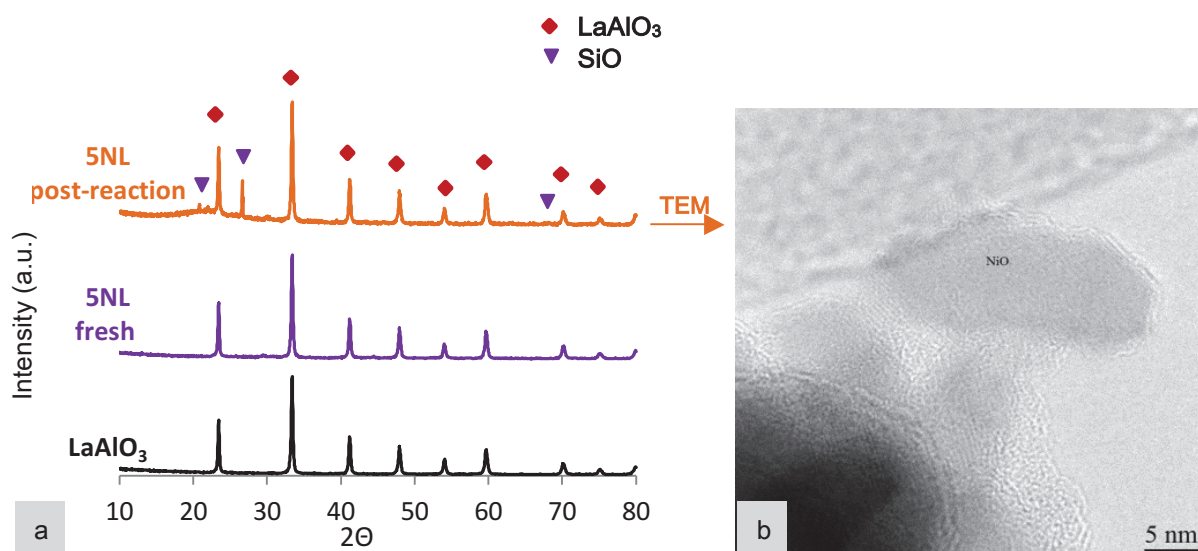


Figure 3.13: a) X-ray diffractograms of LaAlO_3 support, fresh 5NL after calcinations at 550°C in air and post-reaction 5NL b) TEM image of post-reaction 5NL

X-ray diffractograms of 5NM, 10NM and 15NM after reaction were performed as well (Figure 3.14). After deactivation 5NM patterns do not present any major modification. Characteristic lines of a spinel structure are still observed.

10 NM was diluted with a small amount of quartz powder in order to be tested under the same GHSV conditions. The diffractogram is plotted from $2\theta = 28$ because at low angles, SiO_2 characteristic lines similar to those observed on 5NL after reaction are too intense and disturb the analysis.

15NM was still active when the reaction was stopped. Its diffractogram also shows the presence of the spinel structure. More importantly, while no Ni^0 lines were observed on post-reaction 5NM and 10NM, they were clearly evidenced on 15NM diffractogram. This is consistent with the fact that metallic Ni

was still present and active for the reforming reaction when the reaction was stopped. Further deactivation study on NM catalyst will be carried out in Chapter 4.

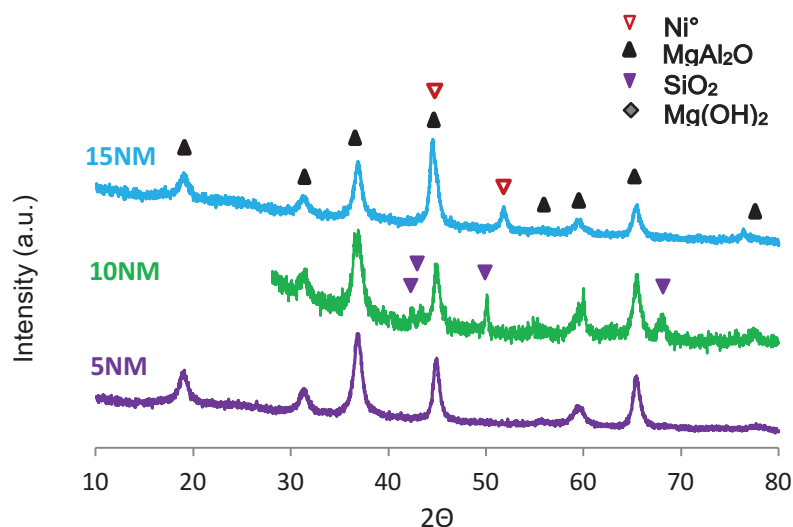


Figure 3.14: X-ray diffractograms of post-reaction 5NM, 10NM and 15NM

While NL showed interesting performances during the screening, NM showed more promising results when a noble metal was added and when nickel loading was increased. Addition of only 0.05 wt.% of Rh considerably increased its performances and resistance to deactivation. Similar improvement was observed when $Mg_{0.7}Al_2O_{3.7}$ was impregnated with 15 wt.% Ni. NRM was identified as a robust catalyst and in-depth study of the deactivation phenomena on NM need to be performed.

3.5. Conclusions

The long-term stability of nickel- based catalysts was assessed for the ATR of biogas. A six-parallel flow reactor was implemented in order to test six catalysts simultaneously under identical reaction conditions. It was first and foremost successfully validated on a nickel steam reforming commercial catalyst. Slight deviation in deactivation time was observed but the system appeared to be powerful enough to discriminate fast-deactivating from stable catalysts.

Perovskites, spinels and mixed oxides supports were prepared and characterized. They all presented different properties and structures. Notably, perovskites presented high cristallinity and low specific surface area. Spinels, selected for their basicity and structures, presented low cristallinity and high specific surface areas. After nickel impregnation and in two cases rhodium impregnation, nine 5 wt.% Ni-based catalysts were prepared. 3 additional catalysts with higher nickel loading (14 and 20 wt.%)

were selected, adding up to 12 catalysts to be tested with the six-parallel flow reactor at 700°C with Steam/CH₄ = 3, O₂/CH₄ = 0.5 and CH₄:CO₂ = 60:40. The order of deactivation time NS-HT-NZA < NZ < NCA < NM < NRL < NC < NL < NA < NRM was observed. The experiment was repeated over 5 catalysts and they showed very similar performances, proving once again the reliability of the set-up.

Comparing the behaviour of the ≈5 wt% Ni catalysts loaded on different supports, our screening shows that the support properties that were shown to be beneficial in methane steam reforming do not appear as relevant when autothermal reforming of methane is involved. 5 wt.% Ni/LaAlO₃ was the last 5 wt.% Ni-only catalyst to deactivate. 5-0.05 wt. Ni-Rh/Mg_{0.7}Al₂O_{3.7} still converted methane fully after 200h and was thus identified as a robust catalyst for the ATR of model biogas.

LaAlO₃ and Mg_{0.7}Al₂O_{3.7} supports were further studied by increasing the nickel loading. While nickel loading showed to have no influence on deactivation time on LaAlO₃ perovskite support, increasing from 5 wt.% to 15 wt.% on Mg_{0.7}Al₂O_{3.7} spinel support had a great influence. 15 wt.% Ni/Mg_{0.7}Al₂O_{3.7} still presented full methane conversions after 350 h.

After O₂ removal and H₂ addition to the feed, it appeared that nickel oxidation seemed to play an important role regarding deactivation. Next chapter will further investigate deactivation on Ni/Mg_{0.7}Al₂O_{3.7} catalysts. Moreover, reduction temperature during the pre-treatment was increased to 800°C for the rest of the study to ensure that nickel interacting strongly with the support is also reduced before reaction.

REFERENCES:

1. Farrusseng, D., *Surface Science Reports*, 63, 487–513, 2008.
2. Singoredjo, L., Korver, R., Kapteijn, F. & Moulijn, J., *Applied Catalysis B: Environmental*, 1, 297–316, 1992.
3. Neeft, J. P. A., Makkee, M. & Moulijn, J. A., *Applied Catalysis B: Environmental*, 8, 57–78, 1996.
4. Alves, H. J. et al., *International Journal of Hydrogen Energy*, 38, 5215–5225, 2013.
5. Takehira, K., Shishido, T., Wang, P., Kosaka, T. & Takaki, K., *Journal of Catalysis*, 221, 43–54, 2004.
6. Slagtern, A. & Olsbye, U. *Applied Catalysis A: General*, 110, 99–108, 1994.
7. Pena, M. A. & Fierro, J. L. G., *Chemical Reviews*, 101, 1981–2017, 2001.
8. Izquierdo, U. et al., *International Journal of Hydrogen Energy*, 38, 7623–7631, 2013.
9. Nowosielska, M., Jozwiak, W. K. & Rynkowski, J., *Catalysis Letters*, 128, 83–93, 2009.
10. Zhang, J., Wang, Y., Ma, R. & Wu, D., *Applied Catalysis A: General*, 243, 251–259, 2003.
11. Yoshida, K. et al., *Applied Catalysis A: General*, 351, 217–225, 2008.
12. Ismagilov, I. Z. et al., *International Journal of Hydrogen Energy*, 39, 20992–21006, 2014.
13. Li, L. et al., *ChemCatChem*, 7, 819–829, 2015.
14. Takanabe, K., Nagaoka, K., Nariai, K. & Aika, K., *Journal of Catalysis*, 232, 268–275, 2005.
15. You, X. et al., *ChemCatChem*, 6, 3377–3386, 2014.

Chapter 4

Investigation of the deactivation process of Ni catalysts supported on $\text{Mg}_x\text{Al}_2\text{O}_{3+x}$

The most stable catalyst for autothermal reforming of model biogas was found to be 5-0.05 wt.% Ni-Rh/MgAl₂O₄ after screening of different formulations. It showed full methane conversion over more than 200 hours. The PGM(Platinum Group Metal)-free nickel based catalyst 5 wt.% Ni/ MgAl₂O₄ deactivated within 2 hours. In the literature, deactivation of nickel catalysts during reforming of hydrocarbons has been attributed to different reasons. The most common causes are poisoning, carbon formation, sintering of nickel particles, nickel oxidation and spinel formation. Although successful and efficient for the screening of catalysts, the parallel-flow system was not suitable for further deactivation study and was replaced with a single reactor.

This chapter will mainly focus on the identification of the deactivation process. The influence of the composition of the Mg/Al spinel support during the ATR of model biogas will be studied in a second part. Finally, the promotion by rhodium of nickel-based catalyst supported on Mg/Al spinel will be addressed.

4.1. Deactivation investigation

4.1.1. Preliminary observations

Before going into deeper investigation, a first look at the colours of a catalyst at different reaction steps gave critical information that could guide our study. The nickel catalysts were black after reduction and light blue/green after complete deactivation. An important observation regarding colours is that when the reaction was stopped before complete deactivation, the catalyst bed showed two different colours: light blue/green at the reactor inlet and black at the outlet (Figure 4.1).

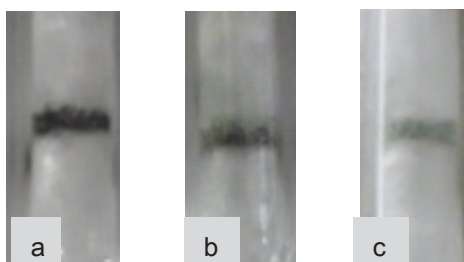


Figure 4.1: Photographs of a) reduced commercial catalyst, b) still-active commercial catalyst and c) deactivated commercial catalyst during ATR of model biogas in standard conditions.

Black metallic nickel species seemed to be replaced by light blue/green species during the ATR reaction. In the Handbook of Chemistry and Physics, metallic Ni is described as black, NiO as green and NiAl₂O₄ as blue.

Given these first-hand observations, it seemed clear that during the reaction, nickel species underwent some changes that could possibly be associated to the formation of NiO, NiAl₂O₄ or a mixture of the two. This will be further discussed in a sub-part of this chapter.

4.1.2. Carbon formation

As described in our literature review, one of the most common deactivation causes of nickel-based catalysts during methane reforming processes is the deposition of carbon or coke. Encapsulating carbon leads to the loss of active metal surface by forming a graphite layer over the nickel particles. Whisker-like carbon formation does not lead to immediate deactivation of the Ni-surface but leads to a blockage of the porosity and catalyst breakdown.

In our study, the small amount of catalyst (20 mg) used for the reaction made it difficult to evidence or quantify carbon by Temperature Programmed Reduction (TPR) or Thermogravimetric Analysis (TGA). The formation of carbon whiskers and graphite on deactivated 5 wt.% Ni/Mg_{0.7}Al₂O_{3.7} was thus first investigated by TEM (Figure 4.2).

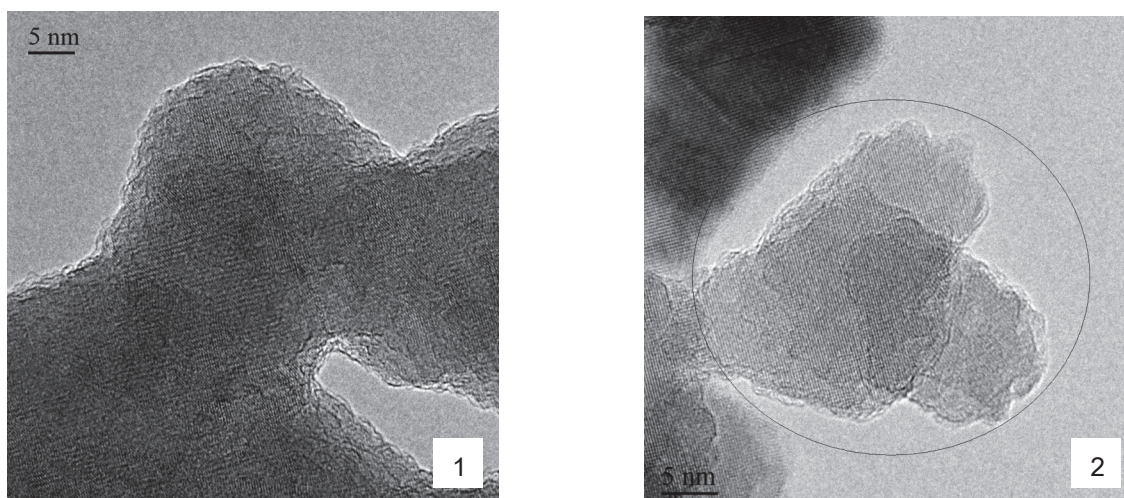


Figure 4.2: TEM images of regions 1) and 2) of deactivated 5 wt.% Ni/Mg_{0.7}Al₂O_{3.7} after ATR of model biogas. Reaction conditions: T = 700°C, Steam/CH₄ = 3, O₂/CH₄ = 0.5, CO₂:CH₄ = 40:60

The images showed no evidence of carbon whiskers and no clear presence of amorphous carbon. The formation of whiskers would have increased the pressure drop during reaction. However, during our tests, the reactor pressure did not increase. Based on the microscopy images and the monitoring of pressure during reaction, carbon whiskers formation was excluded.

Further study of carbon formation was made using XPS technique. The relative atomic concentrations on catalysts surface before reaction (after *in-situ* reduction at 700°C) and after reaction are presented in Table 4.1.

While the reduced catalyst surface was almost carbon-free, the deactivated sample showed 4 at.% (corresponding to 2 wt.%) of carbon.

Table 4.1: Surface compositions of the catalyst before reaction and after 25 h of reaction (complete deactivation occurred after *ca.* 2 h)

	O (at.%)	Mg (at.%)	Al (at.%)	Ni (at.%)	C (at.%)
Fresh reduced catalyst	57.4	8	31.5	2	0.9
Deactivated catalyst	59.3	6.8	28.3	1.5	4

The carbon content deposited on our catalyst surface can be considered to be low and unlikely to cause the complete deactivation of our catalyst. This is consistent with our thermodynamics study (Chapter 1) and the fact that carbon formation is not favoured at such high Steam/CH₄ ratio and high temperature (T > 660°C).

4.1.3. Sintering

Nickel-based catalysts can also suffer from sintering during reforming reactions at high temperature.

TEM images of the fresh catalyst after reduction with a H₂/Ar mixture at 700°C showed that nickel particles were found on the catalyst surface.

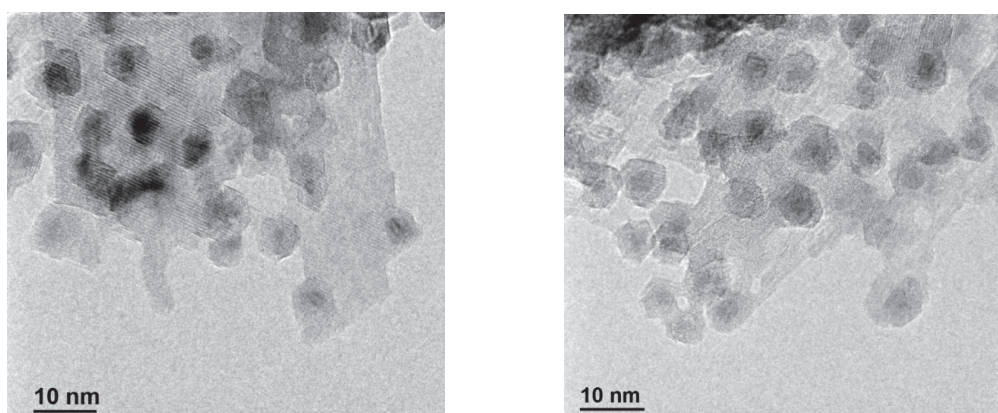


Figure 4.3: TEM images of fresh 5 wt.% Ni/Mg_{0.7}Al₂O_{3.7} before reaction and after reduction at 700°C with a H₂/Ar mixture

However, as observed on Figure 4.2., deactivated 5 wt.% Ni/Mg_{0.7}Al₂O_{3.7} showed no evidence of metallic nickel particles (Figure 4.2). However, EDX analyses on three different regions of the sample revealed the presence of *ca.* 1.4 at.% (3.8 wt.%) of nickel (Table 4.2).

Table 4.2: Chemical composition of 5 wt.% Ni/Mg_{0.7}Al₂O_{3.7} after deactivation by EDX analysis

Region	O (at.%)	Mg (at.%)	Al (at.%)	Ni (at.%)
1	58.9 %	8.3 %	31.5 %	1.3 %
2	61.3 %	9.1 %	28.1 %	1.5 %
3	54.2 %	12.1 %	32.3 %	1.4 %

The absence of metallic nickel particles does not allow to conclude about the possible sintering but the nickel is distributed as oxidized species all over the spinel support.

4.1.4. Quantification of oxidized nickel by hydrogen pulses

The remaining hypothesis is that nickel oxidation and/or nickel spinel formation leads to deactivation. Considering this assumption, the set-up was modified to quantify oxidized nickel species *in-situ*.

a. Method development

As mentioned before, only 20 mg of catalyst with 5 wt.% nickel loading were used in our reaction, corresponding to a total of 17 μmol of Ni. *In-situ* TPR was attempted but precise quantification was unsuccessful on such small catalyst amount. Instead, a 250 μL loop was connected to an automated valve added up-stream to the reactor in order to generate a series of small hydrogen pulses (Figure 4.4). The loop was filled with a 40% H₂/Ar mixture at 160°C (hotbox temperature). Each pulse contained 2.81 μmol H₂.

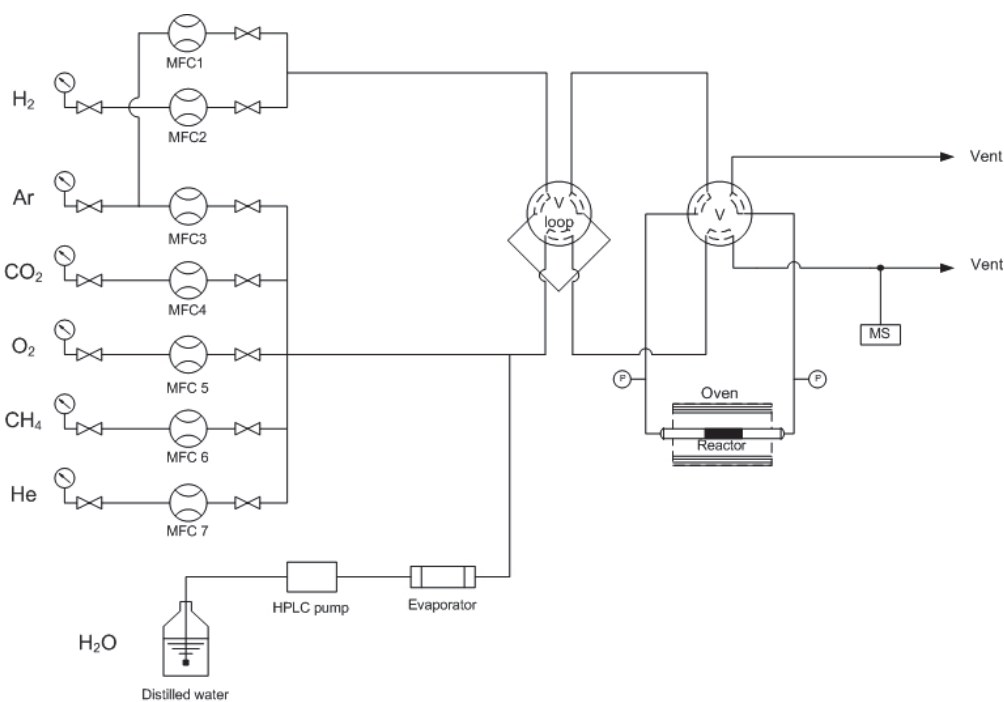


Figure 4.4: Set-up scheme after addition of the loop upstream to the reactor

A commercial catalyst (HiFUEL, R110, Alfa Aesar, ref. 45465) was first used to assess the method accuracy. The pulse was generated by switching a valve, sweeping the loop with argon and thus sending the H₂/Ar mixture to the reactor. After one minute, the loop was refilled with H₂/Ar and swept again automatically after 30 seconds. This process was repeated every 1.5 minutes. By doing so, the catalyst underwent a series of hydrogen pulses. The effluent gases were analyzed by on-line Mass Spectrometer.

The hydrogen consumption was calculated for each pulse. If we consider Reaction 4.1, the reduction of Ni²⁺ requires an equimolar amount of H₂. Water is also formed during the reduction of nickel oxide.



32.5 mg of commercial catalyst (10 wt.% Ni) were used, corresponding to 55.4 μmol of Ni. Prior to the series of pulses, the catalyst was oxidized under O₂ diluted in argon during 4 hours while the oven temperature was increased to 725°C. After purge, a sequence of 40 pulses was started and monitored on the MS. Figure 4.5 presents the output intensities of fragments m/z = 2 (H₂) and 18 (H₂O). For clarity purposes, the intensities of fragment m/z = 18 were multiplied by 10 in the figure.

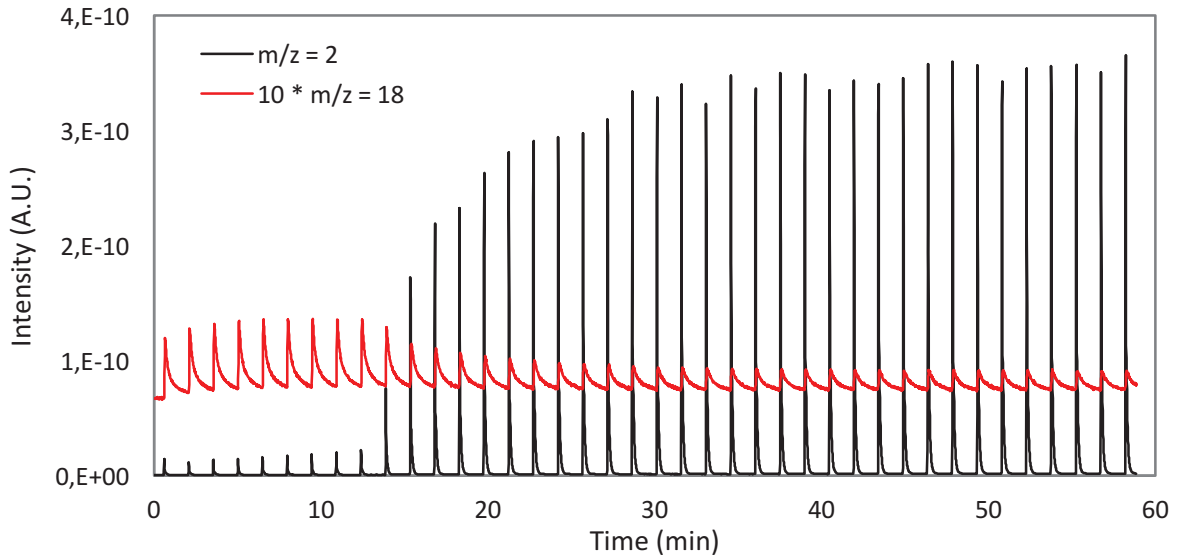


Figure 4.5: Mass spectrometer output from the hydrogen pulses sequence on oxidized commercial catalyst at 700°C: H₂ (m/z = 2) in black, H₂O (m/z = 18) in red

From the MS output file, it could be observed that the first nine hydrogen pulses were fully consumed. Water was produced simultaneously (m/z = 18). After the ninth pulse, the pulses were not fully consumed anymore. It should be noted that the fragment m/z = 15 was also monitored but its intensity was low at all times and no changes were observed during the sequence. This proved that no methane was formed and thus no carbon gasification occurred.

The consumption reached a maximum after the 27th pulse. In order to determine the exact consumption of hydrogen, the ratios of intensities of m/z = 2 (H₂) and m/z = 40 (Ar) were calculated and then integrated for each pulse.

After the 27th pulse ($t_{27} = 39$ min), the integrations remained constant and corresponded to pulses without hydrogen consumption. The area calculated was attributed to zero consumption and thus H₂ consumption for the pulse #1 to #26 was calculated as below:

$$n_i(\text{H}_2) = \frac{\int_{t_i}^{t_i+0.5} I(m/z = 2) / I(m/z = 40)}{\int_{t_{27}}^{t_{27}+0.5} I(m/z = 2) / I(m/z = 40)} \times 2.81$$

with 2.81 being the quantity of hydrogen (μmol) contained in one pulse and t_i equal to the time in minute when the valve is switched for the pulse # $i = 1, 2, \dots, 26$

The hydrogen uptakes $n_i(\text{H}_2)$ are plotted for each pulse in Figure 4.6.

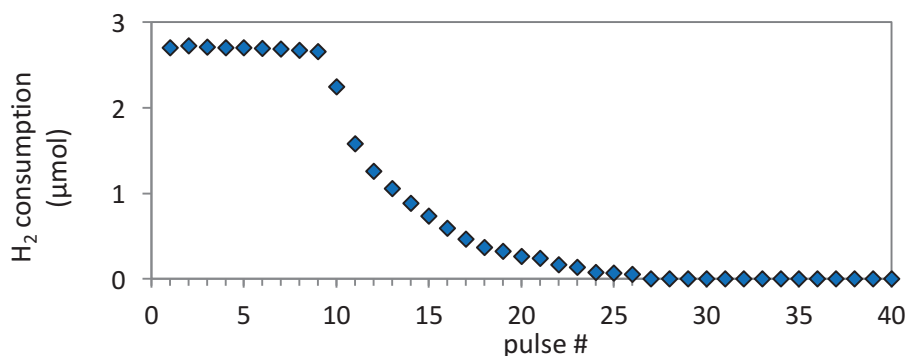


Figure 4.6: Hydrogen uptake per pulse (μmol) calculated from the integrations of hydrogen MS signal intensities at 700°C .

After integration and calculations, the total amount of hydrogen consumed and thus the amount of oxidized nickel was $34.8 \mu\text{mol}$. It is lower than the nominal value of $55.4 \mu\text{mol}$. This could mean that the pulses were unable to reduce all the nickel species.

The temperature might not have been high enough to reduce the nickel species. This was also supported by the results of the TPR performed on the commercial catalyst (Figure 4.7). The TPR profile showed a large peak at around 750°C that could be attributed to nickel strongly interacting with the support.

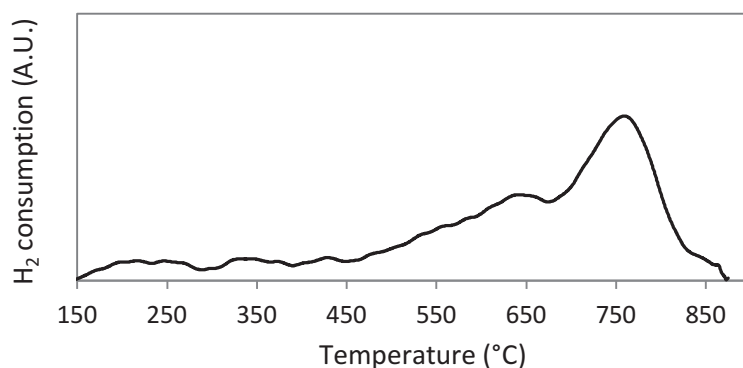


Figure 4.7: H₂-TPR profile of commercial catalyst

Therefore, it was decided to set the temperature at 800°C for the pulses sequence. This time, 4 cycles of pulses were carried out to evaluate the precision of method. The first sequence was carried out after oxidation over night at 800°C . After the first sequence, the catalyst was re-oxidized during 15 minutes at 800°C with a 10% O₂/Ar mixture then purged with Ar only for 10 minutes. This re-oxidation step was performed between each cycle thereafter.

The same calculation method was applied to the four sequences enabling to determine the hydrogen uptake per pulse (Figure 4.8)

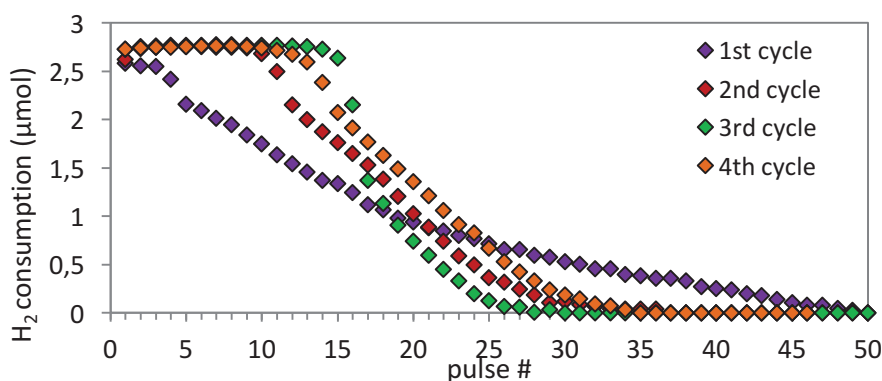


Figure 4.8: Hydrogen uptake per pulse in μmol calculated from the integrations of hydrogen MS signal intensities of the pulses at 800°C .

Contrary to what was observed on the sequence at 700°C the hydrogen consumption never reached a maximum during the first cycle, preventing us from calculating the hydrogen uptake for each pulse. The over-night oxidation at 800°C might modify the structure of the catalyst and the nature of the nickel species, making their reduction more difficult. However, total consumption was assumed at pulse #50 in order to carry out the calculations for comparison purposes.

On the other hand, cycles 2, 3 and 4 have very similar behaviours to the sequence at 700°C . The hydrogen uptake reaches a maximum after the 37th, the 30th and the 35th pulse respectively. Total hydrogen consumptions for each cycle were calculated and are reported in Table 4.3. Overall, the total hydrogen consumption for the 4 cycles were much higher than that of the sequence at 700°C , proving that increasing the temperature to 800°C improved our method.

In agreement with our hypothesis that the nickel species were harder to reduce, the total consumption for the first cycle is lower than the other cycles. 50 pulses were probably not enough to reach the full reduction. Cycles 2, 3 and 4 showed 48.8, 49.5 and 54.9 μmol of NiO respectively. These values are close to the nominal value of 55.4 μmol . If we consider these 3 cycles we can determine that the precision of the method is of 11%.

Table 4.3: Total hydrogen consumption in μmol nominal and calculated after integration of hydrogen MS signal intensities

	Total hydrogen consumption (μmol)
<i>Nominal value</i>	55.4
Pulses at 700°C	34.8
Pulses at 800°C – 1 st cycle	46.6
Pulses at 800°C – 2 nd cycle	48.8
Pulses at 800°C – 3 rd cycle	49.5
Pulses at 800°C – 4 th cycle	54.9

b. Application of the method post-reaction

Three reactions were performed over 32 mg of commercial catalyst. The catalysts were first reduced in-situ with a H₂/Ar mixture (4:1, vol:vol) at 800°C. The ATR reaction was then performed at 700°C with Steam/CH₄ = 3, O₂/CH₄ = 0.7, CO₂:CH₄ = 40:60 and at a GHSV = 250,000 h⁻¹. The O₂/CH₄ ratio was increased to 0.7 in an attempt to accelerate the oxidation rate of the catalyst. The reactions were stopped after different times on stream:

- The first reaction (A) was stopped when the methane conversion was 99% (after t = 60 h).
- The second reaction (B) was stopped when the conversion was 96% (t = 120 h).
- The third reaction (C) was stopped when the conversion reached 91% (t = 200 h).

In all cases, the catalyst bed was swept by inert argon when the reaction was stopped and the temperature was increased from 700°C to 800°C. A series of pulses was then carried out on the catalysts (Figure 4.9).

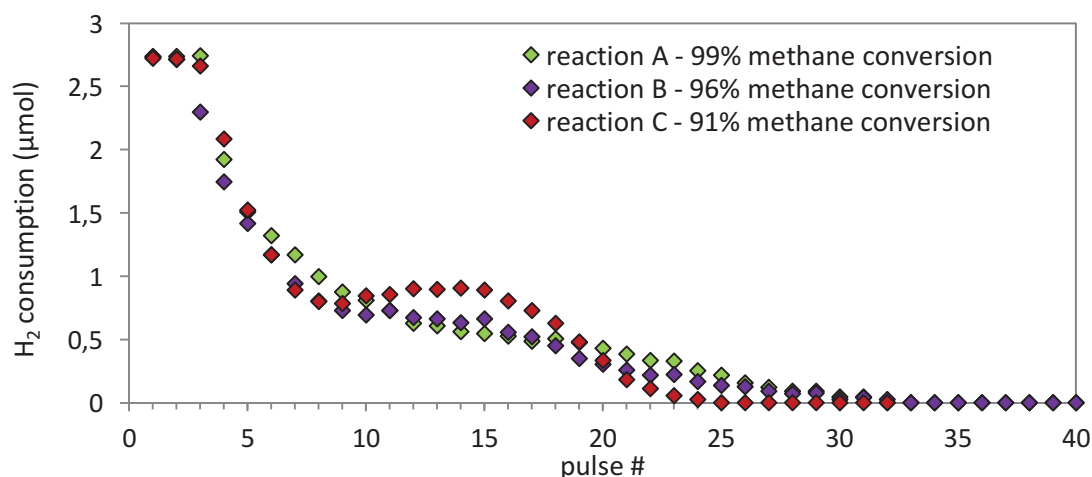


Figure 4.9: Hydrogen uptake per pulse in µmol after reaction A (60 h – 99% methane conversion), reaction B (120 h - 96% methane conversion) and reaction C (200 h -91% methane conversion): calculated from integrations of hydrogen MS signal intensities of the pulses at 800°C.

It can be observed that the consumption profiles were different than those observed with the oxidized fresh catalyst. Instead of having a number of pulses fully consumed and then quickly having no consumption, a different behaviour was observed: the first 2 or 3 pulses were fully consumed, soon after there was a plateau with 0.55-0.9 µmol consumption between pulses #9 and #16 and finally no more hydrogen consumption after 25 or more pulses.

This type of profile could describe the reduction of two types of nickels species. The fully consumed first pulses might be attributed to a species that are easily reduced under our series of pulses, probably NiO or nickel in weak interaction with the support. The other nickel species would be harder to reduce. This could be the case of NiAl₂O₄ or nickel interacting strongly with the support.

Regarding the total uptake, 24.3, 22.2 and 23.9 μmol of hydrogen were consumed after reactions A, B and C respectively. This would imply that 44%, 40% and 43% of the nickel species were present as oxidized nickel after the reactions. We would have expected to see an increase in the number of oxidized sites with time. However, we do not observe a significant difference. Given these results and considering the precision of the method determined earlier (11%), our attempt to quantify nickel oxidation over time was not successful with this approach.

A simple modelling of 8 hydrogen pulses on a catalytic bed still active presenting oxidized nickel at the inlet and reduced nickel at the outlet was implemented in order to understand the failure of the approach.

Figure 4.10-a) displays a scheme that represents a catalytic bed divided in 30 sections. We defined that the nickel in the first section is oxidized and that it is metallic in the remaining 29 sections. Then a series of pulses coming from the upstream part of the bed is modelled.

Figure 4.10-b) shows the progression of the oxygen coverage in sections 5 (green), 10 (red), 15 (light blue), 20 (pink), 25 (yellow) and 30 (black) during pulses. The progression of oxygen-coverage implies that the water formed from the reduction of oxidized nickel in section 1 (reaction 4.1) could oxidize the metallic nickel present downstream in sections 2 to 30.

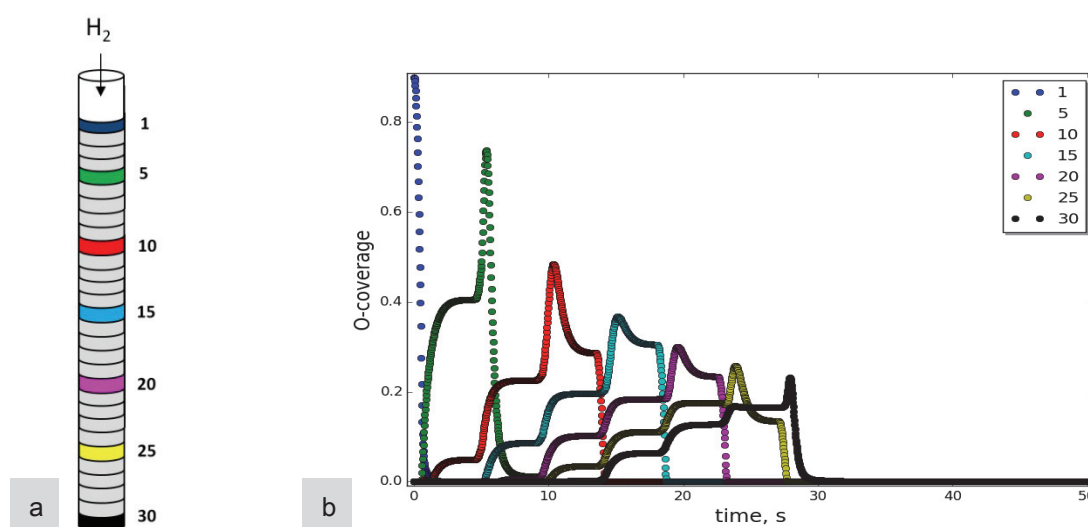


Figure 4.10 : a) Scheme of a model reactor divided in 30 sections b) Model showing the progression of oxygen coverage in sections 1, 5, 10, 15, 20, 25, 20 during a series of 8 hydrogen pulses.

At $t = 0$ sec, the oxygen coverage is maximum in the first section while the other sections show no oxygen coverage, as defined as initial conditions. After the first pulse, the oxygen coverage in section 1 drops while it increases in section 5. After 5 seconds, the oxygen coverage in section 5 drops but increases in section 10, and so on and so forth. Given these results, it seems that more pulses are necessary to fully reduce the catalyst.

Therefore, the presence of metallic nickel associated to the formation of H_2O by reduction of Ni^{2+} in a still-active catalyst seems to limit the performances of our quantification method.

In order to prevent this problem, another approach was implemented. Two more valves were added to our set-up, one upstream and one downstream to the reactor. This enabled to reverse the flow in the reactor during the series of pulse (Figure 4.11). In this configuration, the metallic nickel is not exposed to the water formed during reduction of the oxidized nickel.

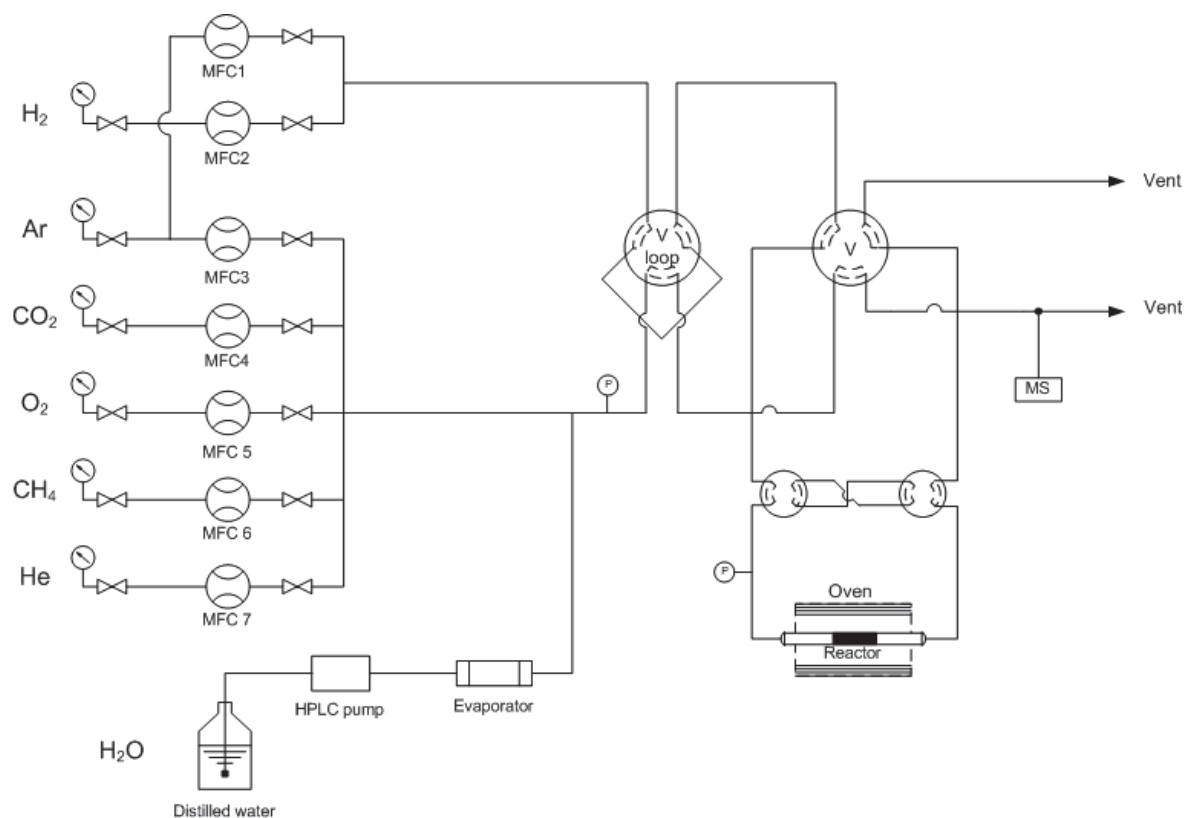


Figure 4.11: Set-up scheme after addition of two valves before and after the reactor in order to perform pulses in reverse flow

Figure 4.12 displays a simplified scheme of the progression of oxidized nickel throughout the bed during a series of pulses carried out in normal and reverse way.

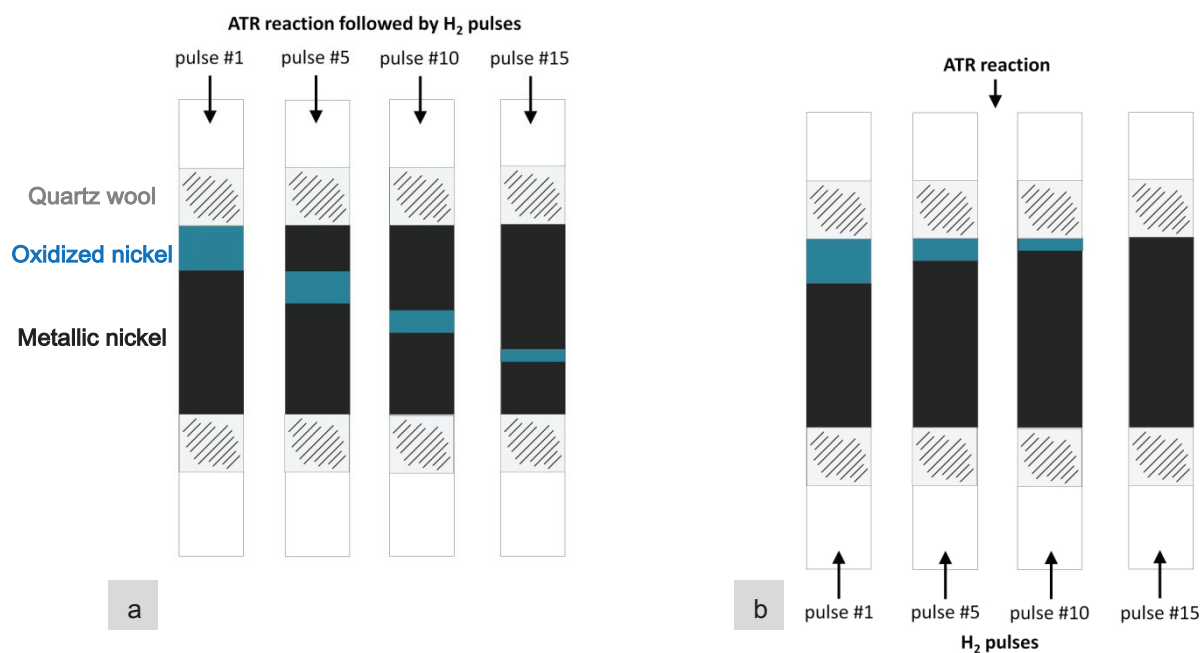


Figure 4.12: Schemes of the progression of oxidized nickel in the catalyst bed under a series of a) normal pulses b) reverse pulses

Two additional ATR reactions were performed over 32 mg of commercial catalyst at 700°C with Steam/CH₄ = 3, O₂/CH₄ = 0.7, CO₂:CH₄ = 40:60 and at a GHSV = 250,000 h⁻¹.

The first reaction (D) was stopped when the methane conversion was 90% (after t = 60 h). The second reaction (B) was stopped when the conversion was 80% (t = 190 h). In both cases, the catalytic bed was swept by argon when the reaction was stopped and the temperature was increased from 700°C to 800°C. A series of pulses was then carried out on the catalysts in reverse flow direction (Figure 4.13).

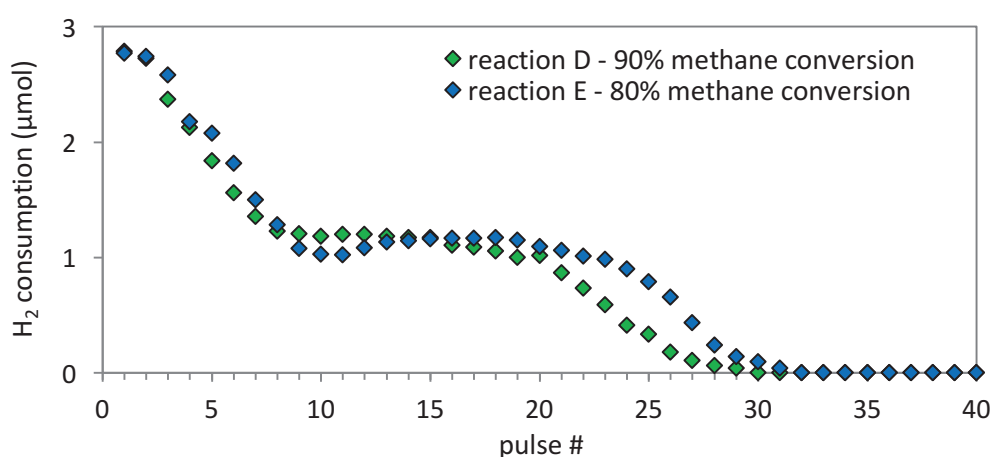


Figure 4.13: Hydrogen uptake per pulse in μmol after reaction D (60 h - 90% methane conversion) and reaction E (190h - 80% methane conversion): calculated from integrations of hydrogen MS signal intensities of the pulses at 800°C.

The consumption profiles are similar to those obtained in normal flow direction. The first two pulses are nearly fully consumed. We also observe a plateau from pulses #8 to #20 for reaction D and from pulses #9 to #23 for reaction E but this time, the consumption is higher than before, ranging from 1-1.2 μmol instead of 0.55-0.9 μmol . After the 30th pulse, no consumption of hydrogen is observed.

Total uptakes of hydrogen were 32.9 μmol for reaction D and 36.7 μmol for reaction E.

Reaction D and the previous reaction C were stopped at similar methane conversions (90% and 91%). Therefore, comparing the total uptakes after these two reactions offers a fair comparison between the normal and reverse flow approaches. After the same number of pulses, 9 more μmol were reduced with the reverse flow approach, proving that the method was improved.

Comparing now reactions D and E, it can be observed that 3.8 more μmol of nickel sites are oxidized when the conversion changes from 90 to 80%, with a precision of $\pm 4 \mu\text{mol}$.

In light of these calculations, we can conclude that even if the method had been improved by reversing the flow, its precision is not sufficient when dealing with such small amount of catalyst. The method would be more suitable if we were dealing with higher amounts of catalyst or higher loading of nickel. Therefore, as we could not validate this method on a 10 wt.% Ni commercial catalyst, it was not applied to our 5 wt.% Ni/Mg_{0.7}Al₂O_{3.7} catalyst.

Some valuable information was nevertheless obtained by this method. There seems to be three different types of nickel species in presence before complete deactivation. The first species would be active metallic nickel. The second species is easily reduced under hydrogen pulses at 800°C. This could be attributed to NiO [1], [2]. Finally, the last species seems to be harder to reduce at 800°C. It could correspond to NiAl₂O₄ or nickel that is interacting strongly with the support [3], [4]. Increasing the temperature at which the series of pulse is made could ease their reduction. We did not consider this solution because increasing the temperature to 900°C or 1,000°C could possibly alter the catalyst structure and change the nature of the nickel species as well.

4.1.5. ATR of model biogas on NiO vs NiAl₂O₄

Assuming that the formation of NiO and NiAl₂O₄ is related to the loss of activity, their performances under ATR reaction were evaluated in order to confirm, indirectly, that their formation would result in deactivation.

Commercial NiO (Sigma Aldrich) and prepared NiAl₂O₄ were tested for the ATR of model biogas at 700°C with Steam/CH₄ = 3, O₂/CH₄ = 0.5, CO₂:CH₄ = 40:60. Prior to testing the two compounds, their chemical composition and structure were analysed by XRD (Figure 4.14).

The patterns showed that NiAl₂O₄ exhibited only the characteristic lines of the spinel phase. No NiO was evidenced. Moreover, ICP analyses confirmed that our spinel was composed of Ni:Al in ratio 0.98:2 (mol:mol).

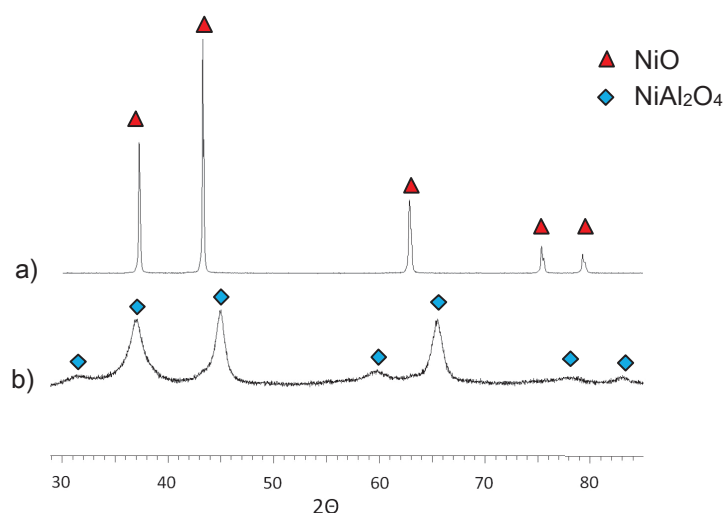


Figure 4.14: X-ray diffractogram of a) commercial NiO and b) prepared NiAl₂O₄

The catalytic tests were performed on 40 mg of powder sieved to obtain a particle size fraction between 100 and 200 microns. No pre-treatment step was included before reaction. NiO was active only for CH₄ combustion but not for reforming. NiAl₂O₄ was even less active (Table 4.4).

Table 4.4: Performances of 40 mg of commercial NiO and prepared NiAl₂O₄ under ATR reaction conditions at 700°C, Steam/CH₄ = 3, O₂/CH₄ = 0.5, CO₂:CH₄ = 40:60.

	NiO	NiAl ₂ O ₄
Oxygen conversion	100%	20%
Methane conversion	25%	3-6%
Hydrogen yield	0%	0%

Deactivated catalyst showed oxygen and methane conversions close to zero. This suggests that catalyst deactivation during ATR should be related essentially to the formation of NiAl₂O₄.

4.1.6. X-ray photoelectron spectroscopy on Ni/Mg_{0.7}Al₂O_{3.7}, NiO and NiAl₂O₄

In order to study the oxidation state of nickel in the surface region and quantify NiO and NiAl₂O₄, XPS analyses of 5 wt.% Ni/Mg_{0.7}Al₂O_{3.7} were performed:

- after *in-situ* reduction at 700°C
- after reduction at 700°C and re-exposure to air
- after ATR reaction (see chapter 3)

For comparison purposes, NiO and NiAl₂O₄ reference samples were also analyzed. Figure 4.15 shows the Ni 2p doublet Binding Energy (BE) in the different samples.

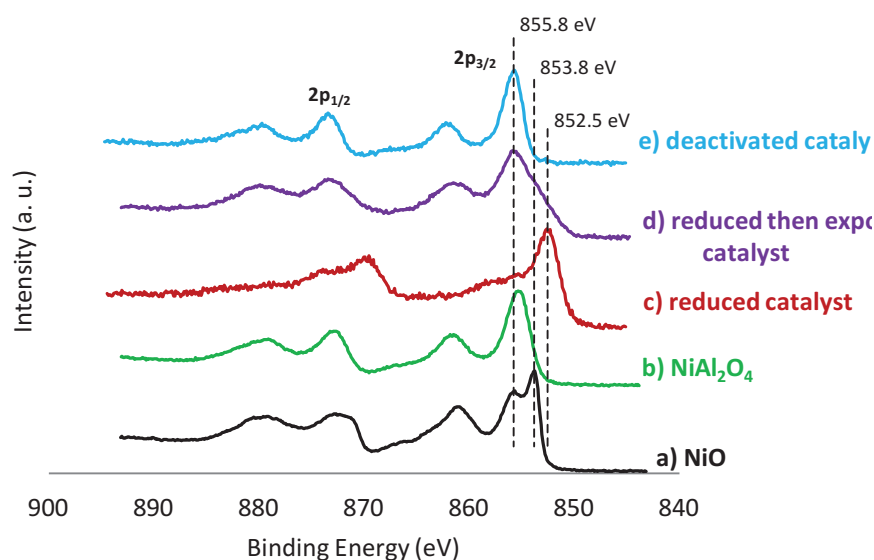


Figure 4.15: X-ray photoelectron spectra (Ni 2p doublet) of a) NiO, b) NiAl₂O₄, 5 wt.% Ni/Mg_{0.7}Al₂O_{3.7} after c) *in-situ* reduction at 700°C, d) reduction at 700°C and re-exposure to air and e) after ATR reaction and deactivation

NiO shows a multiplet splitting of the 2p_{3/2} transition, with two states present at BEs of 853.8 and 855.8 eV. It also exhibits a 2p_{1/2} BE of 871.3 eV which corresponds to a 2p peak separation Δ of 17.5 eV. This is in good agreement with data extracted from the literature [4], [5].

NiAl₂O₄ shows a 2p_{3/2} BE of 855.8 eV and a 2p_{1/2} BE of 872.6 eV. Comparable BE were found in the literature [6], [7].

The *in-situ* reduced sample shows 2p_{3/2} BE of 852.5 eV and 2p_{1/2} BE of 870 eV which corresponds to the BE of metallic nickel [7]–[9].

After *ex-situ* reduction and exposure to air, however, a shift in the BE of $2p_{3/2}$ is observed. The peak is broader and is probably the result of the contributions of different Ni species in presence. Its maximum is at a BE of 855.8 eV. It seems that metallic Ni is easily re-oxidized in surface when exposed to air.

The deactivated catalyst sample shows a $2p_{3/2}$ BE of 855.8 eV and a very similar spectrum as NiAl_2O_4 .

These results demonstrate that after reduction at 700°C , the nickel in the surface region is fully reduced. However, after exposure to air, the surface is partly re-oxidized and it results in what could be a mixture of Ni° , NiO and, although unlikely, NiAl_2O_4 . After reaction and deactivation, surface Ni seems to be NiAl_2O_4 but the sample was exposed to air prior to XPS analysis.

Peaks deconvolution has been done in literature studies in order to determine a relative composition of Ni° , NiAl_2O_4 and NiO [4]. It should also be noted for instance that Araki *et al.* related a BE of 856.3 eV to Ni_2O_3 rather than to NiAl_2O_4 [10]. The binding energies in the Ni 2p doublet region are thus very close and can overlap.

Decomposition of the peaks seems problematic especially when trying to discriminate NiO from NiAl_2O_4 . We have also seen that the oxidation of surface Ni might not be solely the result of the reaction itself but re-exposure to air. Moreover, XPS describes the state of surface Ni species that are not representative of the bulk nickel. Therefore, information extracted from XPS analyses is not straightforward and is thus not suitable for the discrimination of the nickel species in presence.

4.1.7. Temperature profile during ATR of model biogas on 5 wt.% $\text{Ni/Mg}_{0.4}\text{Al}_2\text{O}_{3.4}$

The autothermal reforming reaction relies on the exothermic methane combustion delivering the necessary heat for the endothermic reforming reactions to occur.

Considering an ATR reaction of model biogas under the conditions: $T = 700^\circ\text{C}$, $\text{Steam}/\text{CH}_4 = 3$, $\text{O}_2/\text{CH}_4 = 0.5$, $\text{CO}_2:\text{CH}_4 = 40:60$, if the reaction was carried out adiabatically, the ΔT for the combustion reaction would be $+ 935^\circ\text{C}$. The ΔT for the steam reforming reaction would be $- 721^\circ\text{C}$. The difference, which should be zero in autothermal conditions, is higher than 0 because more oxygen was supplied in the feed to compensate for the heat loss under our non-adiabatic reaction conditions.

A hotspot can thus be expected in the catalytic bed. The exothermic combustion zone was evidenced by introducing a thermocouple well into the reactor. The well had an external diameter of 1.58 mm and was made of high temperature-resistant titanium.

After *in-situ* reduction, an ATR reaction over commercial catalyst was started at $T = 700^{\circ}\text{C}$ Steam/ $\text{CH}_4 = 3$, $\text{O}_2/\text{CH}_4 = 0.5$, $\text{CO}_2:\text{CH}_4 = 40:60$. 100 mg of catalyst were used, making a catalytic bed 20 mm high. After 1 hour of reaction the thermocouple placed inside the well was slid up from the bottom of the bed up to the top. The temperature was measured every 2 or 3 mm in order to determine a temperature profile starting from the outlet of the bed and going up to the inlet. The thermocouple was then placed back at the bottom of the well.

After 10 minutes, the thermocouple was slid up again progressively in order to repeat the measurement. In both cases the highest temperature measured was 718°C and was reached 2 mm from the top of the bed. This temperature is low compared to the adiabatic ΔT calculated previously. It is also lower than results found in the literature where the temperature difference between the inlet and the maximum would reach 50 to 100°C in similar conditions [11], [12].

The experiment was repeated without using a thermocouple well. Instead, a very thin thermocouple of 0.5 mm diameter was introduced directly into the reactor at the bottom of the catalytic bed. The air tightness was achieved by using a septum. After 1 hour of reaction, the thermocouple was slid up again slowly along the bed. In this case, it was impossible to repeat the measurement and put the thermocouple back at the bottom of catalytic bed without disrupting it.

This time, the highest temperature measured was 808°C , which made a 98°C difference between the inlet temperature and the maximum temperature (Figure 4.16). It was also measured at about 2 mm from the entry of the bed. The thermocouple well used in the first attempts undervalued the temperatures. This was likely due to the low thermal conductivity of titanium [13].

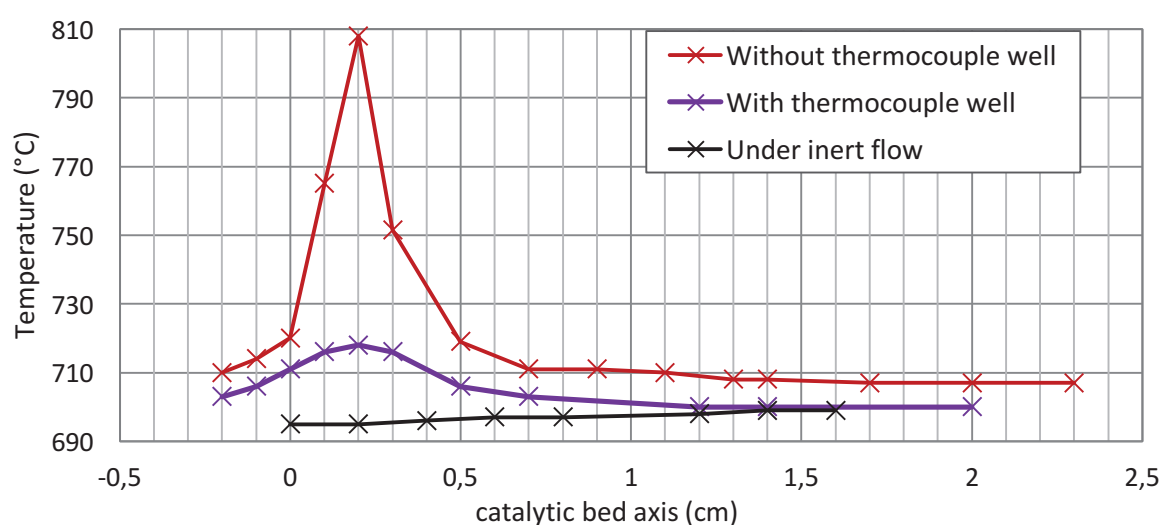


Figure 4.16: Temperature profiles measured in different conditions: during ATR reaction by placing a thermocouple directly inside the catalytic bed (red), using a thermocouple well (purple), and under inert flow for comparison purposes (black). $x = 0$ cm stands for the top and entry of the bed, $x = 2$ cm stands for the exit of the bed.

Two critical conclusions could be drawn from this result:

- The exothermic combustion zone could be clearly evidenced and localized thanks to a thermocouple.
- We could clearly identify that at the beginning of the ATR reaction, the combustion zone was placed at the entry of the bed.

It would be of great interest to follow the evolution of temperature in different parts of the catalytic bed from the start of the reaction over our prepared catalyst until its complete deactivation.

Given the inability to measure more than one profile during the same reaction by sliding up a thermocouple directly placed into the catalytic bed, a different approach was required. A reactor with an internal diameter of 4 mm was filled with 20 mg of 5 wt.% Ni/Mg_{0.4}Al₂O_{3.4} catalyst. Instead of moving one thermocouple along the bed, 6 thin thermocouples were placed into the catalytic bed at 6 different fixed heights. The height of the bed was 17 mm and its diameter was 4 mm. The thermocouples T1, T2, T3, T4, T5 and T6 were placed at $x = 1, 6, 9, 12, 16, 19$ mm respectively (Figure 4.17-a). Each of them presented an external diameter of 0.5 mm.

The catalyst was then tested in ATR reaction conditions at 700°C with Steam/CH₄ = 3, O₂/CH₄ = 0.5, CO₂:CH₄ = 40:60 and at a GHSV = 40 000 h⁻¹. The temperature was monitored continuously and measured automatically every 3 seconds (Figure 4-17-b).

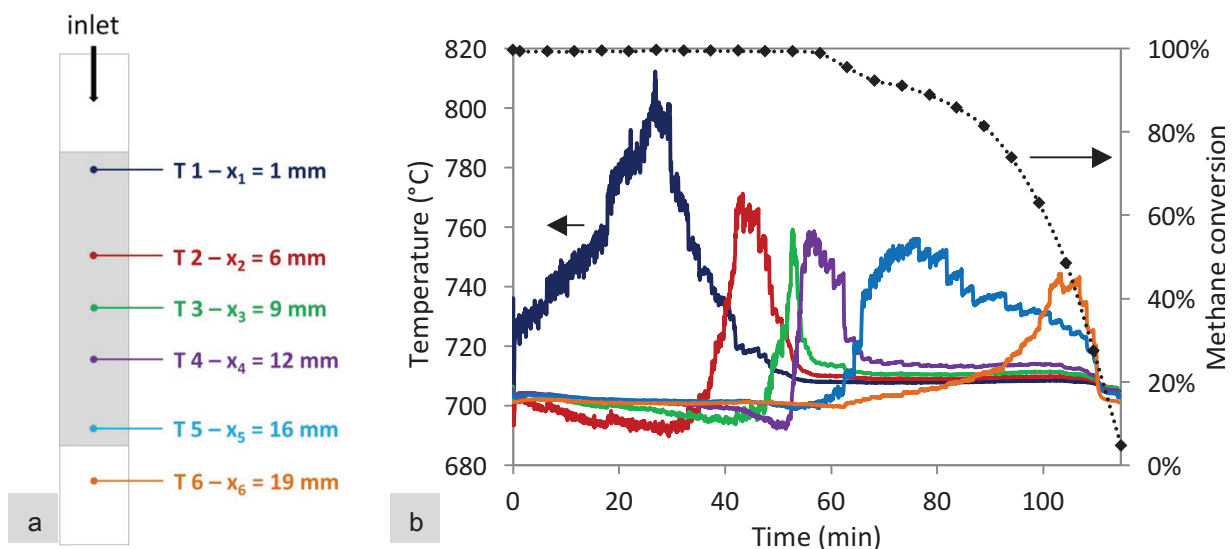


Figure 4.17: a) scheme of the reactor with the positions of the 6 thermocouples b) Evolution of the temperature (left axis) and methane conversion (right axis) over time during ATR reaction over 5 wt.% Ni/Mg_{0.4}Al₂O_{3.4} at 700°C, Steam/CH₄ = 3, O₂/CH₄ = 0.5, CO₂:CH₄ = 40:60, GHSV = 40 000 h⁻¹.

It should be noted that a blank reaction was first performed in these conditions on a reactor containing thermocouples but no catalyst. No methane/oxygen conversion or H₂/CO production were observed, indicating therefore that the activity resulted from the catalysts only.

Complete deactivation occurred after 115 minutes. From the start of the reaction until 26.8 minutes, the temperature T1 measured by the first thermocouple increased steadily until reaching a maximum of 812°C. This temperature was consistent with the results obtained when the thermocouple was slid up inside the catalytic bed during our first attempts (Figure 4.15). Meanwhile, T2 slowly decreased from 700°C to 695°C. The temperatures measured by the 4 other thermocouples situated downstream remained constant, revolving around 700°C. After reaching its maximum, T1 dropped while T2 increased to reach a maximum of 771°C after 43.3 minutes. T3 slowly declined. T4, T5 and T6 stayed stable. The same phenomena were observed for each thermocouple until complete deactivation of the catalyst. After the end of the reaction, the temperatures all returned to their initial values, revolving around 700°C.

In light of these observations, it could be concluded that during reaction, the exothermal combustion zone progressed from the inlet downwards along the bed until complete deactivation.

4.1.8. UV-vis DRS analysis of catalyst at different time-on-stream durations

UV-visible diffuse reflectance spectroscopy (UV-vis-DRS) can be used to study the coordination states of nickel species. Using this technique seemed well suited to discriminate NiO and NiAl₂O₄ since the two compounds display distinct colors (green and blue).

a. Standards UV-vis DRS analyses and calibration

In order to quantify the amount of NiO or NiAl₂O₄ present after reaction, a calibration was made beforehand using 5 samples as standards. The standards B1, B2, B3, B4 and B5 were prepared by mixing commercial NiO and prepared NiAl₂O₄ respecting 5 different NiO/NiAl₂O₄ ratios (Table 4.5). Each mixture was then blended with Mg_{0.4}Al₂O_{3.4} in order to simulate the catalyst used for the reaction. The total amount of nickel to be added was thus calculated in order to correspond to a 5 wt.% Ni catalyst. The relative reflectance was calculated using BaSO₄ as a white reference (see Chapter 2, 2.2.6.).

Table 4.5: Relative composition of NiAl₂O₄ and NiO in the UV-vis-DRS benchmarks

	NiAl ₂ O ₄ (wt.%)	NiO (wt.%)
B 1	0	100
B 2	33.3	66.7
B 3	49.6	50.4
B 4	66.6	33.4
B 5	100	0

The standards were analyzed by UV-vis-DRS. The samples thickness was enough to prevent any transmission effect. Figure 4.18 presents the 5 spectra. For the sake of clarity, the spectra were shifted parallel to the intensity axis. The spectra were also cropped in order to only present the region of interest between 370 nm and 970 nm. It should be noted that the bare support Mg_{0.4}Al₂O_{3.4} is white. It was also analyzed and showed no absorption in the studied 370-970 nm region.

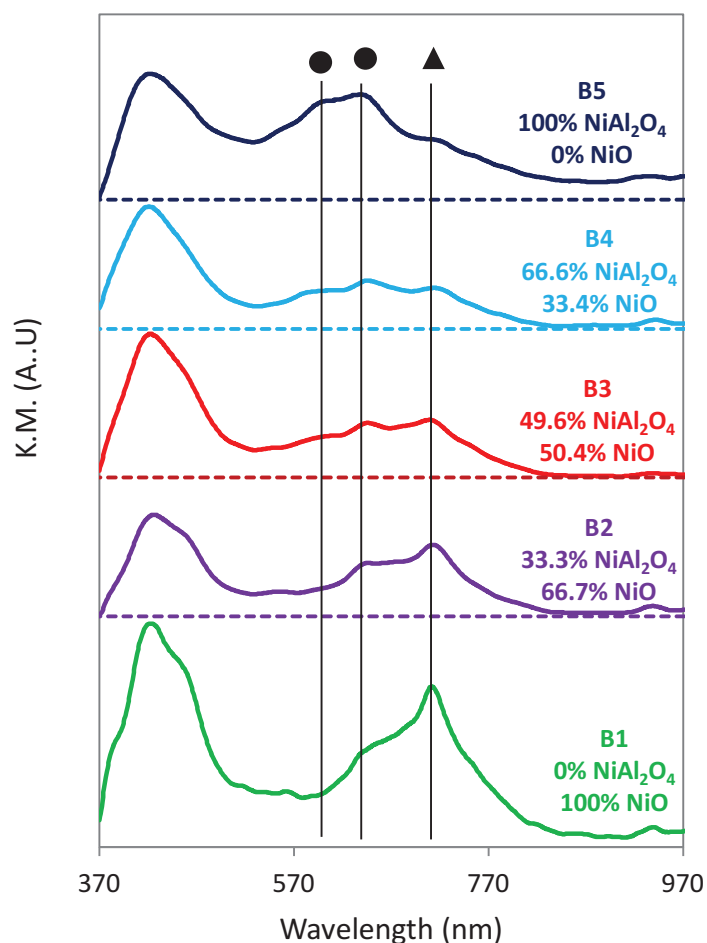


Figure 4.18: Kubelka-Munk spectra of benchmarks presenting (●) tetrahedrally coordinated Ni²⁺ in NiAl₂O₄ at 600 and 640 nm and (▲) octahedrally coordinated Ni²⁺ in NiO at 715 nm

B1 composed of 100% NiO – 0% NiAl₂O₄ displayed one absorption band in this region at 715 nm. B5 composed of 100% NiAl₂O₄ displayed two important absorption bands at 600 nm and 640 nm. The absorption bands at 600 and 640 nm were attributed to Ni²⁺ ions tetrahedrally coordinated in NiAl₂O₄ [14], [15]. The band located at 715 nm is typical of Ni²⁺ ions octahedrally coordinated.

The ratios of the absorptions at 715 nm and 600 nm were calculated for each spinel concentration in % (Figure 4.19).

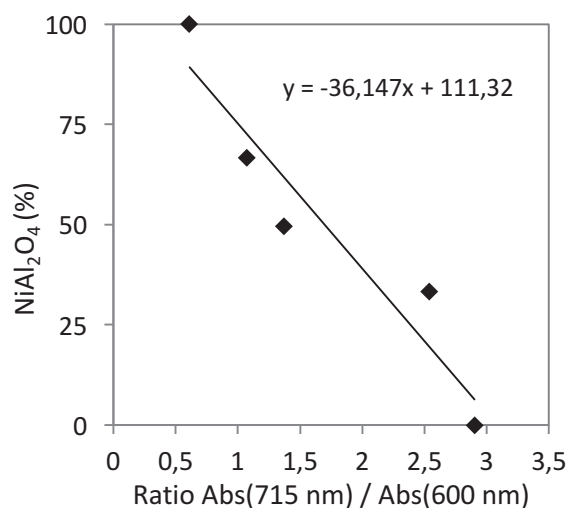


Figure 4.19: Composition in %NiAl₂O₄ (relative to NiO) as a function of the ratio of absorptions taken from the Kubelka-Munk spectra at 715 nm (octahedrally coordinated Ni²⁺ in NiO) and at 600 nm (tetrahedrally coordinated Ni²⁺ in NiAl₂O₄).

Given these observations, it is possible to discriminate and quantify the relative composition of NiO and NiAl₂O₄ with UV-vis DRS analyses.

b. Deactivation study combined with UV-vis DRS analyses

In order to demonstrate the progression of the spinel formation during ATR reaction, 4 tests were performed over 4 identical reactors prepared with 5 wt.% Ni/Mg_{0.4}Al₂O_{3.4}. Each reactor was separated into 4 sections of 10 mg of catalyst. In this way, each section could be analyzed one by one after test. Figure 4.20 depicts the plan of experiments.

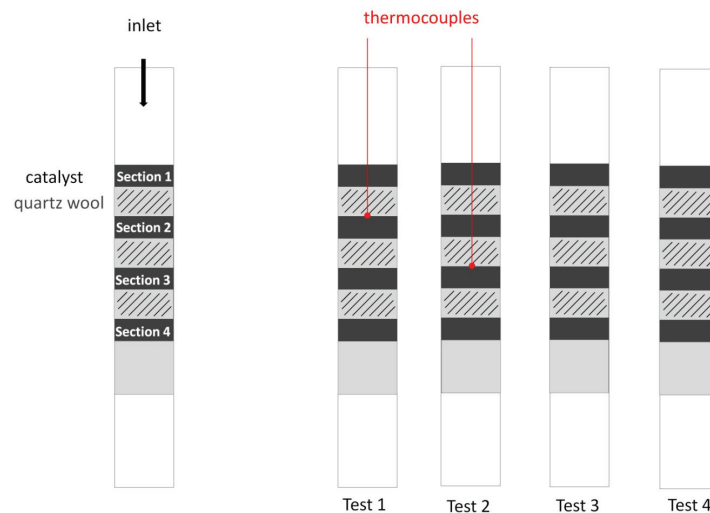


Figure 4.20: Plan of experiments for the 4 ATR tests

The reaction was started at standard conditions at $T = 700^{\circ}\text{C}$, $\text{Steam}/\text{CH}_4 = 3$, $\text{O}_2/\text{CH}_4 = 0.5$, $\text{CO}_2:\text{CH}_4 = 40:60$, at a $\text{GHSV} = 66,700 \text{ h}^{-1}$. Full conversion of methane was observed over the 4 reactors at the beginning of the reaction. For the first test, a thermocouple was placed at the inlet of the second catalyst section. The reaction was stopped when the temperature measured by the thermocouple reached a maximum. For the second test, the thermocouple was placed at the inlet of the third catalyst section. Similarly, the reaction was stopped when the temperature reached a maximum. For the third test, no thermocouple was introduced. The reaction was stopped when the methane conversion was of about 96%. Finally, the fourth test was stopped after complete deactivation. No thermocouple was introduced in this reactor either.

Figure 4.21 displays photographs of the reactors after each test.

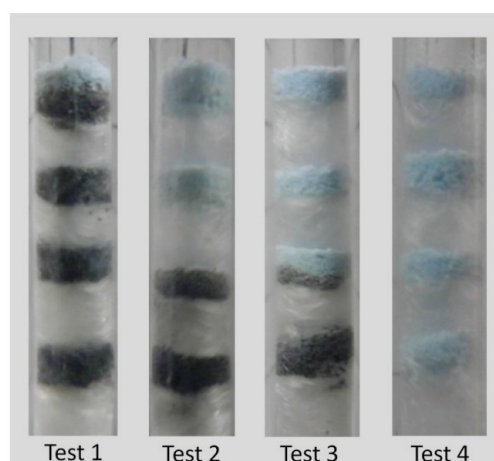


Figure 4.21: Photographs of the catalysts after tests 1, 2, 3 and 4 over 5 wt.% $\text{Ni}/\text{Mg}_{0.4}\text{Al}_2\text{O}_{3.4}$ ($m = 4 \times 10 \text{ mg}$). Reaction conditions: $T = 700^{\circ}\text{C}$, $\text{Steam}/\text{CH}_4 = 3$, $\text{O}_2/\text{CH}_4 = 0.5$, $\text{CO}_2:\text{CH}_4 = 40:60$, $\text{GHSV} = 66,700 \text{ h}^{-1}$.

i. First test

During the first test, the temperature measured by the thermocouple placed at the entry of the 2nd section decreased from 704°C to 691°C within the first 5 hours of reaction. From then, the temperature increased steadily, reaching a maximum of 721°C after 6.8 hours of reaction. This temperature is considerably lower than the maximum measured previously which revolved around 800°C (4.1.6). This is likely related to the fact that the thermocouple was not in direct contact with the catalyst but was rather situated just above, in the quartz wool (Figure 4.22). As the temperature started to decrease, the reaction was stopped after 7 hours. At that point, the methane conversion was still complete.

Given the calibration described previously, the sections of the reactors were analyzed:

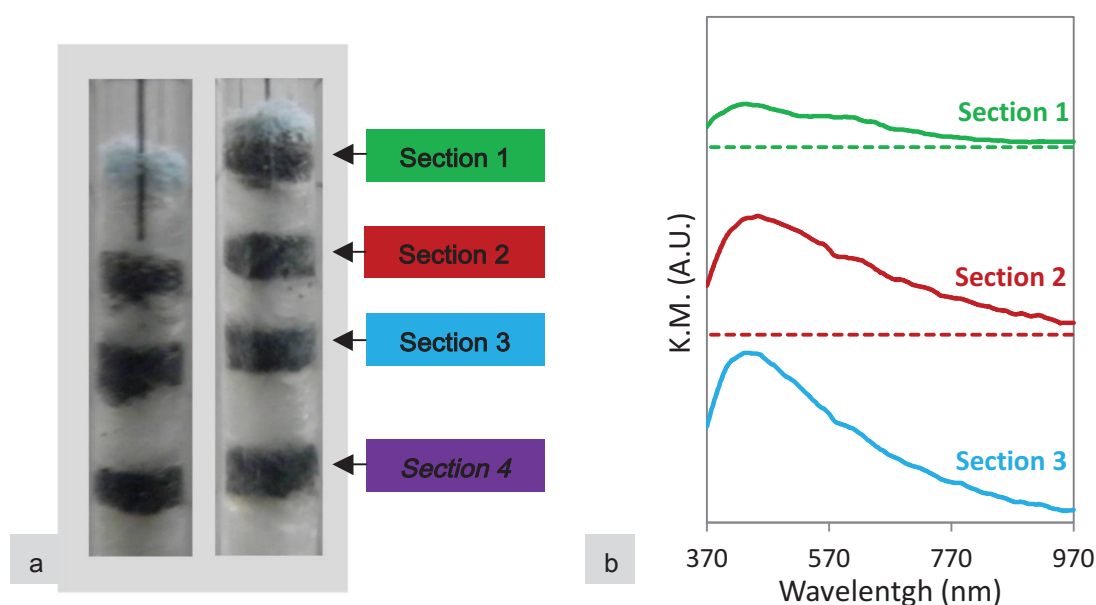


Figure 4.22: a) Photographs of two sides of the reactor and b) Kubelka-Munk spectra of sections 1, 2 and 3 (section 4 was not analyzed) after test 1 on 5 wt.% Ni/Mg_{0.4}Al₂O_{3.4} (m = 4 x 10 mg). Reaction conditions: T = 700°C, Steam/CH₄ = 3, O₂/CH₄ = 0.5, CO₂/CH₄ = 40:60, GHSV = 66,700 h⁻¹.

The photographs show that one side of the first section was light blue while the other side of the section was blue on top and black below (Figure 4.22-a). Blue color observed along the thermocouple suggested that introducing the thermocouple into the catalytic bed created a differential pathway.

The ratio Abs (715 nm) / Abs (600 nm) for the first section was 0.53, corresponding to a composition of 92.2% NiAl₂O₄ and 7.8% NiO (Figure 4.22-b). However, as we mentioned, this section was not homogeneous. It still presented some black nickel species corresponding to metallic nickel. Therefore, our calculations could be biased since metallic nickel shows almost no reflectance in the 370-970 nm region. In any case, given the Kubelka-Munk spectra, it is very likely that section 1 presented some

nickel spinel. However, the presence of NiO was difficult to assess unambiguously. Sections 2 and 3 were analyzed but nothing could be concluded from their UV-vis-DRS spectra in the region 370-970 nm since they present black metallic nickel species. Section 4 was not analyzed as it was expected to show the same result as sections 2 and 3.

ii. Second test

During the 2nd test, the temperature measured by the thermocouple placed at the inlet of the 3rd section decreased from 708°C to 700°C within the first 5 hours of reaction. From then, the temperature increased, reaching a maximum of 728°C after 12.8 hours of reaction. Here again, the thermocouple was not in direct contact with the catalyst. As the temperature started to decrease, the reaction was stopped after 13 hours. The conversion of methane was still complete at that point.

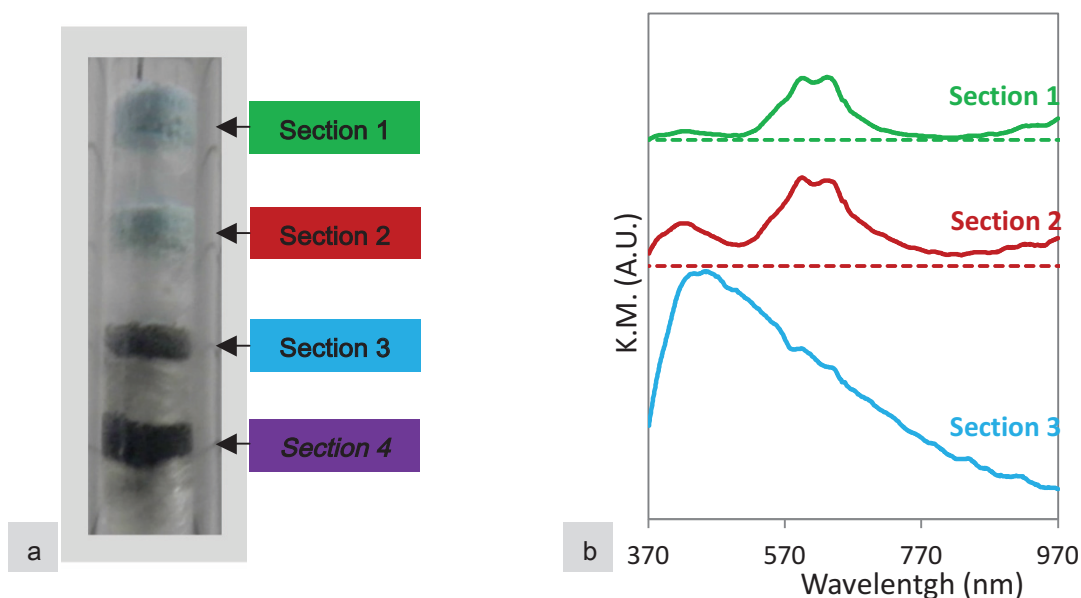


Figure 4.23: a) Photograph of the reactor and b) Kubelka-Munk spectra of sections 1, 2 and 3 (section 4 was not analyzed) after test 2 on 5 wt.% Ni/Mg_{0.4}Al₂O_{3.4} (m = 4 x 10 mg). Reaction conditions: T = 700°C, Steam/CH₄ = 3, O₂/CH₄ = 0.5, CO₂:CH₄ = 40:60, GHSV = 66,700 h⁻¹.

After the 2nd test, the sections colors were homogeneous (Figure 4.23-a). Sections 1 and 2 displayed a light blue color while sections 3 and 4 were black. The ratio Abs (715 nm) / Abs (600 nm) for sections 1 and 2 were 0.16 and 0.35 respectively (Figure 4-23-b). For the first section, this corresponded to a composition of 105% NiAl₂O₄. For the second section, it corresponded to a composition of 98.8% NiAl₂O₄ and 1.2% NiO. Similarly to the first test, analyses of the third section in the region of 370-970 nm showed only the absence of oxidized Ni species. Section 4 was not analyzed.

Given these results, we could observe that the first section was only composed of NiAl_2O_4 . The second section was primarily composed of nickel spinel as well but it is likely that a small part of the nickel species was present as NiO .

iii. Third test

The third test was stopped when the methane conversion reached 96%.

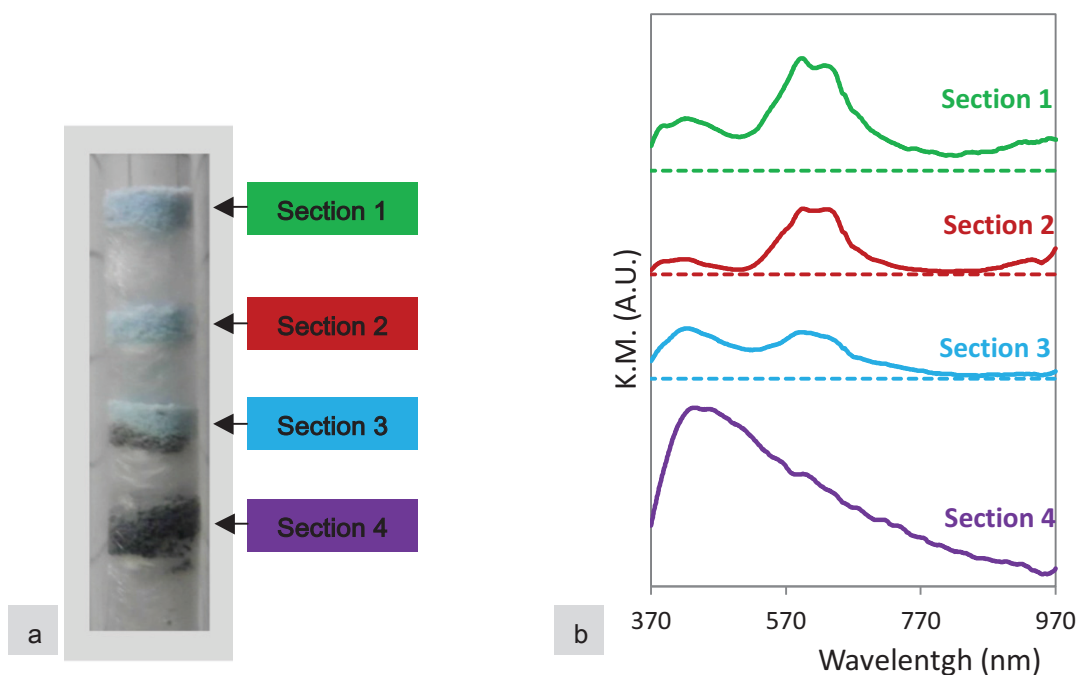


Figure 4.24: a) Photograph of the reactor and b) Kubelka-Munk spectra of sections 1, 2, 3 and 4 after test 3 on 5 wt.% $\text{Ni/Mg}_{0.4}\text{Al}_2\text{O}_{3.4}$ ($m = 4 \times 10 \text{ mg}$). Reaction conditions: $T = 700^\circ\text{C}$, $\text{Steam}/\text{CH}_4 = 3$, $\text{O}_2/\text{CH}_4 = 0.5$, $\text{CO}_2/\text{CH}_4 = 40:60$, $\text{GHSV} = 66,700 \text{ h}^{-1}$.

Sections 1 and 2 displayed a light blue color. Section 3 displayed both light blue and light gray colors while section 4 was entirely black (Figure 4.24-a). The ratio $\text{Abs}(715 \text{ nm}) / \text{Abs}(600 \text{ nm})$ for sections 1, 2 and 3 were 0.3, 0.18 and 0.29 corresponding to compositions of 100%, 105% and 101% of nickel spinel respectively (Figure 4.24-b). Section 4 showed the absence of oxidized Ni species.

iv. Fourth test

Finally the fourth test was performed until complete catalyst deactivation.

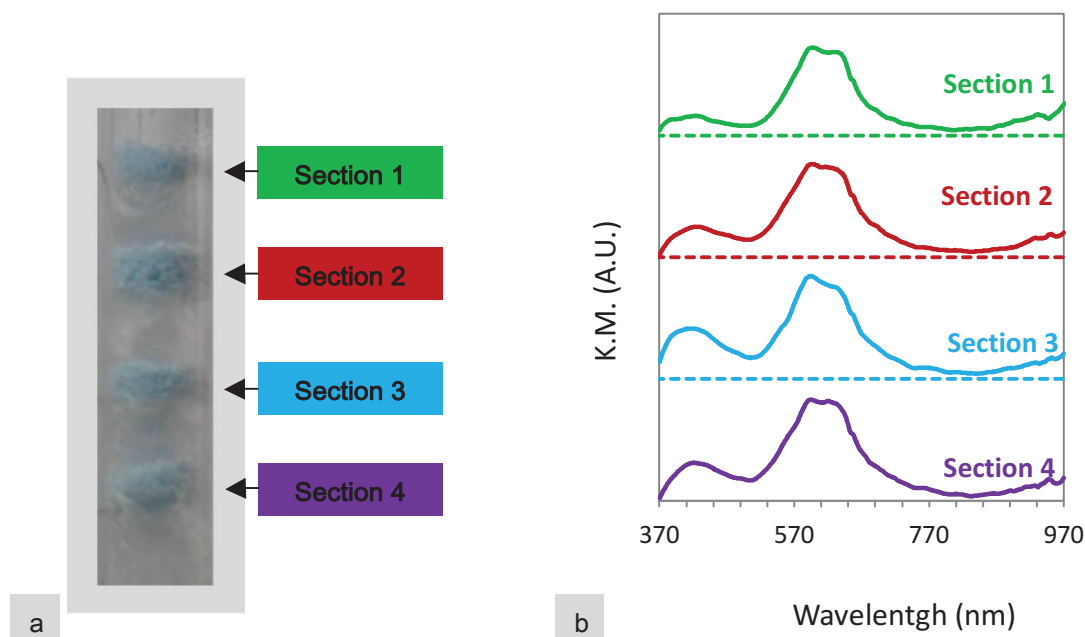


Figure 4.25: a) Photograph of the reactor and b) Kubelka-Munk spectra of sections 1, 2, 3 and 4 after test 4 on 5 wt.% Ni/Mg_{0.4}Al₂O₄ (m = 4 x 10 mg). Reaction conditions: T = 700°C, Steam/CH₄ = 3, O₂/CH₄ = 0.5, CO₂:CH₄ = 40:60, GHSV = 66,700 h⁻¹.

All the sections displayed a light blue color. The ratio of intensities Abs (715 nm) / Abs (600 nm) for sections 1, 2, 3 and 4 were 0.19, 0.25; 0.22 and 0.26 corresponding to compositions of 104%, 102%, 103% and 102% of nickel spinel respectively (Figure 4.25-b). All sections were thus primarily composed of NiAl₂O₄ after complete deactivation.

Performing these tests and coupling them with systematic UV-vis-DRS analyses enabled us to confirm that the formation of nickel spinel progresses along the bed during ATR of model biogas until complete deactivation.

4.2. Influence of Mg:Al ratio

The influence of the magnesium content was investigated by testing 3 nickel catalysts supported on magnesium spinel support with various Mg:Al ratios in the same conditions: 5 wt.% Ni/Mg_{0.4}Al₂O_{3.4}, 5 wt.% Ni/Mg_{0.7}Al₂O_{3.7} and 5 wt.% Ni/Mg_{1.1}Al₂O_{4.1}.

In order to compare the catalysts resistance to deactivation in a systematic manner, the reactions were started in standard conditions (Steam/CH₄ = 3, O₂/CH₄ = 0.5, CH₄:CO₂ =60:40) at a GHSV of 40,000 h⁻¹. During the first 2 hours the three catalysts presented full conversions of both methane and

oxygen. They also presented the same performances in terms of selectivity and molar fractions of H₂, CO and CO₂ (Figure 4.26). H₂/CO molar ratio was equal to 3 for the three reactions.

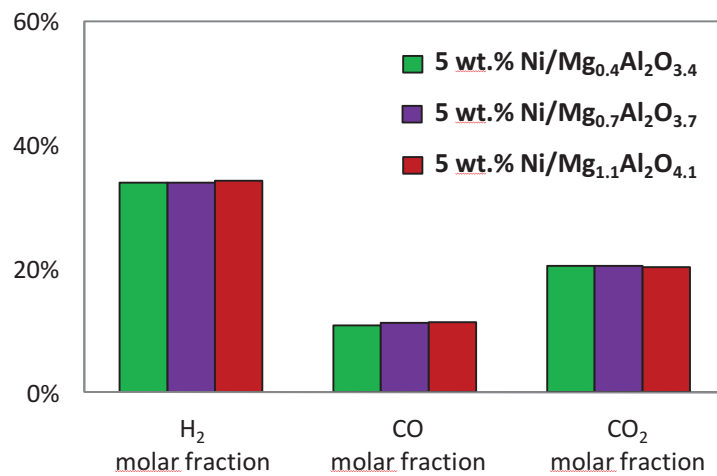


Figure 4.26: Dry outlet gas concentrations during the first two hours of ATR of model biogas over 20 mg of 5 wt.% Ni/Mg_{0.4}Al₂O_{3.4}, 5 wt.% Ni/Mg_{0.7}Al₂O_{3.7} and 5 wt.% Ni/Mg_{1.1}Al₂O_{4.1}. Reaction conditions T = 700°C, Steam/CH₄ = 3, O₂/CH₄ = 0.5, CO₂:CH₄ = 40:60, GHSV = 40,000 h⁻¹

After 2 hours, the GHSV was increased to 60,000 h⁻¹. The 5 wt.% Ni/Mg_{0.4}Al₂O_{3.4} catalyst deactivated immediately. Figure 4.27 shows the performances of this catalyst until deactivation.

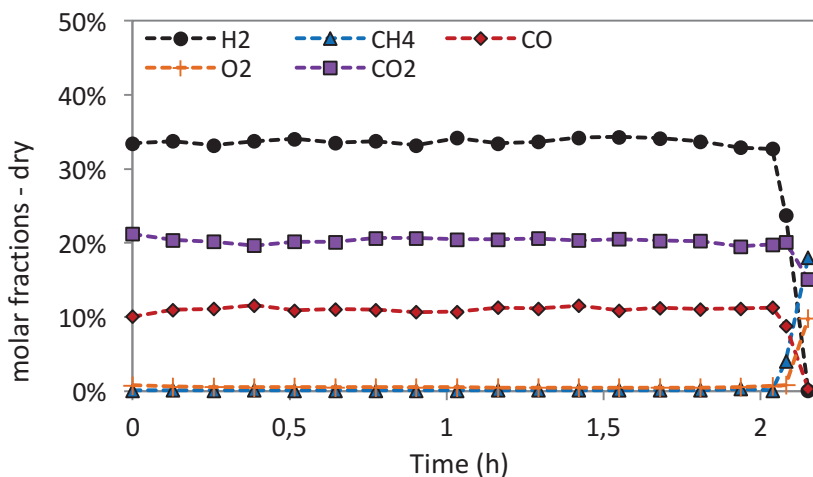


Figure 4.27: Dry outlet gas concentrations during ATR of model biogas over 5 wt.% Ni/Mg_{0.4}Al₂O_{3.4}. Reaction conditions: T = 700°C, Steam/CH₄ = 3, O₂/CH₄ = 0.5, CO₂:CH₄ = 40:60, GHSV = 40,000 h⁻¹ for 2 hours then GHSV = 60,000 h⁻¹.

5 wt.% Ni/Mg_{0.7}Al₂O_{3.7} deactivated 45 minutes later, after 2.75 hours of reaction. However 5 wt.% Ni/Mg_{1.1}Al₂O_{4.1} still showed full conversions of methane and oxygen (Figure 4.28). The GHSV was increased to 100,000 h⁻¹ after a short step at 80,000 h⁻¹. After 20 hours, this catalyst showed 95% methane conversion and complete oxygen conversion.

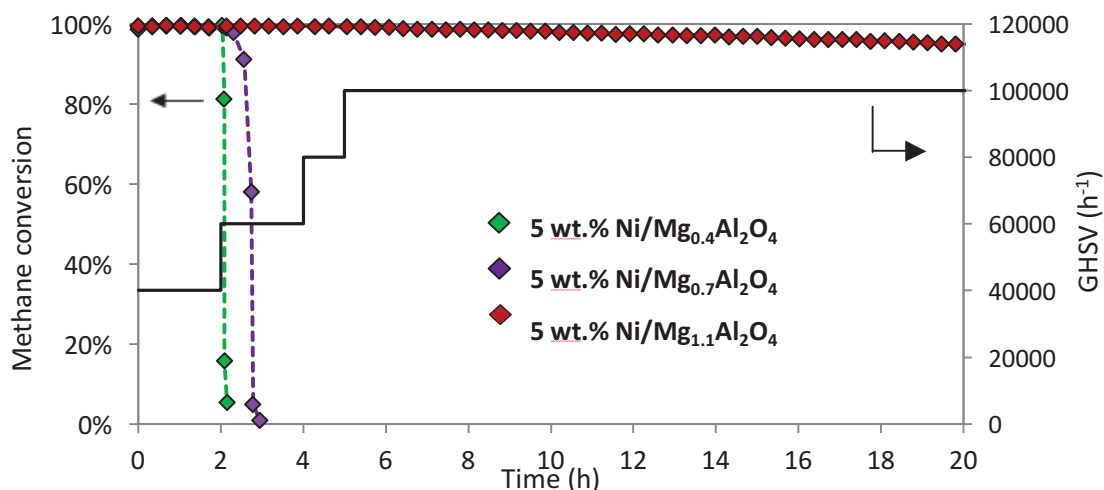


Figure 4.28: Methane conversion during ATR reaction over 20 mg of 5 wt.% Ni/Mg_{0.4}Al₂O_{3.4}, 5 wt.% Ni/Mg_{0.7}Al₂O_{3.7} and 5 wt.% Ni/Mg_{1.1}Al₂O_{4.1}. Reaction conditions: T = 700°C, Steam/CH₄ = 3, O₂/CH₄ = 0.5, CO₂:CH₄ = 40:60, GHSV ranging from 40,000 to 100,000 h⁻¹.

After reaction, 5 wt.% Ni/Mg_{0.4}Al₂O_{3.4} (deactivated), 5 wt.% Ni/Mg_{0.7}Al₂O_{3.7} (also deactivated) and 5 wt.% Ni/Mg_{1.1}Al₂O_{4.1} (still active) were analyzed by UV-vis-DRS, using the method developed in paragraph 4.1.7. The ratio Abs (715 nm) / Abs (600 nm) were calculated (Figure 4.29). 5 wt.% Ni/Mg_{0.4}Al₂O_{3.4} and 5 wt.% Ni/Mg_{0.7}Al₂O_{3.7} were composed of 97% and 98% of NiAl₂O₄ after deactivation. Although 5 wt.% Ni/Mg_{1.1}Al₂O_{4.1} was still active when the reaction was stopped, some spinel could be observed at the inlet of the bed. After UV-vis-DRS analysis and calculations, the nickel that was not metallic was found to be composed of 79% NiAl₂O₄ – 21% NiO.

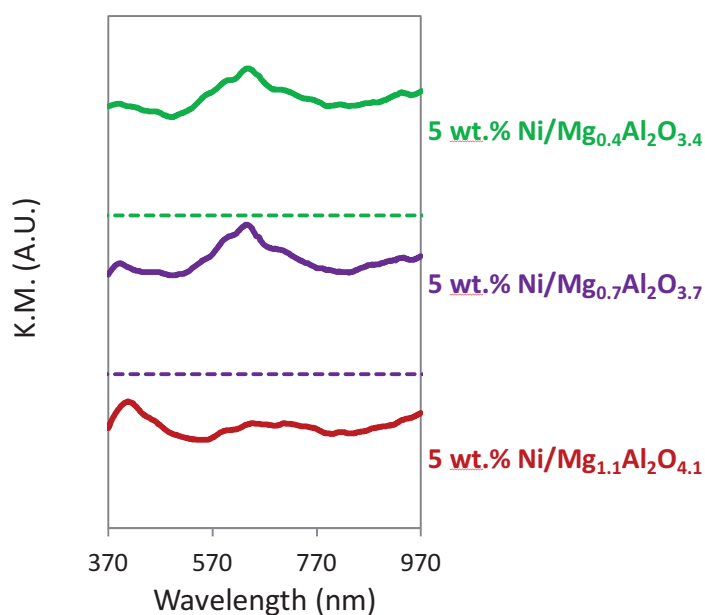


Figure 4.29: Kubelka-Munk spectra of 5 wt.% Ni/Mg_{0.4}Al₂O_{3.4} (deactivated), 5 wt.% Ni/Mg_{0.7}Al₂O_{3.7} (deactivated) and 5 wt.% Ni/Mg_{1.1}Al₂O_{4.1} (still active). m = 20 mg. Reaction conditions: T = 700°C, Steam/CH₄ = 3, O₂/CH₄ = 0.5, CO₂:CH₄ = 40:60

Given these results, it can be concluded that the catalyst resistance to deactivation depends on the nature of the support and more specifically on the Mg:Al ratio.

4.3. Promotion of Ni/Mg_xAl₂O_{3+x} catalyst by rhodium

4.3.1 Addition of Rh on a nickel catalyst

During the screening of different catalysts formulations in Chapter 3, we have observed that the addition of a very small loading of rhodium (0.05 wt.%) on 5 wt.% Ni/Mg_{0.7}Al₂O_{3.7} catalyst improved remarkably its resistance to deactivation.

The effect of Rh on the reducibility of catalysts 5 wt.% Ni/Mg_{1.1}Al₂O_{4.1} and 5-0.05 wt.% Ni-Rh/Mg_{1.1}Al₂O_{4.1} was studied by TPR. Temperature programmed reduction was performed on 100 mg of catalyst in both cases (Figure 4.30). The oven temperature was increased from 100°C to 1000°C with a heating rate of 10°C min⁻¹ under 10 vol% H₂/Ar and total flow of 30 mL min⁻¹. The effluent gases were analyzed by online mass spectrometer.

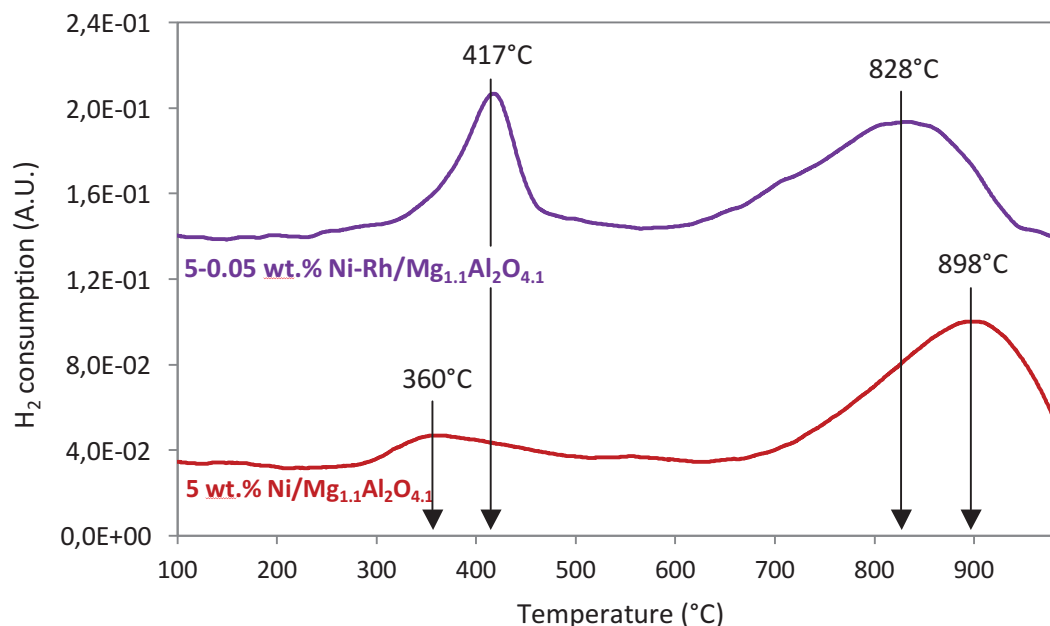


Figure 4.30: TPR profiles of 5 wt.% Ni/Mg_{1.1}Al₂O_{4.1} and 5-0.05 wt.% Ni-Rh/Mg_{1.1}Al₂O_{4.1}.

The TPR profiles showed two clear reduction zones for both catalysts: the first at low temperatures around 350-450°C and the last at high temperature around 700-1000°C.

Two peaks with maxima at 360°C and 898°C were observed in the TPR profile of 5 wt.% Ni/Mg_{1.1}Al₂O_{4.1}. The first peak at low temperature could be attributed to free NiO crystallite weakly interacting with the Mg_{1.1}Al₂O_{4.1} support [16]. The second peak at high temperature could be associated to nickel oxide species strongly interacting with the support or nickel spinel [3], [4].

In the case of 5-0.05 wt.% Ni-Rh/Mg_{1.1}Al₂O_{4.1}, the first peak with a maximum at 417°C was attributed to the methanation of surface carbonates since we observed simultaneous consumption of H₂ and production of CO₂ with the online M-S. It could also be attributed to the reduction of free NiO crystallites. The last peak presenting a maximum at 828°C could be associated to nickel oxide species strongly interacting with the support. These nickel species were reduced at higher temperature on 5 wt.% Ni/Mg_{1.1}Al₂O_{4.1}.

Therefore, one of the beneficial effects of the addition of a very small amount of Rh is to facilitate the reduction of Ni strongly interacting with the support and thus increase the amount of reducible nickel present before reaction.

4.3.2 Dual-bed catalyst coupling 0.05 wt.% Rh/Mg_{1.1}Al₂O_{4.1} with 5 wt.% Ni/Mg_{0.4}Al₂O_{3.4}

A dual-catalyst bed system was implemented. Such a design has already been reported in the literature for the POx of methane [17]–[19].

A Rh catalyst supported on Mg_{1.1}Al₂O_{4.1} was chosen as the first catalyst bed in order to perform the combustion of methane. Rhodium is expected to be a stable methane oxidation catalyst. The second catalyst bed consisted of 5 wt.% Ni/Mg_{0.4}Al₂O_{3.4} to catalyze the reforming reactions, with no O₂ left to form an inactive NiAl₂O₄ spinel phase. The least stable catalyst was chosen in purpose, to highlight the effect of the addition of a Rh catalyst.

Prior to testing the new reactor design composed by a dual-bed, both catalysts were tested individually under the same conditions.

a) ATR reaction of model biogas on 0.05 wt.% Rh/Mg_{1.1}Al₂O_{4.1}

The rhodium catalyst, 0.05 wt.% Rh/Mg_{1.1}Al₂O_{4.1}, was tested alone for the ATR reaction of model biogas in standard conditions (Steam/CH₄ = 3, O₂/CH₄ = 0.5, CH₄:CO₂ =60:40). The reaction was started at a GHSV of 40,000 h⁻¹ then increased step by step to 100,000 h⁻¹ following the same procedure as for 4-2.

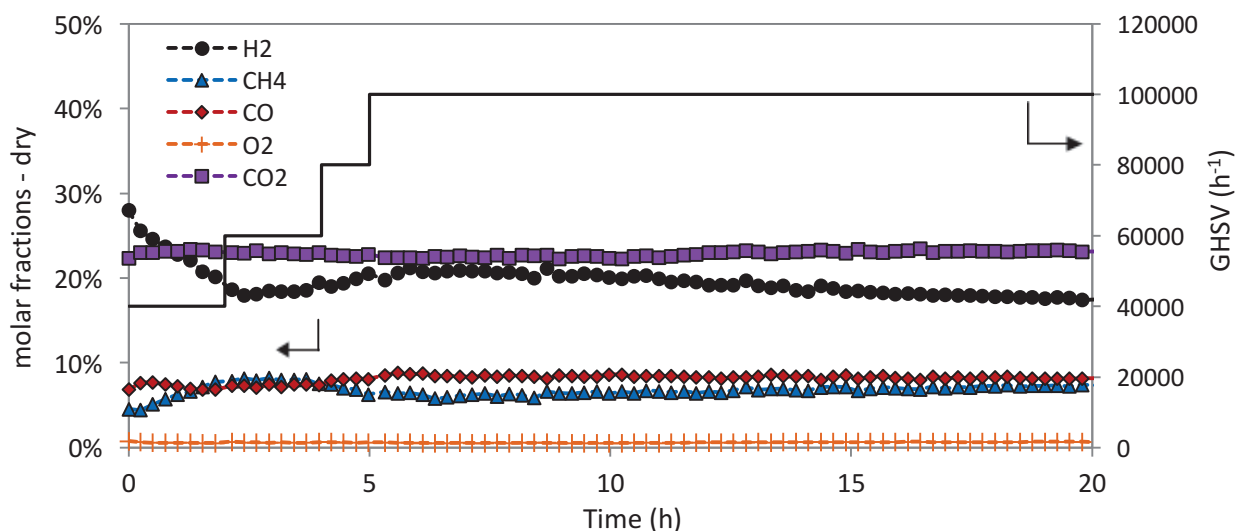


Figure 4.31: Dry outlet gas concentrations during ATR of model biogas over 0.05 wt.% Rh/Mg_{1.1}Al₂O_{4.1}. Reaction conditions T = 700°C, Steam/CH₄ = 3, O₂/CH₄ = 0.5, CO₂:CH₄ = 40:60, GHSV ranging from 40,000 to 100,000 h⁻¹

At all time and any GHSV, the oxygen conversion was complete (Figure 4.31). During the first two hours at GHSV = 40,000 h⁻¹, the methane conversion decreased from 80% until reaching a stable conversion of 64%. The catalyst then showed very high stability for 20 hours even at high GHSV. It showed incomplete methane conversion ranging from 64 to 71% depending on the GHSV.

b) ATR reaction of model biogas on 5 wt. Ni/Mg_{0.4}Al₂O_{3.4}

5 wt.% Ni/Mg_{0.4}Al₂O_{3.4} was chosen as the reforming catalyst. Three tests were performed on 20 mg of this catalyst without thermocouple.

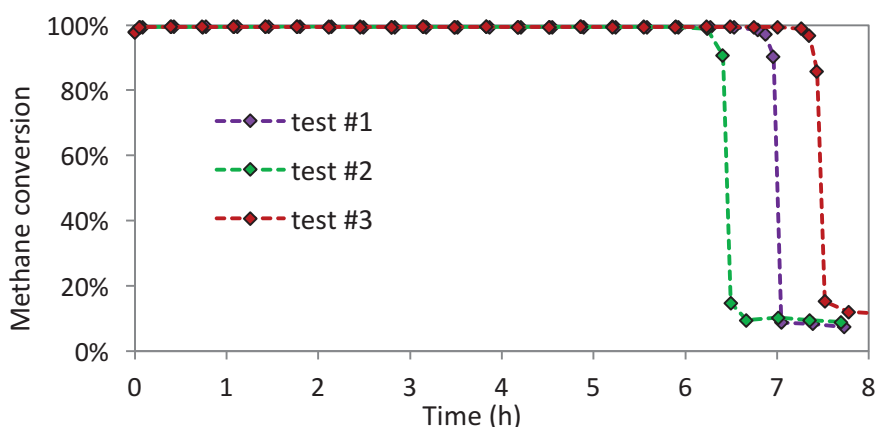


Figure 4.32: Methane conversion during ATR reaction on 20 mg of 5 wt.% Ni/Mg_{0.4}Al₂O₄, 5 wt.% Ni/Mg_{0.7}Al₂O₄ and 5 wt.% Ni/Mg_{1.1}Al₂O₄. Reaction conditions: T = 700°C, Steam/CH₄ = 3, O₂/CH₄ = 0.5, CO₂:CH₄ = 40:60, GHSV = 40,000 h⁻¹.

The catalysts deactivated completely after 6.5, 7 and 7.5 hours (Figure 4.32). It was thus concluded that complete deactivation of 20 mg of 5 wt.% Ni/Mg_{0.4}Al₂O_{3.4} occurs after 7 hours on average. The performances in terms of H₂/CO selectivity and CO₂ production were similar to those presented in Chapter 4.2. At full methane conversion, H₂/CO molar ratio was equal to 2.5 during the three tests.

c) ATR reaction of model biogas over a dual-bed catalyst

Knowing the performances of these two catalysts tested individually, a dual-bed catalyst was prepared with 8 mg of 0.05% Rh/Mg_{1.1}Al₂O_{4.1} placed on top of 2 times 10 mg of 5 wt.% Ni/Mg_{0.4}Al₂O_{3.4} (Figure 4.33). The sections were separated with quartz wool.

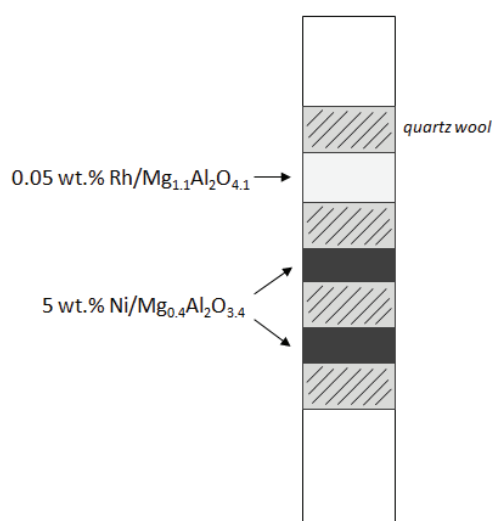


Figure 4.33: Scheme of the reactor prepared with 8 mg of 5 wt.% Rh/Mg_{1.1}Al₂O_{4.1} on top of 2 times 10 mg of Ni/Mg_{0.4}Al₂O_{3.4}

The ATR reaction was performed at standard conditions at 700°C (Steam/CH₄ = 3, O₂/CH₄ = 0.5, CH₄:CO₂ =60:40). It showed full oxygen and methane conversion for 20 hours (Figure 4.34). The performances in terms of H₂/CO selectivity and CO₂ production were similar to those of 5 wt.% Ni/Mg_{0.4}Al₂O_{3.4} alone. Indeed, H₂/CO molar ratio was equal to 2.5.

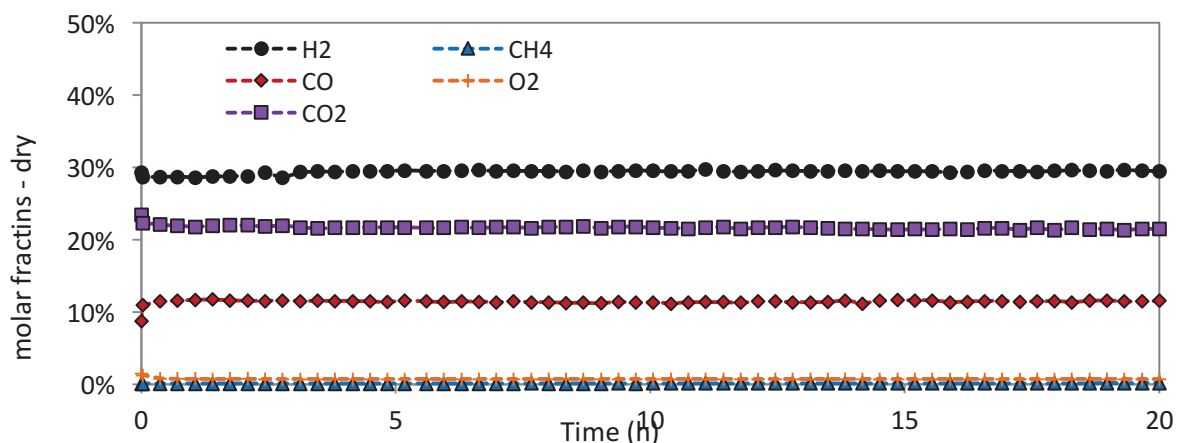


Figure 4.34: Dry outlet gas concentrations during ATR of model biogas on dual bed catalyst composed of 8 mg of 0.05 wt.% Rh/Mg_{1.1}Al₂O_{4.1} and 20 mg of 5 wt.% Ni/Mg_{0.4}Al₂O_{3.4}. Reaction conditions T = 700°C, Steam/CH₄ = 3, O₂/CH₄ = 0.5, CO₂:CH₄ = 40:60, GHSV = 57,000 h⁻¹

The reaction was stopped after 20 hours. Both sections of nickel-based catalyst were black and did not display any trace of blue spinel. UV-vis-DRS analyses were carried out on the two sections in order to confirm these observations (Figure 4.35). The spectra of these two sections were similar to some sections presented in Figure 4.22 when the catalyst contained only metallic nickel.

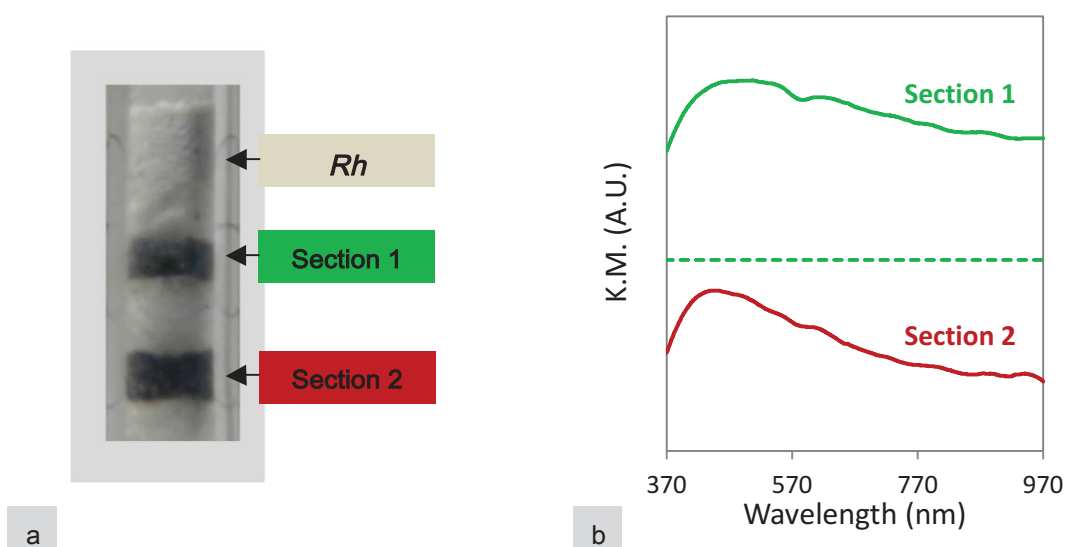


Figure 4.35: a) Photograph of the reactor and b) Kubelka-Munk spectra of sections 1 and 2 of 5 wt.% Ni/Mg_{0.4}Al₂O₄ after test on dual-bed catalysts (m = 2 x 10 mg). Reaction conditions: T = 700°C, Steam/CH₄ = 3, O₂/CH₄ = 0.5, CO₂:CH₄ = 40:60, GHSV = 57,000 h⁻¹

Performing the ATR of model biogas over a dual-bed reactor composed by a Rh catalyst on top of a Ni reforming catalyst prevented the formation of nickel spinel and deactivation. It should be noted that the nickel reforming catalyst used was the most sensitive to deactivation, presenting the lowest Mg:Al

molar ratio. Only a small amount of 0.05 wt.% Rh catalyst was sufficient to perform the combustion and protect this reforming catalyst from high temperatures and oxidizing conditions.

4.4. Discussion

During the ATR of model biogas over $\text{Ni/Mg}_x\text{Al}_2\text{O}_{3+x}$, complete methane conversion is observed over a certain period of time, which depends on the reaction conditions and catalyst composition, followed by a very rapid drop of the methane conversion to zero, with a corresponding drop of the syngas production. This deactivation profile is very different from the profiles reported for coking or sintering of the catalysts, where a gradual decrease of the conversion with time is observed. At the same time temperature measurements inside the catalyst bed showed that the hot spot moves from the reactor inlet to the outlet during catalyst deactivation (Figure 4.17). This hot spot is associated with the zone where methane combustion takes place. Thus the first process in the overall catalyst deactivation is the loss of the active sites for methane combustion. Once the active sites for methane combustion at the inlet of the catalyst bed are deactivated, the combustion takes place further down the bed, and simultaneously converts the metallic nickel into nickel-oxide. The nickel-oxide reacts with the support to form an inactive spinel labeled as " NiAl_2O_4 " but which might consist in a mixed $\text{Mg}_{1-x}\text{Ni}_x\text{Al}_2\text{O}_4$ composition. NiAl_2O_4 is hardly active for either methane combustion or methane reforming, as shown in Table 4.4 (3-6% methane conversion). This process will continue until the end of the catalyst bed is reached and all oxidation sites have been deactivated. This is consistent with the fact that the methane conversion drops to zero, while the methane combustion reaction proceeding without reforming would lead to 25% methane conversion.

As described in the literature review in Chapter 1, NiO can react with alumina to form inactive NiAl_2O_4 through the diffusion of Ni^{2+} ions into the cationic vacancies present in $\gamma\text{-Al}_2\text{O}_3$. Thus the presence of NiO and high temperatures favor the formation of NiAl_2O_4 . MgAl_2O_4 used here as a support rather than Al_2O_3 is expected to prevent or at least limit the diffusion of nickel ions into the vacancies. However, some NiAl_2O_4 was evidenced by UV-vis-DRS analyses on our catalysts after reaction. This might be related to the crystal structures of the two spinels, MgAl_2O_4 and NiAl_2O_4 .

In Chapter 2, MgAl_2O_4 was described as a "normal" spinel structure. Only 1/8 of the tetrahedral sites and 1/2 of the octahedral sites are occupied by cations, which means that many cationic sites are vacant. On the other hand, NiAl_2O_4 is considered to be a partially "inverse" spinel since Ni^{2+} cations can occupy both octahedral and tetrahedral sites, although Ni^{2+} in octahedral coordination should be favored.

The temperature has a strong influence on cation inversion in normal and inverse spinels, and the high temperature reached in the methane combustion zone induces important structural modifications and disorder in MgAl_2O_4 [20]. Mg^{2+} and Ni^{2+} cations have the same valence and similar effective ionic radii (0.72 and 0.69 Å, respectively, in six-fold coordination [21]), but should not compete for the same coordination sites. Indeed, Mg^{2+} ions are favored in tetrahedral sites while Ni^{2+} ions are favored in octahedral sites. The spinel structure is versatile, however, and Ni^{2+} cations can diffuse in both tetrahedral and octahedral sites, whereas any sub-stoichiometric possible composition $(\text{MgNi})_{1-x}\text{Al}_2\text{O}_{4-x}$ ($x = 0-1$) can be formed.

The combination of high temperatures, disorder in the MgAl_2O_4 crystal structure and presence of NiO leads to the formation of NiAl_2O_4 or a mixed $\text{Mg}_{1-x}\text{Ni}_x\text{Al}_2\text{O}_4$ spinel.

The catalyst stability increases with an increasing Mg content (Figure 4.26). Adjusting the Mg:Al ratio to 1.1:2 slowed down the diffusion rate of nickel ions into the support. NM0.4 deactivated before NM0.7 and both deactivated before NM1.1. Redfern *et al.* pointed out that Mg-deficiency significantly reduces the degree of order in the MgAl_2O_4 spinel [20]. Therefore, stoichiometry appears to be a critical parameter. Moreover, the fact that NM0.4 and NM0.7 deactivated more quickly when the GHSV was increased from 40,000 to 60,000 h^{-1} pointed out that the higher the temperature, the quicker the spinel is formed. Indeed, as the GHSV is increased, the quantities of O_2 and CH_4 at the inlet increased as well, leading to a higher hot spot temperature.

The deactivation of the $\text{Ni/Mg}_x\text{Al}_2\text{O}_{3+x}$ catalyst as described above was confirmed by UV-vis-DRS analysis and visual inspection of the four catalyst bed sections as a function of time on stream. Figure 4.36 presents a scheme of the elucidated deactivation process:

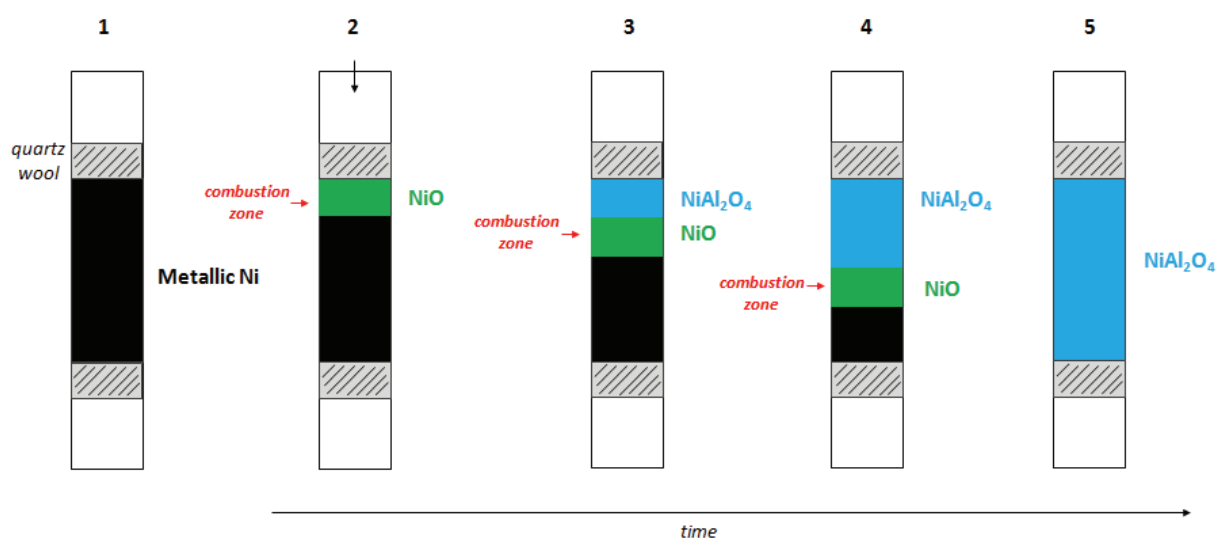


Figure 4.36: Scheme of the deactivation process occurring during ATR of model biogas over $\text{Ni/Mg}_x\text{Al}_2\text{O}_{3+x}$.

1. Before reaction, the nickel is mostly present as metallic nickel after reduction at 800°C
2. The reaction is started, Ni is oxidized at the inlet of the bed. NiO is active for the combustion of methane. Downstream, the nickel is still metallic and perform the reforming of methane
3. At the inlet, the high temperatures reached because of the exothermic combustion lead to a disorder in the crystal structure of the support. Ni²⁺ ions are then able to diffuse into the vacancies, forming the inactive Ni spinel NiAl₂O₄. The combustion zone progresses downwards where NiO is formed again.
4. and 5. The process repeats itself until all the nickel species are present as NiAl₂O₄. The catalyst is deactivated.

During the screening (See Chapter 3), the most stable catalyst for autothermal reforming of biogas was found to be 5-0.05 wt.% Ni-Rh/Mg_{0.7}Al₂O_{3.7}. The promotion of the nickel catalyst by Rh is thus beneficial. Temperature programmed reductions on promoted and non-promoted nickel catalysts proved that Rh facilitated the reduction of Ni strongly interacting with the support (Figure 4.30). Moreover, Rh is a very active combustion catalyst and might also prevent the oxidation of Ni species in this zone. In the presence of Rh₂O₃, Rh³⁺ ions might be able to diffuse into the support to form inactive MgRh₂O₄ or MgAlRhO₄ phases. However, this phenomenon seems unlikely to occur in the combustion zone where Rh is expected to be present as metallic Rh⁰ due to the high temperatures reached [22]. To our knowledge, this spinel formation between Rh₂O₃ and MgAl₂O₄ has not been reported during methane reforming reactions. Ruckenstein *et al.* studied the effect of the nature of the support on the performance of Rh-based catalysts in the partial oxidation of methane to synthesis gas [23]. No spinel compounds were formed on the Rh/Al₂O₃ catalyst. On the Rh/MgO catalyst, the formation of MgRh₂O₄ was observed and the authors suggested that this strong interaction between Rh and magnesium oxides was responsible for the high stability of the catalyst. Therefore, should the formation of MgRh₂O₄ occur during autothermal reforming of model biogas, it would probably not be detrimental to the catalyst activity and stability. The addition of Rh thus helps stabilizing the combustion zone.

Finally, by using a dual-bed system with a rhodium based catalyst for the methane combustion at the reactor inlet, the deactivation of the Ni/Mg_xAl₂O_{3+x} reforming catalyst could be prevented. Rhodium is a stable combustion catalyst that is not inclined to form an inactive spinel phase. All oxygen is converted over the rhodium catalyst and the Ni/Mg_xAl₂O_{3+x} catalyst is therefore no longer exposed to oxygen and will not form NiO and thus no NiAl₂O₄ neither.

4.5. Conclusions

The deactivation of PGM-free nickel supported on magnesium spinel during autothermal reforming of model biogas was investigated. Carbon formation and sintering were ruled out as the main causes. Black metallic nickel underwent changes during the reaction that resulted in the formation of light blue/green nickel species that could correspond to NiAl_2O_4 and NiO species.

Our attempt to reduce and quantify these oxidized nickel species *in-situ* with a series of small hydrogen pulses was unsuccessful. However it evidenced that the nickel species in presence were reducible at high temperatures $> 800^\circ\text{C}$. Such temperatures are typical for nickel strongly interacting with the support or NiAl_2O_4 .

XPS analyses showed that after exposure to air, the surface Ni present on a reduced catalyst is partly re-oxidized and results in a mixture of Ni^0 , NiO and NiAl_2O_4 . In addition, the binding energies in the Ni 2p doublet region are very close and can overlap. Therefore XPS analyses were not suitable for our study.

By measuring the evolution of the temperature profile until deactivation, it was observed that the exothermic combustion zone progressed along the bed. UV-vis-DRS analyses of nickel supported on magnesium spinel at different times of reaction showed the progression of NiAl_2O_4 formation until complete deactivation. The deactivation phenomenon was evidenced: high temperatures reached in the methane combustion zone lead to a disorder in the spinel support structure that will, in the presence of NiO , facilitate the diffusion of Ni^{2+} ions into the supports vacancies, forming the inactive NiAl_2O_4 .

The composition of the spinel support and more specifically the Mg:Al ratio had a great influence on the catalyst resistance to deactivation. Adjusting the Mg:Al ratio to 1.1:2 slowed down the diffusion rate of nickel ions into the support but did not fully prevent it.

Finally, a new reactor design was implemented. A dual-bed catalyst composed by a Rh oxidation catalyst and a Ni reforming catalyst proved to be highly active and resistant to deactivation. The addition of a very small amount of Rh catalyst prevented the formation of spinel on the Ni catalyst downstream. For further investigations, some optimizations could be considered in terms of bed lengths, Rh content and Ni content.

REFERENCES :

1. Salhi, N., Boulahouache, A., Petit, C., Kiennemann, A. & Rabia, C., *International Journal of Hydrogen Energy*, 36, 11433–11439, 2011.
2. Teixeira, A. C. S. C. & Giudici, R., *Chemical Engineering Science*, 54, 3609–3618, 1999.
3. Li, G., Hu, L. & Hill, J. M., *Applied Catalysis A: General*, 301, 16–24, 2006.
4. Boukha, Z. et al., *Applied Catalysis B: Environmental*, 158-159, 190–201, 2014.
5. Payne, B. P., Biesinger, M. C. & McIntyre, N. S., *Journal of Electron Spectroscopy and Related Phenomena*, 175, 55–65, 2009.
6. Davidson, A., Tempere, J. F., Che, M., Roulet, H. & Dufour, G. *Journal of Physical Chemistry*, 100, 4919–4929, 1996.
7. Heracleous, E., Lee, A., Wilson, K. & Lemonidou, A., *Journal of Catalysis*, 231, 159–171, 2005.
8. Grosvenor, A. P., Biesinger, M. C., Smart, R. S. C. & McIntyre, N. S., *Surface Science*, 600, 1771–1779, 2006.
9. Galtayries, A. & Grimblot, J., *Journal of Electron Spectroscopy and Related Phenomena*, 99, 267–275, 1999.
10. Araki, S., Hino, N., Mori, T. & Hikazudani, S., *International Journal of Hydrogen Energy*, 34, 4727–4734, 2009.
11. Yoshida, K. et al., *Applied Catalysis A: General*, 351, 217–225, 2008.
12. Tomishige, K., Kanazawa, S., Suzuki, K. & Asadullah, M., *Applied Catalysis A: General*, 233, 35–44 (2002).
13. Ezugwu, E. O. & Wang, Z. M., *Journal of Materials Processing Technology*, 68, 262–274, 1997.
14. Scheffer, B., Heijeinga, J. J. & Moulijn, J. A., *The journal of Physical Chemistry*, 91, 4752–4759, 1987.
15. López-Fonseca, R., Jiménez-González, C., de Rivas, B. & Gutiérrez-Ortiz, J. I., *Applied Catalysis A: General*, 437-438, 53–62, 2012.
16. Damyanova, S., Pawelec, B., Arishtirova, K. & Fierro, J. L. G., *International Journal of Hydrogen Energy*, 37, 15966–15975, 2012.
17. Meng, F., Chen, G., Wang, Y. & Liu, Y., *International Journal of Hydrogen Energy*, 35, 8182–8190, 2010.
18. Tong, G. C. M., Flynn, J. & Leclerc, C. A., *Catalysis Letters*, 102, 131–137, 2005.
19. Nguyen, B. N. T. & Leclerc, C. A., *Journal of Power Sources*, 163, 623–629, 2007.
20. Redfern, S. A. T., Harrison, R. J., O'Neill, H. S. C. & Wood, D. R. R., *American Mineralogist*, 84, 299–310, 1999.
21. Shannon, R. D., *Acta Crystallographica A*, 32, 751–767, 1976.
22. Jacob K.T., Prusty D., Kale G.M., *Journal of Alloys and Compounds*, 513, 365-372, 2012.
23. Ruckenstein E. & Wang H.Y., *Journal of Catalysis*, 187, 151-159, 1999.

Chapter 5

Kinetic modelling of autothermal biogas reforming over NiRh catalyst supported on SiSiC foams

A screening of catalysts for the ATR reaction led to the selection of a NiRh/MgAl₂O₄ catalyst, which showed a stable performance over more than 200 hours. SiSiC foams were manufactured and coated with a NiRh/MgAl₂O₄ washcoat by partners involved in the European project BioRobur. These foams were to be used in the final demonstration plant. SiSiC foams are promising catalyst supports for small size ATR units. They have excellent thermal characteristics and low pressure drops, permitting a very compact reformer. An optimal reformer design requires information on the kinetics of the reaction. A kinetic model of the biogas ATR reaction is thus highly desirable.

In this chapter, SiSiC foams are described. The structured catalysts were characterized and tested. Operating parameters such as temperature, gas hourly space velocity as well as steam/CH₄, CO₂/CH₄ and O₂/CH₄ ratios were varied. Finally, a kinetic model was developed for the ATR of model biogas.

5.1. SiSiC foams as catalyst supports for autothermal reforming of biogas

5.1.1. SiSiC foams

Foams, sometimes also referred to as sponges, are cellular materials made of interconnected struts. It results in irregular structures presenting high external surface area and high porosities. It makes them attractive as catalyst supports since they present a lower pressure drop than traditional beds made of packed catalyst pellets.

They can be made of materials presenting high thermal conductivity which will enhance axial and radial heat transfer. Foams are thus expected to minimize hotspots and prevent mechanical-strength and thermal-shock limitations [1]. It is a critical factor for our reaction which presents both highly exothermic and endothermic reactions.

In order to implement an adequate kinetic model, the structure and properties of the foams must be described. In our case, silicon-infiltrated silicon carbide (SiSiC) foams were manufactured and designed by BioRobur partners SUPSI and Erbicol SA. These materials present high oxidation-resistance. Figure 5.1 presents a photograph of the SiSiC foam. The geometry of such cellular materials is complex. It can be characterized by their high porosity (85%), by the average pore and cell diameters (d_p and d_c) and by the strut thickness.

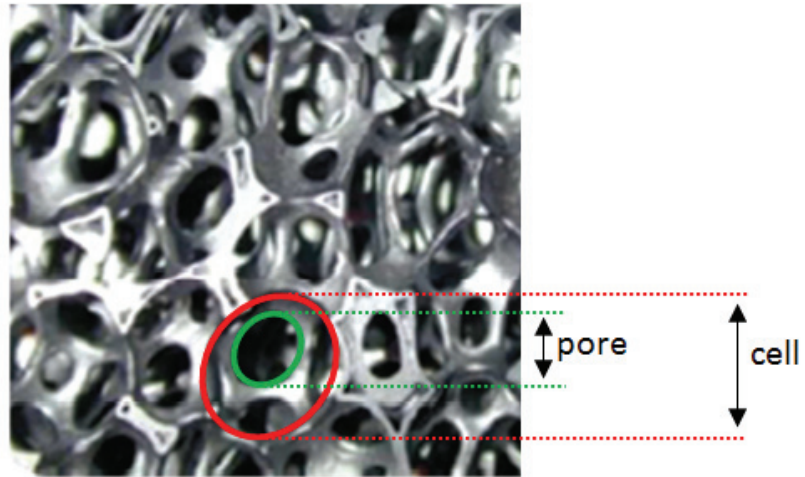


Figure 5.1: SiSiC foams with indication of cell and pore

The description of the heat dispersion on such materials during ATR reaction is also essential. Heat transfer properties of different metallic foams were investigated by Bianchi *et al.* by 2-Dimensional model analysis of heat transfer experiments in a tubular reactor configuration [1][2]. Effective radial and axial thermal conductivities and the wall heat transfer coefficient were estimated.

Radial conductivity was shown to depend on intrinsic conductivity of the material. The porosity was also an important parameter. The effective conductivity decreases with increasing porosity. However, for a given porosity, the pore size had no impact on the conductivity of the foam.

Axial conductivity is usually not considered during heat transfer studies when using low conductivity material. Bianchi *et al.* suggested that such simplification was not valid with high conductivity materials such as SiC foams [1].

Moreover, the heat transfer coefficient at the wall turns out to be an important factor in controlling heat transfer in the case of materials with high effective thermal conductivities. The wall heat transfer coefficient increases with increasing cell density and thus an inverse dependency of the wall coefficient on the foam cell size. No clear dependency on the material conductivity and density was observed. The wall coefficient increased with increasing temperature and increasing gas flow rate [2].

Table 5.1 lists the geometrical and thermal properties of the foams.

Table 5.1: Properties and characteristics of the SiSiC foams

Density	2.8 g/cm ³
Pores per inch (PPI)	10
Cellular porosity	85 vol.%
Pore diameter (dp)	3 mm
Cell diameter (dc)	6 mm
Strut porosity	0 vol.%
Strut thickness	1.5 mm
Maximum temperature (air and inert)	1,400°C
Thermal conductivity at 500°C	60 W/m K
Thermal conductivity at 1000°C	42 W/m K

5.1.2. Characterizations of the coated SiSiC foams

The foams were coated with NiRh/MgAl₂O₄ by BioRobur partner MET, following a procedure described in Chapter 2. Figure 5.2 presents a photograph of the foam after coating and before reaction. Two different sizes of foams were provided (2.5 cm diameter; 2.5 or 1.4 cm heights) and thus tests were performed with a wide range of GHSV on “half” or “entire” foams.

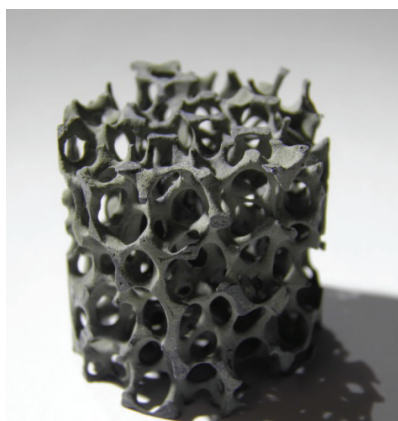


Figure 5.2: Photograph of an entire foam as provided by partners: SiSiC foam coated with a NiRh/MgAl₂O₄ catalyst

The morphology of the fresh coated foam was studied by Scanning Electron Microscopy (SEM) (Figure 5.3)

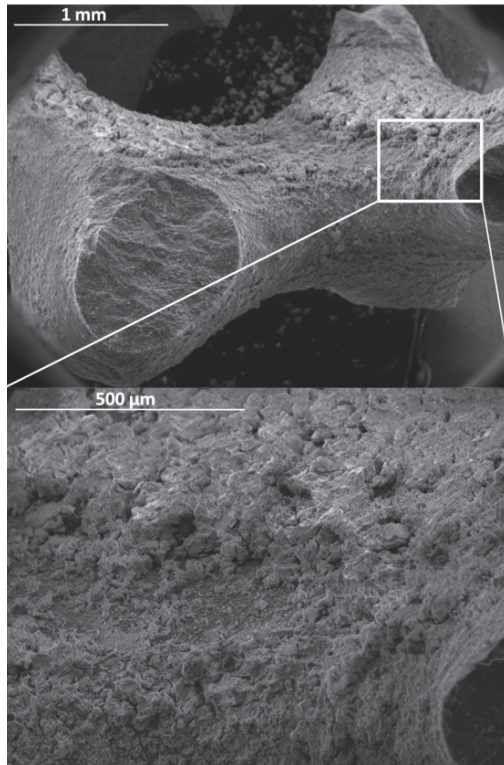


Figure 5.3: SEM Images of foam coated with NiRh/MgAl₂O₄ washcoat

The washcoat was generally well deposited on the SiSiC foams, although in some regions, as shown in Figure 5.3, the homogeneity of the washcoat seemed to be quite limited as the thickness appeared to vary. In average, the thickness of the washcoat was 80 μm.

ICP analyses were performed on the 3 different samples of the NiRh/MgAl₂O₄ washcoat detached from the foam: one from a half-size foam and two from entire foams. Table 5.2 presents the composition in wt.% of Ni, Rh, Mg and Al.

Table 5.2: Washcoat composition (wt.%) of Ni, Rh, Mg and Al.

	Nominal	ICP1 (half-foam)	ICP2 (entire foam)	ICP3 (entire foam)
Ni (wt.%)	15	17.0	11.0	9.5
Rh (wt.%)	0.05	0.4	0.3	0.3
Mg (wt.%)	14.5	5.2	6.6	5.1
Al (wt.%)	32.2	33.0	31.0	28.6

The nickel loading on the half-size samples was 17 wt.%, which is slightly higher than the nominal value of 15 wt.%. On the two different entire foams, it was 11 and 9.5 wt.%, which is lower than the nominal value. The rhodium loading was 9 times higher on half-size foams and 6 times higher on entire foams than the nominal value. Finally, the Mg/Al molar ratios were 0.18, 0.26, 0.20 and therefore all lower than the nominal value of 0.5.

This results in compositions of *ca.* 17-0.4 wt.% NiRh/Mg_{0.4}Al₂O_{3.4} for half foams and an average composition of 10.3-0.3 wt.% NiRh/Mg_{0.5}Al₂O_{3.5} for entire foams. In Chapter 3, the Mg/Al molar ratio has been shown to be a critical parameter for the catalyst stability. A Mg/Al molar ratio of *ca.* 0.2 can lead to stability issues related to the formation of inactive spinel aluminate. However, the Rh loading being higher than 0.05 wt.% will be beneficial for both stability and activity.

5.2. Autothermal reforming of model biogas over nickel catalyst supported on SiSiC foams

5.2.1. Activity and stability of the coated SiSiC foams

Prior to the kinetic study, preliminary experiments were carried out to ensure that the coated foams were active and stable for the ATR of model biogas. These tests were performed on a set-up that was designed to reach higher flows (up to 3,000 mL min⁻¹).

The coated foams were reduced *in-situ* at 700 °C in a mixture of H₂-Ar (4:1; vol:vol). Considering the amount of Rh deposited, 700 °C should be high enough to activate the catalyst. It should be noted that the GHSV has been calculated using the apparent volume of the foam (including empty spaces).

ATR of biogas was first performed over an entire foam at 700 °C at standard conditions (Steam/CH₄ = 3, O₂/CH₄ = 0.5, CH₄:CO₂ =60:40). A thermocouple was placed in the middle of the foam. The oven set-point was adjusted so that the temperature measured by thermocouple was 700 °C. The experiment was started at a GHSV of 3,500 h⁻¹. After 24 hours, the GHSV was then increased to 5,000 h⁻¹ for 2 hours and 7,000 h⁻¹ for 2 additional hours. Figure 5.4 presents the methane and oxygen conversions as well as the outlet H₂/CO molar ratios.

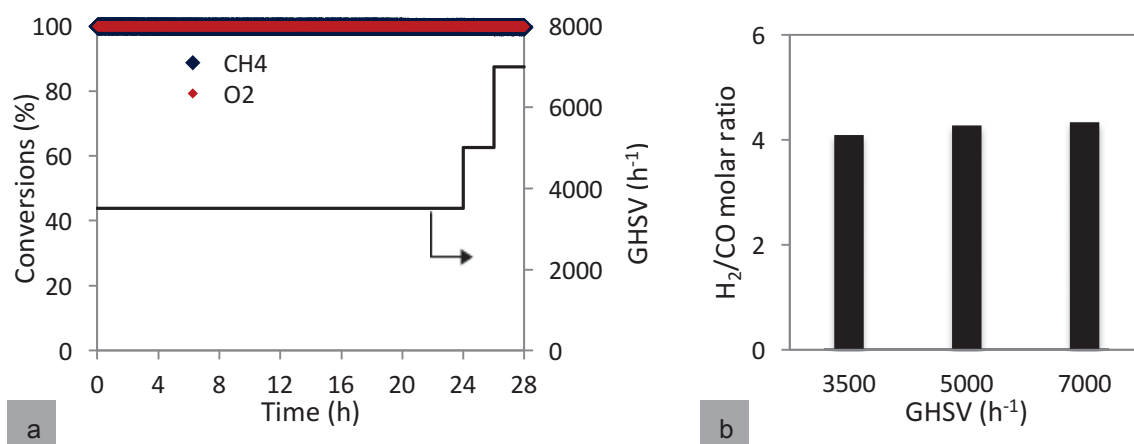


Figure 5.4: a) CH₄ and O₂ conversions and b) H₂/CO molar ratio during ATR of model biogas over SiSiC foam coated with NiRh/MgAl₂O₄ catalyst. Reaction conditions T = 700°C, Steam/CH₄ = 3, O₂/CH₄ = 0.5, CO₂:CH₄ = 40:60, GHSV ranging from 3,500 to 7,000 h⁻¹

At all times and any GHSV, the oxygen and methane conversions were complete. The H₂/CO molar ratio was 4 at all GHSV's. It should be noted that a SiSiC foam coated only with magnesium spinel support (no active metal) was tested under similar conditions and showed no activity. This shows that the foam and support alone is inactive. After this 28 hours test, the foam displayed a black color. The nickel appears to be still reduced. No trace of inactive blue NiAl₂O₄ could be observed at the inlet (Figure 5.5).



Figure 5.5: Photograph of a SiSiC foam coated with NiRh/MgAl₂O₄ catalyst after ATR of model biogas

The coated foam proved to be active for the ATR of model biogas at 700°C and showed no sign of deactivation.

5.2.2. Temperature profile

In chapter 4, the temperature profile was measured during ATR of model biogas on a catalytic bed made of powders. We have seen that there is a temperature gradient over the catalytic bed. When the

catalyst is stable, the highest temperature is found at the inlet section of the bed due to the exothermic combustion of methane. At the outlet section, the temperature is lower due to the endothermic reforming reaction of methane.

The temperature profile is an important parameter for our kinetic model. A temperature profile was measured on a foam during ATR reaction under standard conditions (Steam/CH₄ = 3, O₂/CH₄ = 0.5, CH₄:CO₂ =60:40) at a GHSV of 15,000 h⁻¹ and with an oven set-point of 725°C. Figure 5.6 shows that the highest temperature measured reached *ca.* 800 °C at the very inlet of the foam. It also points out that the temperature in the gas phase starts to increase slightly before the foam.

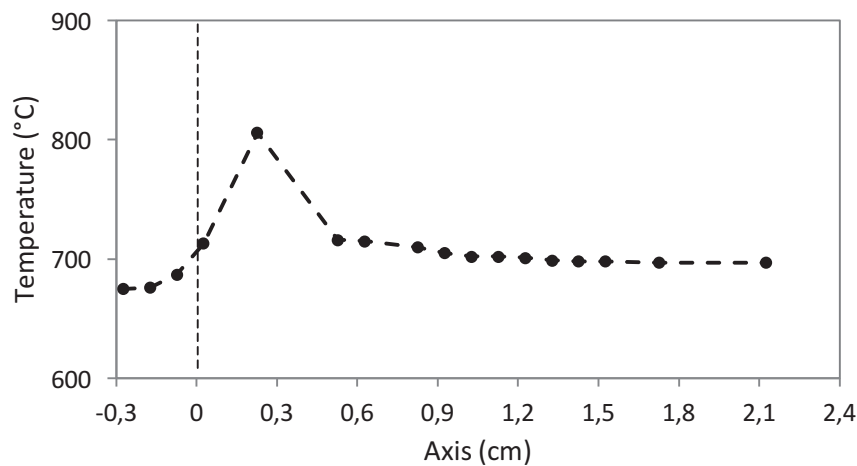


Figure 5.6: Temperature profile in the foam coated with NiRh/MgAl₂O₄ during ATR of model biogas in standard conditions at T = 700°C (Steam/CH₄ = 3, O₂/CH₄ = 0.5, CO₂:CH₄ = 40:60) GHSV = 15,000 h⁻¹

The temperature profile depends on the inlet gas composition. However, measuring the temperature profile precisely at any given time and reaction conditions is a difficult task. Indeed, the foams were designed with a complex geometry to favour a good radial mixing of the flow while presenting low pressure drops. It was thus difficult to introduce and slide thermocouples along an axis to measure multiple profiles under different conditions. Instead, the effect of GHSV on the temperature was studied by placing thermocouples at 5 different points in the foams. Figure 5.7 shows the effect of GHSV on the temperature profile during ATR reaction in standard conditions (Steam/CH₄ = 3, O₂/CH₄ = 0.5, CH₄:CO₂ =60:40) with an oven set-point of 725°C.

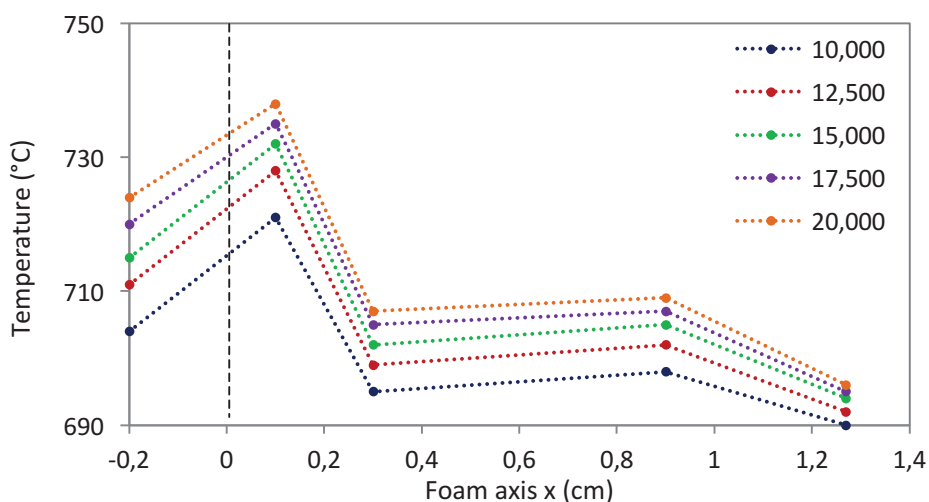


Figure 5.7: Effect of GHSV (h^{-1}) on temperature at five different places in the foam during ATR of model biogas (oven set-point 725°C) at standard conditions (Steam/ $\text{CH}_4 = 3$, $\text{O}_2/\text{CH}_4 = 0.5$, $\text{CO}_2:\text{CH}_4 = 40:60$)

As the GHSV increases, the temperature increases in the foam at all points. The maximum temperature is probably reached between 0 and 0.1 cm but could not be measured precisely. There is a 10 to 20°C difference in the temperature in the foam when the GHSV is doubled from 10,000 to 20,000 h^{-1} . However, the temperature difference at the outlet ($x = 1.3$ cm) appears to be much less important.

5.3. Kinetic model

To obtain reaction kinetics relevant to the BioRobur ATR demonstration unit, kinetic experiments were carried out over the coated SiSiC foams.

Several kinetic models for methane reforming have been published in the literature but only a few models exist for methane ATR [3], [4].

The operating conditions are listed in Table 5.3. The molar ratios of steam/ CH_4 , CO_2/CH_4 , O_2/CH_4 were varied as well as the temperature and the GHSV. To assess the catalyst stability, the coated foams were tested under standard conditions before each tests performed under different conditions. The temperatures used were lower than 700°C and high GHSV were used in order to reach conversions lower than 90%. Indeed, the higher the temperature, the closer the outlet mixture is to the thermodynamic equilibrium composition. When studying reaction kinetics, it is preferable to examine the effects of operational parameters far from the equilibrium conversion.

Table 5.3: Operating conditions

	Range	Standard
Steam/CH ₄	1.5 – 3	3
O ₂ /CH ₄	0.1-0.5	0.5
CO ₂ /CH ₄	0.15-0.64	0.64
Temperature	525 - 700	700°C
GHSV	10,000 – 27,500	15,000

A total of 98 data were collected. The performance of the model was tested by using three objectives functions: the methane conversion, the outlet temperature and the H₂/CO ratio at the reactor exit.

5.3.1. Influence of temperature, CO₂/CH₄ and Steam/CH₄ ratio on methane conversions and H₂/CO ratio

Observing the effect of the space time on the objectives functions is interesting when studying the kinetics of a reaction. However, in our case, when the GHSV or when the space time W/F_{CH_4} were varied, it led to important variations of the temperature profile. Therefore, instead of studying the effect of the variation of one parameter on the conversion, we were actually observing the effect of the variation of two parameters.

The interpretation was thus less straightforward and could be misleading. Instead, the effects of the inlet CO₂/CH₄ and Steam/CH₄ molar ratios on the catalyst performances at a fixed W/F_{CH_4} space time (0.7 kg_{cat} s mol⁻¹), fixed GHSV (15,000 h⁻¹) and at a fixed O₂/CH₄ ratio (0.5) for two inlet temperatures (650 and 700°C) are shown in Figure 5.8.

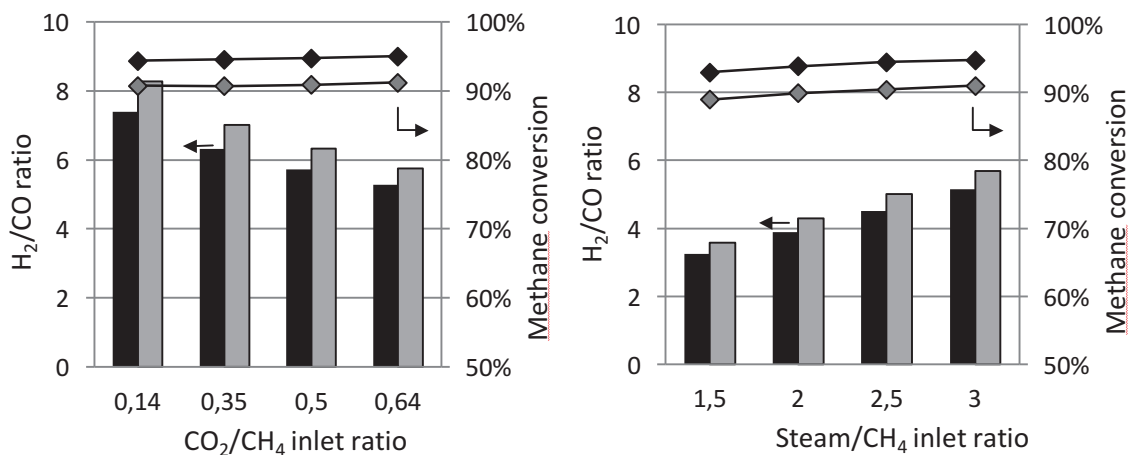


Figure 5.8: Methane conversion at 700°C (◆) and 650°C (◊) as well as H₂/CO ratio at 700°C (■) and 650°C (▒) as a function of (a) the CO₂/CH₄ ratio (Steam/CH₄ fixed at 3) and (b) the Steam/CH₄ ratio (CO₂/CH₄ fixed at 0.64) during the ATR reforming of biogas with O₂/CH₄ = 0.5 (GHSV = 15000 h⁻¹)

Oxygen was fully converted at all temperatures and conditions. Methane conversions increased with temperature. The highest methane conversions were reached at 700°C but remained < 95%. From the thermodynamics of the reaction (see Chapter 1, Figure 1.7), full oxygen and methane conversions could be expected at 650 and 700°C.

High H₂/CO ratios and high methane conversions were observed even at severe GHSV conditions. H₂/CO ratio was higher at 650 °C than at 700 °C, which can be explained by the thermodynamics of the WGS shift reaction. H₂ production from CO and H₂O is favoured at low temperatures (see Chapter 1, Figure 1.4).

At 650 and 700°C, the CO₂/CH₄ ratio had no effect on methane conversion, but the H₂/CO ratio decreased with the CO₂/CH₄ ratio. When the Steam/CH₄ ratio increased, higher methane conversions were reached. H₂/CO ratios increased as well. Indeed, the water gas shift reaction is greatly influenced by the inlet partial pressures of CO₂ and H₂O.

When comparing the H₂/CO molar ratios in Figure 5.4 and Figure 5.8, it seemed that the molar ratio increased with the GHSV. However, it is actually an indirect consequence of the decreasing of the outlet temperature. Indeed, during these two sets of tests, the oven set-point was adjusted so that the temperature at the middle of the foam remained 700°C. When the GHSV was higher, the maximum temperature was higher (see Figure 5.7) and the mid-point temperature was higher. Therefore, at higher GHSV, the oven set point was lower than at lower GHSV. It was *ca.* 650°C at 15,000 and 20,000 h⁻¹ whereas it was generally higher than 750°C for GHSV lower than 10,000. Therefore, the H₂/CO ratio varied with the outlet temperature rather than with the GHSV. This showed that the H₂/CO ratio was greatly influenced by the WGS reaction. The higher the oven set-point, the higher the outlet temperature and thus the lower the H₂/CO ratio.

5.3.2. One-dimensional model assumptions

Experiments for kinetic modelling are ideally performed in the absence of temperature and concentration gradients. The presence of gradients can a priori be taken into account in a reactor model, but will induce uncertainties as the transport phenomena are for the most part described by empirical correlations that have limited validity. In this case, however, it was not possible to reduce the size of the foam, especially the diameter, to avoid temperature gradients in the reactor. Therefore the temperature profile over the catalyst bed was calculated by integrating the heat balance and by using an effective bed conductivity. By using the usual criteria for the identification of transport limitations (see Chapter 2, 2.5) it was further found that internal concentration gradients were present in the

washcoat. Initially these gradients were accounted for in the model by taking into account the mass and heat balance over the washcoat explicitly, but it was found that these gradients were under certain conditions too important leading to excessively long computation times or even instabilities. Therefore, as carried out in numerous kinetic studies on reforming and ATR in the literature ([3], [5]) an effectiveness factor was calculated and the corresponding rates were corrected for the catalyst efficiency.

The major assumptions in the model are listed below:

1. One dimension (axial profiles only)
2. Pore diffusion limitations taken into account by effectiveness factors
3. Plug flow conditions with negligible radial gradients (no axial dispersion, flat radial velocity and concentration profile)
4. Pseudo-homogeneous conditions with no temperature and concentration gradients around or inside the catalyst particles and thus no distinction between fluid and solid phase
5. Ideal gas law applies
6. Wall temperature is constant
7. Steady-state (no changes as a function of time, e.g. catalyst deactivation)
8. Six reactive species (CH₄, CO₂, H₂O, O₂, CO and H₂) and one inert gas (Ar) involved

5.3.3. Reactions

ATR of model biogas can involve many reactions. Table 5.4 presents the main possible reactions.

Table 5.4: Possible reactions in model biogas autothermal reforming

N°		Reactions
1	Steam Reforming	$\text{CH}_4 + \text{H}_2\text{O} \rightleftharpoons \text{CO} + 3\text{H}_2$
2	Water Gas Shift	$\text{H}_2\text{O} + \text{CO} \rightleftharpoons \text{CO}_2 + \text{H}_2$
3	Steam Reforming	$\text{CH}_4 + 2\text{H}_2\text{O} \rightleftharpoons \text{CO}_2 + 4\text{H}_2$
4	Total Combustion	$\text{CH}_4 + 2\text{O}_2 \rightleftharpoons \text{CO}_2 + 2\text{H}_2\text{O}$
5	Partial Oxidation	$\text{CH}_4 + 1/2 \text{O}_2 \rightleftharpoons \text{CO} + 2\text{H}_2$
6	Partial Combustion	$\text{CH}_4 + \text{O}_2 \rightleftharpoons \text{CO}_2 + 2\text{H}_2$
7	Dry Reforming	$\text{CH}_4 + \text{CO}_2 \rightleftharpoons 2\text{CO} + 2\text{H}_2$
8	Dry Reforming	$\text{CH}_4 + 3\text{CO}_2 \rightleftharpoons 4\text{CO} + 2\text{H}_2\text{O}$
9	Boudouard	$2\text{CO} \rightleftharpoons \text{C(s)} + \text{CO}_2$
10	Methane pyrolysis	$\text{CH}_4 \rightleftharpoons \text{C(s)} + 2\text{H}_2$
11	Reverse gasification	$\text{CO} + \text{H}_2 \rightleftharpoons \text{C(s)} + \text{H}_2\text{O}$

A few studies exist in the literature for the kinetics of methane steam reforming. Notably, Xu & Froment studied the kinetics of methane steam reforming over Ni supported on MgAl₂O₄ [6]. Hou & Hugues performed a similar study over Ni/α-Al₂O₃ [7]. After comparison between the thermodynamics and experimental results, both studies proposed that the steam reforming process could be described using only the first three reactions of Table 5.4: two reactions of steam reforming and the water gas shift.

The steam reforming studies were obviously performed in absence of O₂. Combustion kinetics need to be considered to describe the ATR reaction kinetics. Trimm & Lam studied the kinetics of methane combustion on Pt/Al₂O₃ and proposed a well-accepted model [8].

During the ATR test on foams coated with NiRh/MgAl₂O₄, we have observed that methane conversion increases with steam/CH₄ ratio indicating that steam reforming is one of the prevailing reactions (Figure 5.8). The WGS reaction seems to influence the H₂/CO ratio depending on the partial pressures of steam and CO₂ as well as the outlet temperature. Combustion is also one of the prevailing reactions as it occurs faster than the others. Reaction network analysis has shown that only four reactions have to be taken into account to describe the overall kinetics: methane steam reforming reactions, water gas shift and methane combustion [3]. The rates of partial oxidation, dry reforming and reactions leading to carbon formation such as the Boudouard reaction were too low to be considered [7]. Therefore, to simplify the model, only 4 reactions were considered:

- Reaction 1 - Steam reforming: $\text{CH}_4 + \text{H}_2\text{O} \rightleftharpoons \text{CO} + 3\text{H}_2$
- Reaction 2 - Water Gas Shift: $\text{H}_2\text{O} + \text{CO} \rightleftharpoons \text{CO}_2 + \text{H}_2$
- Reaction 3 - Steam reforming: $\text{CH}_4 + 2\text{H}_2\text{O} \rightleftharpoons \text{CO}_2 + 4\text{H}_2$
- Reaction 4 - Total Combustion: $\text{CH}_4 + 2\text{O}_2 \rightleftharpoons \text{CO}_2 + 2\text{H}_2\text{O}$

As mentioned before, Xu & Froment proposed that the first three reactions should be considered for the steam reforming of methane. They led to 21 possible sets of equations. After model discrimination, they chose one mechanism (described in Chapter 1) which relies on the adsorption of methane and the adsorption of steam and its dissociation. H₂O dissociates to H₂ and adsorbed O [9].

Hou and Hugues proposed a mechanism which relies on the adsorption of steam and methane and their dissociations. Methane dissociates to CH₂ and H₂ or adsorbed H while H₂O dissociates to H₂ and adsorbed O [7].

Regarding the combustion, the kinetic mechanism proposed by Trimm & Lam is based on the reaction between adsorbed CH₄ with surface oxygen adsorbed monoatomically and diatomically on two different sites [8].

Therefore, two models were used and tested to describe the ATR reaction kinetics over coated SiSiC foams:

- **Model (A):** combination of the steam reforming kinetics taken from Hou & Hughes and combustion kinetics from Trimm & Lam.
- **Model (B):** combination of the steam reforming kinetics taken from Xu & Froment and combustion kinetics from Trimm & Lam.

Model (B) is actually inspired by the work by Halabi *et al.* who studied the autothermal reforming of methane over a Ni-based catalyst [3].

The reaction rates r_1 , r_2 , r_3 and r_4 for reactions 1, 2, 3 and 4 (respectively) for these 2 models are listed below:

- **Model A:**

$$\left. \begin{aligned} r_1 &= \frac{\frac{k_1}{p_{H_2}^{1.25}} (p_{CH_4} p_{H_2O}^{0.5} - \frac{p_{CO} p_{H_2}^3}{K_{p1} p_{H_2O}^{0.5}})}{\Omega^2} \\ r_2 &= \frac{\frac{k_2}{p_{H_2}^{0.5}} (p_{CO} p_{H_2O}^{0.5} - \frac{p_{CO_2} p_{H_2}}{K_{p2} p_{H_2O}^{0.5}})}{\Omega^2} \\ r_3 &= \frac{\frac{k_3}{p_{H_2}^{1.75}} (p_{CH_4} p_{H_2O} - \frac{p_{CO} p_{H_2}^4}{K_{p3} p_{H_2O}})}{\Omega^2} \end{aligned} \right\} \text{From Hou \& Hughes}$$

$$\text{where } \Omega = 1 + K_{CO} p_{CO} + K_H p_H^{0.5} + K_{H_2O} (p_{H_2O}/p_{H_2})$$

$$r_4 = \frac{k_{4a} p_{CH_4} p_{O_2}}{(1 + K_{CH_4}^C p_{CH_4} + K_{O_2}^C p_{O_2})^2} + \frac{k_{4b} p_{CH_4} p_{O_2}}{(1 + K_{CH_4}^C p_{CH_4} + K_{O_2}^C p_{O_2})}$$

- **Model B:**

$$\left. \begin{aligned} r_1 &= \frac{\frac{k_1}{p_{H_2}^{2.5}} (p_{CH_4} p_{H_2O} - \frac{p_{CO} p_{H_2}^3}{K_{p1}})}{\Omega^2} \\ r_2 &= \frac{\frac{k_2}{p_{H_2}} (p_{CO} p_{H_2O} - \frac{p_{CO_2} p_{H_2}}{K_{p2}})}{\Omega^2} \\ r_3 &= \frac{\frac{k_3}{p_{H_2}^{3.5}} (p_{CH_4} p_{H_2O}^2 - \frac{p_{CO} p_{H_2}^4}{K_{p3}})}{\Omega^2} \end{aligned} \right\} \text{From Xu \& Froment}$$

$$\text{where } \Omega = 1 + K_{CO} p_{CO} + K_{H_2} p_{H_2} + K_{CH_4} p_{CH_4} + K_{H_2O} (p_{H_2O}/p_{H_2})$$

$$r_4 = \frac{k_{4a} p_{CH_4} p_{O_2}}{(1 + K_{CH_4}^C p_{CH_4} + K_{O_2}^C p_{O_2})^2} + \frac{k_{4b} p_{CH_4} p_{O_2}}{(1 + K_{CH_4}^C p_{CH_4} + K_{O_2}^C p_{O_2})}$$

In both models, reactions 1, 2 and 3 are assumed to take place on the same active sites (metallic nickel). Therefore, rates equation r_1 , r_2 and r_3 have the same denominator Ω . Reaction 4 does not take place on metallic nickel but rather on NiO and therefore the denominator is different.

The rate of consumption or formation of a species is determined by summing up the reaction rates of the reactions where it intervenes. Effectiveness factors η_j (of each Reaction j), are taken into account.

$$r_{CH_4} = -\eta_1 R_1 - \eta_3 R_3 - \eta_4 R_4$$

$$r_{O_2} = -2 \eta_4 R_4$$

$$r_{CO_2} = \eta_2 R_2 + \eta_3 R_3 + \eta_4 R_4$$

$$r_{H_2O} = -\eta_1 R_1 - \eta_2 R_2 - 2 \eta_3 R_3 + 2 \eta_4 R_4$$

$$r_{H_2} = 3 \eta_1 R_1 + \eta_2 R_2 + 4 \eta_3 R_3$$

$$r_{CO} = \eta_1 R_1 - \eta_2 R_2$$

where the effectiveness factors η_j were calculated at any point of the reactor and

$$\eta_j = \frac{\tanh \phi}{\phi} .$$

The Thiele modulus, ϕ , describes internal diffusion limitations (see Chapter 2, 2.5). It was calculated considering first-order reactions.

5.3.4. Mass, energy and momentum balance equations

The mass and energy balance equations are set up over a small amount of catalyst and are written in the differential form. The momentum equation is not taken into account as the pressure drop induced by the foam is very small and can be neglected.

The continuity equation used for the fluid phase for each component j :

$$\frac{dF_j}{dW} = R_j \quad [\text{mol/s/kg}_{\text{cat}}] \quad (\text{Eq. 5.1})$$

where F_j : molar flow of component j [mol/s] and component j stands for all gas phase components, e.g. CH_4 , O_2 , H_2O , CO_2 , etc.

W : the catalyst mass [kg].

R_j : reaction rate of component j [mol/s/kg_{cat}].

$$R_j = \sum_{i=1}^{n_r} \alpha_{ij} r_i \quad [\text{mol/s/kg}_{\text{cat}}] \quad (\text{Eq. 5.2})$$

α_{ij} : stoichiometric coefficient of component j in reaction i.

The heat balance equation is expressed as:

$$\frac{dT}{dW} = \frac{-\frac{4U}{\rho_s d_t} (T - T_{\text{wall}}) + \sum_{i=1}^{n_r} (-\Delta H_{R_i}) r_i}{C_p F_t} \quad [\text{K/kg}_{\text{cat}}] \quad (\text{Eq. 5.3})$$

where T: temperature in the radial center of the reactor at each axial position [K].

U: overall heat transfer coefficient [J/m²/s/K].

ρ_s : bulk density of the solid phase [kg/m³].

d_t : internal tube diameter [m].

T_{wall} : wall temperature [K].

ΔH_{R_i} : Heat of reaction i [J/mol].

r_i : reaction i [mol/s/kg_{cat}].

n_r : total number of reactions.

ρ_g : density of the gas phase [kg/m³].

C_p : Heat capacity of the fluid phase [J/mol/K].

F_t : Total molar flow [mol/s].

U is given by:

$$\frac{1}{U} = \frac{1}{\alpha_i} + \frac{d_t}{\lambda_w} \frac{A_b}{A_m} + \frac{1}{\alpha_u} \frac{A_b}{A_u} \quad (\text{Eq. 5.4})$$

where α_i : heat transfer coefficient on the bed side [J/m²/s/K].

α_u : heat transfer coefficient, heat transfer medium side [J/m²/s/K].

A_b : heat exchanging surface, bed side [m²].

λ_w : heat conductivity of the wall [J/m/s/K].

A_u : heat exchanging surface, heat transfer medium side [m²].

A_m : log mean of A_b and A_u [m²].

Then by using an equivalent one-dimensional model, α_i is given by Froment & Bischoff [10]:

$$\frac{1}{\alpha_i} = \frac{1}{\alpha_w} + \frac{d_t}{8\lambda_{eff}} \quad (\text{Eq. 5.5})$$

where α_w : heat transfer coefficient at the wall [J/m²/s/K].

λ_{er} : effective thermal conductivity in the radial direction [J/m/s/K].

These last two coefficients, α_i and λ_{er} , are calculated according to the effective transport concept (see Froment & Bischoff [10]) using the equations given by Yagi & Kunii [11] and Kunii & Smith [12].

The thermal conductivity of the SiSiC foam was expressed as a function of the temperature as:

$$\lambda_{foam} = 3749.4T^{-0.62} \text{ W m}^{-1}\text{K}^{-1} \quad (20^\circ - 1500^\circ\text{C}) \quad (\text{Eq. 5.6})$$

To calculate the effective thermal conductivity a correlation proposed by Bianchi *et al.* [1] was used:

$$\lambda_{eff} = \frac{1-\varepsilon_b}{3}\lambda_{foam} + 0.06Re_KPr\lambda_{mix} + \frac{16\sigma T^3}{3\beta} \quad (\text{Eq. 5.7})$$

The expression for the effective thermal conductivity consists of three terms. The first term corresponds to the contribution of the pure thermal conductivity (stagnant conductivity) and is the most important term. The second term corresponds to the dispersive conductivity and is important for foams with low intrinsic thermal conductivity. The third term corresponds to the radiative conductivity and will be important at high temperatures. More details as well as the values for the constants in Eq. 5.7 are given in Bianchi *et al.* [1].

The wall heat transfer coefficient was calculated by a correlation given by Bianchi *et al.* [2]:

$$\alpha_w = \frac{\lambda_{mix}}{d_c} (7.18 + 0.029Re_{dc}^{0.8}); \quad 4 < Re_{dc} < 255 \quad (\text{Eq. 5.8})$$

where d_c is the cell diameter.

Other values of different variables used in estimating the transport properties are listed in Table 5.5.

Table 5.5: Variables taken into account for the estimation of the transport properties

α_u	1000 W m ⁻² K ⁻¹
λ_w (quartz)	2.0 W m ⁻¹ K ⁻¹
h_{ext}	1000 W m ⁻² K ⁻¹
$L_{washcoat}$	80 microns
$\rho_{washcoat}$	3500 kg m ⁻³
$\epsilon_{washcoat}$	0.4
BET _{washcoat}	100 m ² g ⁻¹
r_{pore}	7.6 nm
$D_{eff}(CH_4) @ 700^\circ C$	7.1 10 ⁻⁷ m ² s ⁻¹
$D_{eff}(O_2) @ 700^\circ C$	2.0 10 ⁻⁶ m ² s ⁻¹

The 7 species involved and the heat balance equation will lead to 8 differential equations that are integrated simultaneously. The integration is performed by an ODE (Ordinary Differential Equations) integrator from ODEPACK [13]. At each integration step the physical properties are updated, as well as the transport correlations and efficiency factors. All this is implemented in a FORTRAN code.

5.3.5. Results

The models A (Hou & Hugues + Trimm & Lam) and B (Xu & Froment + Trimm & Lam) were compared to the experimental data.

Initial simulations showed that the rate of methane combustion was too low, resulting in a very flat temperature profile for both models. In fact both models were developed for specific Ni-based catalysts and do not contain a parameter accounting for the number of active sites for the oxidation and the reforming/shift reactions. To make the model more general and allow to describe the data over different Ni catalysts two parameters, one for the number of oxidation sites and one for the number of reforming and water-gas shift were introduced. The model was then optimized by regression analysis of the experimental data and the number of active sites as two adjustable parameters.

After optimization, the sums of squares were respectively 0.17 and 0.14 for model A & B.

The temperature profiles were estimated with both models. Figure 5.9 presents a comparison between the two estimated profiles and the temperature profile measured experimentally at Steam/CH₄ = 3, O₂/CH₄ = 0.5, CO₂:CH₄ = 40:60, and GHSV = 15,000 h⁻¹.

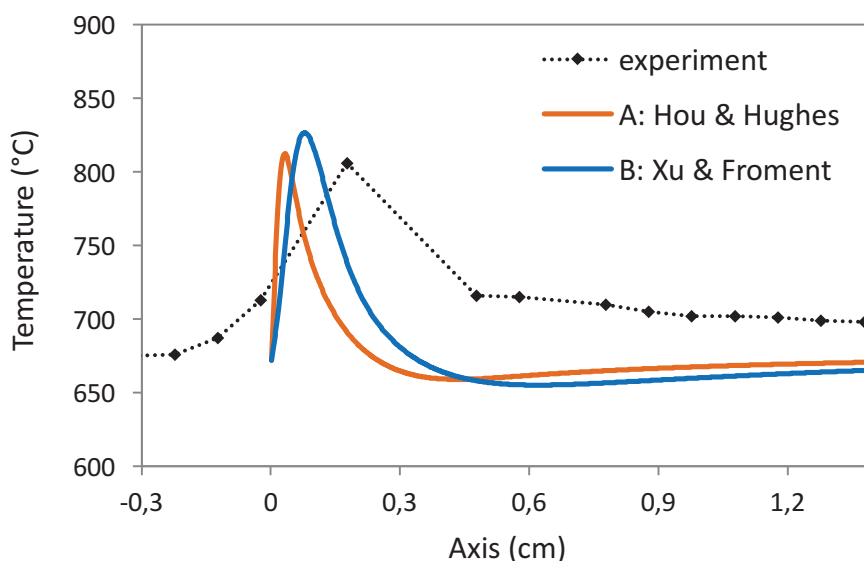


Figure 5.9: Temperature profile over foam axis during ATR of model biogas in standard conditions (Steam/CH₄ = 3, O₂/CH₄ = 0.5, CO₂:CH₄ = 60:40)

The highest temperature measured experimentally was 800°C. The corresponding estimated values are both slightly higher: 812 °C with model A and 827°C with model B. The rate of the oxidation reaction is very fast. The temperature peak is observed at the very inlet of the foam inlet ($x < 1$ mm). This explains the difficulty faced when measuring the temperature experimentally in such conditions. Unfortunately, at the position where the model predicts the hot spot, no thermocouple was located and thus the calculated temperature profile cannot be validated completely experimentally. The model predicts a rather strong temperature gradient over the SiSiC foam, which consists of SiSiC, which has a rather good thermal conductivity. The high porosity of this type of material, however, lowers the effective heat transfer characteristics.

The hotspot peaks estimated with models A & B are both narrower than the experimental measurement. This might be caused by the exclusion of the axial dispersion of heat in the model, which would lead to a broader peak.

For both models, the number of oxidation sites was *ca.* 500 times higher than the original model. However, the number of reforming sites was 100,000 times higher in model A but only 8 times higher in model B than the original equations.

The higher activity of our catalysts might be attributed to either the higher concentration of Ni surface sites (the amount and dispersion of the nickel catalysts in references Xu & Froment and Trimm & Lam are not given) but also due to the presence of rhodium in our sample. Noble-metals are known to be more active than nickel both for oxidation and reforming [14], [15].

Given these first observations, the model B seemed more appropriate to describe our reaction.

The pre-exponential factors, the activation energies and adsorption enthalpies are listed in Table 5.6 for the four rate equations of model B. Note that these constants were not adjusted to fit the experimental data.

Table 5.6: Reaction equilibrium constants and Arrhenius kinetic parameters of model B:

Equilibrium constant	parameter value	
K _{P1}	$\exp(-26830/T + 30.114) \text{ bar}^2$	
K _{P2}	$\exp(4400/T - 4.036)$	
K _{P3}	$K_{P1} * K_{P2} \text{ bar}^2$	
Rate constants	pre-exponential factor	activation energy (kJ/mol)
k ₁	$1.17 \cdot 10^{15} \text{ bar}^{0.5}$	240.1
k ₂	$5.43 \cdot 10^5 \text{ bar}^{-1}$	67.1
k ₃	$2.83 \cdot 10^{14} \text{ bar}^{0.5}$	243.9
k _{4a}	$8.11 \cdot 10^5 \text{ bar}^{-2}$	86.0
k _{4b}	$6.82 \cdot 10^5 \text{ bar}^{-2}$	86.0
Van 't Hoff equilibrium constants	pre-exponential factor	heat of adsorption (kJ/mol)
K _{CO}	$6.65 \cdot 10^{-4}$	- 38.3
K _{H2}	$8.23 \cdot 10^{-5}$	- 70.7
K _{CH4}	$6.12 \cdot 10^{-9}$	-82.9
K _{H2O}	$1.77 \cdot 10^5 \text{ bar}$	88.7
K ^C _{CH4}	$1.26 \cdot 10^{-1}$	-27.3
K ^C _{O2}	$7.78 \cdot 10^{-7}$	-92.8

A parity plot presents the comparison between the predicted values and the measured values of methane conversion in Figure 5.10.

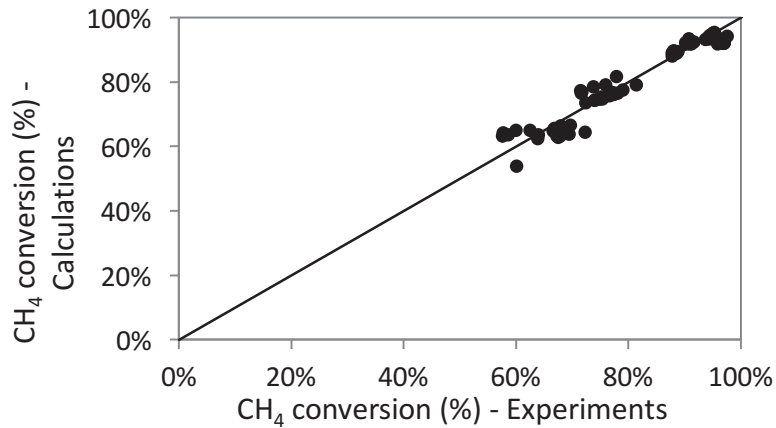


Figure 5.10: Parity plot comparing methane conversions estimated and measured experimentally

The estimations are in good agreement with the experiments. The calculation of the residuals ($X_{CH_4_calculated} - X_{CH_4_experiment}$) showed that the model faced limitations at low space time W/F_{CH_4} .

Figure 5.11 shows the comparison between the measured and estimated values of H_2/CO molar ratio and the outlet temperature for the 98 data collected. The data are separated into two sections: the first part (from data n°1 to 52) were carried out at high GHSV and low temperature resulting in methane conversions $< 80\%$. The second part of the tests (starting from data n°52 to 98) were carried out at lower GHSV and higher temperatures resulting in methane conversions $> 80\%$. In both cases, the estimations were in good agreement with the measured values. The outlet temperature is very well estimated, resulting also in a good estimation of the H_2/CO molar ratio.

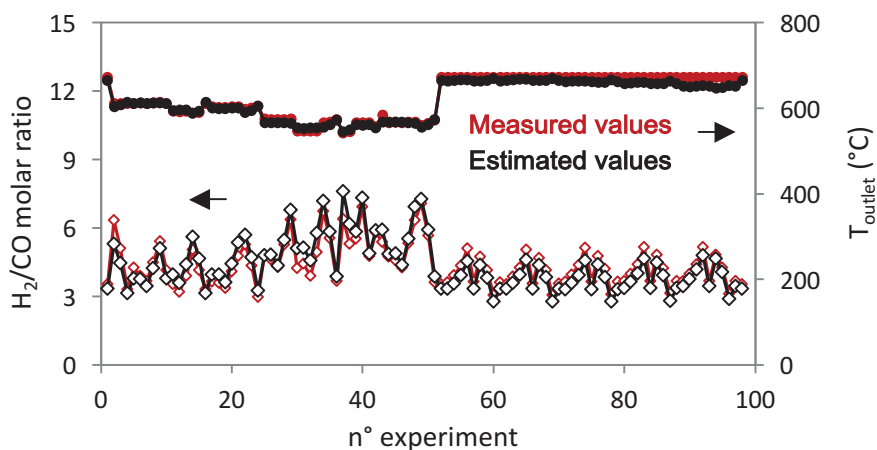


Figure 5.11: Comparison between the measured and estimated values of H_2/CO molar ratio and outlet temperature for the 98 data collected.

5.3.6 Discussion

The composition profiles of the gas species are presented in Figure 5.12.

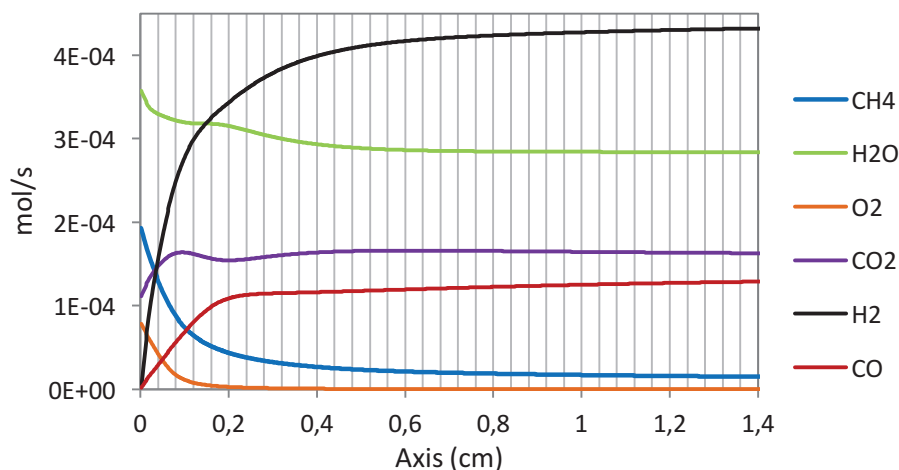


Figure 5.12: Composition profile over foam axis during ATR of model biogas in standard conditions (Steam/CH₄ = 3, O₂/CH₄ = 0.5, CO₂:CH₄ = 60:40)

Oxygen is fully consumed to burn a fraction of methane in the first millimetres of the coated foam, resulting in the production of CO₂ and H₂O. The reforming also starts at the inlet, consuming part of the steam and methane and producing H₂ and CO. The composition profile shows that the main reactions occur in the first 3-4 millimetres of the structured catalyst. The rest of the catalyst is mostly performing the water gas shift reaction. From 6 mm onwards the concentration profiles are no longer changing showing that the two reforming and WGS reaction are at equilibrium.

Given the composition profile presented in Figure 5.12, it appears that both the oxidation and the steam reforming reactions occur at the inlet. O₂ and H₂ are both present in the first millimetres. This is due to the fact that in the model B, adapted from Halabi *et al.*, the oxidation and reforming sites are not in competition. The model takes into account two different active sites that are physically homogeneously distributed in the catalytic reactor: one for the oxidation reaction, the other for the water gas shift and reforming reactions [3].

However, in Chapter 4, we have shown that during the autothermal reforming reaction, the catalyst bed is actually separated into two zones with two different active sites. The first zone at the inlet is composed of NiO. NiO is active for the combustion of methane but inactive for the reforming reactions. The second zone is mostly composed by metallic Ni over which the reforming reactions and water-gas shift take place.

In order to improve the model, the competition between the oxidation and reforming reactions should be included.

One solution would be to modify the equation of the oxidation reaction rate and have a common denominator with the reforming reactions so that there is a competition for the active sites. At the inlet, for instance, this would result in an oxygen coverage close to 1 on the surface of the catalyst, preventing the reforming reactions to occur in this zone. As the oxygen coverage would decrease downstream, the methane reforming could take place.

Another option would be to separate the reactor into two different zones: the first zone for the combustion reaction at the inlet, the second for the steam reforming reaction which would start when 90% of the oxygen is consumed by combustion. The model was thus adapted to describe this system. The composition profiles of the gas species are presented in Figure 5.13.

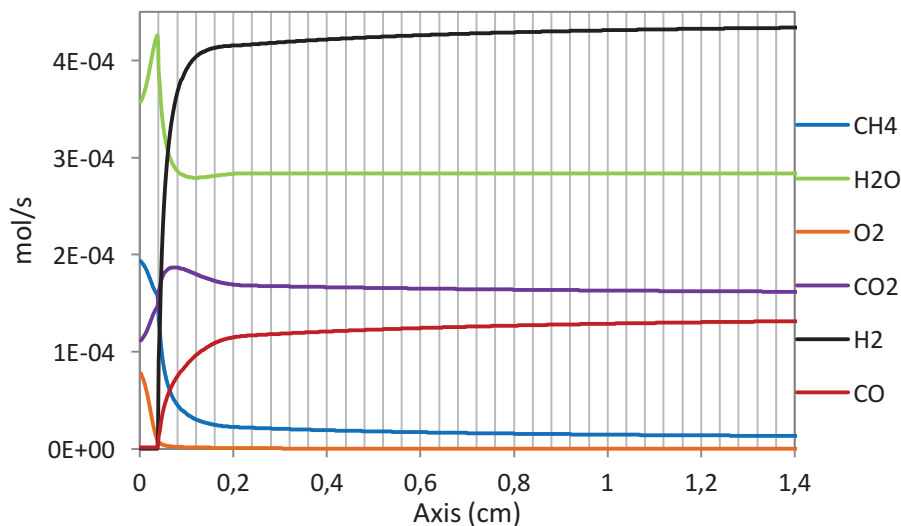


Figure 5.13: Composition profile over foam axis during ATR of model biogas in standard conditions (Steam/CH₄ = 3, O₂/CH₄ = 0.5, CO₂:CH₄ = 60:40)

Combustion occurs in the first 0.05 cm resulting in the production of H₂O and CO₂. When 90% of the oxygen is consumed, steam reforming occurs, consuming part of the steam and part of the methane and producing CO and H₂. The composition profile is more consistent with the observations in the previous chapters while the conversion and H₂/CO ratio at the reactor outlet are still adequately described by this model.

Figure 5.14 presents the resulting temperature profile.

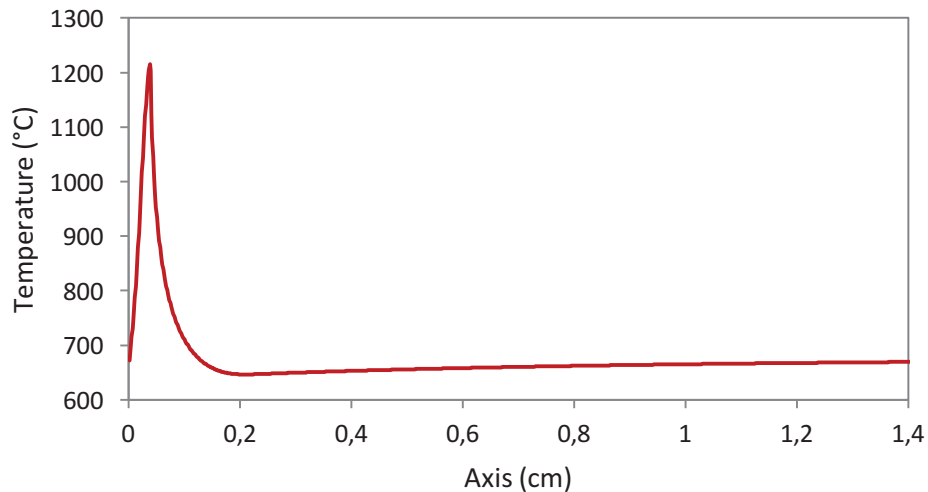


Figure 5.14: Estimation of the temperature profile over foam axis during ATR of model biogas in standard conditions (Steam/CH₄ = 3, O₂/CH₄ = 0.5, CO₂:CH₄ = 60:40)

The hotspot is much higher and narrower than before, reaching more than 1,200°C compared to 800°C measured experimentally. It is possible that the highest temperature in the reactor is higher than the measured 800°C but it is hardly plausible that it would reach 1,200°C given the high thermal conductivity of the SiSiC materials. However, the model does not take into account the axial dispersion of heat. Therefore, by separating the two zones, the heat transfer cannot be well accounted for.

In order to improve the model, a reactor model that takes the axial heat conduction explicitly into account should be developed.

5.4. Deactivation profile over Ni/Mg_xAl₂O_{3+x} catalyst powders

In Chapters 3 and 4, we have observed that the methane conversion profiles during ATR of model biogas over unstable catalysts were singular: the methane conversion is total during the first hours of reaction but after some time a sudden decrease to zero occurs. In Chapter 4, the deactivation process was identified and related to the formation of spinel NiAl₂O₄.

To get further insight into the deactivation profile, the methane conversion as a function of time was simulated for a fixed bed reactor including heat transfer using the kinetics for the ATR reaction as given by the model B detailed in part 5.3. A further assumption was a linear decrease of the number of sites as function of time, progressively from the inlet of the reactor towards the outlet, as suggested in Chapter 4. Figure 5.15 shows a comparison between the simulated and experimental methane conversion as a function of the time on stream.

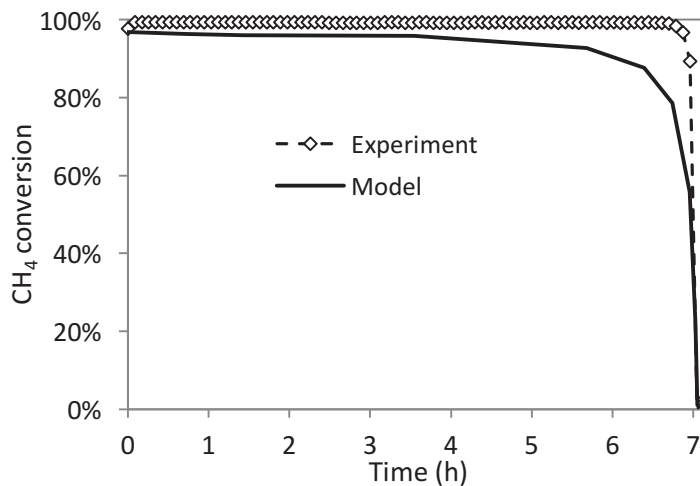


Figure 5.15: Comparison between the experimental methane conversion over 5 wt.% Ni/Mg_{0.4}Al₂O_{3.4} (presented in Figure 4.32) and the simulated conversion.

The model is able to predict the sudden decrease in the methane conversion. The simulations showed that indeed, a hot spot moves through the bed as observed experimentally (Figure 4.17) and that the reaction kinetics are consistent with the deactivation process proposed in Chapter 4.

5.5. Conclusions

SiSiC foams, previously coated with a NiRh/Mg_{0.4}Al₂O_{3.4} catalyst, were provided by the European project partners. The coated foams were tested for the autothermal reforming of model biogas under standard conditions during 28 hours. Methane and oxygen were fully converted over this time on stream. Post-reaction characterizations revealed no evidence of NiAl₂O₄ formation. The coated foams thereby showed good activity and stability for the ATR reaction of model biogas at 700°C.

Two models were tested for the ATR reaction over coated SiSiC foams. They were both based on a combination of oxidation kinetics and steam reforming kinetics. Both model involved the oxidation kinetics originally proposed by Trimm and Lam [8], but with parameters adapted for Ni catalysts. However, for the steam reforming kinetics, one model was based on the mechanism given by Hou & Hughes [7] and the second model on that by Xu & Froment [6].

The second model was in better agreement with the experiments. However, the accuracy of the estimations was found to be limited due to the reaction conditions. Indeed, the temperature profile is a critical and a key parameter but it is also difficult to measure it and to model it with good accuracy. It is determined by the gas inlet temperature, by the inlet Steam/CH₄ and O₂/CH₄ ratios and by the heat

transfer properties of the foam/reactor configuration. Catalyst bed temperature is critical for different reasons. The temperature will influence the presence and the nature of carbon on nickel particles (see Chapter 1). We have also demonstrated in Chapter 4 that temperature was a critical parameter in the formation of nickel aluminate phase and thus influences the stability of the catalyst. But more importantly, the temperature governs the thermodynamics and kinetics of the reaction and notably the methane and oxygen conversions. Moreover, the outlet H_2/CO molar ratio depends on the WGS reaction equilibrium, which is governed by the catalyst outlet temperature. Therefore, the differences between the model and the experiments are likely to be related to the difficulty to estimate complex temperature profiles and to measure the real catalyst temperature.

The second model was also used to get further insight into the deactivation profile observed on powders in the previous chapters. The model was able to predict the sudden decrease in the methane conversion, proving the consistency of the described deactivation process and the reaction kinetics.

This chapter showed that it is impossible to attain conditions where the intrinsic kinetics of the methane ATR can be studied. Even by using a highly thermally conductive foam with a thin catalyst washcoat resulted in strong temperature and concentration gradients. Consequently these gradients have to be taken into account into the reactor model. Verification of the calculated hotspot temperatures and the experimental ones has been complicated due to the restricted amount of thermocouples that can be located inside the foam. The temperature measurement can be improved by using an annular reactor configuration and using a highly thermally conductive support [16]. This approach will not eliminate pore diffusion limitations inside the washcoat, however. Then, of course, these kinetics need to be incorporated into a reactor model based on the catalytic foam.

REFERENCES:

1. Bianchi, E. et al., *Chemical Engineering Journal*, 198-199, 512–528, 2012.
2. Bianchi, E. et al., *Catalysis Today*, 216, 121–134, 2013.
3. Halabi, M., Decroon, M., Vanderschaaf, J., Cobden, P. & Schouten, J., *Chemical Engineering Journal*, 137, 568–578, 2008.
4. Hoang, D. L. & Chan, S. H., *Applied Catalysis A: General*, 268, 207–216, 2004.
5. De Groote, A. M. & Froment, G. F., *Applied Catalysis A: General*, 138, 245–264, 1996.
6. Xu, J. & Froment, G. F., *American Institute of Chemical Engineers Journal*, 35, 88–96, 1989.
7. Hou, K. & Hughes, R., *Chemical Engineering Journal*, 82, 311–328, 2001.
8. Trimm, D. L. & Lam, C. W., *Chemical Engineering Science*, 36, 1405–1413, 1980.
9. Rostrup-Nielsen, J. R., *Catalysis*, 5, 1–117, 1984.
10. Froment, G. F. & Bischoff, K. B., *Chemical Reactor Analysis and Design*, Wiley & Sons, New York, 1990.
11. Yagi, S. & Kunii, D., *American Institute of Chemical Engineers Journal*, 3, 373–381, 1957.
12. Kunii, D. & Smith. *American Institute of Chemical Engineers Journal*, 6, 71–78, 1960.
13. Hindmarsh, A. C., ODEPACK, A systematized collection of ODE solvers, *Elsevier*, 1983.
14. Jones, G. et al., *Journal of Catalysis*, 259, 147–160, 2008.
15. Firth, J. G. & Holland, H. B., *Transactions of the Faraday Society*, 65, 1121–1127, 1969.
16. Beretta, A., Groppi, G., Majocchi, L. & Forzatti, P., *Applied Catalysis A: General*, 187, 49–60, 1999.

General conclusions & Perspectives

General conclusions

Hydrogen is perceived to be a major energy carrier in the future. Nowadays, it is mainly produced from fossil fuels and notably by the reforming of natural gas. The industrial process is well established. However, as the demand for hydrogen increases, finding renewable sources for the production of hydrogen presents great interests. Biogas is a renewable resource composed primarily of methane and carbon dioxide. It is obtained from the anaerobic digestion of organic matter. Biogas can be reformed into a hydrogen-rich syngas.

The objectives of this Ph.D. work were associated with those of the European project "BioRobur". The project involved both academic and industrial partners. It sought to develop a robust and efficient biogas reformer for the production of hydrogen with applications in the production of electricity from fuel-cells. The first objective of this work was thus to select a stable and active catalyst for the autothermal reforming of biogas. The second objective was to provide a kinetic model to optimize the process for the demonstration plant.

The reaction was carried out at 700°C and atmospheric pressure with a model biogas composed by 60% methane and 40% carbon dioxide. Oxygen and steam were supplied as well. Oxygen was added to the feed in order to provide the heat necessary for the steam and/or dry reforming reactions to take place.

First and foremost, a screening of various nickel based catalysts was carried out using a six-parallel flow reactor. Using this technology, six catalysts could be tested simultaneously under the same feed composition and the same conditions of temperature and pressure. It enabled to save time for time-consuming long-term stability tests. Twelve nickel catalysts presenting different supports were tested. Most of the catalysts deactivated before 20 hours. The best PGM-free catalyst with 5 wt.% Ni loading was found to be 5 wt.% Ni/LaAlO₃ and deactivated after 16 hours. On the other hand, 5-0.05 wt. Ni-Rh/Mg_{0.7}Al₂O_{3.7} still fully converted methane after 200 hours. It was thus identified as an active and very stable catalyst for the ATR of model biogas.

Its PGM-free equivalent, 5 wt.% Ni/Mg_{0.7}Al₂O_{3.7} deactivated after only two hours. Complete methane conversion is observed over a certain period of time followed by a very rapid drop of the methane conversion to zero. This deactivation profile is singular compared with profiles reported for coking or sintering of the catalysts. While deactivation during steam reforming, dry reforming or partial oxidation of methane over Ni-based catalyst has been well investigated over the years, few deactivation studies have been carried out on autothermal reforming of methane and even less of biogas. The second part of our study dealt with the identification and understanding of the deactivation process.

In the literature, the most common causes of deactivation of Ni catalysts during hydrocarbon reforming are carbon formation, sintering of nickel particles, poisoning, nickel oxidation and spinel formation. In our case, no evidence of whisker carbon or encapsulating carbon was found on the deactivated catalyst. No poisoning occurred since model biogas was studied and no sintering of metallic particles could be observed. However, the catalyst color turned from black before reaction to light blue after reaction. This indicated a change in the nature of the nickel species from metallic nickel to possible NiO or NiAl₂O₄. Different approaches were considered in order to identify and quantify the nickel species in presence after deactivation. The deactivation process was finally investigated by measuring the temperature profile during reaction and performing complementary UV-vis-DRS analyses. The hot-spot, related to the combustion reaction happening at the inlet of the catalytic bed, was found to move through the bed from the inlet at the beginning of the reaction, towards the outlet until complete deactivation. Moreover, UV-vis-DRS analyses showed that inactive Ni spinel NiAl₂O₄ was formed during reaction.

Given these observations, the deactivation process was evidenced: After activation and reduction, most of the nickel is present as metallic nickel. After a short period of time, the inlet section is partly turned into NiO due to the presence of O₂ in the feed while the remaining of the bed is still reduced nickel. NiO is able to perform the combustion of methane while the reduced nickel downstream can perform the reforming reaction. However, the high temperatures reached at the inlet zone create a disorder in the crystal structure of the support and Ni²⁺ ions are able to diffuse into its vacancies, forming inactive Ni spinel. Progressively, from the inlet towards the reactor outlet the reduced nickel phased turned into inactive NiAl₂O₄. Eventually, the catalyst becomes entirely inactive.

The stability of the bimetallic NiRh catalyst observed in the first chapter was thus likely related to the stabilization of the combustion zone by Rh, a catalyst very active for both combustion and reforming of methane. Deactivation was prevented. Another strategy implemented to prevent deactivation was to use a dual bed catalyst with a Rh catalyst used as a combustion catalyst on top of a Ni catalyst used as a reforming catalyst. Rh is very stable and does not react with alumina to form an inactive spinel phase. All oxygen and part of the methane are converted over the rhodium catalyst. The reforming reaction occurs downstream on the Ni/MgAl₂O₄ catalyst which is now no longer exposed to oxygen or high temperatures. The formation of NiO or NiAl₂O₄ was not observed on the Ni catalyst after reaction, proving its resistance to deactivation.

Finally, the last part of our study focused on modelling the autothermal reforming reaction over SiSiC foams coated with NiRh/MgAl₂O₄ catalyst. In the scope of the BioRobur project, autothermal reforming of biogas is performed on structured catalysts at the pilot plant. SiSiC foams were chosen as supports

since they present high thermal conductivity, low pressure drop and are resistant to high temperatures. Kinetic information is required for the design and optimization of the process at such scale. The coated foams were active and very stable in ATR reaction conditions.

Two kinetic models inspired by literature studies were compared with the experiments. They combined the kinetics of the oxidation reaction described by Trimm & Lam with the kinetics of the steam reforming reaction taken from Hou & Hughes for the first model, and from Xu & Froment for the second. The second combination provided a better description of the experimental values. The differences and limitations of the model are likely related to the complexity of the temperature profile in the foam due to presence of the hotspot. The temperature profile depends on many parameters such as the inlet temperature, inlet gas composition and thermal conductivity properties of the foam. It will partly determine the catalyst performances. In spite of these limitations, the model was in good agreement with the experiments. It was also able to predict the sudden decrease in the methane conversion observed over unstable catalysts, proving the consistency of the described deactivation process and the reaction kinetics.

Perspectives

The six-parallel flow reactor has proven to be a convenient tool for the ageing studies of catalysts and the screening of different compositions under similar conditions. The technology could also be applied to other purposes. The variation of the catalyst mass in each reactor would allow studying a wide range of conversions in one single experiment. The presence of mass transfer limitations could also be investigated. One could for instance imagine preparing reactors with different particle sizes to rapidly verify the effect of intra-particle limitations.

Moreover, without the presence of steam, it could be easier to control the distribution of flows in the reactors by adding individual mass flow controllers upstream to each reactor. This would result in better accuracy. In this configuration, flow rates could also be different in each reactor. The effect of the gas flow rate at constant space-time could then be studied and would give insight about the effect of extra-particle limitation.

Regarding the choice of catalyst formulation, Ni is usually preferred for industrial steam reforming process because of its low price compared to noble metals. However, we have seen that activation and deactivation of Ni-based catalysts are critical parameters. High reduction temperatures must be reached in oxygen-free conditions during activation. This should be taken into account during the design of the process and more especially for the choice of high-temperature resistant materials. Noble metals are more expensive but activation can be carried out at lower temperature ($< 700^{\circ}\text{C}$). This would be beneficial to the process design at higher scale.

The dual bed composed by a small amount of Rh and a Ni catalyst appears to be a good compromise. However, optimizations could be carried out in order to use the smallest amount of noble metal and thus find the optimal relative bed length of the rhodium and nickel. Heat transfer properties could also be investigated in order to make sure that the heat generated in the Rh catalyst is well convected to the Ni catalyst downstream with the lowest heat loss. High heat losses would be detrimental to the methane reforming reactions and thus to the performances of the system.

This study focused on model biogas. It would be interesting to study the effect of traces compounds such as hydrogen sulfide, chlorine or limonene. Even though these compounds are, for the most part, removed from biogas after the purification step, they can still be present in small concentrations.

Finally, improvements of the kinetic model could be achieved if the strong temperature and concentration gradients could be evaluated thoroughly. Other techniques such as IR thermography could be used for the determination of the temperature profile inside the reactor. Another solution

would be to implement an annular reactor configuration using a highly thermally conductive support. A better description of the temperature profile would improve the kinetic model.

In conclusion, the objectives of this Ph.D. work have been achieved. A NiRh catalyst supported on magnesium spinel was active and stable for the autothermal reforming of model biogas at 700°C in the presence of steam and oxygen and at atmospheric pressure. A kinetic model was adapted from the literature to describe the reaction over a structured catalyst made of SiSiC foams coated with NiRh/MgAl₂O₄. This catalyst has been successfully tested in a pilot reactor on a SiSiC foam (26 cm diameter; 25 cm height) at a GHSV of 10,000 h⁻¹ at TUBAF in Germany.

Annex



Cite this: DOI: 10.1039/c5cy00702j

Received 13th May 2015,
Accepted 21st June 2015

DOI: 10.1039/c5cy00702j

www.rsc.org/catalysis

High-throughput assessment of catalyst stability during autothermal reforming of model biogas

M. Luneau, Y. Schuurman, F. C. Meunier, C. Mirodatos and N. Guilhaume*

The long-term stability of Ni-based catalysts for autothermal reforming of model biogas has been assessed in a six parallel-flow reactor set-up implemented to test simultaneously six different catalysts at 700 °C under a feed consisting of 42% H₂O, 14% CH₄, 9% CO₂, and 7% O₂ in argon. The reproducibility of catalyst performance measured in the 6 parallel reactors was ascertained using a commercial Ni-based catalyst. A screening of 12 catalyst formulations identified 5–0.05 wt% Ni–Rh/MgAl₂O₄ as a robust catalyst for autothermal reforming of model biogas over 200 h time-on-stream.

Introduction

Biogas is a complex gas mixture produced from the anaerobic digestion of biomass, which contains methane and carbon dioxide as main components.¹ Biogas can be combusted directly, although exhibiting a lower heating value than natural gas. Biogas can also be reformed into hydrogen, which is a base feedstock for the chemical industry and can also be used as a fuel in fuel-cells to produce electricity.²

Since biogas essentially contains methane and carbon dioxide, the dry reforming (DR) of methane (eqn (1)) is an obvious pathway to produce syngas:



Yet, this reaction is strongly endothermic and must be conducted at high temperatures (800–900 °C), whereas the CH₄/CO₂ ratio in biogas (generally closer to 1.5 than to 1) is not suitable for complete methane conversion. Methane can also be converted into syngas by steam reforming (SR, eqn (2)):



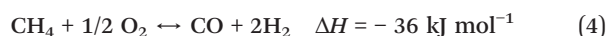
SR is also an endothermic reaction but yields more hydrogen than DR. SR limits carbon deposition and steam is generally introduced in excess in order to shift the water-gas shift equilibrium (eqn (3)) towards more H₂ and less CO production at the reactor outlet.

Water-gas shift (WGS):



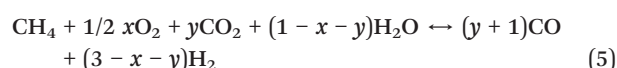
Partial oxidation is a slightly exothermic reaction, actually the result of two consecutive reactions: first the highly exothermic combustion of methane at the beginning of the catalyst bed, followed by steam and CO₂ reforming of the remaining methane and the WGS reaction.

Catalytic partial oxidation (CPO):



Autothermal reforming (ATR) is seen as a practical option to minimize energy supply to the reactor. ATR consists of adding oxygen (or air), which results in combustion of a portion of methane into carbon dioxide and water followed by reforming and WGS reactions.

The general equation for ATR is:



in which the O₂/CH₄ ratio has to be adjusted to reach the thermal balance between exothermic and endothermic reactions. According to thermodynamic calculations (HSC chemistry software), formation of CO and H₂ by steam and dry reforming is favored at temperatures above *ca.* 630 °C.

Catalytic reforming of methane has been widely studied and carried out using different catalysts. Few studies have focused on biogas. The most commonly used catalysts are nickel- and noble metal-based catalysts (Ru, Rh, Pd, Ir, and Pt).^{3,4} Nickel-based catalysts are often used because those combine low cost and acceptable catalytic activity. The main issues with nickel are the deactivation caused by deposition of carbon and/or sintering of metal particles.^{5,6} Noble metals, notably Pt and Ir, are more active than Ni.⁷ Noble metals present better performance since they are less prone to oxidation, coking and sintering,⁸ but are more expensive and hence not the preferred option. Furthermore, the nature of

Université Lyon 1, Institut de Recherches sur la Catalyse et l'Environnement de Lyon IRCELYON, UMR5256 CNRS, 2 avenue Albert Einstein, F-69626, Villeurbanne Cedex, France. E-mail: Nolgen.Guilhaume@ircelyon.univ-lyon1.fr; Tel: +33 472 445 389

the catalyst supports and metal–support interaction may play a significant role in the catalytic activity. Alumina is widely used as a support. However, the nickel spinel phase (NiAl_2O_4) can be formed at high temperature during the reforming reaction. NiAl_2O_4 is inactive and its formation leads to a faster deactivation.^{9,10} Therefore, supports have been designed in order to prevent coking and oxidation. Incorporation of basic alkali-earth metals such as Mg and Ca into Al_2O_3 -based catalysts has been carried out in order to improve both stability and activity.^{11–13} Other supports exhibiting oxygen mobility properties were studied in order to promote the gasification of deposited carbon.^{14–16}

Biogas composition varies depending on the origin of the biomass. Although mainly composed of methane and carbon dioxide, biogas also typically contains sulphur compounds.¹⁷ The presence of H_2S is a major problem due to its irreversible poisoning effect on metals.¹⁸ Biogas can also contain volatile organic compounds such as chlorinated compounds. Methyl chloride was shown to impact on the H_2/CO ratio by increasing the surface acidity of the alumina support.¹⁹ Model biogas composed of clean methane and carbon dioxide (60:40 vol:vol) was used in our study.

Many catalysts have been tested for methane or biogas reforming with different combinations of active metals on various supports.²⁰ However, these tests were performed under different conditions of temperature and pressure with different feed ratios, flow rates and reactor designs, making a fair comparison difficult.

High-throughput catalyst testing has become a widely accepted tool in catalyst development. However, it is mainly used in the screening and discovery of new catalyst formulations,^{21,22} less commonly to characterize specific catalyst properties²³ or long-term performance. On the other hand, this technology is hardly reported for the study of long-term catalyst stability. This is rather surprising as an obvious gain in time can be obtained for these kinds of tests, compared to testing each sample separately.

In the present study, long-term catalyst stability was assessed using a six parallel-flow reactor set-up, specially implemented to test simultaneously six catalysts under essentially identical flow rate, temperature and feed composition. Four types of supports were investigated: spinels, mixed oxides, perovskites and hydrotalcite-type precursors. The supports were impregnated with nickel and tested under similar conditions.

Experimental

Catalyst preparation

Magnesium spinel (MgAl_2O_4) was prepared by co-precipitation. An aqueous solution containing Mg and Al nitrates (Sigma-Aldrich and Fluka) with an Al:Mg molar ratio of 2:1 (concentrations of 0.66 and 0.33 mol L^{-1} , respectively) was added drop by drop into an aqueous solution of ammonium carbonate (Sigma-Aldrich) under vigorous stirring. The ammonium carbonate solution was prepared in order to

contain large excess of carbonates, ensuring precipitation of all the metallic cations. The precipitate was aged for 3 h at room temperature. After centrifugation and washing with de-ionized water, the powder was dried overnight at 120 °C. The dry deposit was then calcined at 800 °C for 5 h in air.

The same procedure was applied to synthesize ZnAl_2O_4 spinel, using nitrates of Al and Zn (Sigma-Aldrich) with an Al:Zn molar ratio of 2:1.

LaAlO_3 was prepared by a modified sol-gel method (Pechini). Ethylenediaminetetraacetic acid (EDTA, Sigma-Aldrich) was added to an aqueous solution containing the metal nitrates (concentration of 0.5 mol L^{-1} , Sigma-Aldrich) with a La:Al molar ratio of 1:1. EDTA is used as a chelating agent. A few milliliters of ammonia solution were added to obtain a clear solution. Finally, a solution of citric acid (2.5 mol L^{-1} , $n(\text{citric acid}) = n(\text{Al}) + n(\text{La})$) was added to the solution containing the chelated metals. The temperature of the solution was slowly heated to 100 °C. Stirring was continued until evaporation of water lead to a transparent gel. The gel was then dried and calcined following four different steps (120 °C – 3 h; 300 °C – 3 h; 400 °C – 3 h; and 800 °C – 5 h).

The same procedure was applied to prepare LaNiO_3 with nitrates of lanthanum and nickel with a La:Ni molar ratio of 1:1.

$\text{CeO}_2\text{-Al}_2\text{O}_3$ was prepared by co-precipitation. An aqueous solution containing Ce and Al nitrates (Fluka) with a Ce:Al molar ratio of 1:2 (concentrations of 0.17 and 0.34 mol L^{-1}) was gradually added to an aqueous solution of ammonium carbonate under fast stirring. The carbonate solution was prepared in order to contain large excess of carbonates, assuring precipitation of all metallic cations. The precipitate was aged for 3 h. After centrifugation and several washing cycles with de-ionized water, the precipitated powder was dried overnight at 120 °C, then calcined at 800 °C for 5 h.

The same method was used to prepare $\text{ZrO}_2\text{-Al}_2\text{O}_3$ with nitrates of zirconium and aluminium (Aldrich and Fluka) with a Zr:Al molar ratio of 1:2.

Ni was deposited on the different supports (spinel, perovskites, mixed oxides) by deposition-precipitation using nickel nitrate $\text{Ni}(\text{NO}_3)_2 \cdot 6\text{H}_2\text{O}$ (Fluka) and urea (Sigma-Aldrich). Stirring was continued for 4 h while the temperature was increased to 100 °C in order to remove excess urea. After centrifugation and several washing with de-ionized water, the samples were dried at 120 °C overnight and calcined at 550 °C for 4 h in air.

5 wt% Ni–0.05 wt% Rh/ MgAl_2O_4 and 5 wt% Ni–0.05 wt% Rh/ LaAlO_3 were also prepared by wet impregnation of MgAl_2O_4 or LaAlO_3 with a solution containing nickel nitrate ($\text{Ni}(\text{NO}_3)_2 \cdot 6\text{H}_2\text{O}$, Fluka) and rhodium nitrate ($\text{Rh}(\text{NO}_3)_3 \cdot 2\text{H}_2\text{O}$, Alfa Aesar). Stirring was continued for 6 h. After evaporation of water, the slurry was dried at 120 °C overnight and calcined at 550 °C for 4 h in air.

Hydrotalcite-type precursors were prepared by co-precipitation. An aqueous solution containing nitrates of Ni, Mg and Al (Fluka and Sigma-Aldrich) was added dropwise to a saturated solution containing NaHCO_3 and NaOH. The

precipitate was aged for 1 h. After centrifugation and washing with de-ionized water, the deposit was dried overnight at 120 °C. The dry deposit was then calcined at 800 °C for 5 h in air.

A commercial Ni-based catalyst (HiFUEL R110, Alfa Aesar, ref. 45465) was used as reference catalyst.

Catalyst characterization

Powder X-ray diffraction patterns (XRD) were recorded using a Bruker D5005 diffractometer with CuK α radiation at $\lambda = 1.5418 \text{ \AA}$.

Elementary analysis of the fresh catalysts was performed by ICP-AES using a Jobin Yvon Activa Spectrometer D ICP-OES to determine the Ni loading.

Specific surface areas (SSA) were measured by nitrogen adsorption on catalysts at $-196 \text{ }^\circ\text{C}$ on a BELSORP-Mini (Bel-Japan).

Thermal analyses (DTA-TGA) were performed in air with a SETARAM analyser equipped with a mass spectrometer for online gas analysis. The samples were placed in a Pt crucible and heated at $10 \text{ }^\circ\text{C min}^{-1}$ under a flow of synthetic air (50 mL min^{-1}).

Catalytic activity and stability measurements

A proprietary automated six-parallel reactor technology was implemented (Fig. 1) to perform high-throughput long-term testing of the catalysts. The liquid water flow rate was controlled by a HPLC pump (Shimadzu LC 20-AD) and vaporized in a custom-made evaporator at $200 \text{ }^\circ\text{C}$, before mixing with the gaseous reactants whose flow rate was controlled by mass-flow controllers. All gas lines and valves were heated at $160 \text{ }^\circ\text{C}$ to prevent steam condensation. Six tubular quartz reactors (length 180 mm, 4 mm ID) were placed in a tubular furnace with six positions. The temperature in each reactor was measured under inert gas flow and at $700 \text{ }^\circ\text{C}$, differences of $\pm 8 \text{ }^\circ\text{C}$ between the 6 reactors were found. Taking an activation energy of 110 kJ mol^{-1} for the steam reforming of methane,²⁴ this will lead to a $\pm 10\%$ variation in the reaction rate

at $700 \text{ }^\circ\text{C}$. After mixing the reactants, the main gas stream was split into six flows, each being directed into a reactor. Special attention was given to distribute the flows equally, since the six different catalyst beds each create different pressure drops and can cause unequal flow distribution. To solve this issue, six identical stainless steel capillaries with small internal diameters ($1/16''$ OD, $0.01''$ ID, 200 mm length) were placed upstream to the reactors. The pressure drop created by the capillaries was much more important than that created by the catalyst bed. Measurement of the individual flows through the reactor showed deviations of $\pm 4 \text{ mL min}^{-1}$ for a flow of 80 mL min^{-1} per reactor. A 6-port automatic selection valve placed at the reactor exit allowed selection of the effluent of one specific reactor to be sent to a mass spectrometer for gaseous product analysis. The selection valve was automatically switched every five minutes in order to measure sequentially the performance of each reactor using an online mass spectrometer. Pressure transducers placed upstream and downstream the reactors also measured the pressure drop in each reactor being analysed, to check for a possible increase in the pressure due to extensive coke deposition.

Catalytic tests

Tests were performed at $700 \text{ }^\circ\text{C}$ and at a pressure of 1.6 bar. Prior to testing, the catalyst samples were pelletized, crushed and sieved to obtain a particle size fraction between 100 and 200 microns. Catalyst beds were composed of 20 mg of catalyst and diluted with quartz powder (100–200 microns), to obtain a similar bed length of 8 mm whatever the catalyst density. The catalysts were reduced *in situ* with a H₂–argon mixture (4:1, vol:vol) for 3 hours at $700 \text{ }^\circ\text{C}$. The reaction mixture consisted of 42% steam, 14% CH₄, 9% CO₂, 7% O₂ in an argon balance. This composition represents a model biogas containing 60% CH₄ and 40% CO₂, which is reacted with a mixture of O₂ and H₂O under the conditions O₂/CH₄ = 0.5 and H₂O/CH₄ = 3. If oxygen were supplied as air, the balance gas would be nitrogen. Argon was substituted for nitrogen because N₂ would forbid analyzing CO by mass spectrometry (same molecular ion), and Ar was also used as internal standard for quantification of products. The total flow rate of the reactant gases was 380 mL min^{-1} resulting in a gas hourly space velocity (GHSV) in each reactor of $38000 \text{ m}^3 \text{ m}^{-3} \text{ h}^{-1}$ and a weight hourly space velocity (WHSV) of $190 \text{ L (h g}_{\text{cat}})^{-1}$. Online analysis of the reactors' exit streams was performed with a mass spectrometer (MS) monitoring m/z fragments 2 (H₂), 4 (He), 15 (CH₄, this fragment was chosen rather than the molecular ion because it is nearly as intense (90%) as mass 16 in the methane fragmentation spectrum, whereas O₂ significantly contributes to mass 16, and also CO, CO₂ and H₂O to a lesser extent), 18 (H₂O), 28 (CO, corrected for the contribution of CO₂ to this fragment), 32 (O₂), 40 (Ar), and 44 (CO₂). Quantitative analysis was performed by calibrating the MS response using different partial pressures of all relevant compounds diluted in argon. The Ar signal was used as an internal standard and the other ion current intensities were

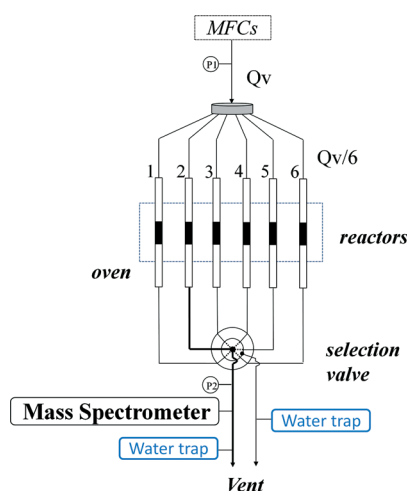


Fig. 1 Set-up for the reactors' inlet and outlet.

converted to molar flows knowing the molar flow rate of Ar and the sensitivity coefficient of each m/z fragment relative to Ar, which is constant. Accurate water quantification with a MS is difficult, but the liquid water flow rate was precisely controlled by a calibrated HPLC pump, therefore the molar flow rate of steam at the reactor inlet was known accurately.

Results and discussion

Catalyst characterization

The nickel loading and surface areas of the tested catalysts are reported in Table 1. A similar amount of Ni, around 5 wt%, was generally deposited on the catalysts, with the exception of sample NRL, which exhibited a lower loading (3.9 wt%), and sample LN (LaNiO₃ perovskite) for which the bulk nickel concentration was 26 wt%. Four catalysts (NC, NS, NA, CC) with higher Ni loadings (10–20%) and two catalysts doped with a small amount of Rh (NRL and NRM) were also included in the screening. The catalysts exhibited substantial variations in specific surface areas. It was generally high for spinel and hydrotalcite-type catalysts, with NM presenting the highest value (158 m² g⁻¹). The perovskites had lower surface areas, ranging from 2.7 to 15 m² g⁻¹. The specific surface areas of mixed oxides catalysts were 57 and 119 m² g⁻¹ for NCA and NZA, respectively.

The selection of catalysts and support for the screening was based on general trends found in the literature related to steam and dry reforming of methane over Ni-based catalysts: basic supports are preferred over acidic supports, which are prone to coking due to cracking reactions taking place on the acid sites. The basic character enhances steam activation as hydroxyl groups, which react with the coke and improve its gasification. Ceria combines the basic character with oxygen mobility properties and has also been shown to improve the gasification of coke in dry reforming reactions.

The Mg–Al–Ni hydrotalcite-type catalyst (HT) has also a basic character and a high surface area. Ni ions are initially incorporated in a mixed hydroxy-carbonate structure, then extracted upon reduction as metallic Ni, which should lead to the formation of well-dispersed Ni particles. The LaNiO₃

perovskite catalyst (LN) was intended to behave similarly (synthesis of a mixed oxide and surface reduction leading to well-dispersed metallic Ni particles on LaNi_{1-x}O₃), but its very low SSA might forbid a good dispersion of Ni.

Since Ni²⁺ tends to react with alumina at high temperature to form the inactive spinel NiAl₂O₄ (and any possible sub-stoichiometric Ni_{1-x}Al₂O_{4-x} composition), MgAl₂O₄ and ZnAl₂O₄ spinels were used as supports because they combine a high surface area, a basic character in the case of MgAl₂O₄, whereas Mg²⁺ and Zn²⁺ ions occupy the crystallographic positions where Ni²⁺ ions migrate in the alumina structure. Therefore, these supports should prevent, or at least limit, the migration of nickel in the support.

Six-parallel reactor set-up validation with a commercial catalyst

In order to obtain reliable information about the catalyst performance and to assess the repeatability of the results, the set-up was validated by testing the same mass of commercial Ni-based catalyst in the 6 reactors (Fig. 2).

Methane was fully converted at $t = 0$ in all the reactors, but declined steadily. The production of hydrogen and of carbon monoxide was similar in each reactor at full conversion and decreased with decreasing methane conversion. At $t = 0$, the production of H₂ was of about 1 μmol min⁻¹ and that of CO about 0.3 μmol min⁻¹. The H₂/CO ratio remained around four until the sharp drop in the methane conversion. The deactivation profiles were similar: a slow deactivation was observed followed by an abrupt loss of the activity although scattered over a range of about 5 h. As the methane

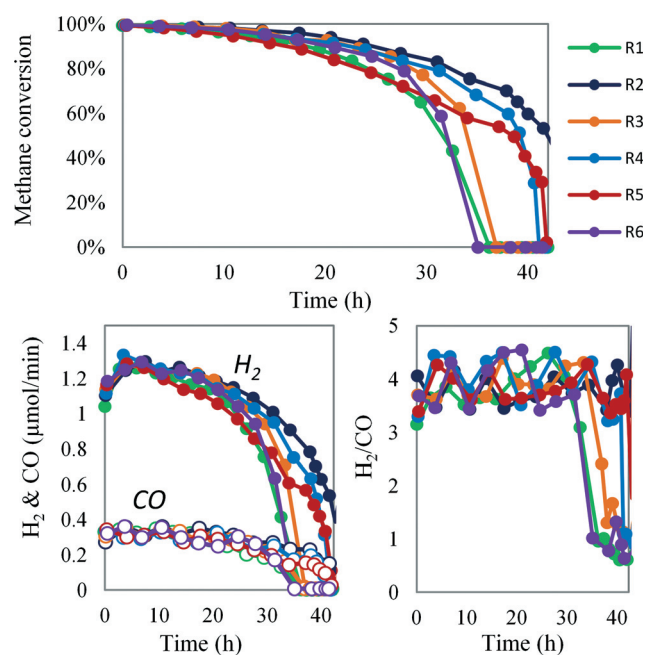


Fig. 2 Autothermal reforming of model biogas (60%–40%; CH₄–CO₂) at $T = 700$ °C with $S/C = 3$, $O/C = 0.5$. a) Methane conversion (%), b) H₂ and CO production, and c) H₂/CO ratio over time.

Table 1 Ni loading and specific surface area of prepared catalysts

Catalysts	Code	Ni loading (%)	BET surface area (m ² g ⁻¹)
5 wt% Ni/MgAl ₂ O ₄	NM	5.1	158
5–0.05 wt% NiRh/MgAl ₂ O ₄	NRM	5.1	118
5 wt% Ni/ZnAl ₂ O ₄	NZ	4.5	99
5 wt% Ni/LaAlO ₃	NL	4.5	15
5–0.05 wt% NiRh/LaAlO ₃	NRL	3.9	7.8
LaNiO ₃	LN	26	2.7
5 wt% Ni/CeO ₂ –Al ₂ O ₃	NCA	5	57
5 wt% Ni/ZrO ₂ –Al ₂ O ₃	NZA	5	119
Hydrotalcite-type precursor	HT	4.3	116
NiO/CaAl ₁₂ O ₁₉	NC	14	10
20 wt% Ni/SiO ₂	NS	20	40
20 wt% Ni/Al ₂ O ₃	NA	20	123
Commercial catalyst	CC	10	16

conversion fell to zero, the hydrogen and monoxide productions were simultaneously suppressed.

Fig. 3 shows the composition (on a dry basis, *i.e.* not taking the steam into account) of reactor 6 exit stream. With an S/C ratio of 3, the steam is in large excess and is only partly consumed during the reaction. H₂ and CO molar fractions reach about 40% and 10%, respectively, at full methane conversion. Complete conversion of methane and oxygen is observed during the first hours. After 15 hours, the methane molar fraction increases while the oxygen molar fraction remains zero. When the methane molar fraction reaches 10% (corresponding to 60% conversion), the oxygen conversion is no longer complete. Methane and oxygen conversions suddenly drop to zero and hydrogen and carbon monoxide productions drop similarly. The catalyst is fully deactivated. Similar behavior was observed on all the reactors.

The catalyst stability in the six reactors varied around 40 ± 5 hours. This corresponds rather well to the variation of the methane steam reforming rate of ±10% which can be attributed to slight differences in the reactor temperatures, catalyst loadings and reactant flow rates. The six deactivation profiles, however, were sufficiently similar to allow unambiguous discrimination between fast-deactivating and stable catalysts.

The role of oxygen in the catalyst deactivation is evidenced by the experiments shown in Fig. 4. After 43 hours, oxygen was removed from the feed gas, and the catalyst in reactors 2 and 5 started to convert methane again. Before oxygen removal, the O₂/CH₄ ratio in the feed stream is 0.5, which means that 25% of the methane is immediately burnt into CO₂ at the reactor inlet (the stoichiometry for methane combustion is O₂/CH₄ = 2). Oxygen is totally converted and Ni is likely to be oxidized in the CH₄ combustion zone, but the metallic Ni still present downstream in the reactor ensures the reaction of the remaining methane with steam, and possibly with CO₂. As soon as the catalyst is sufficiently deactivated that some of the oxygen is unconverted (this should theoretically happen when the methane conversion falls below ≈25%, but it might also happen before since NiO is not a very good catalyst for methane combustion),²⁵ the

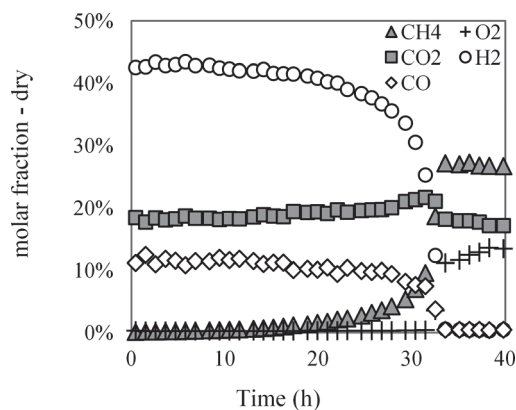


Fig. 3 Dry outlet gas concentrations during autothermal reforming of model biogas (60%–40%; CH₄–CO₂) at $T = 700$ °C with S/C = 3, O/C = 0.5.

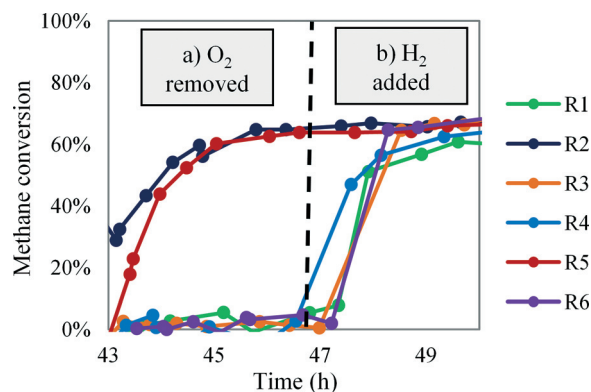


Fig. 4 Methane conversion (%) during autothermal reforming of model biogas: a) (60%–40%; CH₄–CO₂) at $T = 700$ °C with S/C = 3 and in the absence of oxygen and b) (60%–40%; CH₄–CO₂) at $T = 700$ °C with S/C = 3 and addition of hydrogen.

gaseous oxygen will rapidly oxidize the metallic Ni and deactivate the catalyst. These catalysts will not be reactivated when O₂ is removed from the feed because Ni is fully oxidized and unable to catalyse the steam reforming reaction. In reactors 2 and 5 the catalyst was not completely deactivated and still produced small amounts of H₂ + CO, which suggests that some metallic Ni was still present, and upon oxygen removal the hydrogen produced by methane steam reforming was able to reduce again the oxidized Ni. After *ca.* 47 hours, hydrogen was added to the feed. Methane conversions ranging from *ca.* 65 to 70% were observed in all the six reactors. Oxidation of Ni appears to play an important part in the deactivation process.

Catalyst screening for ATR of model biogas

The results of catalyst screening in terms of methane conversion are shown in Fig. 5.

The catalyst performance at 700 °C *versus* time-on-stream depended strongly on catalyst composition.

Comparing the behaviour of the ≈5 wt% Ni catalysts loaded on different supports, our screening shows that the support properties that were shown to be beneficial in methane steam reforming do not appear as relevant when

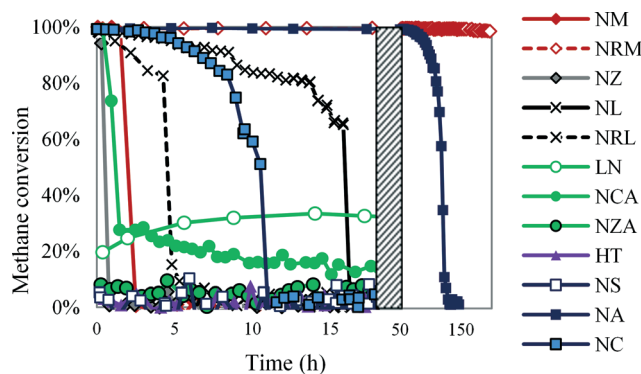


Fig. 5 Methane conversion (%) during autothermal reforming of model biogas (60%–40%; CH₄–CO₂) at $T = 700$ °C with S/C = 3, O/C = 0.5.

autothermal reforming of methane is involved: NM, NZ and NCA exhibited full initial conversion but deactivated within 2 hours, while NZA deactivated almost instantly. HT was found fully inactive, but the catalyst reduction temperature was probably too low to reduce and extract Ni from the mixed-oxide structure, since the Ni reduction in Ni-Mg-Al hydroxalcalite catalysts has been shown to take place between 750 and 900 °C.²⁶ NL catalyst (5% Ni/LaAlO₃) deactivated more gradually and was fully deactivated after 16 h. Therefore LaAlO₃ appears as an interesting support, despite its low SSA.

Increasing the Ni loading was expected to delay the catalyst deactivation, since more Ni is available in the reactor, provided that it is dispersed enough and that the support exhibits the appropriate acid-base properties. This was generally verified since all 5 wt% Ni catalysts except NL deactivated before CC (10% Ni) and NC (14% Ni) catalysts, which in turn deactivated before NA (20% Ni). A noticeable exception was NS (20% Ni/SiO₂), which deactivated so rapidly that no methane conversion was observed, evidencing that SiO₂ is not a good support in this reaction. LN catalyst (26 wt% Ni) revealed peculiar performance, with a moderate but constant methane conversion ($\approx 30\%$), which gradually dropped to zero after 20 h (not shown), probably due to the negative combination of high Ni loading and very low surface area.

Rh doping had a very strong influence on the stability of NM since NRM still fully converted methane after 200 h of reaction. In contrast, NRL deactivated before NL, which might be attributed to the very low surface area of the catalyst after its second impregnation with Rh. Ni-Rh bimetallic catalysts have been shown to exhibit enhanced stability for methane tri-reforming²⁷ and dry-reforming reactions,²⁸ similar to Ni-Pd^{29–31} Ni-Pt³² and Ni-Co formulations.^{33,34}

With the exception of LN, the deactivation profiles of all the tested catalysts were rather similar to that of the commercial catalyst: the methane conversion decreased slowly for a certain time, then rapidly fell to zero. Hydrogen production *versus* time is shown in Fig. 6. The order of deactivation time NS-HT-NZA < NZ < NCA < NM < NRL < NC < NL < NA < NRM was observed.

The hydrogen production profiles matched well the conversion profiles of methane shown in Fig. 5. In agreement with the low methane conversion, the reaction on LN produced much less hydrogen than the other catalysts.

The abrupt changes in the slopes of the deactivation profiles exhibited by most catalysts suggested different deactivation mechanisms for each stage. For the slow initial deactivation: nickel and/or support sintering eventually combined with coke deposition may progressively deactivate the catalysts. Our reaction conditions imply working with an excess of steam ($H_2O/CH_4 = 3$) that can promote the sintering of oxides and metals, known to be a rather slow process. However, whatever be its origin, such a slow initial deactivation cannot account for the subsequent sharp collapse in the catalytic activity. The latter might be related to the presence of oxygen in the feed stream, leading to nickel oxidation. As mentioned previously, the ATR of methane combines the

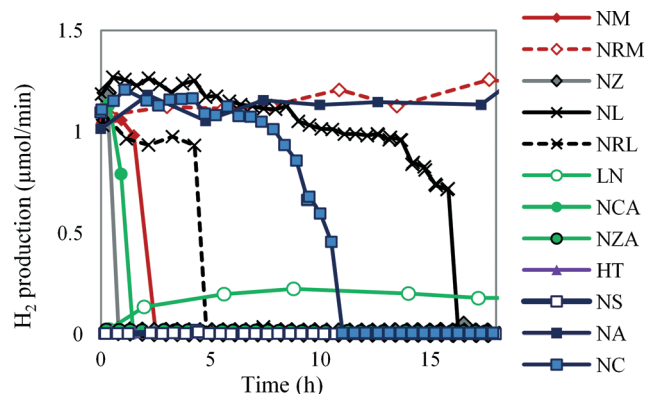


Fig. 6 Hydrogen production ($\mu\text{mol min}^{-1}$) during autothermal reforming of model biogas (60%–40%; CH_4 - CO_2) at $T = 700$ °C with $S/C = 3$, $O/C = 0.5$.

combustion of methane (to provide heat) with steam/dry reforming of the remaining methane. Since methane combustion is much faster than the reforming reactions and is strongly exothermic ($\Delta H = -801$ kJ mol⁻¹), it takes place at the catalyst bed inlet and leads to the formation of hotspots and temperature gradients along the bed.^{30,35} As shown in the case of methane partial oxidation,³⁶ the combination of high temperature and the presence of oxygen in the feed stream is likely to oxidize the nickel particles, which no longer participate in the reforming reactions. The high temperature front will diffuse further down the bed, leaving less metallic Ni available for the reforming reactions. Once the combustion zone reaches the end of the catalyst bed, the methane conversion will drop to zero.

Post-reaction characterization of catalysts showed that XRD patterns were not significantly modified compared to fresh catalysts. Fig. 7 presents the diffractograms of NM catalyst before and after the ATR reaction. Both diffractograms exhibited the characteristic lines of the spinel phase $MgAl_2O_4$, whereas no Ni or NiO lines were evidenced.

However, the small amount of catalyst in each reactor (20 mg, mixed with quartz powder) provided only a low-resolution diffractogram, which did not allow a thorough comparison of fresh and used catalyst diffraction patterns. TGA-DTA-TPO analysis of the commercial catalyst after reaction revealed two small mass losses with maxima at *ca.* 350 °C (-0.12% , exothermic) and 690 °C (-0.11% , endothermic), associated with CO_2 production in sub-ppm amounts. The CO_2 production at low temperature might be attributed to the combustion of very reactive carbon, in direct contact with Ni. The high temperature CO_2 production is endothermic and thereby suggests the decomposition of carbonates formed on the basic support. Limited carbon deposition is consistent under the reaction conditions in which the H_2O/CH_4 ratio of 3 and the high CO_2 partial pressure should prevent extensive coking (carbon can be gasified by steam and by CO_2 through the reverse Boudouard reaction³⁷). TEM examination of the deactivated commercial catalyst samples also revealed the presence of a carbon film on some Ni

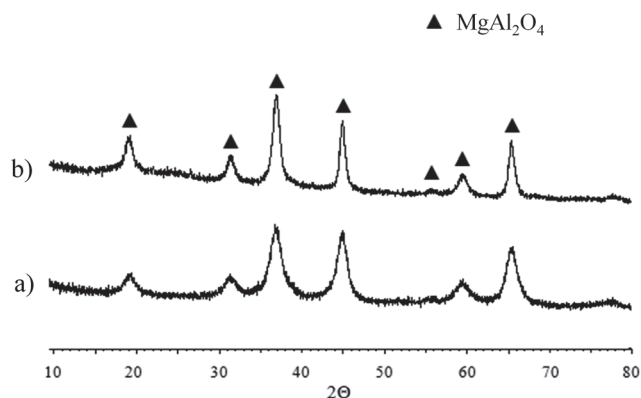


Fig. 7 X-ray diffractogram of NM catalyst a) after reduction at 700 °C and b) after deactivation.

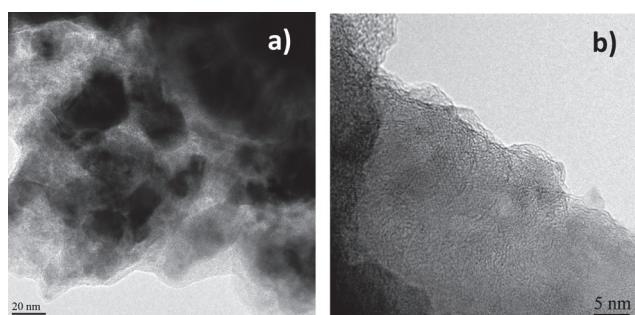


Fig. 8 TEM images of deactivated commercial catalyst after ATR reaction showing the presence of a) oxidized nickel and b) carbon deposits.

particles, although not on all of them (Fig. 8), which probably corresponds to the carbon burning at low temperature in the TGA-TPO experiments. Such carbon films are likely to participate in the slow initial deactivation, by progressively encapsulating the metal particles. There was no evidence of carbon whisker formation, also known as a potential long-term deactivation process. High resolution and electron diffraction also revealed the presence of oxidized nickel, which is clearly an issue for long-term stability in ATR.

Depending on its level of deactivation, the initially black-coloured catalyst bed exhibited after reaction a ring of light blue-green colour at its inlet, or was found fully blue-green for deactivated catalysts, which suggests the formation of inactive NiO or NiAl₂O₄. In this sense, the addition of small amounts of Rh to Ni appears to effectively promote nickel reduction and prevent bulk oxidation. Rh addition is also effective in inhibiting carbon deposition.³⁸ Therefore, a 0.05 wt% Rh addition has a positive effect on the catalyst resistance to deactivation under ATR conditions.

Conclusions

Assessing the stability of catalysts in the ATR of biogas requires long-term experiments, since catalysts might deactivate rapidly after exhibiting apparently stable performance

for several hours. A six-parallel flow reactor is a powerful tool to assess the long-term stability of six catalysts simultaneously in the ATR of biogas. A screening of catalysts was performed in a short time demonstrating an order of deactivation time NS-HT-NZA < NZ < NCA < NM < NRL < NC < NL < NA < NRM. A slow initial deactivation process could be related to some carbon deposition, but the main fast final deactivation process is likely associated with nickel oxidation. Rh promotes Ni stability and thus 5–0.05 wt% Ni-Rh/MgAl₂O₄ was identified as a robust catalyst for autothermal reforming of model biogas.

Acknowledgements

The research leading to these results has received funding from the European Community's Seventh Framework Programme ([FP7/2007–2013] under grant agreement no. 325383 (BioRobur). The authors thank Bernadette Jouguet for performing timely TGA-DTA analyses.

References

- 1 A. Demirbas, *Energy Convers. Manage.*, 2008, **49**, 2106–2116.
- 2 J. Xuan, M. K. H. Leung, D. Y. C. Leung and M. Ni, *Renewable Sustainable Energy Rev.*, 2009, **13**, 1301–1313.
- 3 J. R. Rostrup-Nielsen and J.-H. Bak Hansen, *J. Catal.*, 1993, **144**, 38–49.
- 4 P. Ferreira-Aparicio, A. Guerrero-Ruiz and I. Rodríguez-Ramos, *Appl. Catal., A*, 1998, **170**, 177–187.
- 5 J. Sehested, *Catal. Today*, 2006, **111**, 103–110.
- 6 S. Helveg, J. Sehested and J. R. Rostrup-Nielsen, *Catal. Today*, 2011, **178**, 42–46.
- 7 J. Wei and E. Iglesia, *J. Catal.*, 2004, **224**, 370–383.
- 8 P. O. Sharma, M. A. Abraham and S. Chattopadhyay, *Ind. Eng. Chem. Res.*, 2007, **46**, 9053–9060.
- 9 A. M. Gadalla and B. Bower, *Chem. Eng. J.*, 1988, **43**, 3049–3062.
- 10 K.-H. Lin, H.-F. Chang and A. C.-C. Chang, *Int. J. Hydrogen Energy*, 2012, **37**, 15696–15703.
- 11 G. Xu, K. Shi, Y. Gao, H. Xu and Y. Wei, *J. Mol. Catal. A: Chem.*, 1999, **147**, 47–54.
- 12 A. A. Lemonidou and I. A. Vasalos, *Appl. Catal., A*, 2002, **228**, 227–235.
- 13 C. Papadopoulou, H. Matralis and X. Verykios, Utilization of Biogas as a Renewable Carbon Source: Dry Reforming of Methane in *Catalysis for alternative energy generation*, ed. L. Guzzi and A. Erdöhelyi, Springer, New York, 2012, pp. 57–127. ISBN: 978-1-4614-0343-2.
- 14 Y. J. O. Asencios, J. D. A. Bellido and E. M. Assaf, *Appl. Catal., A*, 2011, **397**, 138–144.
- 15 Y. J. O. Asencios, C. B. Rodella and E. M. Assaf, *Appl. Catal., B*, 2013, **132–133**, 1–12.
- 16 O. A. Bereketidou and M. A. Goula, *Catal. Today*, 2012, **195**, 93–100.
- 17 S. Rasi, A. Veijanen and J. Rintala, *Energy*, 2007, **32**, 1375–1380.

- 18 S. Appari, V. M. Janardhanan, R. Bauri, S. Jayanti and O. Deutschmann, *Appl. Catal., A*, 2014, **471**, 118–125.
- 19 M. P. Kohn, M. J. Castaldi and R. J. Farrauto, *Appl. Catal., B*, 2014, **144**, 353–361.
- 20 H. J. Alves, C. Bley Junior, R. R. Niklevicz, E. P. Frigo, M. S. Frigo and C. H. Coimbra-Araújo, *Int. J. Hydrogen Energy*, 2013, **38**, 5215–5225.
- 21 J. Pérez-Ramirez, R. J. Berger, G. Mul, F. Kapteijn and J. A. Moulijn, *Catal. Today*, 2000, **60**, 93–109.
- 22 J. K. van der Waal, G. Klaus, M. Smit and C. M. Lok, *Catal. Today*, 2011, **171**, 07–210.
- 23 P. Laveille, G. Biauxque, H. Zhu, J.-M. Basset and V. Caps, *Catal. Today*, 2013, **203**, 3–9.
- 24 J. R. Rostrup-Nielsen, Catalytic Steam Reforming, in *Catalysis*, ed. J. R. Anderson and M. Bouchard, Springer-Verlag Berlin, 1984, vol. 5, pp. 1–117. ISBN: 978-3-642-93249-6.
- 25 O. Dewaele and G. F. Froment, *J. Catal.*, 1999, **184**, 499–513.
- 26 K. Takehira, T. Shishido, P. Wang, T. Kosaka and K. Takaki, *J. Catal.*, 2004, **221**, 43–54.
- 27 U. Izquierdo, V. L. Barrio, J. Requies, J. F. Cambra, M. B. Guñemez and P. L. Arias, *Int. J. Hydrogen Energy*, 2013, **38**, 7623–7631.
- 28 M. Nowosielska, W. K. Jozwiak and J. Rynkowski, *Catal. Lett.*, 2009, **128**, 83–93.
- 29 J. Zhang, Y. Wang, R. Ma and D. Wu, *Appl. Catal., A*, 2003, **243**, 251–259.
- 30 K. Yoshida, K. Okumura, T. Miyao, S. Naito, S. Ito, K. Kunimori and K. Tomishige, *Appl. Catal., A*, 2008, **351**, 217–225.
- 31 I. Z. Ismagilov, E. V. Matus, V. V. Kuznetsov, M. A. Kerzhentsev, S. A. Yashnik, I. P. Prosvirin, N. Mota, R. M. Navarro, J. L. G. Fierro and Z. R. Ismagilov, *Int. J. Hydrogen Energy*, 2014, **39**, 20992–21006.
- 32 L. Li, L. Zhou, S. Ould-Chikh, D. H. Anjum, M. B. Kanoun, J. Scaranto, M. N. Hedhili, S. Khalid, P. V. Laveille, L. D'Souza, A. Clo and J.-M. Basset, *ChemCatChem*, 2015, **7**, 819–829.
- 33 K. Takanabe, K. Nagaoka, K. Nariai and K. Aika, *J. Catal.*, 2005, **232**, 268–275.
- 34 X. You, X. Wang, Y. Ma, J. Liu, W. Liu, X. Xu, H. Peng, C. Li, W. Zhou, P. Yuan and X. Chen, *ChemCatChem*, 2014, **6**, 3377–3386.
- 35 J. A. C. Dias and J. M. Assaf, *Appl. Catal., A*, 2008, **334**, 243–250.
- 36 D. Dissanayake, M. P. Rosynek, K. C. C. Kharas and J. H. Lunsford, *J. Catal.*, 1991, **132**, 117–127.
- 37 H. Düdler, K. Kähler, B. Krause, K. Mette, S. Kühl, M. Behrens, V. Scherer and M. Muhler, *Catal. Sci. Technol.*, 2014, **4**, 3317–3328.
- 38 M. Nurunnabi, K. Fujimoto, K. Suzuki, B. Li, S. Kado, K. Kunimori and K. Tomishige, *Catal. Commun.*, 2006, **7**, 73–78.